THESIS

INVESTIGATIONS OF THE UNCERTAINTIES ASSOCIATED WITH HID ALGORITHMS AND GUIDING INPUT TO A NOVEL, SYNTHETIC POLARIMETRIC RADAR SIMULATOR

Submitted by

Julie I. Barnum

Department of Atmospheric Science

In partial fulfillment of the requirements

For the Degree of Master of Science

Colorado State University

Fort Collins, Colorado

Spring 2018

Master's Committee:

Advisor: Steven Rutledge

Steven Reising
Michael Bell
Brenda Dolan

ABSTRACT

INVESTIGATIONS OF THE UNCERTAINTIES ASSOCIATED WITH HID ALGORITHMS AND GUIDING INPUT TO A NOVEL, SYNTHETIC POLARIMETRIC RADAR SIMULATOR

A methodology for model evaluation against observations is presented. With the advent of polarimetric radars, the need to produce simulated radar observables from model has also become apparent, in order to directly compare the same quantities between observations and models (e.g. rain rate calculations, hydrometeor identification - HID). To the end of evaluating model performance, for both a spectral bin microphysics (SBM) scheme and bulk microphysics scheme (BMS), a novel, synthetic polarimetric radar simulator created by Matsui et al. (2017) was implemented in this study: POLArimetric Radar Retrieval and Instrument Simulator (POLARRIS). POLARRIS takes in model data and simulates polarimetric radar variables in the forward component (POLARRIS-f), and then the inverse component of POLARRIS (iPOLARRIS) utilizes retrieval algorithms that are also employed in observations to make direct 1-to-1 comparisons between model simulations and observations. This inverse component is novel in its ability to help bridge the gap between model output and observations due to the fact that model output and observations without this framework are not directly comparable.

The simulation of ice hydrometeors is not straightforward, and several assumptions are required to create polarimetric data for these species, such as the assumption of the size distribution, particle densities, particle melting, the input axis ratio, and canting angle assumptions. The last two variables are notoriously difficult to pin down for ice hydrometeors. This work aims to narrow down the appropriate inputs for axis ratio and canting angle assumptions that create the most comparable results

with observations for three ice hydrometeors: aggregates, ice crystals, and graupel for two different meteorological regimes (mid-latitude supercell and tropical, monsoon MCS). Rain was also carried through as a check on model output. Through various sensitivity tests, it was concluded that, when run through the range of potential values, changes in axis ratio had a larger impact on the resulting polarimetric data than did changes in the canting angle assumptions.

With this in mind, the 18 Z integrated hour from the 23 January 2006 monsoon MCS TWP – ICE case and the 22 Z integrated hour mid-latitude supercell from the 23 May 2011 MC3E case were simulated to help determine, for each hydrometeor type, the most appropriate axis ratio value(s) and canting angle assumptions that produced comparable results with observations. It was found using co-variance plots that, for 4ICE, the use of a singular axis ratio, mean canting angle, and degree of particle tumbling often produced differential reflectivity and specific differential phase values that converged to one value. While these values were within the observed values, they did not manage to simulate the breadth of observed values. Reflectivity values were also much too low compared to observations. SBM results, regardless of the type of input assumptions, tended to produce broader ranges for these variables, and also managed to better capture the reflectivity range seen in observations than was the case for the BMS. However, the reflectivity ranges seen in SBM were at times too expansive. The differences between SBM output and BMS output is likely due to the differing inherent assumptions in each microphysical scheme. The sensitivity of the simulated hydrometeors' polarimetric data was also probed against changing axis ratio and canting angle input assumptions. It was found that, in particular, BMS differential reflectivity values were quite sensitive to changes in input assumptions, regardless of the regime (tropical MCS vs. mid-latitude supercell).

HID was found to be the most effective method to evaluate the performance of the two different model microphysical schemes (SBM vs. BMS) with respect to observations. Input assumptions that produced the most comparable results with respect to observations for each hydrometeor were compared using HID stacked frequency by altitude (SFAD) diagrams for convective and stratiform precipitation. This analysis found that although the co-variance plots revealed many model shortcomings, the HID proved to be fairly robust, especially for MC3E. The sensitivity of the HID retrieval itself was also investigated with respect to changing inputs (i.e. the membership beta functions) to the HID algorithm. The resulting HID was fairly sensitive to changes in the inputs to HID, particularly for model simulations. Observations seemed less responsive to changes in these input assumptions to HID. Longer simulation time frames, the potential inclusion of simulated melting hydrometeors, and investigation of other radar wavelengths are all suggested to help further utilize this methodology for evaluating model microphysical schemes' abilities to accurately simulate polarimetric data and HID retrievals with respect to observations.

ACKNOWLEDGEMENTS

First and foremost, I would like to thank my advisor, Dr. Steven Rutledge, for his guidance and support throughout my journey to this point in my master's degree. His many comments, counterpoints, critiques, and suggestions have helped me to understand how to critically evaluate information and to really get at the "why" behind the science. I express my gratitude towards Dr. Brenda Dolan for her endless patience, programming help, countless discussions of the science behind this work (oftentimes long after the 5 o'clock hour had past), and her excellent sense of humor. I would also like to thank my other committee members, Dr. Michael Bell, and Dr. Steven Reising, for their time and their comments, questions, critiques, and suggestions to help improve this work.

I thank Dr. Toshi Matsui for his time in explaining how to use POLARRIS, and for the numerous e-mails sent back and forth debugging POLARRIS issues and explaining the inner workings of it. I also thank the rest of the NASA Goddard team – Dr. Wei-Kuo Tao, Dr. Takamichi Iguchi, Dr. Stephen Lang, and Di Wu - involved with this project for their time, their input, and their shared scientific discussions. Paul Hein deserves a special thanks for all the times he managed to save the day for me when I "broke" something, be that due to receiving the notorious "segmentation fault" to simpler programming issues. The rest of the radar group – Karly Reimel, Trent Davis, Dr. Brody Fuchs, Dr. Elizabeth Thompson, Dr. Doug Stolz, Dr. Weixin Xu, Kyle Chudler, and Joe Messina - all merit a huge thanks for their support and helpful conversations. Finally, I extend my deepest appreciation to my family, friends, key members of the CSU health network community – Dr. Michele Faris and Laura Whitcomb, and my boyfriend, Adam Brandt, for helping me get to this point while staying grounded, and for always believing in my ability to do the thing.

Many thanks are extended towards the members of the atmospheric science community who generously provided data for this work. MC3E CSAPR radar data was processed and provided by Alyssa Matthews (PNNL) and Dr. Angela Rowe (University of Washington). For TWP – ICE, Berrima data was provided by Dr. Scott Collis (Argonne National Laboratory) and much of the backend processing was done by Dr. Brenda Dolan (CSU). CPOL and NPOL data was provided by David Wolff (Wallops Flight Facility), where backend processing was then done by Dr. Brenda Dolan (CSU). The POLARRIS framework was created/provided by Dr. Toshi Matsui (NASA Goddard) and Dr. Brenda Dolan (CSU). NU WRF simulations were run and provided by Dr. Takamichi Iguchi. UND Citation II data was provided by Dr. Aaron Bansemer (NCAR). This work was supported by the DOE ASR grant DE-0000000SC14371.

TABLE OF CONTENTS

LIST OF TABLES

LIST OF FIGURES

CHAPTER 1: INTRODUCTION

With the advent of polarimetric radar, several improvements in observations have been made with accurately measuring rainfall, hydrometeor identification (HID), and quality controlling of radar data (Ryzhkov et al. 2005b). Dual-polarization has the benefit of helping improve weather model microphysical parameterizations, as well as the assimilation of radar data into models (Ryzhkov et al. 2011; hereafter R11). Additionally, models can help understand polarimetric radar data via quantitatively evaluating and deciphering their signatures. Models also have the ability to help us understand hydrometeor distributions in areas of convection where collecting in situ data is not straightforward, or even dangerous (R11). With all the potential benefits provided by comparisons of these types of quantities, there is then a great need to evaluate models against observations.

The importance of ensuring the accuracy of cloud-resolving models (CRMs) is critical, due to their ever-growing use in the climate research community. Several studies have developed and tested polarimetric radar simulators to evaluate CRMs for both bulk microphysics schemes (BMSs) (e.g. Vivekanandan et al. 1993; Huang et al. 2005; Pfeifer et al. 2008; Jung et al. 2008, 2010; Putnam et al., 2014 and 2017) and spectral bin microphysics (SBM) schemes (e.g. R11). The constraints in using simulated polarimetric radar variables and radar retrievals (e.g. HID) to validate a CRM's output are better than those utilized when polarimetric variables are not available (i.e. when using single radar reflectivity data, which can be calculated in a model from the 6^{th} moment of drop size distribution). To this end, this work tests the ability of a novel polarimetric radar simulator's ability to accurately reproduce radar observables with respect to observations. This simulator is termed, POLArimetric Radar Retrieval and Instrument Simulator (POLARRIS). POLARRIS, described in detail in Section 2.3, has the capability to take in model data and simulate polarimetric radar variables, which are

then run through an analysis framework identical to that applied to observations (e.g. HID, dual-Doppler analysis, rainfall retrievals). Finally, model output and observations are actually made comparable, thus allowing the opportunity to evaluate both model microphysics and the use of retrievals that have long been applied to observations.

However, there are several assumptions that have to be made when computing polarimetric variables from model output, such as wavelength, temperature, particle density, particle shape and fall mode. The various properties of rain, such as its general size, shape, canting behavior and tumbling behavior, and its particle size distributions have been studied in-depth (e.g. Pruppacher and Beard 1970; Pruppacher and Pitter 1971; Green 1975; Goddard et al. 1982; Goddard and Cherry 1984; Beard and Chuang 1987; Keenan et al. 2001; Brandes et al. 2002) and now fairly accurate polarimetric radar variable values can be calculated for that category (R11). Ice phase hydrometeors are notoriously more difficult to simulate, in part due to the fact that observations of particle shape, fall mode, and density are relatively rare for ice particle types such as graupel and aggregates. To this end, this work aims to help clarify the assumptions needed to properly simulate snow aggregates, graupel, and ice crystals. Rain will also be carried through the simulations as a check on how well POLARRIS is performing overall, given that rain should be the most straightforward to simulate (based on the extensive literature studying its various behaviors).

The above-mentioned assumptions include the values for axis ratio (which describes a particle's shape) and canting angles, which determine a hydrometeor's shape and its tendency to flutter/tumble. These have historically been difficult to determine for ice hydrometeors. Some in situ analysis has been performed for certain hydrometeor types (Garret et al. 2015, Kumjian et al. 2016), however more needs to be done to document the observed ranges in axis ratio and canting angle values. There could be large variability in these values in nature, possibly being a function of storm type or location. This all has to be captured in the simulations run with POLARRIS in

order for the resulting HID analysis to compare with what is observed. Therefore, the objective is to determine axis ratio and canting angle values for aggregates, ice crystals, and graupel that produce the closest possible output as is seen in HID analysis performed on observational data.

The sensitivity of simulated polarimetric radar variables is investigated with respect to changing inputs for axis ratio and canting angle assumptions. Since these assumptions are not as well understood for ice hydrometeors as for rain, it is important that the uncertainties and sensitivities associated with them are explored. That is, how much of an impact does a change in either the axis ratio or canting angle assumption have on the resulting radar observables, or the resultant retrieved parameters in iPOLARRIS? Thus, ideally, the gap between simulated and observed radar observables is decreased by implementing values for axis ratio and canting angle assumptions that output results from the POLARRIS framework which are comparable to observations.

Another important component of this work is the comparison of the Colorado State University (CSU HID) algorithm with model output and observations. The way in which variations in axis ratio and canting angle assumptions affect the classification of HID underscores the importance of a proper range of inputs for axis ratio to POLARRIS. Comparisons of iPOLARRIS HID output between simulations and observations helps understand the amount to which different microphysical schemes drive model results, as well as the amount to which differing regimes (where the microphysics may greatly differ) impact model results and their comparability to observations. From this, one can glean which factor may be the bigger driver in differences between observations and model output, as well as the extent to which the HID is sensitive to each of these factors. Note that the goal is to make the model simulation results comparable to observations. THE CSU HID also has to make some assumptions to retrieve hydrometeor types in a 3D radar volume. This means it cannot be taken as truth, thus

this work is focused solely on improving the comparability of simulated data results to observations through the POLARRIS framework.

One could make the argument that to evaluate the hydrometeor identification of the model against observations, the intermediate step of creating a radar forward model simulator is unnecessary. Not only does it introduce more uncertainty and potential for error, but the model outputs mixing ratio values for each hydrometeor type for every point in the 3D grid. Combined with the synthetic reflectivity field, this could be sufficient to classify hydrometeors. While true, there's more merit to what is done in this thesis with the creation of a radar forward model simulator than simply comparing model output and radar output apples-to-apples. Simulating polarimetric radar variables also allows for evaluation of the model microphysics, as to how they are able, or unable, to reproduce known polarimetric radar signatures (e.g., the Z_{dr} arc that appears because of the presence of large drops at the leading edge of convection created due to size sorting processes, or the Z_{dr} column showing the presence of supercooled liquid water drops lofted above the 0° C level). In doing this, we gain valuable information that helps to identify regularly-occurring model errors, which in turns helps to improve the model microphysics. It also then, in a sense, allows for the evaluation of the utility of an HID algorithm. Simulating polarimetric radar variables also, as has been mentioned already, allows for evaluation of polarimetric radar signatures in regions of storms from which it's not straightforward, or not practical, to obtain in situ observations (e.g., tornado debris region or graupel/hail regions). Finally, as will be shown in the results, while the HID algorithm used is highly dependent on the reflectivity, there are changes that are introduced in the classification results whenever the differential reflectivity and specific differential reflectivity ranges are modified (via changes in axis ratio and canting angle assumptions, or in manual modification of the HID algorithms themselves). Hence, although we glean a good amount of information with the synthetic reflectivity field already output by the model, it is worthwhile to take the next step of trying to pull out the

other polarimetric radar variables as well. Thus, although the introduction of a forward simulator introduces uncertainties of its own, the potential benefits gained from doing so merits the effort.

The final component of this work involves further probing the sensitivity of the HID algorithm, and investigating the impact of modifying inputs to HID (based on analysis performed on observations) on resultant HID retrievals. Membership beta functions (MBFs, described in more detail in section 2.2) visualize the ranges that polarimetric radar variables and temperature occupy for specific hydrometeors types. The MBFs are modified in iPOLARRIS and applied to both observations and simulated POLARRIS-f output to better fit results from observations used here in. With these modified MBFs, the HID calculations are rerun for both model output and observations, where the impact of these modified MBFs can be studied. Thus, the same questions as mentioned earlier are probed here as well (i.e. to what extent is the HID classification affected by each microphysical scheme, by each regime, to what extent does the model output match what is seen in observations).

However, with these modified MBFs, new questions arise, including what effects does the chosen inputs to the HID itself affect the HID classification process? Are there certain hydrometeors that are more sensitive to changes in these inputs than others? Is one microphysical scheme (BMS vs. SBM), or regime, more sensitive than the other to these changes? In doing these simulations, and simulations with the original inputs to HID, this work demonstrates that comparing model-derived HIDs to observed HIDs is an effective way to validate the cloud model's microphysical parameterizations, as well as an effective means for characterizing the uncertainty in the CSU HID. Additionally, these tests allow the evaluation of whether the fit between model results and observations is dependent more so on the regime in question, or rather on the type of microphysics scheme employed. Note that due to the limited nature of the locations and times chosen to simulate in the POLARRIS framework, this work makes no attempt to

actually “improve” the CSU HID (which is the HID used in POLARRIS). Rather the aim is to probe the sensitivity of of HID classification to changing MBF functions.

1.1. ORGANIZATION

The organization of this master’s work is as follows. In Chapter 2, important background components to the research are outlined, including an overiew of differences between the two different microphysics scheme employed here in, an explanation of theoretical scattering simulations, the CSU HID, a description of POLARRIS, and some background on the simulated cases. In Chapter 3, the methodology from the initial data quality control (QC), up through comparisons between POLARRIS analysis using simulations and actual observations is discussed. In essence, the process to get to that end point is explained. From there, Chapter 4 details the results, including important findings related to the various sensitivity tests, and the MBF modifications in CSU HID. Chapter 5 wraps up conclusions and discusses areas for future research and other questions brought up by this work.

CHAPTER 2: BACKGROUND

In this chapter, we explore fundamental concepts related to model microphysical schemes, the simulation of polarimetric radar variables and discussion of polarimetry, as well as the background on the HID implemented in this study, POLARRIS, and field campaign cases that relate to this work. This background knowledge serves as a primer for the methodology employed in Chapter 3. Note that the dual-Doppler background information is given primarily because the results from those analyses were used to characterize echoes, as well as being used to facilitate initial comparison between model results and observations. This was done to ensure the most comparable results between WRF simulation results (for both 4ICE and SBM) and observations.

2.1. MODEL AND MICROPHYSICS SCHEMES

There are two basic schools of thought when it comes to implementing a microphysical scheme, that of using BMSs, and that of SBM schemes. POLARRIS is set up to be able to take in NASA-Unified Weather Research and Forecasting (NU-WRF) model output that implemented either of these microphysics schemes (for more information on WRF run configurations, see Table 2.1). Both have some similarities, however they both also evolve very differently and do not have a similar method for treating, for example, a hydrometeor's size distribution. This has the potential to then affect the simulated radar observables, and thus the HID classification. To understand what is being compared later on between POLARRIS output and observations, an overview of the two considered types of microphysics scheme is warranted.

Khain et al. (2015) summarize the most up-to-date information on differences between bulk microphysics and SBM. Bulk parameterizations are significantly less computationally expensive/more computationally efficient (i.e. they require less memory and run much faster than SBM) when compared to SBM due to the fact that they

parametize many aspects of cloud properties. The deeper reason, however, behind bulk microphysics efficiency is due to the fact that the microphysical equations are related to the number of particle size distribution (PSD) moments, and not related specifically to PSDs of various hydrometeors. Single-moment/one-moment, and two-moment schemes, which predict mass content, and mass content and number concentrations (usually), respectively, are the most common. Sometimes a three-moment scheme is used, wherein the predicted variables are (usually) number concentration, mass density, and reflectivity. Every PSD is represented by mathematical equations that are only dependent on a few parameters. Though there are now several different flavors of bulk microphysical schemes, every single one assumes a certain shape for the PSDs of individual hydrometeors. Typically, the shapes are approximated by a gamma or an exponential distribution (Khain et al. 2015).

The particular bulk microphysics scheme employed here in is the single-moment four-ice class (1M 4ICE) that was created for the Goddard Cumulus Ensemble (GCE) model (Lang et al. 2014; Tao et al. 2016). The 1M 4ICE scheme used in the GCE is built upon modifications made to the Goddard 1M three-ice (3ICE) class bulk microphysics scheme (Lang et al. 2007; Lang et al. 2011). The above BMSs are based upon work done in Lin et al. (1983), with additional features brought in from Rutledge and Hobbs (1983, 1984). Included in 4ICE is cloud ice, snow, graupel, and hail-frozen drops (Lang et al. 2011). While the above papers have provided an excellent basis on which to create the improved BMS in Lang et al. (2011), they have their limitations (e.g. having arbitrarily set thresholds for graupel initiation; Rutledge and Hobbs 1984). Work has been done to modify some of these assumptions and make them more realistic (Lang et al. 2007; Lang et al. 2011). Hail accounts for large reflectivity values and higher fall speeds compared to graupel, and its inclusion allows the Goddard 1M BMS to cover a wider range of meteorological situations than if graupel were upgraded to a two-moment scheme (Lang et al. 2014).

While being more computationally taxing, SBM makes its goal that of simulating microphysics and precipitation processes more accurately (e.g. closer in line with what is observed in nature) for various cloud types. In SBM, PSDs do not need to be assumed, but rather are solved by a bin model arrangement, where microphysical processes lead to constantly changing particle concentrations as a function of size. That is, where 4ICE prescribes a set semi-empirical size distribution for PDFs, SBM allows it to develop for each particle size. This makes SBM more computationally taxing than 4ICE, since there are no assumptions made about how particles are distributed in the various assigned bins.

The SBM microphysical package utilized in this work is the Hebrew University Cloud Model (HUCM) SBM (Khain and Sednev 1995; Phillips et al. 2007; Khain et al. 2011; Iguchi 2012a and 2012b). Within HUCM's SBM cloud hydrometeors there is one liquid hydrometeor type (water droplets, ranging from cloud droplets to precipitation-sized droplets), and six ice hydrometeor types (ice crystals, comprised of plates, columns, and dendrites; snow aggregates; graupel; and hail). Aerosols acting as cloud condensational and ice nuclei are also included (Khain et al. 2011; Iguchi et al. 2012a, 2012b). PSDs of individual hydrometeors are described with 43 doubling mass bins (Khain et al. 2011; Iguchi et al. 2012a).

2.2. POLARIMETRIC RADAR OBERVABLES

Before delving into the methodology used to simulate polarimetric radar variables, a discussion on the variables to be simulated is warranted. Radar reflectivity is the most basic of the variables, and the most widely-used variable, considering it was an observable that could be calculated before the advent of polarimetric radar. Radar reflectivity is sensitive to the size and the concentration of particles (as well as the phase of particles). As such, large, wet hail will have much larger reflectivity values than drizzle or ice crystals, for example. Similarly, a region of heavy rainfall would have high

reflectivity, as would heavy rainfall mixed with hail (the latter of which is distinguishable with the inclusion of specific differential phase, which will soon be defined). As is defined by Bringi and Chandrasekar (2001),

$$Z_h = \frac{\lambda^4}{\pi^5 |K_p|^2} \int |S_{hh}(r, D)|^2 N(D) dD \quad (1)$$

where λ is the radar's wavelength, S_{hh} is the horizontal component of the transmitted and backscattered waves, K_p is the particle's dielectric constant, D is the particle's diameter, and N(D) is the PSD for the range of diameters. To calculate reflectivity for a vertically-polarized wave, the calculation is quite similar, where S_{hh} is instead replaced by S_{vv}. Since S_{hh} scales approximately as D^6 for Rayleigh conditions, this substitution ($S_{hh} \cong D^6$) can made made into Eqn. 1, yielding

$$Z_h = \frac{\lambda^4}{\pi^5 |K_p|^2} \int D^6 N(D) dD. \quad (2)$$

Thus, Z_h can be said to represent the sixth moment of the particle size (Bringi and Chandrasekar 2001). In Eqns. 1 and 2, Z_h has units of $mm^6\ m^{-3}$. Radar reflectivity, depending on the incident wavelength, can measure anything from fog to very large, wet hail, and the reflectivity values therefore can range several orders of magnitude. To circumvent this issue, and to make values more physically comprehensible, logarithmic values are employed:

$$Z_h = 10 \log_{10}(z) \quad (3)$$

where z is the reflectivity in linear units ($mm^6\ m^{-3}$), and Z_h is the logarithmic radar reflectivity, measured in units of dBZ (Rinehart 2010).

Differential reflectivity is simply the ratio of the horizontal to vertical power returned to the radar from hydrometeors (given in dB). That is, as is given in Bringi and Chandrasekar (2001) (for matrix form, 4, and logarithmic form, 4a),

$$Z_{dr} = \frac{\int |S_{hh}(r,D)|^2 N(D) dD}{\int |S_{vv}(r,D)|^2 N(D) dD} \quad (4)$$

$$Z_{dr} = 10\log_{10}\left(\frac{Z_h}{Z_v}\right) \quad (5)$$

where Z_v is calculated in the same way as Z_h in Eqn. 1. Differential reflectivity is a function of size, shape, and particle phase. Z_{dr} measurements are particularly useful for determining particle shape. If the backscattered components of both the horizontal and vertical components of a wave are approximately equal, Z_{dr} tends towards zero. This would be the case for drizzle, or tumbling hail (where the particles in a radar volume look like spheres to the radar). However, with increasingly oblate axis ratios ($a/b < 1$), more energy is scattered back to the radar in the horizontal direction than in the vertical, which causes Z_{dr} to increase. This would be the case for large raindrops, which begin to flatten out as they increase in size (this is shown in Fig. 2.1, for rain drops). Note that axis ratio is also known as aspect ratio, or the ratio of the length of the vertical to horizontal axis. A value of one indicates the same length in the horizontal and vertical axes, or a sphere. A value of less than one indicates an oblate, or flattened (e.g. like a pancake) particle. A value greater than one indicates a prolate particle (e.g. such as a vertically aligned needle).

Specific differential phase is different from reflectivity and differential reflectivity in that its measurement does not depend on the strength of the received backscattered energy, but rather it depends on the phase of the received signal (Rinehart 2010). The electromagnetic (EM) energy emitted by a radar travels much faster through air than it does through ice, and especially through water. As the EM energy passes through, for example, raindrops, since there is more dielectric material in the horizontal than in the vertical, the horizontal component of the EM wave begins to lag behind the vertical component of the EM wave, which had less dielectric material to pass through. Thus, when the backscattered energy reaches the radar again, the phase of the horizontal component of the wave will lag that of the vertical component. This effect becomes more and more noticeable with increasing concentrations of liquid water and ice in a

volume of air. From this, a phase difference can then be measured, which is referred to as the differential propagation phase (Rinehart, 2010). This quantity is represented as the degree difference in phase shift between the horizontal and vertical component, and is given by

$$\varphi_{dp} = \varphi_{hh} - \varphi_{vv} \tag{6}$$

where the subscript hh refers to horizontally-polarized received signal, and the horizontally-polarized transmitted signal. The convention is the same for the subscript vv, but this refers to a vertically-polarized signal (Rinehart 2010). This quantity is dependent upon the length chosen for the range gate, as well as the concentration of particles in the range gate (i.e. the intensity of precipitation), and a particle's orientation/shape as it falls. The problem with this quantity, as given by Otto (2007) is that it is cumulative, and the longer a ray travels, the larger the value (usually) becomes. Identifying the exact region of heavy precipitation then becomes difficult. Additionally, at low rain rates and low elevation angles, the signal can become quite noisy. Reflectivity gradients can also affect the value of differential phase. However, this measurement is also not dependent on the power of the signal, and is not affected by signal attenuation, or calibration errors in a radar (Otto 2007).

In order to address these issues in differential phase, the quantity specific differential phase (K_{dp}) was created:

$$K_{dp} = \frac{\varphi_{dp}(r_2) - \varphi_{dp}(r_1)}{2(r_2 - r_1)} \tag{7a}$$

where K_{dp} is essentially a range derivative of ϕ_{dp} and is given in ° km^{-1} (Bringi and Chandrasekar 2001; Rinehart 2010), where the factor of 2 accounts for the outgoing and incoming signal. Though K_{dp} has several qualities that make it a desirable quantity (as mentioned below), the process that has to be done before the above calculation of K_{dp} can take place makes this radar observable sometimes difficult to obtain. That is, phase folding in ϕ_{dp} first has to be unwrapped, then a threshold is placed on the data to

ensure only good values of K_{dp} appear (usually a minimum allowed correlation coefficient – defined shortly – value), and then some sort of low pass filter is then applied to ϕ_{dp} to help take out some of the wild variations that can occur in the data, especially in the case of strong convection (Otto 2007). Finally, one must select a path length over which to calculate K_{dp}, the value of which determines the amount of smoothness in the final field. Only after steps such as these can K_{dp} then be calculated from Eqn. 7 (Otto 2007).

K_{dp} can also be defined in two other ways, where these two relationships show how K_{dp} is proportional to the liquid-water content and to the ice-water content. The equation relating K_{dp} to liquid water content is given in Bringi and Chandrasekar (2001) as

$$\mathrm{K_{dp}} = \left(\frac{180}{\lambda}\right) 10^{-3} \mathrm{CW}(1 - \bar{\mathrm{r}}_{\mathrm{m}}) \tag{7b}$$

where λ indicates the chosen radar wavelength (m), C≅ 3.75 is a dimensionless unit and is independent of the radar wavelength chosen, $\bar{r}_{\mathrm{m}}$ is the mass-weighted mean axis ratio, and W is the rain-water content (i.e. the liquid water content) and is defined by Bringi and Chandrasekar (2001) as the following equation:

$$\mathrm{W} = \left(\frac{\pi}{6}\right) \rho_w \int_0^\infty D^3 N(D) dD \tag{7c}$$

where ρ_w is the density of water and is set to 1.0 g cm^{-3}, D is the particle diameter, and N(D) is the PSD. In the form where K_{dp} is proportional to the ice-water content, K_{dp} is given in Bringi and Chandrasekar (2001) as

$$\mathrm{K_{dp}} = \left(\frac{180}{\lambda}\right) 10^{-3} \mathrm{C}\rho_{\mathrm{p}}(\mathrm{IWC})(1 - \mathrm{r}) \tag{7d}$$

where λ indicates the chosen radar wavelength (m), C≅ 1.6 (g cm^{-3})$^{-2}$, ρ_p is the particle density (g cm^{-3}), IWC is the ice-water content (g cm^{-3}), and r is the particle radius.

K_{dp}, as was the case with ϕ_{dp}, is not dependent on the calibration of the radar, any attenuation of the radar signal, or beam blockage. It is instead dependent upon the particle size, phase (since the index of refraction is different from water to ice), and particle shape/orientation. It is also inversely dependent on λ (see eqns. 7b and 7d). Thus, as the larger wavelengths are considered, the overall magnitude of K_{dp} values decreases. Since K_{dp} is not a path integrated quantity, its readability and usefulness in locating areas of heavy precipitation are more useful than ϕ_{dp}. K_{dp} is particularly useful in determining locations of heavy rain, and in conjunction with Z_{dr}, areas of heavy rain mixed with hail. Since hail tumbles as it falls, the random orientation of hail appears to the radar as if they were isotropic particles (i.e. spherical particles). K_{dp} is insensitive to these types of particles, since there is not a large difference in phase between horizontally- and vertically-polarized waves travelling through a region of spherical particles. However, the rain is likely to be fairly oblate (if the drops are large), and thus a positive phase shift will still occur in those volumes of heavy rain with hail. Hence, K_{dp} is helpful for locating areas of heavy rain, regardless of the presence or not of large hail, because of its insensitivity to spherical particles and because it is proportional to liquid water content. Further confirmation of the presence of hail and rain can also be verified if that region shows high Z_h and low, or near zero, Z_{dr} values. Negative values of K_{dp} can also occur if a particle has its larger axis oriented in the vertical rather than in the horizontal, such as conical graupel or vertically aligned ice crystals such as those aligned in a strong electric field (Caylor and Chandrasekar 1996; Rinehart 2010).

The last simulated quantity is the co-polar correlation coefficient. This is given in Bringi and Chandrasekar (2001) as

$$|\rho_{hv}| = \frac{|\langle nS_{hh}S_{vv}\rangle|}{(\langle n|S_{hh}|^2\rangle\langle n|S_{vv}|^2\rangle)^{1/2}} \tag{8}$$

where n is the number of particles per unit volume. Rinehart (2010) gives a good overview of this radar observable. Correlation coefficient describes the correlation

between the vertically- and horizontally-polarized signals at a point in space, at one exact time. This quantity is not sensitive to the radar calibration or propagation effects. However, it is sensitive to noise, and shape/orientation of particles in the volume. In the instance where the horizontally- and vertically-polarized signals are perfectly correlated, the co-polar correlation coefficient value would be 1.0. Drizzle almost attains this value, though is slightly lower than 1.0 because not all drizzle is perfectly spherical. Rain has a lower value yet, although it is generally greater than 0.95. In the case of irregularly-shaped ice crystals, snow, and other frozen hydrometeors this value depresses even more to almost 0.8. Additionally, non-meteorological targets, such as insects or ground clutter, depress ρ_{hv} values to usually less than 0.9. In the mixed-phase region of storms, ρ_{hv} is usually depressed, due to the mixtures of ice and water hydrometeors which have different dielectric constants and different liquid (or liquid equivalent) water contents. Water and ice hydrometeors are also usually shaped very differently, and do not necessarily tumble or cant in the same fashion. Thus, ρ_{hv} can be used to identify rain from ice, from non-meteorological targets (Rinehart 2010).

Simulating accurate values of ρ_{hv} can be quite difficult simply because it is not always straightforward to capture the true range of observed axis ratios, unless there is a situation with a homogeneous set of particles (which rarely occurs in nature). In particular, the correlation coefficient is challenging to simulate in mixed-phase regions. There are not only axis ratios of various degrees of eccentricity (i.e. some particles may be quite oblate, some nearly spherical, and some even slightly prolate), but there are also various mean canting angles and tumbling behaviors occurring, various sizes of the particles in general, as well as changing dielectric constants due to the fact that it is a mixed-phase region (Zrnic et al. 1994). These all heavily influence the depression of ρ_{hv} in mixed-phase precipitation.

2.3. THEORETICAL CALCULATIONS OF POLARIMETRIC RADAR OBSERVABLES

The forward component of POLARRIS (POLARRIS-f) uses the methodology described herein to calculate synthetic polarimetric radar variables. More on the exact details of how this process relates to POLARRIS-f are given in section 2.5.

Carrying out theoretical scattering simulations involves the input of transition (T) matrices into Muller matrices to calculate radar moments (Barber and Yeh 1975, Vivekanandan et al. 1991). Essentially, as Matsui et al. (2017; hereafter M17) summarize the complicated mathematics in Vivekanandan et al. (1991), "the effect of a scattering field on the polarization can be determined by constructing the Stokes vector for the input radiation field and applying Mueller matrix to obtain the Stokes vector of the radiation leaving the system", where the set of values that make up the Stokes parameters defines the electromagnetic radiation's polarization state. T-Matrix calculates the 2x2 scattering matrix (phase and amplitude). That is, the T-Matrix gives the resultant backscattering cross-section of single hydrometeor of a given size (Vivekanandan et al. 1991). The T-Matrix calculations are performed for an arbitrary non-spherical dielectric body (Barber and Yeh 1975). Hence, required inputs to the T-matrix for a specific hydrometeor type include particle diameter (specifically, equivalent volume spherical diameter), axis ratio, temperature, radar wavelength, and particle bulk density.

The important variables for discussing tumbling tendencies of particles are the mean canting angle θ (the average degree at which a particle is tilted during free fall), and the standard deviation of the canting angle σ (the degree to which a particle flutters or tumbles as it falls). The importance of the particular canting angle distribution (i.e. the assumed shape of the distribution) to changes in simulated radar observables is not explored here in, but could be investigated in future studies. The canting angle distribution can be simplified to a one-dimensional distribution, where generally a

Gaussian distribution is assumed (R11; Putnam et al. 2017; Kollias and Tatrevic 2017). This distribution is employed in this work. Of particular interest is identifying the most appropriate ranges for axis ratio and canting angle distributions that result in the most realistic radar observables. Thus, several different sets of assumptions for these variables will be input to the T-Matrix, Mueller matrix framework.

Transformations are then applied to the resulting 2x2 T-matrices, for one radar elevation angle, for a given canting angle distribution, and for a given axis ratio assumption, based on the scattering angle of the incident wave. The result of this is a single-particle 4x4 Mueller Matrix. In the case of SBM, the PSD is explicitly expressed through 43 doubling mass bins. These mass bins are integrated based on how the model evolved that hydrometeor's particle size distribution (PSD). For 4ICE simulations, the PSD is prescribed. There are 70 defined effective radii (which describe the distribution of mass in the prescribed PSD). For each of those potential forms of the PSD, results are integrated over size. From these integrations results a size-integrated Mueller matrix for that hydrometeor species (Vivekanandan et al. 1991; M17). Just as the T-matrix outputs results for a single hydrometeor, the Mueller matrix also outputs a single value of a radar moment for a given size distribution, or "radar volume". In other words, the assumed size distribution resides within that particular radar volume. Note that, after integrating over size, the Mueller matrices for 4ICE are scaled by the corresponding model mixing ratio for that hydrometeor. For SBM, each mass bin (after the model has evolved the hydrometeor's size distribution) is scaled by the output model mixing ratio prior to integration over the mass bins. In order to obtain mixtures of variables, the size-integrated Mueller matrices for SBM and the Mueller matrices calculated for 4ICE were then summed over all species. Following this integration step, polarimetric radar observables (reflectivity, Z_h, differential reflectivity, Z_{dr}, specific differential phase, K_{dp}, and correlation coefficient, ρ_{hv}) are then calculated.

2.4. COLORADO STATE UNIVERSITY HYDROMETEOR IDENTIFICATION (CSU HID)

The technique utilized to classify hydrometeors in the CSU HID is fuzzy logic. Fuzzy logic uses membership functions that define ranges of expected variability for different measurements, using functions that permit overlap between different hydrometeor types (Liu and Chandrasekar 2000; Zrnic et al. 2001; Dolan and Rutledge 2009, hereafter DR09; Dolan et al. 2013). For example, both light rain and snow can have similar reflectivity membership functions. In the fuzzy logic framework, measurements such as radar moments and temperature are fit to a membership set and are assigned a score (from zero implying no fit, to one implying a perfect fit) for each hydrometeor based on their consistency with the fit (Liu and Chandrasekar 2000). In HID analysis, a membership set for each radar moment is made up of hydrometeor types' membership functions that are specific to that moment (e.g. a membership set for Z_{dr} is made up of the Z_{dr} MBFs belonging to each hydrometeor considered in the HID).

In general, membership functions are expected to have an expansive, flat region where the membership value assumes a value of unity for a given hydrometeor. For rain, reflectivities can easily span from 25 dBZ to 60 dBZ, so its membership value in that range would be unity (Liu and Chandrasekar 2000). Since there is no sharp cut-off at which membership functions cease to be uniquely related to real hydrometeors, one which embodies this smoothly decaying edge is preferred. For these reasons, beta functions are chosen as the ideal form for a membership function (example set of MBFs for reflectivity in Fig 2.2), where the shape of this function is given by Eq. 9, where x is the observational value, m is the midpoint, a is the half-width of the membership beta function, and b is the slope (DR09),

$$\beta = \frac{1}{1+\left[\left(\frac{x-m}{a}\right)^2\right]^b}. \tag{9}$$

Different variables have weights applied to them depending on the confidence in the measurement which are factored into the scoring of each hydrometeor type. These weights were determined subjectively, where reflectivity and temperature are heavily weighted compared to differential reflectivity (weight of 0.8), specific differential phase (weight of 1.0), and correlation coefficient (weight of 0.1) (Dolan et al. 2013). The validity of these subjectively-determined weights leaves obvious/significant room for investigation and possible modification. After summing the scores for each hydrometeor type, the highest-scoring hydrometeor is chosen as the hydrometeor type that best explains the various polarimetric measurements within the radar volume (DR09; Dolan et al. 2013). The overall score assigned to a hydrometeor is shown in Eq. 10, where i represents the hydrometeor type, W is each variable's assigned weight, and β is the score awarded to a certain hydrometeor for a particular polarimetric radar variable (Eq. 9) (Dolan et al. 2013). The fact that reflectivity and temperature influence the overall score the most, reflecting the confidence in these variables over the others, is shown in that each hydrometeor score is multiplied by the scores for reflectivity and temperature in a so-called 'hybrid –scoring' method (Lim et al. 2005; DR09)

$$\mu_i = \frac{\left(W_{Z_{dr}}\beta_{Z_{dr},i}+W_{K_{dp}}\beta_{K_{dp},i}+W_{\rho_{hv}}\beta_{\rho_{hv},i}\right)}{W_{Z_{dr}}+W_{K_{dp}}+W_{\rho_{hv}}}\beta_{T,i}\beta_{Z_h,i}. \quad (10)$$

Determination of the specific ranges of values associated with each polarimetric radar variable and each hydrometeor type can be made several different ways, including from observations, subjective experience, and theoretical simulations. Several studies have developed theoretical simulations of radar moments for various hydrometeor types (Liu and Chandrasekar 2000; DR09; Dolan et al. 2013; Thompson et al. 2014). With these simulations, a standard set of MBFs can be defined for each hydrometeor type and radar moment (set up similarly those those seen in Fig. 2.2).

These theoretical functions are particularly useful when radar wavelengths shorter than 10 cm are employed due to non-Rayleigh scattering impacting the radar moments in complicated ways (DR09; Dolan et al. 2013). The DR09 and Dolan et al. (2013) MBFs that serve as the foundations of this study were developed from a theoretical standpoint, where extensive literature reviews of the different parameters (particle density, size distributions, canting angles, etc.) were undertaken for ten different hydrometeor types: drizzle, rain, big drops, ice crystals, snow /aggregates, wet snow, low-density graupel, high-density graupel, hail, and vertically aligned ice crystals.

2.5. POLARRIS

The overall goal of POLARRIS is to help evaluate/validate model output, to help with data assimilation, and to allow for self-consistent testing of polarimetric radar retrievals, in an attempt to evaluate model output when compared with retrievals from observations. POLARRIS is composed of two parts: a forward model (POLARRIS-f) which calculates synthetic radar observables based on model outputs, and an inverse model (iPOLARRIS) that performs the same radar retrievals on model output as is done for observations, and serves as the tool with which one can evaluate a CRM's performance (M17). To facilitate better understanding of how POLARRIS functions, Fig. 2.3 shows a visual schematic of the POLARRIS framework.

2.5.1 POLARRIS-f

POLARRIS-f runs through the same process indicated for the theoretical calculation of polarimetric radar variables in section 2.3. The forward component has its roots in the Goddard Satellite Data Simulator Unit (G-SDSU) that has an "end-to-end multi-instrument satellite simulator" specially made for CRMs (M17). POLARRIS-f runs through the T-Matrix and Mueller-Matrix processes to produce polarimetric radar variables (as well as Doppler and radial velocity), where the single-scattering properties

are guided by the PSDs, density, and phases of BMSs and SBMs found in CRMs (M17).

One of the inputs to the T-Matrix includes the "effective" dielectric constant (ε_{ff} which is dependent upon the particle density and water content) (R11). POLARRIS-f allows a choice between three different dielectric constants (M17): Maxwell-Garnett (Maxwell Garnett 1904), effective medium (Bruggeman 1935) and Debye (Debye 1929). In the end, the Maxwell-Garnett function, which assumes ice inclusion within an air matrix, was input as the dielectric constant for all simulations herein. The other constants were explored, and while they modified results slightly, the largest differences still seemed more dependent on the axis ratio and canting angle assumptions. Once ε_{ff} is calculated, it can then be mixed with water so that mixed-phase hydrometeors can be derived (e.g. aggregates or graupel; M17).

In T-Matrix, as was mentioned previously, the assumption of an arbitrary non-spherical, dielectric body is used to calculate the T-Matrix. POLARRIS-f allows the user to define a specific axis ratio that applies to all simulated diameters in T-matrix (M17). This ability is utilized extensively in this work to try and pull out the most optimal value for axis ratio (though, this proves to be not straight forward). The canting angle distribution can be simplified to a one-dimensional distribution, which is often a Gaussian distribution (M17). For this kind of distribution, the main factors to take into consideration are θ and σ (see Sec. 2.3; M17). The ability to change these variables is also available, although their effect (to an extent) had much less impact on the simulated polarimetric radar variables than that of axis ratio. Finally, the equi-volume spherical diameters, temperatures, and particle bulk density are supplied by the model output, while the radar wavelength is the other input to T-Matrix specified by the user (M17).

2.5.2 The Look-up Table (LUT)

One part of POLARRIS that is particularly remarkable is the use of a look-up table (LUT) to significantly cut down the computer time to run POLARRIS-f. Running several hours of standard WRF output explicitly through the T-Matrix and Mueller Matrix modules as they are requires a few hours with 1600 cores utilizing parallel processing (M17). To reduce computational time, a LUT was created. Given a user-specified axis ratio (or axis ratio distribution), canting angle assumptions, and given the type of microphysics employed (the single-particle SBM approach, or the use of size-integrated BMS), the 2x2 forward-scattering amplitude matrix from T-Matrix and the 4x4 Mueller scattering matrix are computed (M17). This is done for the ranges of size bins, temperatures, and radar elevation angles given in section 3.6 for SBM (where the mass bins are related to the size of the particle) and BMSs.

Since BMSs are assigned a pre-determined, semi-empirical PSD, this process need only be done once assuming a unit mixing ratio, for the range of effective radii given in Sec. 3.6. In the case of SBM, however, as has been described previously, the PSD is allowed to develop naturally. HUCM SBM has 43 doubling mass bins in which the particular mass is allowed to evolve organically (accounting as well for the effects of particle riming in the process). For a given mass bin and unit mixing ratio, the scattering matrices are calculated. Note that no integration is performed over the mass bins in the SBM LUT, whereas the 4ICE LUT includes integration over sizes. This results in a longer LUT generation time for size-integrated bulk microphysics processes than for SBM processes (M17).

M17 states that each radar frequency and microphysics scheme has its own generated LUT. Once these are generated, multiple tests at each radar frequency and microphysics scheme in POLARRIS-f and iPOLARRIS can be performed without having to re-generate the LUT each time. Capitalizing on this fact, these processes can be parallelized, resulting in LUT generation times of a quarter of an hour for BMSs and just

a few minutes for SBM. After the generation of the LUT, as was described in Sec. 2.3, 4ICE radar observables are scaled by the output model mixing ratio and then the size-integrated Mueller Matrix is integrated over all species to produce radar observables at each grid point. In SBM, the species still need to first be integrated over the mass bins based on how the model evolved the PSD. These resultant radar observables are then scaled by the output model mixing ratio. After this, as was done in 4ICE, the integrated Mueller Matrices for SBM radar observables are then integrated over all species (M17).

2.5.3 iPOLARRIS

The iPOLARRIS framework was created to help bridge the gap between the way model output is presented as compared to observations and retrievals from observations, since on their own the parameters are not directly comparable. iPOLARRIS is composed of retrieval algorithms utilized in observations, allowing the model output to be visualized in the same method as is done with observations. This allows a direct comparison between the synthetic radar variables produced with POLARRIS-f output and observations (M17). Hence, one can use the iPOLARRIS framework to evaluate the model microphysics/dynamics, while also validating the retrieval algorithms themselves.

With iPOLARRIS, several different methods can be used to compare model output (run through the POLARRIS-f framework) and observations. For example, the same HID algorithm described in section 2.4 for the CSU HID can be applied to simulation polarimetric radar variables from POLARRIS-f. This could be analyzed for different microphysics schemes, and then a comparison of whether bulk vs. bin microphysics performs more in accordance with observed polarimetric radar variables can be conducted via stacked frequency by altitude (SFAD) HID plots. This can also be broken down into convective vs. stratiform components of rainfall and how HID compares from the model to observations in these specific precipitation types. HID

classifications of observations can also be compared to mixing ratio quantities of hydrometeors from the model. Also, the polarimetric radar variables (simulated and observed) themselves can be compared. That is, after using mixing ratios from the model to limit hydrometeors to one of choice, a joint probability distribution function (PDF), Z-Z_{dr} plot from model results can be compared to a Z-Z_{dr} plot from observations (where a retrieval of these variables for a certain hydrometeor was made with the CSU HID). These plots are also referred to as 2D co-variance of radar variable plots. Comparisons can even be made between polarimetric rainfall retrievals or vertical velocity retrievals from the model and from observations. The utility of iPOLARRIS is quite great, as it allows for an evaluation/validation of model microphysics, kinematics, and dynamics, as well as validating the use of the retrieval algorithms that have been applied widely to observations.

2.6. MC3E

One of two datasets used in this work is from the Midlatitude Continental Convective Clouds Experiment (MC3E). The United State Department of Energy (DOE) Atmospheric Radiation Measurement (ARM) Program and the National Aeronautics and Space Administration's (NASA) Global Precipitation Measurement (GPM) mission led the project. MC3E ran from April 22nd to June 6th of 2011, centered in the DOE ARM Southern Great Plains (SGP) site in north-central Oklahoma (Jensen et al. 2016).

As is shown in Fig. 2.4, a wide variety of instruments were employed, including a pentagon-shaped sounding network, a disdrometer network, the array of atmospheric state measurements at the ARM SGP facility, and several ground-based radars, as well as a few different aircraft (though not picture in Fig. 2.4, data was also taken with the highly instrumented UND Citation II aircraft). Of interest to this work were some of the scanning radars: ARM's scanning precipitation radars (C-SAPR and X-SAPR), and NASA's S-Band dual-polarization Doppler radar (N-POL), as well as data from the

Citation II aircraft. The C-SAPR radar scanned with six-minute volumes of 360° plan position indicator (PPI) scans, with 17 elevation angles for better vertical resolution (ranging from 0.5° to 42°; Collis et al. 2012). Additionally, range height indicator (RHI) scans were performed in conjunction with aircraft overflies as they occurred. NPOL performed a variety of pre-determined scans based on scientific objectives. Data from NPOL became available very late on May 23rd, since the radar was down before that time, and thus this work's concentration is on CSAPR data taken on the 23rd May (additionally, comparisons from the POLARRIS framework are made with CPOL from TWP-ICE, thus using another C-Band radar to compare against was ideal).

MC3E provided a rich dataset of several different modes of convection in the southern Great Plains. For this thesis, the supercell event (May 23rd, for the integrated 22 Z hour) was chosen as the case of interest. Largely this had to do with the fact that this particular case was reasonably represented in the Nu-WRF simulations. Additionally, the location of the supercell was favorable with respect to CSAPR and the X-Band XSAPR radars. This event began with a strong southwest to northeast oriented dryline (Fig. 2.5) whose advancement was the genesis of the day's intense convection. This dryline triggered eastward travelling convection that reached the MC3E domain by 22 Z (hence, the use of the 22 Z hour for analysis). The core of the convection, which reached up to 15 km in depth, showed high reflectivities (reaching into the low 60 dBZs) that contained a large amount of hail (Fig. 2.6 shows example of convection at 2229 Z). Melting hail and big rain drops reached the surface as indicated by the HID (see Fig. 11b in Jensen et al. 2016). Updrafts exceeded 25 m s^{-1}, with upward air motion out ahead of the supercell as well (Jensen et al. 2016). Citation II flew in areas of both rainfall and ice crystal/dry snow areas (see Fig 2.7). The HVPS probe, which flew on the UND Citation II, data sampled in the latter of the two areas was used to create an axis ratio – size dependent relationship to be used for snow aggregates.

2.7. TWP – ICE

The second of the two datasets used in this work comes from the Tropical Warm Pool International Cloud Experiment (TWP-ICE) campaign that took place in Darwin, Australia in January and February of 2006. The setup for instrumentation employed in TWP-ICE is shown in Fig. 2.8. TWP-ICE had a rich ground network of observations, as well as some aircraft observations. The ground network included the Bureau of Meteorology (BoM) instrumentation, the DOE ARM Program Atmospheric Cloud and Radiation Facility, a radiosonde network, surface energy flux systems, radar wind/cloud profilers, microwave instrumentation, Atmospheric Emitted Radiance Interferometers, ocean observations, and a lightning detection network. Of interest to this work is the BoM's Doppler C-Band (non-polarimetric) radar, Berrima, and the BoM's C-Band, dual-polarization, Doppler radar (CPOL). Dual-Doppler analysis was performed on these two radars and microphysical studies were perform with polarimetric radar data form CPOL (which contributes to analysis shown later).

The TWP-ICE campaign collected a great observational dataset, including two distinct convective regimes. There were several days of active "monsoon" conditions. Flow in this setup comes from over the Indian Ocean, bringing with it plenty of moisture. During these periods, mesoscale convective system (MCS)-like storms passed through the area, with leading convection propagating through first, followed by large swaths of stratiform precipitation (May et al. 2008). Following these active monsoon conditions are break convection periods, where easterly low-level flows are observed. With this setup, less moisture is available and CAPE values are higher than during monsoon periods, owing to reduced cloudiness and increased surface heating. More intense, discrete continental convection develops during these periods (May et al. 2008). The same methodology to determine monsoonal vs. break convection as was employed in Dolan et al. (2013) is used here: when the sustained mean zonal wind at 850-hPa is greater than 2 m s^{-1} (for at least 24 hours) the regime is determined to be monsoonal, whereas

if the sustained mean zonal wind at 850-hPa were less than -2 m s^{-1}, this would result in a break convection classification. This mean zonal wind flow at 850-hPa was calculated from Modern-Era Retrospective Analysis for Research and Applications (MERRA) reanalysis data that was centered on C-POL's location (Dolan et al. 2013).

Chosen from this was the integrated 18Z hour of the 23 January 2006 monsoon case. This was an interesting case, as while winds at the 700 mb level were indicated as westerly, convection observed is still travelling westward. Although this was the case, the convection itself was monsoon-like in nature: initially intense pockets of convection moved through the area (with reflectivities reaching up to the mid 60 dBZs), which conglomerated into one larger area of intense convection, followed by large areas of stratiform precipitation (characterized by lower-intensity, large raining areas; see Fig. 2.9). These MCS-like events are marked by large rain accumulation from the swaths of stratiform rain associated with MCSs, compared to the intense, but quickly passing break convection (Keenan and Carbone 1992; Rutledge et al. 1992; May and Ballinger 2007).

Table 2.1: WRF model simulation configurations for the 23 January 2006 TWP-ICE and the 23 May 2011 MC3E cases

	TWP-ICE	**MC3E**
Simulation Length/Time Frame	120 hours run from 00 UTC 21 - 00 UTC 26 January 2006	24 hours run from 12 UTC 23 - 12 UTC 24 May 2011
Horizontal Domain	9 km : 300x300, 3 km: 286x286, 1 km: 334x334	9 km : 513x389, 3 km: 496x424, 1 km: 673x595
Vertical Domain	20 km height, with 60 layers (intervals increasing with altitude)	20 km height, with 60 layers (intervals increasing with altitude)
Parameterizations	Grid-scale cloud microphysics: Goddard Cumulus Ensemble (GCE) single-moment 4ice bulk microphysics (Tao et al. 2014) Sub-grid cumulus: Grell Freitas ensemble cumulus parameterization (Grell and Freitas 2014; only for 9-km grid intervals)	Grid-scale cloud microphysics: Goddard Cumulus Ensemble (GCE) single-moment 4ice bulk microphysics (Tao et al. 2014) Sub-grid cumulus: Grell Freitas ensemble cumulus parameterization (Grell and Freitas 2014; only for 9-km grid intervals)
Atmospheric Radiation	Goddard shortwave and longwave radiation schemes (2014 version) (Chou and Suarez 1999 & 2001)	Goddard shortwave and longwave radiation schemes (2014 version) (Chou and Suarez 1999 & 2001)
Planetary Boundary Layer and Sub-grid Scale Turbulence	Level 2.5 Mellor-Yamada Janjic turbulence closure scheme (Janjic 1990)	Level 2.5 Mellor-Yamada Janjic turbulence closure scheme (Janjic 1990)
Land Surface Processes/ Surface Heat Flux	Unified community Noah land surface model (Tewari et al. 2004)	Unified community Noah land surface model (Tewari et al. 2004)
Initial Meteorological Conditions (all domains), Lateral Boundary Condition (9 km domain)	Calculated from interim reanalysis data from European Centre for Medium-Range Weather Forecasts (ECMWF) model (Dee et al. 2011) (spectral T255 horizontal resolution) *WRF coupled with spectral bin microphysics (WRF-SBM; Iguchi et al. 2014) simulated innermost domain (1 km) on only 23 January 2006	National Centers for Environmental Prediction (NCEP) final (FNL) operational global analysis data (NCEP/NWS/NOAA/U.S. Dept. of Commerce, 2000), with grid spacing of 1° (latitude and longitude) *WRF coupled with spectral bin microphysics (WRF-SBM; Iguchi et al. 2014) simulated innermost domain (1 km) for all times

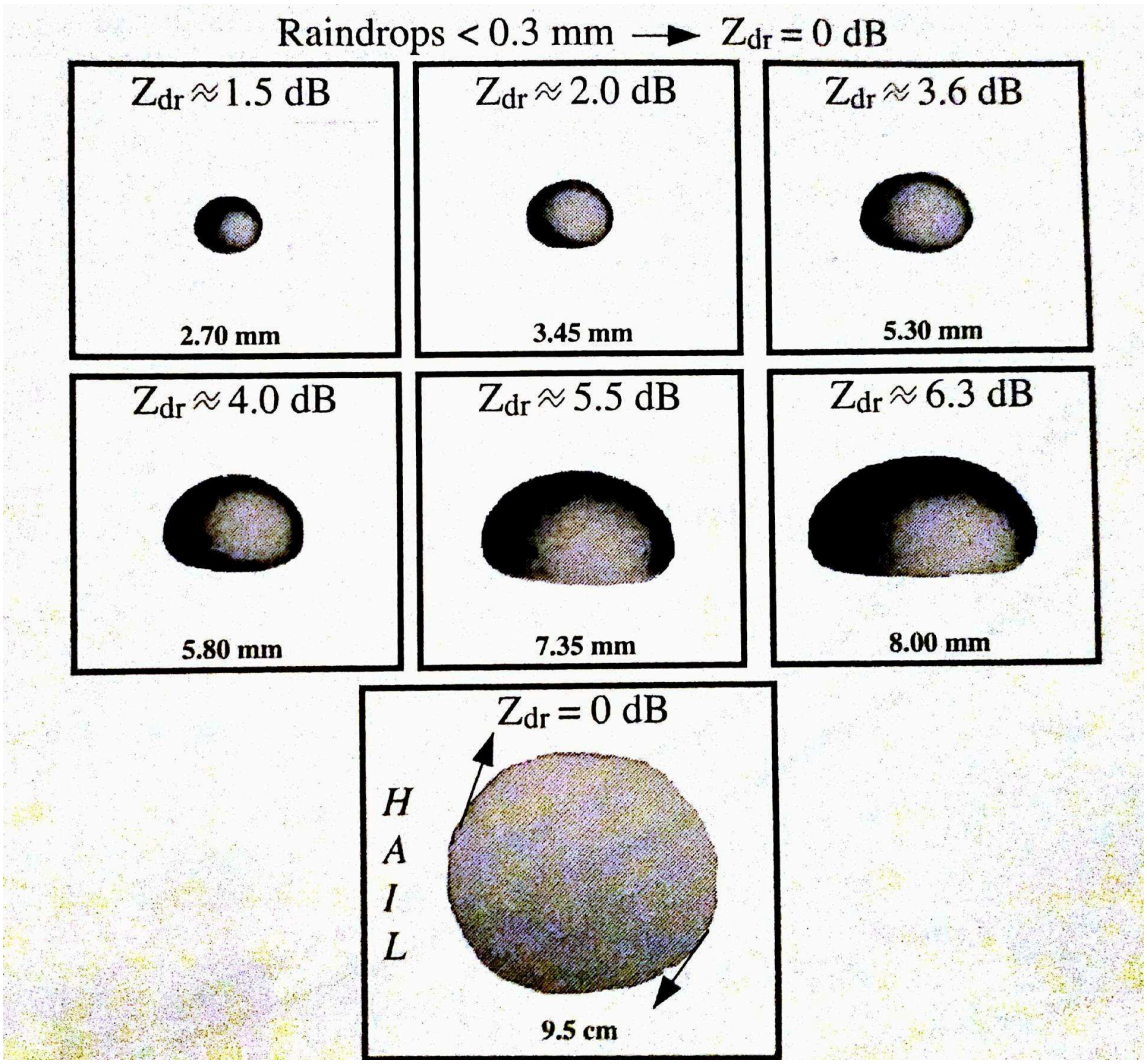

Figure 2.1: Average Z_{dr} values seen for rain (and hail), as a function of the size. This demonstrates the increase in Z_{dr} as rain becomes increasingly oblate due to the need to balance gravitational and surface tension forces (Bringi and Chandrasekar, 2001).

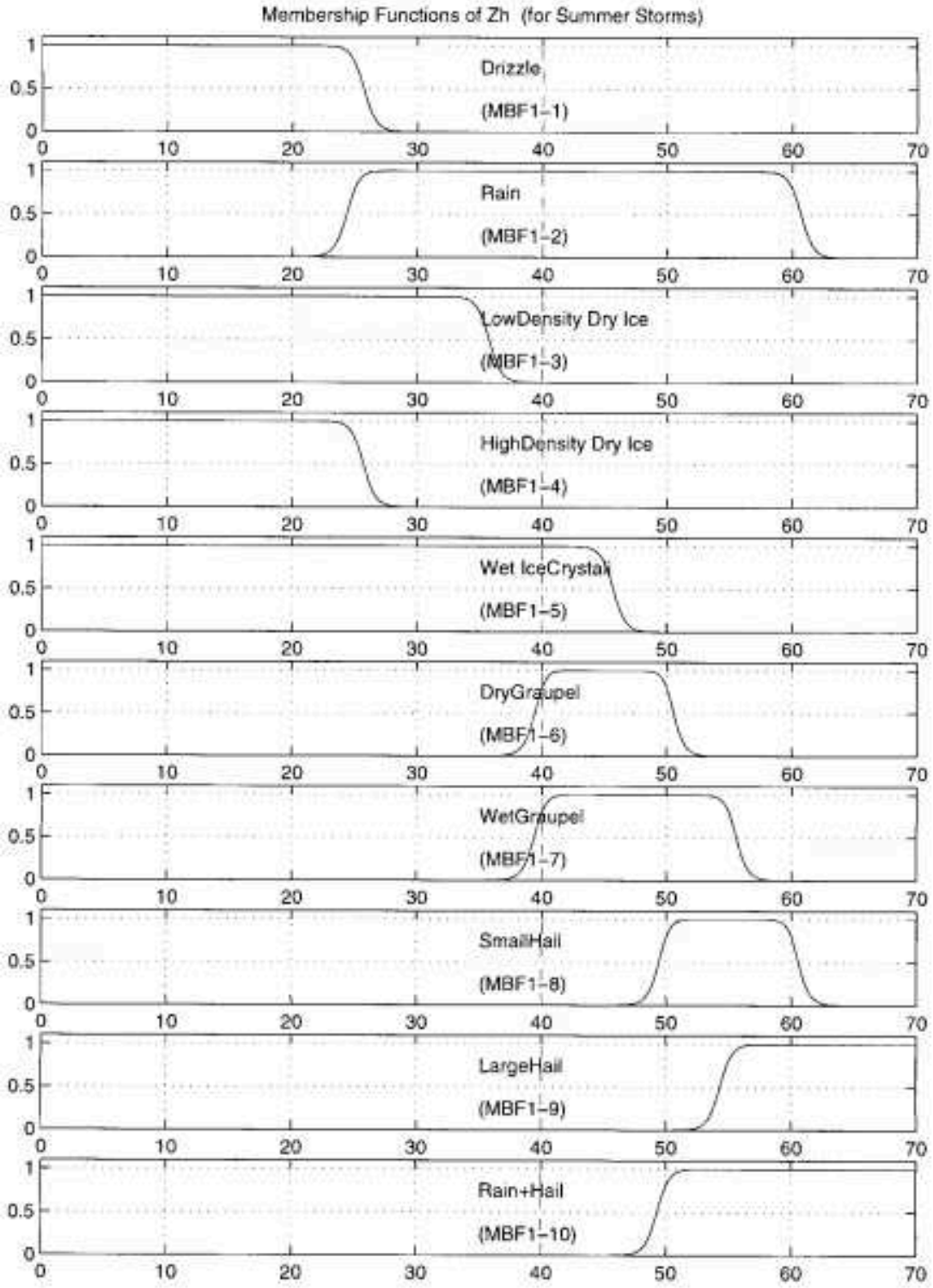

Figure 2.2: Example of summer-time reflectivity MBFs from Liu and Chandrasekar (2000). CSU HID MBFs have a similar shape, and thus this serves as a good example.

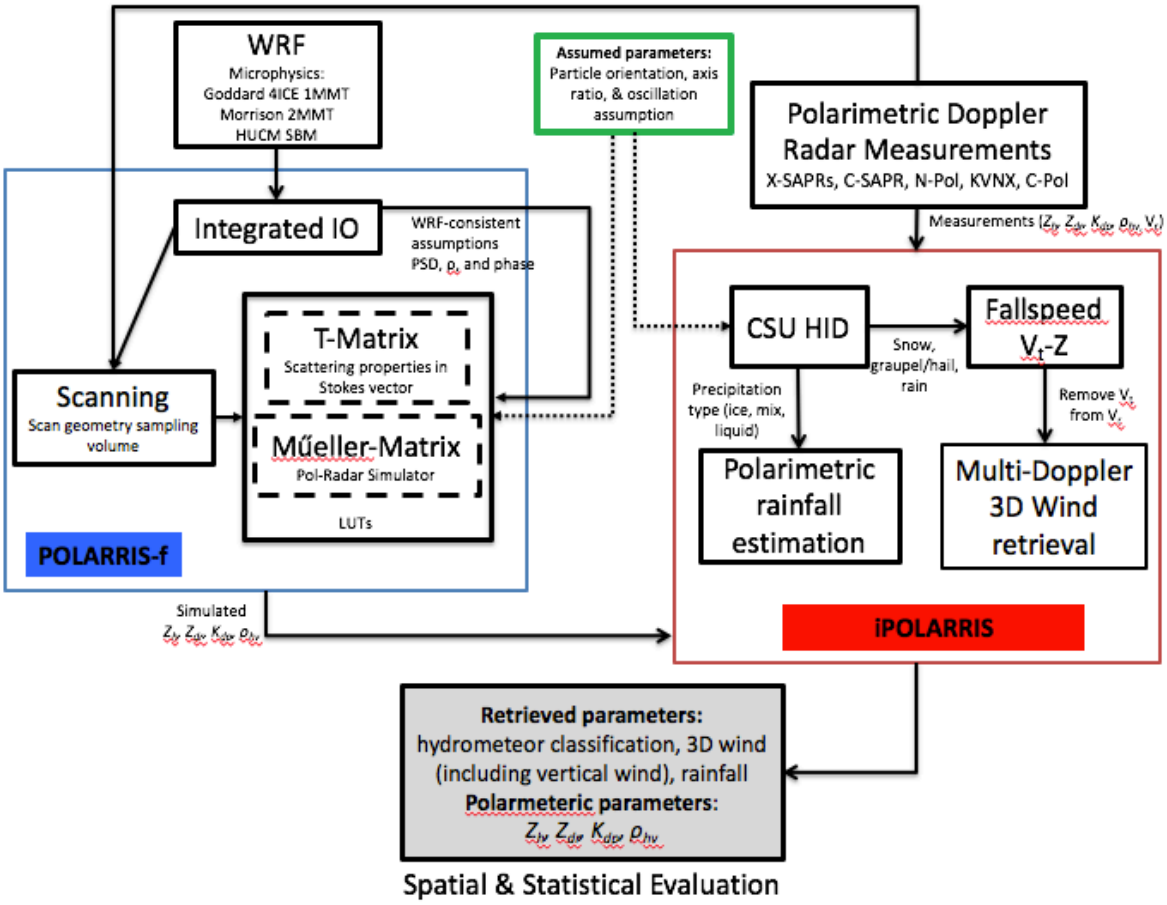

Figure 2.3: POLARRIS flow chart, showing the separate POLARRIS-f and iPOLARRIS components, which in the end yield retrieved parameters and polarimetric parameters.

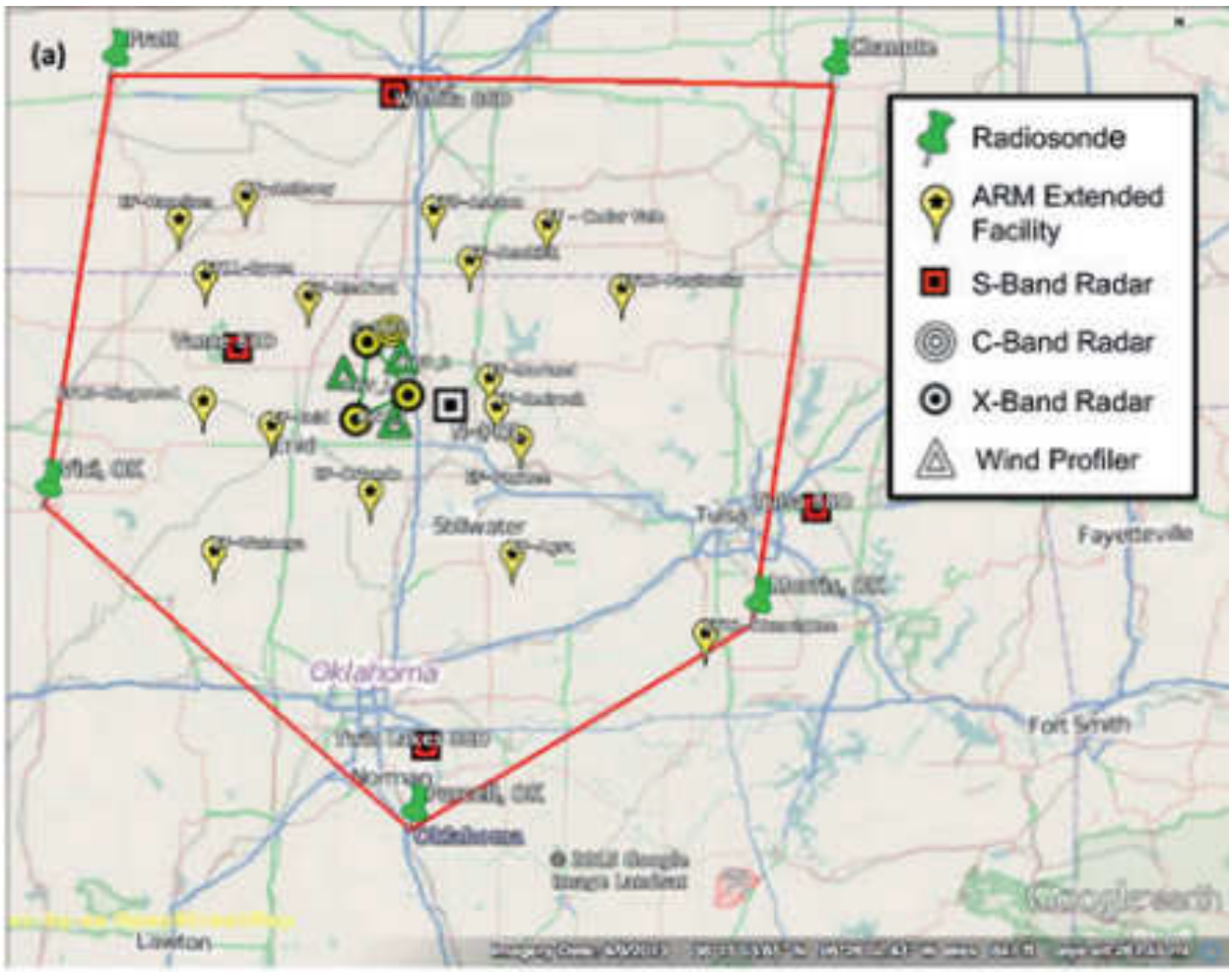

Figure 2.4: MC3E field campaign design. This shows how the sounding network encompasses the central radar array (N-Pol, C-SAPR, triangular array of X-band radars in yellow, and 915-MHz profilers in green triangles) and SGP CF (Jensen et al. 2016).

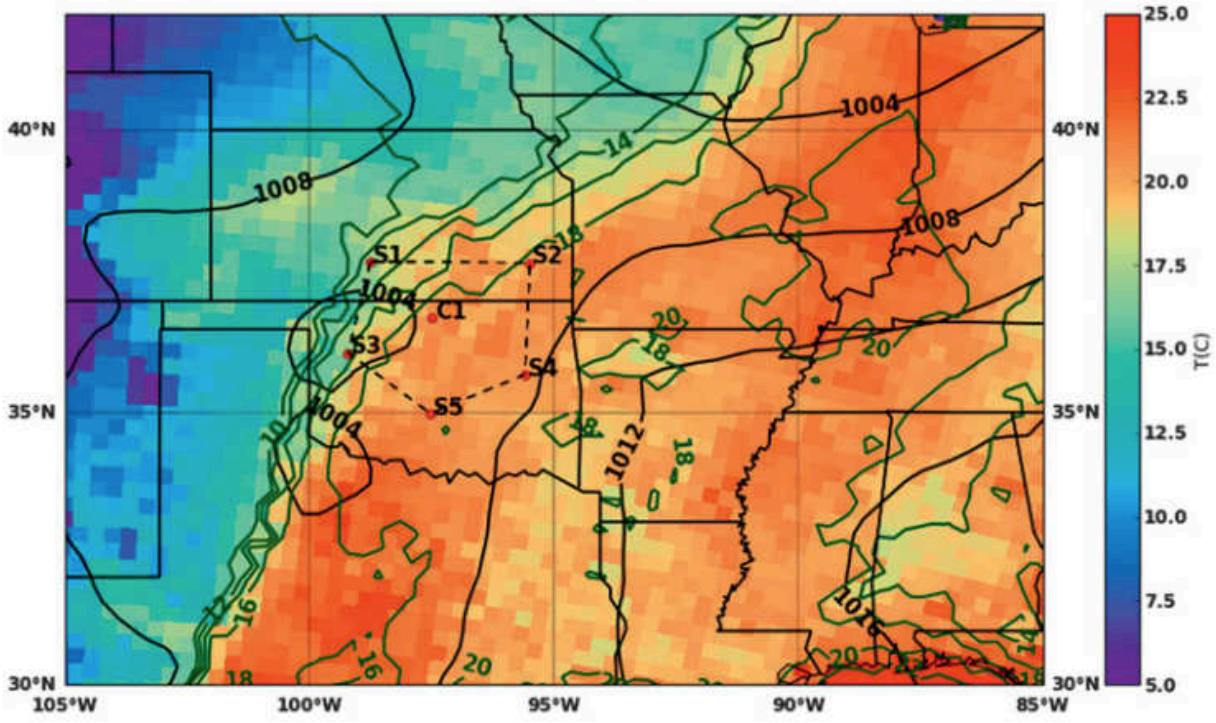

Figure 2.5: 1200 UTC 23 May 2011 surface meteorological analysis based on NARR output showing the surface pressure (hPa; contours) and surface temperature (colors). The MC3E sounding array hexagon is indicated by the dashed lines (Jensen et al. 2016).

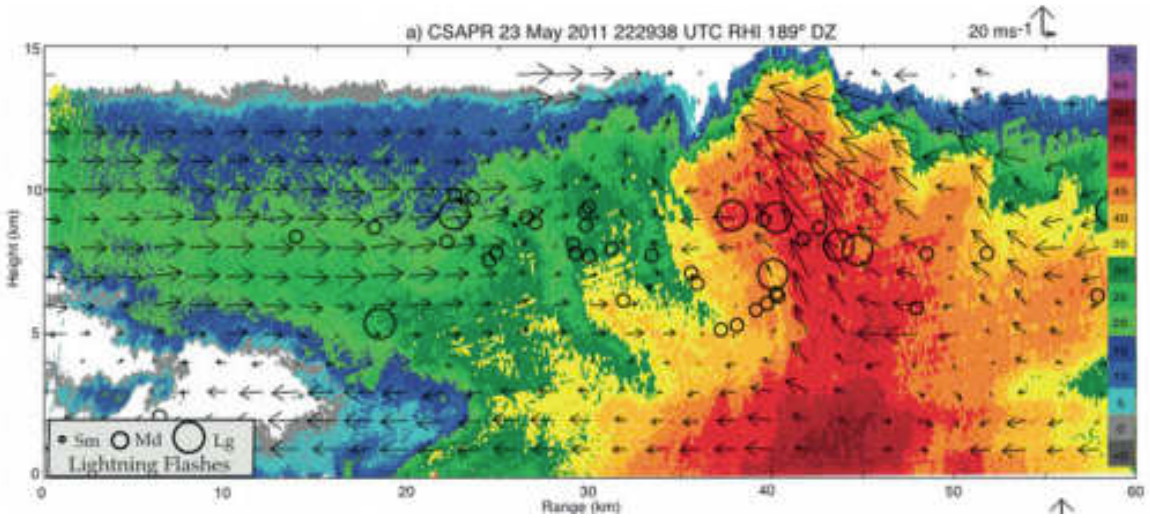

Figure 2.6: C-SAPR RHI of reflectivity along a 189° azimuth at 222938 UTC. Vectors are storm-relative winds resulting from a multiple-Doppler synthesis from C-SAPR, two X-SAPRs, and KVNX at 2223 UTC (Jensen et al. 2016).

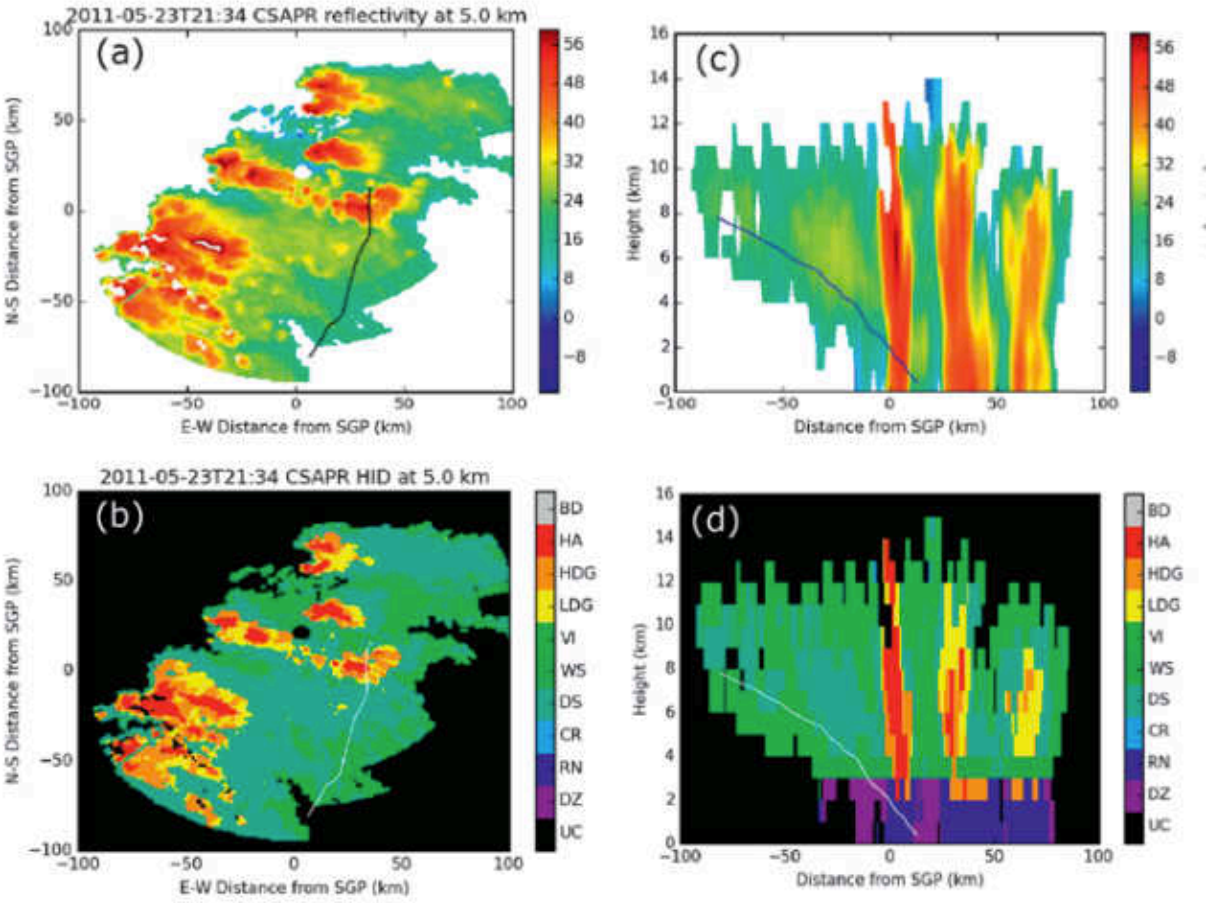

Figure 2.7: CSAPR (a) Reflectivity CAPPI, (b) HID CAPPI, (c) Reflectivity RHI, and (d) HID RHI for the 23 May 2011 MC3E case at 21:34 UTC. The black/white lines show the path of the UND Citation II aircraft.

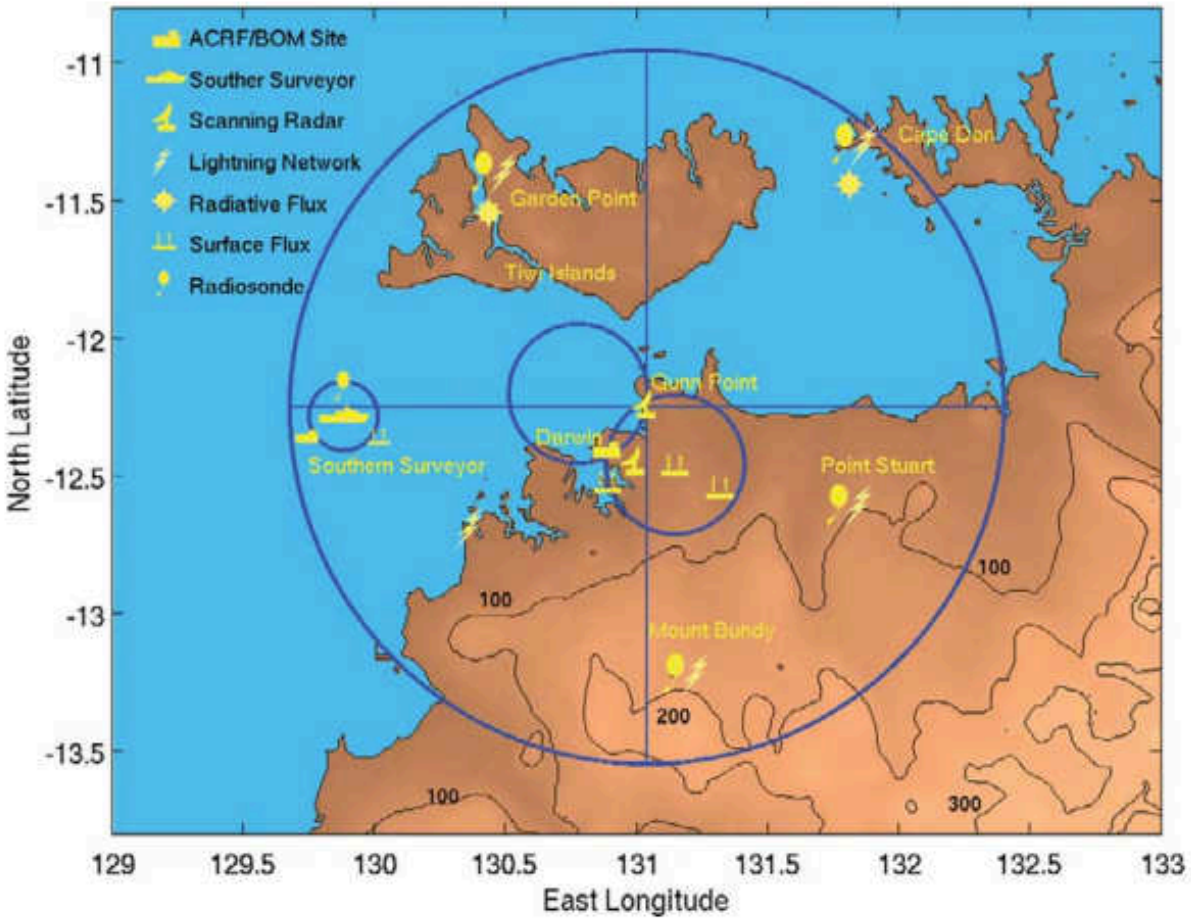

Figure 2.8: The TWP-ICE domain setup. The large blue circle indicates a 150-km radius centered on the C-Pol radar. The two interlocking circles near the center of the domain indicate the dual-Doppler lobes associated with the C-Pol and Berrima radars (May et al. 2008).

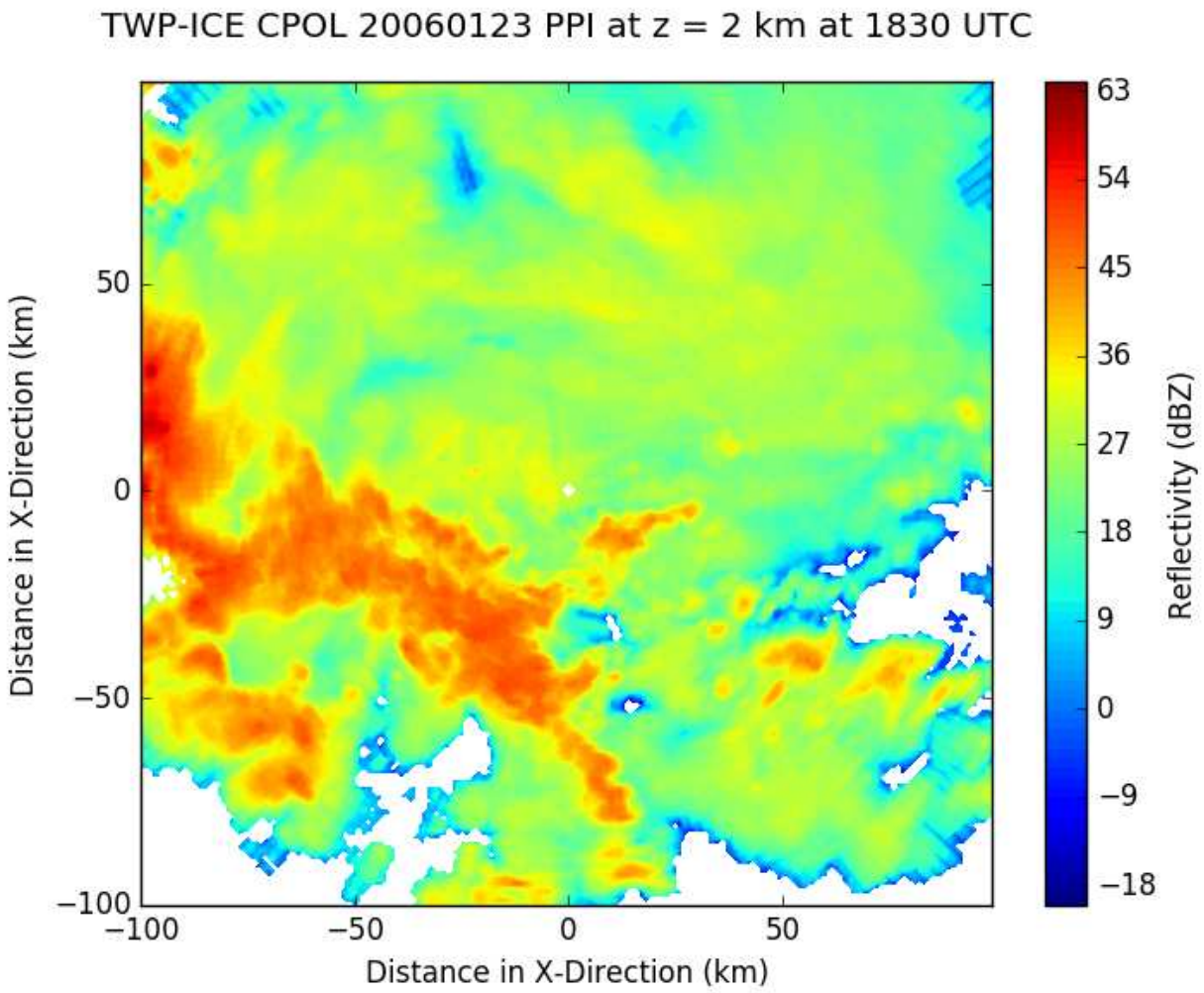

Figure 2.9: C-POL TWP-ICE PPI of convection at 2 km in height at 1830 UTC, 23 January 2006.

CHAPTER 3: METHODOLOGY

In this chapter, the specific methodology for implementing radar data quality control, dealiasing, and dual-Doppler framework are discussed. Additionally, the data analysis between the POLARRIS framework output and observations methodology is presented.

3.1 QUALITY CONTROL

Different methods were utilized in order to correct data from C-SPAR (MC3E) and C-POL and Berrima (TWP-ICE), as the data was provided in differing states. First, the quality control (QC) performed on C-POL and Berrima in TWP-ICE will be discussed, followed by the methods used to QC C-SAPR in MC3E.

For the C-POL radar used in TWP-ICE, the reflectivity and differential reflectivity biases were already accounted for, as well as attenuation and differential attenuation, and K_{dp} had already been calculated (see Dolan et al. 2013 for a review of how these processes were completed). Therefore, what remained was to clear up general noise in the data, as well as to remove second-trip echoes, and to attempt to unfold aliased velocity data with automatic algorithms. In order to remove second-trip echoes, a threshold was placed on the reflectivity data based on bad/noisy velocity. Remaining noise in the data was handled by employing the despeckle function from the CSU Radar Tools python package (https://github.com/CSU-Radarmet/CSU_RadarTools; https://doi.org/10.5281/zenodo.1035908). This array was then run through the despeckle function, where it checked along each ray (for each azimuth and elevation angle) for bad values. For this data, if eight contiguous gates were identified with good data (i.e. data with no values identified as bad), then no masking of the data occurred. Otherwise, the data was flagged as bad. For Berrima, only its radial velocity was used in this analysis, with the only necessary correction being unfolding. Dealiasing velocity on

both radars took a significant amount of time and effort, the process for which is described in section 3.2.

Previously gridded, velocity-corrected C-SAPR data for the MC3E case (23 May 2011) with all QC performed was available for this study (Matthews 2014). However, radar data for 24 May 2011 had had none of these processes performed. Since 24 May 2011 was initially also under consideration, and due to the fact that other users were interested in using this radar data in POLARRIS, it had to be run through the same processes applied to the 23 May 2011 case. The Dual-Polarization Radar Operational Processing System (DROPS) was used to bias correct reflectivity and differential reflectivity, as well as calculate K_{dp} (based on methods described in Wang and Chandrasekar, 2009) and a flag field for bad and good values based on thresholds of ρ_{hv} and standard deviation of the differential phase. Despeckling to remove noise, second trip echo removal, and automatically unfolding velocities was performed with the same framework as was done with TWP-ICE.

3.2 RADIAL VELOCITY CORRECTIONS

In order to be able to perform dual-Doppler wind synthesis, at times pretty significant treatment of aliased velocities had to be undertaken. Velocity aliasing, otherwise known as velocity folding, occurs when the the range of unambiguous velocities is smaller than the range of actual velocities observed in nature (American Meteorological Society 2017). The range of unambiguous velocities is determined based on the Nyquist velocity, which is given by

$$\mathrm{V_{max}} = \frac{\pm \mathrm{f_{max}} \lambda}{2} \tag{11}$$

where f_{max} is given by

$$f_{\max} = \frac{\mathrm{PRF}}{2} \tag{12}$$

and the PRF is the radar's pulse repetition frequency (Rinehart 2010). Subbing Eqn. 12 into 11, we get

$$V_{max} = \frac{\pm PRF\lambda}{4} \quad (13)$$

from which we see that that the value of the Nyquist velocity is largely dependent on the chosen PRF and radar wavelength (Rinehart 2010). Velocities in the Nyquist velocity range create a +- π radians phase shift (Rinehart 2010). Velocity aliasing occurs when there is a phase shift greater than +/- 180° of the transmitted phase (Rinehart 2010). On a radar, this appears as regions of velocity where there are both the maximum-possible velocities towards, and away, from the radar directly next to each other (Rinehart 2010).

In order to correct aliased (or folded) velocities, several steps were taken. First, aliased velocities were unfolded via two different automatic unfolding python programs available in PyART (Heistermann et al. 2014): a region-based method, and a scheme using the four-dimensionality (time, the vertical axis and the horizontal axes) of Doppler radar. In the region-based method (Helmus et al. 2015; Helmus and Collis, 2016), the velocity unfolding is similar to what occurs with hand unfolding of velocities. Velocity differences in a region are minimized between bordering edges for regions of similar velocities. The algorithm starts with the largest area of similar velocities, and works from there. The other scheme (4DD) was created to deal with the often complex nature of aliasing, and in initial studies found that it performed well even in complex aliased situations and low Nyquist velocities. This method dealiases for each radar tilt based on either a previously unfolded radar volume, or a background sounding wind field. The method attempts to make minimize differences between nearest gates, and even reverts to velocity azimuth display (VAD) if previous methods to correct velocities fail (James and Houze Jr. 2001).

For C-POL, the 4DD method seemed to work the best for initial unfolding of aliased velocities, while for C-SAPR and Berrima the region-based method performed significantly better. Despite these initial corrections, however, hand-unfolding of velocities was still required. These user-driven corrections of velocities were performed with the ARM Radar Toolkit Viewer (ARTview, https://doi.org/0.5281/zenodo.594051) that is built on Py-ART (Helmus and Collis, 2016). Although automatic unfolding helped cut down time spent on hand unfolding, significant unfolding was required for Berrima. C-POL required far less and unfolding done in this master's work on C-SAPR did not require any additional hand unfolding.

3.3 GRIDDING RADAR DATA

C-SAPR data was gridded to a Cartesian grid, centered at the location of the Central Facility (CF) of the SGP Atmospheric Radiation Measurement (ARM) site in Lamont, OK via the Radx2Grid function in the Radx package (https://ral.ucar.edu/projects/titan/docs/radial_formats/radx.html). The horizontal and vertical resolution were set to 1 km. The vertical part of the domain ranges from 1 km to 18 km in altitude, and the domain ranges 100 km from the center of the grid (thus, 200 km by 200 km in the x- and y-direction). C-POL and Berrima follow the same gridding process, where the grid was centered on C-POL, and possess the same horizontal resolution and domain size in the horizontal, however, the vertical resolution was set to be 0.5 km, and ranged from 0.5 to 20 km.

3.4 DUAL-DOPPLER AND MULTI-DOPPLER ANALYSIS

Once data was gridded, the data was run through the NCAR CEDRIC package (Mohr and Miller 1983). This package was designed to calculate three-dimensional air motions based on information from two or more Doppler radars (i.e. dual- or multiple-Doppler analysis). The 700 mb level of the most closely matching times to C-POL/Berrima radar volumes from soundings taken in Darwin, Australia (DWN) were

used as input to advect these radar volumes to a common time. This advection correction was required based on the fact that both Berrima and C-POL scan complete six-minute PPI volumes followed by RHI scan and vertically-pointing scans. These add up to be 10-minute long scan periods. Since convection tends to evolve fairly quickly, this 10-minute period does not adequately sample the storm's actual advection. In that 10-minute period, the storm evolved and, potentially, was located in a different location at the end of that period. Hence, an advection correction is applied to account for this shortcoming. This resulted in 10 minute intervals of output dual-Doppler files from the NCAR CEDRIC package.

Fall speeds from particles were removed from the radial velocity components via fall speed – reflectivity ($V_t - Z_h$) relationships based different hydrometeor types (Giangrande et al. 2013). The radar data is first run through an HID (for this work, the CSU HID) to determine bulk hydrometeor types. Areas where there are liquid particles (drizzle, rain, and big drops), where there are graupel/hail particles (low-density graupel, high-density graupel, and hail), areas where there are snow particles (ice crystals, snow aggregates, and vertical ice crystals), and areas where wet snow are identified. The corresponding $V_t - Z_h$ relationships were then applied to each respective hydrometeor type (save for areas of wet snow), with the following equations (where Z_h is expressed as dBZ),

$$\mathrm{V_{t,rain}} = 3.15 * \left(10^{\left(Z_{h,rain}/10\right)}\right)^{0.098} \quad (14)$$

$$\mathrm{V_{t,graupel/hail}} = 2.2 + \sqrt{10^{\left(\mathrm{Z_{h,graup/hail}}-33/10\right)}} \quad (15)$$

$$\mathrm{V_{t,dry\ snow}} = 1.0. \quad (16)$$

The fall speed, calculated at each radar point from the above equations for CPOL, was then utilized to remove a particle's fall velocity from the radial velocity field. After this, the three-dimensional velocities were calculated in CEDRIC via the MASS2 command. MASS2 integrates the mass continuity equation for 2-radar synthesis as according to the CEDRIC manual (Mohr and Miller 1983). Vertical velocities are then calculated using INTEGRATE from the convergence of u and v winds calculated in MASS2, using a variational integration (W_{var}) approach (Mohr and Miller 1983). In the calculation of W_{var}, vertical velocities at the surface are forced to be equal to 0 m s^{-1} after downward integration of the continuity equation is performed, and any remaining vertical velocities at the surface are redistributed through a column of a specified height to keep the surface boundary condition satisfied (O'Brien 1970; Dolan and Rutledge 2010).

3.5 SENSITIVITY TESTS WITH ORIGINAL T-MATRIX, MUELLER MATRIX FRAMEWORK

Before modifying and testing anything in the POLARRIS framework, one goal was to determine the extent to which polarimetric radar data is affected by either changes in axis ratio, or changes in canting angle assumptions. To investigate these sensitivities, experiments were designed for aggregates, high-density graupel, and low-density graupel in the "original" T-Matrix and Mueller Matrix framework (i.e. tests were run for the setup described in section 2.3 not using the LUT framework described in section 2.5.2). The reasoning behind the choices of aggregates and the two types of graupel was because of the desire to incorporate in these sensitivity tests results from in-situ data of these hydrometeors reported in Garrett et al. (2015). In that study (from hereon, termed GE15), almost 73,000 photos were taken with a Multi-Angle Snowflake Camera (MASC) of snow, rimed particles, and graupel. In the analysis of these pictures, GE15 found that there is a larger range of orientation angles than what has been shown in previous studies. Not only are there larger ranges of orientation angles at which

particles flutter, but the mean canting angle at which ice hydrometeors tend to fall can be much greater than what is usually assumed (normally, 0°).

Assumptions from both DR09 and GE15 were input to the T-Matrix, Mueller Matrix framework to see which assumptions in the end had a larger impact on the resulting polarimetric radar data, or if both axis ratio and canting angle assumptions mattered equally. To ensure that differences seen were largely attributable to either axis ratio or canting angle, several other parameters were set, based on DR09. These are described in Table 3.1. Results from these tests are found in section 4.1.

3.6 SENSITIVITY TESTS IN LUT OF POLARIMETRIC RADAR VARIABLES TO MICROPHYSICAL ASSUMPTIONS

The 1M 4ICE BMS is simulated for six species – cloud droplets, rain, cloud ice, snow, graupel, and hail/frozen drops (though the ones of importance herein are rain, snow, graupel, and ice crystals). The scheme includes temperature range for ice hydrometeor temperatures ranging from 180 K to 280 K and was comprised of 12 values. Scaling of these temperature ranges are different for liquid versus ice hydrometeors. Sizes are referenced in terms of “effective radius” (related to the slope of the particle size distribution, PSD). There are 70 discrete effective radii sizes ranging from 10^{-3} to 10^{2} μm for cloud ice and 10^{-1} to 10^{4} μm (10 mm) for other ice hydrometeors. Simulated elevation angles go from 0° to 90° (in increments of 1°).

In SBM, temperatures associated with specific hydrometeor types vary as they do in the BMS, and the radar elevation angles are also the same. Homogeneous and heterogeneous nucleation (deposition, condensation-freezing, and immersion-freezing) of ice particles is simulated, as well as ice multiplication (Iguchi et al. 2012a). There are 43 doubling mass bins in which allow the particle at that mass/size is allowed to evolve organically in a model simulation. Riming is taken into account as well in these mass bins. These mass bins range from 3.35×10^{-11} g to 1.47×10^{2} g, which corresponds to

sizes of 2 μm to 32.8 mm (Iguchi et al. 2012a). SBM is simulated for one liquid hydrometeor species (ranging in size from cloud droplets to large raindrops), and six ice hydrometeor species (ice crystals: plates, columns, and dendrites; snow aggregates; graupel; and hail). Additionally, aerosols are included but not considered here.

Once the LUT in POLARRIS was operational, tests were performed to do an overall check on whether or not the LUT output reasonable polarimetric radar variable values, as well as, again, to examine how various input affected the polarimetric radar data output, and also to help guide which values would be input into POLARRIS later on. Different axis ratio and canting angle assumptions were used, including values from DR09, GE15, Straka et al. (2000) (hereafter S00), R11 and the "control" assumptions, or M17 (See Table 3.2). Note in the case of differing ice crystal habits, the assumed axis ratio and set of canting angle assumptions was the same. That is, all ice crystal habits had the same assumptions for both of these variables. Additionally, for all runs where a singular axis ratio assumption was used, that axis ratio was the same across all input sizes of that particular hydrometeor. Tests were also performed where the dielectric constant was modified however not much difference was seen when using varying values, so this was set to be the default function in POLARRIS (Oblique Maxwell-Garnett function that assumes ice inclusion within an air matrix, see Sec. 2.5.1).

Recall in Section 2.5.2 the description of the LUT implemented in the POLARRIS framework. In this description, we learn that the LUT is produced for a given hydrometeor species, for a given elevation angle, for a given temperature, and a given effective radii size (where in 4ICE there are 70 discrete effective radii and then in the HUCM SBM there are 43 doubling mass bins). These are all produced based on the provided input axis ratio and canting angle assumptions. In the case of 4ICE, the species is integrated over the size for the assigned PSD, resulting in a set of polarimetric radar values for the assumed hydrometeor species, elevation angle,

temperature, and input axis ratio and canting angle assumptions. In SBM, however, values are not yet integrated over the mass bins for each assumption. Due to this, the values shown in the LUT were for single-particle scattering (as opposed to a single hydrometeor) polarimetric radar data. Comparisons then with 4ICE LUT simulations did not make sense as the results were not comparable, thus SBM LUT visualizations were eliminated. Since 4ICE was size-integrated, although not all sizes are always reasonable each elevation angle and the chosen temperature (275 K), the entirety of the results was plotted.

The most straight-forward method for visualizing the LUT results is to plot the results of LUT output using box and whisker plots (see Fig. 3.1 for an example). A quick overview of box and whisker plots is warranted to understand what the results mean. The box represents the interquartile range. The lower end of the interquartile range is the 1st quartile, the higher end is the 3rd quartile, and the median of the whole dataset is the 2nd quartile. Whiskers are then added to these plots, which are calculated on the larger end of numbers by taking the last number that is less than the 3rd quartile + 1.5*IQR, and on the smaller end of numbers, the whisker extends to the first number that is greater than the 1st quartile – 1.5*IQR. Anything past these whiskers is considered outlier values.

In this work, these plots were created for various assumptions of axis ratio and canting angle for the above-mentioned sources, and results were split up from 0-30° (l), 30-60° (m), and 60-90° (h) in elevation. This was necessary because to the radar, the same hydrometeor can produce different results at different elevation angles in the radar. For example, for a hamburger-shaped raindrop the radar will see an increasingly larger amount of the apparent diameter of the particle with increasing elevation, which results in the radar seeing a larger backscattering cross section. This would result in an increase in reflectivity. Differential reflectivity and specific differential reflectivity would

decrease, however, with a particle that looks more and more spherical as the radar is tilted upward at higher elevation angles.

With these results, and the spread of values created for polarimetric radar variable for each different input assumption could be seen, and the most appropriate values (i.e. the assumptions that had the most all-encompassing spread of values) to input to POLARRIS-f were then determined. Assumptions that were varied input to the LUT for sensitivity tests are detailed in Table 3.2. Note that a temperature of 275 K was used for all simulations as it showed values close to 273.1 K (i.e. the freezing temperature, or 0° C).

3.7 POLARRIS EVALUATION

Inputs to POLARRIS were chosen based on results from both the original T-Matrix Mueller Matrix sensitivity tests, as well as the tests done with the LUT. Output LUT files were then run through POLARRIS-f, and through iPOLARRIS (based on the methods described in section 2.5). In order to ensure that only type of hydrometeor was considered at a time in iPOLARRIS results (when looking at polarimetric radar variable data), mixing ratios of other hydrometeors were set to zero in POLARRIS-f simulations. For observations, radar variables were input to the CSU HID and then the radar variables corresponding to the hydrometeor of interest were considered. This methodology of computing radar observables based on hydrometeor type is a bit circular. That is, you get back the computed HID based on values that were pre-defined by the user and thus, in a certain sense, you get back what you gave. In order to avoid this circularity, in situ data from aircraft, drones, etc. are necessary in order to validate the HID retrievals. Without much in the way of in situ data for the chosen ice hydrometeors to guide the choice in HID parameters, however, this circularity is unavoidable.

Special attention was given to the type of desired output from POLARRIS in regards to comparisons with observations. There was concern that if one considered only one polarimetric radar variable at a time between POLARRIS output and observations that, for example, even if K_{dp} followed the same pattern and intensity in both frameworks, that other variables, for example, Z_{dr}, would not also vary in the same way between the model and observations. To the end of trying to mitigate that issue, co-variances between two polarimetric radar variables at a time were analyzed (i.e. Z-Z_{dr}, Z-K_{dp}, and K_{dp}-Z_{dr} plots were created for comparison between POLARRIS output and observations). An example of MC3E 4ICE and observations co-variance of radar variable plots is shown in Fig. 3.2. This type of comparison guided the decision on which axis ratio and orientation angle assumptions "best" compared with results seen in observations. Several additional runs through the entire POLARRIS framework (creating a LUT, then running that through POLARRIS-f, and finally iPOLARRIS), where axis ratios were modified to reach a closer comparison with observations, were required before a final decision was reached on the appropriate inputs for each hydrometeor (See Tables 4.1 and 4.2).

In order to achieve the most comparable results with observations, POLARRIS-f needed guidance on what inputs were best to use. The findings herein are also applicable to polarimetric radar simulators apart from POLARRIS itself, thus revealing one of the utilities of this master's work. When a decision was reached for the "best" inputs for each hydrometeor, for each regime (MC3E vs. TWP-ICE), for each microphysics assumption (4ICE vs. HUCM SBM), these assumptions, for each of these identifiers, were conglomerated together in a "best" run through the POLARRIS framework. Note that throughout this process, rain was also carried through and compared with observations to ensure that the model was simulating rain as closely as possible to observations. This is important since there is an abundance of literature studying the various properties of rainfall (e.g. studies of the size distribution of rain, the

general shape of falling rain from both wind tunnel studies and in situ data, comparisons of situ data and theoretical/empirical relationships), and thus its simulation should be fairly comparable with observations (e.g. Pruppacher and Beard 1970; Pruppacher and Pitter 1971; Green, 1975; Goddard et al. 1982; Goddard and Cherry 1984; Beard and Chuang 1987; Keenan et al. 2001; Brandes et al. 2002). Otherwise, POLARRIS would have some fairly concerning problems to attend to apart from trying to simulate ice hydrometeors. In this work, cloud droplets and hail in 4ICE were not considered, and in HUCM SBM assumptions, ice columns, ice plates, and ice dendrites were all given the same axis ratio/orientation angle assumptions to simplify the task at hand. Additionally, no melting particles are considered (in the theoretical scattering simulations), and no turbulence is applied to particles in the scattering simulations.

Recall, the goal of POLARRIS is to simulate, as closely as possible, the same results found with the observations and the CSU HID. To this end, the combined set of "best" values for each hydrometeor was then run through the POLARRIS framework. Co-variances between polarimetric radar variables were analyzed for POLARRIS output and observations. More importantly, however, the resulting HID from POLARRIS and the HID output from observations were compared to see how well the "best" assumptions were handled for each microphysical scheme, and each regime, in the fuzzy logic framework. Were results more robust than the co-variance plots? Worse? Did the comparisons fair better for a certain regime or a certain microphysical scheme? These were all questions asked during the analysis of HID output. Again, the overarching concept for this work is that not only does comparing observations and model results with HID validate the utility of HID for model and observation comparisons, but also that the use of HID is a robust way of evaluating model microphysics.

In order to evaluate HID performance in the model in comparison to observations, SFADs were compared. Additionally, precipitation in the model and in

observations were separated into convective and stratiform components via the methods described in Powell et al. (2016). Then, HID SFADs of convective and stratiform precipitation (such as those in Fig. 3.3) were compared between the model and observations, to see how well these different types of precipitation were captured by the model.

Using the HID SFADs, and the co-variances of polarimetric radar variables, results are compared and contrasted between POLARRIS and observations, to evaluate the simulations, and understand whether differences are most attributable to a differing regime (e.g. MC3E vs. TWP-ICE), microphysics scheme (e.g. 4ICE vs. SBM), or fundamental assumptions (e.g. particle size distribution, axis ratio, density, etc.).

3.8 POLARRIS: SENSITIVITY TO AXIS RATIO AND ORIENTATION ANGLE ASSUMPTIONS

One interesting component of the POLARRIS runs was looking at the sensitivity of the resulting polarimetric data for different hydrometeors to changes in axis ratio and canting angle assumptions. Multiple axis ratios and orientation angles were run in the POLARRIS framework in order to ascertain the combination that produced the most comparable results to observations (See Tables 4.1 and 4.2). In order to get an idea of the sensitivity of the radar observables for each hydrometeor type to changes in the input assumptions, for different sets of axis ratio assumptions, plots such as the one shown in Fig 3.4 were created. In these plots, we see each of the simulated most-frequently occurring polarimetric radar variable values, for a certain hydrometer, plotted as a function of height. This was done for each time period in the hour (in 10 minute intervals). What is plotted, then, is actually the mean for each kilometer in altitude of the most-frequently occurring radar observable values as a function of height for each axis ratio and canting angle assumption. Red lines denote the assumption that was chosen as the “best” assumption for each hydrometeor (with respect to ensuring the joint PDFs results were comparable with observations). Blue lines denote simulations using GE15.

Dotted lines indicate the larger of the two values for canting angle (i.e. 30° for aggregates and ice crystals, and 20° for graupel), while solid lines indicate the smaller of the two canting angle assumptions (15° for aggregates and ice crystals, and 10° for graupel). In the case of rain, there are no dotted lines, and solid lines simply indicate the different rain relation (i.e. axis ratio – size dependent equations) assumptions. By utilizing these sensitivity plots for all simulated axis ratio and canting angle assumptions, one can better internalize the effect that changing these input variables has on the resultant polarimetric radar variable values and HID categorization for each hydrometeor type (in this work, limited to ice crystals, aggregates, graupel, and rain).

3.9 MODIFICATIONS TO MBFS IN CSU HID

The MBFs used in the CSU HID (and also in POLARRIS's HID) were determined based on literature values for each radar wavelength (DR09; Dolan et al. 2013). The goal of this particular study was to test the sensitivity of the HID retrievals to changing MBF input. This also helps illustrate the characterization of the uncertainty in the HID retrievals (i.e. these studies give an idea of potential ranges of values observed when the MBFs themselves are changed).

The MBFs were modified for C-Band (5 cm) radar values to fit what was seen when both CPOL and CSAPR data were run through the CSU HID analysis, and then plotted with the MBFs as they are currently defined in the CSU HID. That is, for each campaign, radar data was processed with the CSU HID. Then, for each polarimetric radar variable, locations of the different types of hydrometeors in the HID were identified. Then, a frequency of occurrence plot was created for each of these hydrometeors, for each polarimetric radar variable. These frequency plots display how often a particular polarimetric radar variable value was identified for a particular hydrometeor. These were created by making histograms for each radar volume of each polarimetric radar variable, sub sectioned to the regions of each identified hydrometeor,

and then summing that histogram at each height in altitude (every kilometer for CSAPR and every half kilometer for C-POL). These frequency plots then were plotted with the MBF for whichever polarimetric radar variable and hydrometeor were under consideration (see example in Fig. 3.5). For MC3E, C-SAPR data was used from four campaign days to create the frequency of occurrence plots: 11-13 Z (inclusive) 01 May 2011, 06-09 Z (inclusive) 20 May 2011, 20-23 Z (inclusive) 23 May 2011, and 00-21 Z (inclusive) 24 May 2011. For TWP – ICE, CPOL data from 7 field campaign days was used: 00-23 Z (inclusive) for 19-24 January 2006 (monsoon) and 18 February 2006 (break).

Looking at these combined frequency plots and MBF plots, we can see how well, or not, the MBF fits data. To modify these MBFs, visual comparisons between the MBF range and the range of identified values for each polarimetric radar variable, for each hydrometeor, displayed in the frequency plots were done. If it was shown that the MBF perfectly fit the range for a certain hydrometeor, then it was not modified. If the MBF's range, however, was too large, too small, or even if the tails of the MBF function were too steep or gradual, then the values input to the MBF for that hydrometeor, for that radar variable, were changed to make the MBF better fit what was identified in CSPAR and CPOL. In the end, correlation coefficient was not modified, as results from CSAPR and CPOL were fairly noisy, making analysis difficult.

The CSU HID was then run again with these new, modified MBFs. The same types of HID SFADs as in Figs. 3.3 were created again for observations, as well as for simulations. In addition to these plots, to give another perspective on how modifying the MBFs resulted in changes in HID in model simulations and observations, HID pie chart plots were created (see Fig. 3.6). While looking at the overall convective and stratiform HID SFADs are helpful and informative in discerning differences between iPOLARRIS output for model simulations and observations, a more quantitative approach was desired to hone in on the differences between model output and observations for each

bulk hydrometeor category under consideration. These bulk hydrometeor categories include “rain”, composed of drizzle, rain, and big drops, “crystals”, composed of ice crystals and vertical ice, aggregates, which were composed only of dry aggregates and no wet snow, and “graupel”, which was composed of both low- and high-density graupel. In these plots, HID for each of these bulk hydrometeor categories is queried, and then for every kilometer in altitude, these categories are split into convective and stratiform components. Then, for every two kilometers in altitude, the number of identified points for each hydrometeor, for either convection or stratiform precipitation is counted, and then normalized by dividing by the total number of either convective or stratiform points identified for these bulk hydrometeor categories over the two kilometers of altitude under consideration. The results of this are then plotted in the form of a pie chart for convective and stratiform components, every two kilometers, with percentage of each bulk hydrometeor category identified after normalization displayed.

These results were used to investigate the effect of modifying the MBFs on both simulated and observed data. Additionally, these studies helped identify sensitivities in the HID retrievals to changing MBF input. These sensitivities helped then characterize the uncertainty associated with the HID retrievals themselves. The uncertainty is related to the types of microphysical scheme used, the various properties associated with the simulated hydrometeors (e.g. the assumed bulk density, the size distribution type, the input axis ratio and canting angle assumptions), as well as the values used for the MBFs.

Table 3.1: Inputs to the sensitivity tests with the original T-Matrix, Mueller Matrix framework for aggregates, low-density graupel, and high-density graupel. Inputs include the temperature, radar wavelength, bulk density, diameter and its interval, rain rates, canting angle distributions, mean canting angle (θ), and standard deviation of canting angle (σ).

	Temperature [°C]	Radar Wavelength [cm]	Particle Bulk Density [g/cm3]	D [cm]	ΔD [cm]
Aggregates	-10	5,10	0.2	0.1 to 0.2	0.1
Low-Density Graupel	-10	5,10	0.4	0.1 to 1.0	0.1
High-Density Graupel	-10	5,10	0.73	0.1 to 1.2	0.1
	Equivalent Rain Rate [mm/hr]	Canting Angle Distribution	Axis Ratio	$\boldsymbol{\theta}$ [°]	$\boldsymbol{\sigma}$ [°]
Aggregates	10	Gaussian	0.2,0.9	DR09: 0, GE15: 13	DR09: 23, GE15: 14
Low-Density Graupel	1	Gaussian	0.65, 1.25	DR09: 0, GE15: 16	DR09: 15, GE15: 14
High-Density Graupel	1	Gaussian	0.5, 1.25	DR09: 0, GE15: 20	DR09: 15, GE15: 14

Table 3.2: Inputs to the LUT sensitivity tests for aggregates (snow), ice crystals, and high-density graupel. Varied inputs include axis ratio, θ and σ.

	Axis Ratio	$\boldsymbol{\theta}$ [°]	$\boldsymbol{\sigma}$ [°]
Aggregates	DR09: 0.2,0.9 S00: 0.2, 0.6, 1.0 R11: 0.8 M17: max(0.2, 1-0.05*D) GE15: 0.65	DR09: 0 S00: 0 R11: 0 M17: 0 GE15:14	DR09: 15,30 S00: 15,30 R11: 40 M17: 10 GE15: 13
Ice Crystals	DR09: 0.125, 0.35 S00: 0.5, 1.0, 1.3 R11: 2.0 M17: 2.0	DR09: 0 S00: 0 R11: 0 M17: 0	DR09: 15,30 S00: 15,30 R11: random M17: random
High-Density Graupel	DR09: 0.5, 0.9, 1.25 S00: 0.5, 0.75, 1.0, 1.2 R11: max(0.8, 1-D*0.02) M17: max(0.8, 1-0.02*D) GE15: 0.75	DR09: 0 S00: 0 R11: 0 M17: 0 GE15:14	DR09: 10, 20 S00: 10, 20 R11: 40 M17: 10 GE15: 16

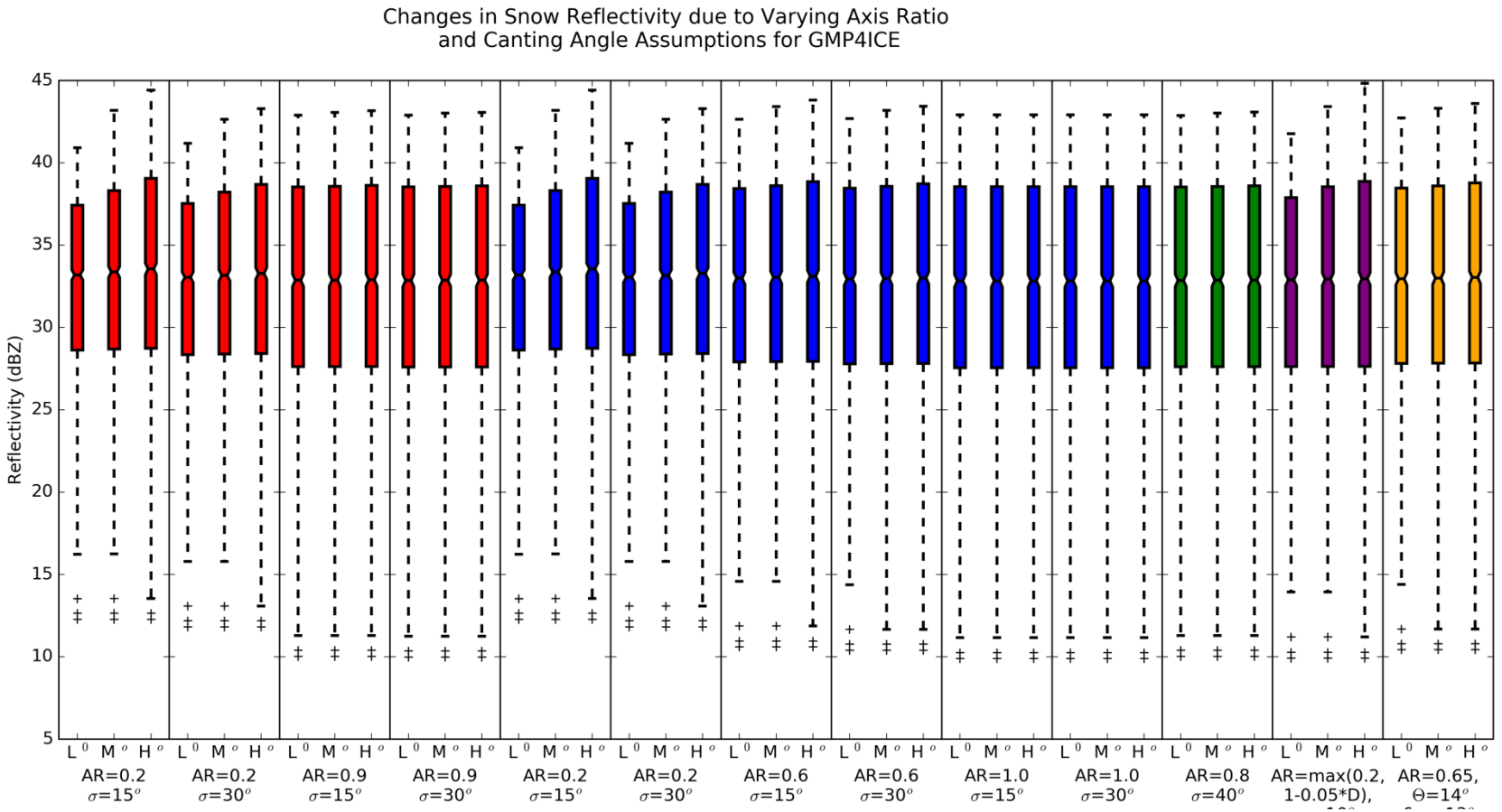

Figure 3.1: An example of the box and whisker plots for TWP-ICE, 4ICE aggregate reflectivity values. Red colors denote assumptions from DR09, blue from S00, green from R11, purple from M17, and yellow from GE15. Results for each input assumptions were stratified by “low”, “medium”, and “high” elevation angles, as is described in the text.

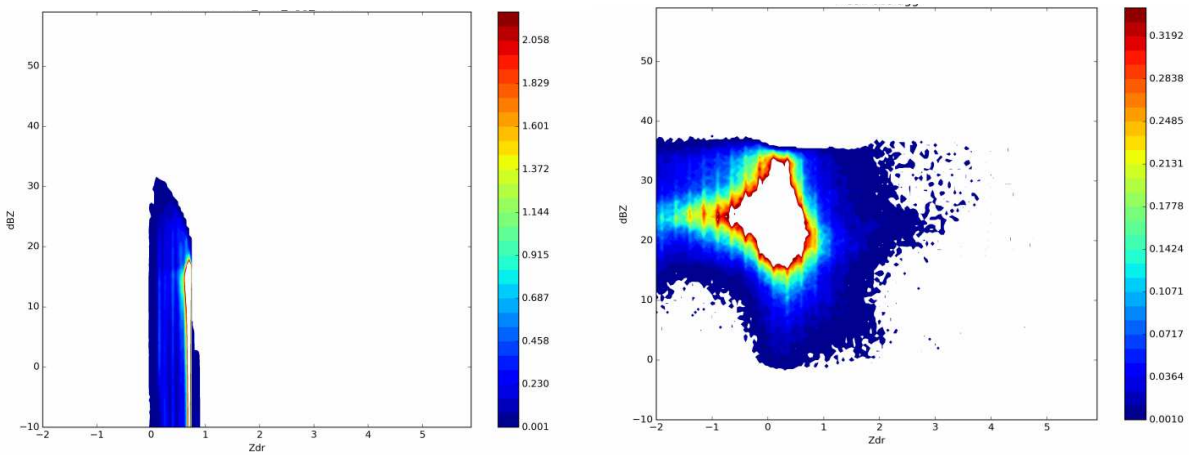

Figure 3.2: Comparison between iPOLARRIS output for model simulations and observations for Z-Z_{dr} co-variances. Left is iPOLARRIS output for 4ICE, MC3E, Aggregates, where input was an axis ratio-size dependent relationship derived from Citation II in situ data collected during the MC3E campaign. Right is iPOLARRIS output for MC3E observation aggregates from the CSU HID.

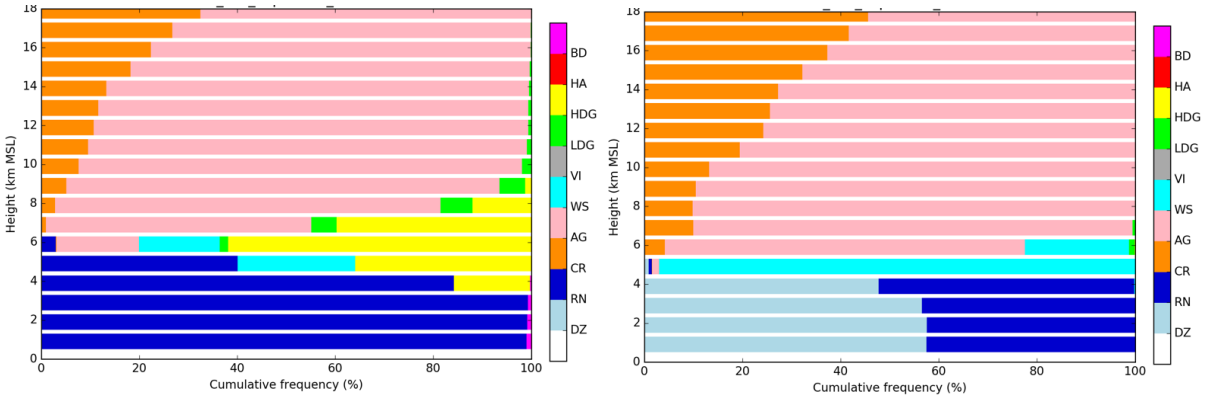

Figure 3.3: Example of HID SFAD from TWP-ICE observations. Precipitation identified as convective was input to the SFAD on the left, and stratiform-identified precipitation was input to the SFAD on the right.

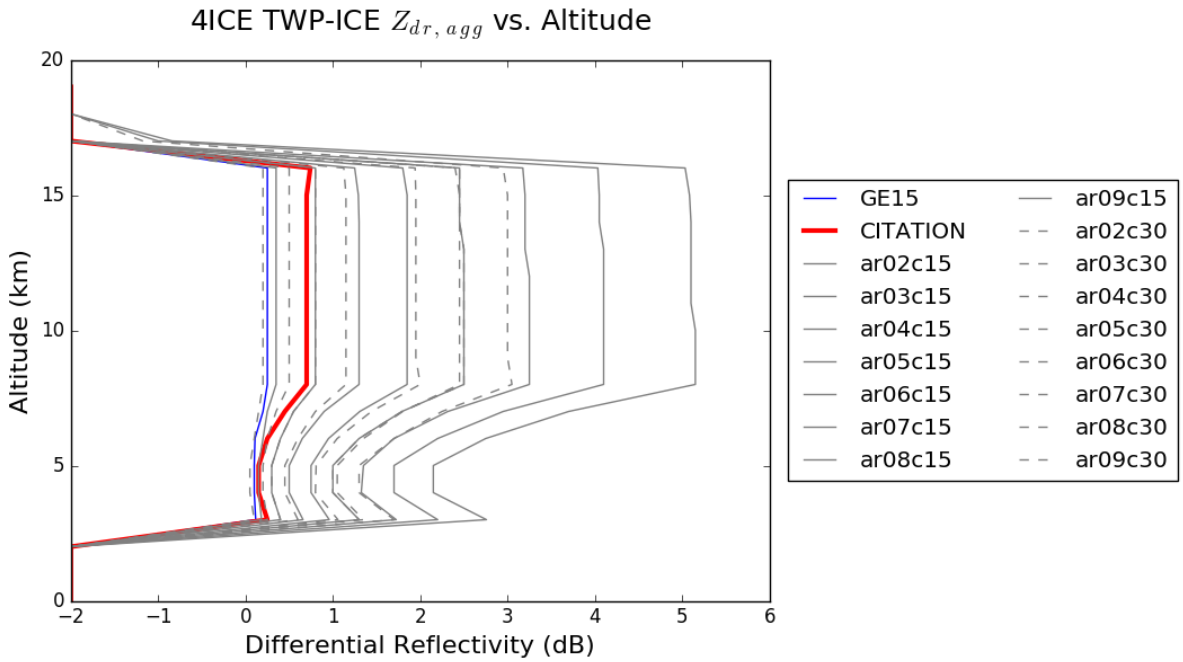

Figure 3.4: Example of a plot of the mean of the most frequently identified polarimetric radar value with respect to height for various axis ratio and canting angle assumptions for TWP-ICE, 4ICE aggregates. The Citation II data input line is red and bolded, as that was considered the "best" input when co-variance plots between iPOLARRIS output for the model and observations were compared. GE15 values are highlighted in blue. Other values are colored in grey, where dashed lines indicate the larger of the two σ assumptions

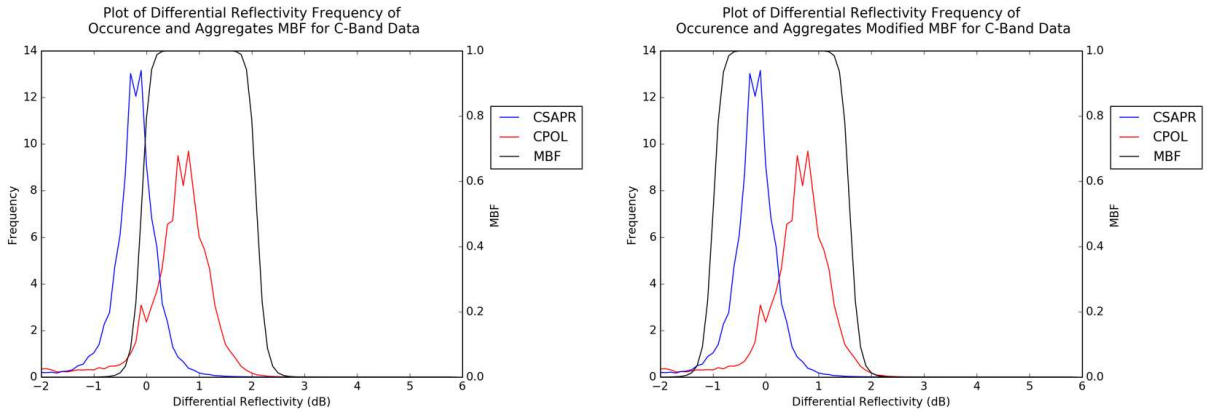

Figure 3.5: Plots of the CSU HID MBFs overlaid on top of frequency of occurrence data of, in this case, C-Band aggregates for differential reflectivity. The plot with the original CSU HID MBFs is shown to the left, and that of the modified CSU HID MBFs is shown to the right

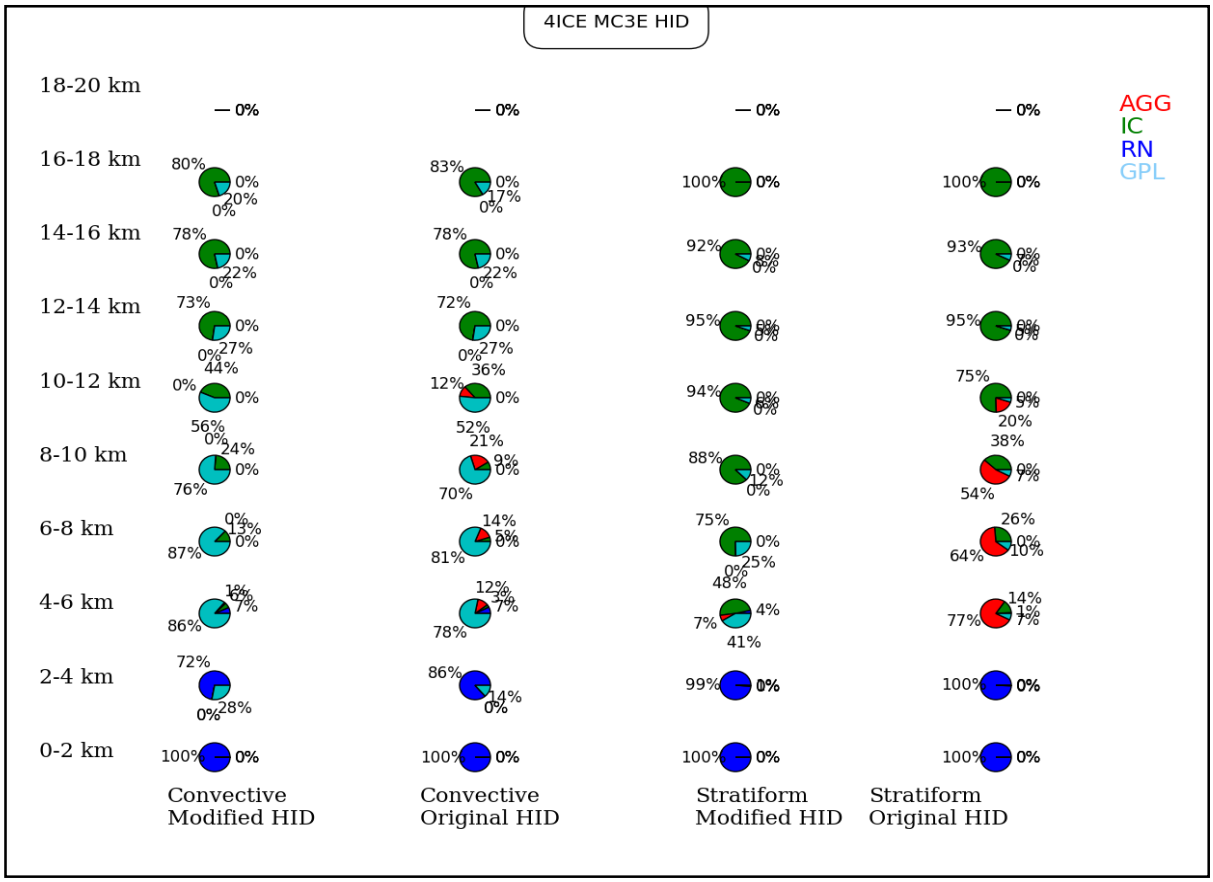

Figure 3.6: Example of an HID pie chart plot. Shown for 4ICE MC3E simulations.

CHAPTER 4: RESULTS

In this chapter, results of the various experiments outlined in the methodology will be discussed. These will include looking first at the original T-Matrix, then the Mueller Matrix framework sensitivity tests, then the LUT sensitivity test results. This will be followed by case analyses for MC3E (23 May 2011), and TWP-ICE (23 January 2006), sensitivity tests of polarimetric observables to changing input axis ratio and canting angle assumptions, followed by a discussion of what is seen with modification of the CSU HID MBFs, also applied to the POLARRIS HID MBFs.

4.1 *ORIGINAL T-MATRIX, MUELLER MATRIX FRAMEWORK SENSITIVITY TEST RESULTS*

In order to ascertain the relative impacts on resultant simulated polarimetric radar data of changes in axis ratio and canting angle, the setup described in section 3.5 was employed. Values based on those used in DR09 for aggregates, high-density graupel, and low-density graupel were input to the T-Matrix, Mueller Matrix framework (See Table 3.1). These particular variables were chosen because a direct comparison of results from DR09 values could be compared with values reported in GE15. This was ideal since GE15 made direct in-situ measurements of the observed axis ratios and canting angles of falling ice hydrometeors. This was rather difficult to find in literature due to the lack of experiments performed wherein in-situ data was taken of various frozen hydrometeors. Tests in this framework were done for both C- and S-Band, though only the former is discussed herein, as it relates directly to the radar wavelengths utilized in other parts of the results section (C-SAPR and C-POL).

Fig. 4.1 shows the results of the tests, with inputs as described for aggregates in Table 3.1. Red lines denote canting angle assumptions (which includes both θ and σ) reported in GE15, and black lines denote those from DR09. Solid lines denote an axis

ratio of 0.2, while dotted lines represent an axis ratio of 0.9. Hence, we compare nearly spherical particles (axis ratio of 0.9) to very oblate particles (axis ratio of 0.2).

The first, and most important remark to be made of these results is the stark contrast in values seen for each polarimetric radar variable when the axis ratio is modified (change from solid to dotted lines), as opposed to the comparatively small changes that occur when canting angle assumptions are varied. Notice that in Fig. 4.1 a and d, the differences for different canting angle assumptions, implemented for an axis ratio of 0.9, are so small for the simulated radar observables that the dashed lines are indiscernible. Indeed, the difference for one set of canting angle assumptions, but different axis ratios, can result in differences of up to 1 dB for Z_{dr}, 0.8 dBZ for Z_h, and 0.14 ° km^{-1} for $K_{dp.}$ Differences in ρ_{hv} are also observed, but are much smaller than the other variables, and because of this behavior, ρ_{hv} will not be discussed with the same weight as the other variables.

For an axis ratio of 0.2 for Z_{dr} (Fig. 4.1c), for example, changes between the two different types of canting angle assumptions result in a difference of about 0.1 dB at 0° elevation angle, which decreases to almost zero at larger elevation angles. This difference is even smaller for differential reflectivity when considering an axis ratio of 0.9. The differing results between the two axis ratios makes sense because if a nearly spherical particle cants slightly more or less, or falls at a certain average angle that deviates from 0°, it is going to be less noticeable to the radar than in the case of a fairly oblate particle whose average canting angle is not 0°, or whose tendency to flutter is fairly large, since that will greatly affect the radar power returns in the polarized horizontal and vertical planes. Overall, it would seem, at least for these specific set of inputs, varying the axis ratio has a larger influence on the resulting polarimetric radar variable output than varying the θ and σ (especially in the case of differential reflectivity).

Also interesting to note in these simulations is the fidelity by which Z_{dr}, K_{dp}, and Z_h change in value with increasing elevation angle. It is well known that as elevation angle increases that Z_{dr} should decrease due to the viewing angle (Bringi and Chandrasekar 2001; Ryzhkov et al. 2005a). This is especially evident for the more oblate of the two axis ratios. Specific differential phase also would decrease for the same reason (due to the fact that K_{dp} is a function of both concentrations of particles and particle shape; Bringi and Chandrasekar 2001). By this same line of thought, as the radar beam penetrates higher into the atmosphere, looking at an oblate particle, it would see increasingly larger apparent diameters with increasing elevation angles, and it would then see the inverse for a more prolate particle (axis ratio greater than one). Since Z_h is a function of the diameter of the particle to the sixth power, increases in the apparent diameter (to the radar) would mean a larger Z_h value, and decreases in the apparent diameter would mean a smaller Z_h value (Bringi and Chandrasekar 2001). Hence, this is the reason why one might see a small increase in reflectivity value with increasing elevation.

The importance of whether or not to simulate a prolate hydrometeor was investigated, since these do not occur as frequently as compared to oblate, or nearly spherical particles. Despite few in situ observations of graupel, prolate graupel has been shown to occur in both winter and springtime storms (Evaristo et al. 2013; Kennedy et al. 2015). To the end of gathering more data in support (or not) of the need to include prolate particles in the simulations of graupel, a frequency map of the occurrences of negative Z_{dr} values with data from NPOL during MC3E was analyzed (Fig. 4.2). C-band radar can be quite affected by attenuation and resonance effects, leaving biases in the polarimetric radar observables (Ryzhkov and Zrnic 2005). This can be seen with the HID MBF and frequency of occurrence plots for graupel (Figs. 4.55 c and d and 4.56 c and d), where C-SAPR Z_{dr} values exhibit a low bias due to bad differential attenuation that was not able to be completely removed. Hence, if C-SAPR data were used to probe

the appearance of negative Z_{dr} for graupel in the MC3E dataset, then results might be biased as actual graupel Z_{dr} was likely not as low as is shown for C-SAPR. S-band is not nearly as affected by this issue as is C-band, and thus data from the NPOL was used for this particular test. Dates with NPOL data included in the analysis were cases from 24-27 April 2011, and 01, 11, 20 and 23-25 May 2011. The map was created by locating all negative Z_{dr} values, binned by reflectivity (0 to 60 dBZ at 1 dBZ increments) and temperature (-40 to 20°C at 1 C increments) and then for each of those intersecting bins, finding the mean of the negative Z_{dr} values, and plotting this number (with the color shown in the color bar corresponding to the negative Z_{dr} value) as a function of temperature and reflectivity. Note that temperature was obtained from the sounding (either 0 or 12 Z) closest in time to the occurrence of convection for each day of MC3E field campaign operations. The black box indicates the region where high-density graupel resides in the CSU HID MBFs (DR09; Dolan et al. 2013). This heat map hinted that in later spring which this data was collected, negative Z_{dr} do values exist, which supports the evidence to include simulations of prolate graupel.

With the utility of simulating a prolate graupel particle established, low-density graupel simulations were run. Similar results are found when considering low-density graupel as were seen for aggregates (Fig. 4.3). Indeed, axis ratio plays a much larger role than canting angle assumptions for low-density graupel, now shown with an example of a prolate particle (axis ratio of 1.25). As discussed earlier, as elevation increases, the reflectivity value decreases as the apparent diameter observed by the radar decreases. Additionally, as the view angle increases, the particle appears less and less prolate and thus the negative Z_{dr} and K_{dp} values decrease in value towards zero.

Finally, simulations for high-density graupel (where low-density graupel was simulated with a particle bulk density of 0.4 g cm^{-3} and high-density graupel was simulated with 0.73 g cm^{-3}) were run, including for prolate particles (as with low-density

graupel, an axis ratio of 1.25 was simulated), as well as a fairly oblate particle (axis ratio of 0.5). General trends are similar to what was observed in the case of aggregates and low-density graupel, although the effect of changing canting angle assumptions (the mean canting angle and the standard deviation of canting angle, i.e. the amount to which a particle flutters as it falls) were more impactful on the resultant polarimetric radar data (as seen in Fig. 4.4). Additionally, overall simulated Z_h, Z_{dr}, and K_{dp} values were larger for high-density graupel than low-density graupel. Differences of up to ~0.5 dBZ, 1 ° km^{-1}, and ~ 1 dB for Z_{dr} were observed due to changes in canting angle assumptions (where in high-density graupel, σ was 14°, as was the case for low density graupel, but θ was increased from 16° to 20° for high-density graupel). These differences for Z_{dr} and K_{dp} were larger than what was observed for low-density graupel. Although, differences between the amount of change in Z_h between the different canting angle assumptions for high-density graupel and low-density graupel was not as stark. Though the differences are still quite small, values of ρ_{hv} dipped lower than in the previous two simulated hydrometeor types. Perhaps part of the explanation for the stronger effects (larger changes in polarimetric radar data due to changing input values to the T-Matrix, Mueller Matrix framework) seen with this high-density graupel hydrometeor type as opposed to low-density graupel and aggregates results from the larger dielectric constant associated with high-density graupel.

If the canting angle assumptions had been varied over the whole range of possible values 0° to 90° (for θ or σ), of course, large changes in the simulated radar observables would have been seen. Similarly, if small differences in axis ratios had been simulated (e.g. changing the axis ratio from 0.1 to 0.11), the changes compared to changing the axis ratio by 0.1, for example, would be small. However, larger relative changes are seen when the axis ratios are varied over the potential range of values

than when canting angles are varied over their potential range of values, as demonstrated by Fig. 4.1, 4.3, 4.4).

At a certain point, it is apparent that mean canting angle and the variability of the canting angle incurred by a falling hydrometeor become important, and have a noticeable impact on resultant polarimetric radar data (as seen for this high-density graupel situation). Large changes in canting angle will certainly have a noticeable impact on the values resulting from polarimetric radar simulations. However, for relatively small changes σ and even larger changes in θ (here, σ changed by only 1° between DR09 and GE15 while θ varied by 20° between DR09 and GE15 assumptions), changes in canting angle assumptions are not as impactful on the resultant simulated polarimetric radar output as changes in axis ratio. Therefore, a great deal of emphasis will be placed from this point going forward on finding the most appropriate axis ratio, or range of axis ratios, for the three ice hydrometeors under consideration in this work (aggregates, ice crystals, and graupel).

4.2 *LUT SENSITIVITY TEST RESULTS*

Prior to running any set of assumptions through the entirety of the POLARRIS framework with real simulated Nu-WRF data, visualizations with LUT results were performed in order to examine the general output (that is, are simulated values reasonable in comparison with previous literature values – e.g. did they compare well with S00), as well as to see which inputs seemed to best capture the range of possible values. The latter was helpful in paring down the amount of runs that were going to be put into the POLARRIS framework. Shown in Figs. 4.5-4.13 are the results for 4ICE simulations. Results are stratified as “low”, “medium”, and “high” radar elevation angle (i.e. 0°-30°,30°-60°, and 60°-90°). Red values correspond to DR09 assumptions, blue values correspond to S00 assumptions, green values correspond to R11 assumptions, purple corresponds to a set of control run values (M17), and yellow corresponds to

GE15 values. The inputs for each of these assumptions are outlined in Table 3.2. Note that now, graupel refers to an overall graupel category.

Save for the prolate assumptions for ice crystals (Fig. 4.8, for an axis ratio of 1.25), various input assumptions did not appear to change the values for reflectivity by a significant amount from low to high radar elevation angle, and from one set of assumptions to another (see Figs. 4.5, 4.8, Fig. 11). In the case of graupel (Fig. 4.11), the reflectivity values for the most part seem to fall in a range from ~5 dBZ to just over 50 dBZ. The lower value is fairly low for graupel in comparison to literature values (e.g. S00), however, the skew of the data is toward higher reflectivity values (the bulk of which is found between ~25 dBZ and 42 dBZ). Aggregate (Fig. 4.5, termed in these plots as “snow”) reflectivity values seem to be in line with literature (generally, less than 45 dBZ; S00). The bulk of values are found between ~28 dBZ and ~38 dBZ, with data overall skewed towards higher values of reflectivity. The higher reflectivity values are perhaps a bit large for dry snow aggregates, although they are not unreasonably large (Thompson et al. 2014). Ice crystal reflectivity seems to be quite low (Fig. 4.8) compared to literature (S00; DR09; Thompson et al. 2014). Certainly, negative values to around -30 dBZ have been simulated (S00; DR09), however it is not uncommon to see ice crystal reflectivity values reach up to 20 dBZ. However, in the LUT visualization, even outlier values never manage to reach 0 dBZ. This is potentially due to the fact that the PSD for ice crystals does not simulate particles large enough to actually capture the proper reflectivity values. This is a detail which will need to be kept in mind as simulations in the overall POLARRIS framework are run.

Also, recall the discussion in Section 3.6 in how LUT values were generated. Any potential temperature/size/elevation angle combination were allowed in the LUT visualizations (from the range of assigned values), for the particular axis ratio and canting angle assumptions. Thus, there are some combinations of the above variables that likely resulted in the values that are either too small or too large, as is indicated

above. Hence, the focus is instead of the data held in the actual box part of the box and whisker plot, as that houses the majority of the data, and leaves out the simulated radar observable outliers, that do not make sense with regards to literature values for each hydrometeor. This detail should also be kept in mind as this discussion continues.

Differential reflectivity values vary a great deal from low to high radar elevation angle, and from one set of assumptions to the other (see Figs. 4.7, 4.10, and 4.13). Values seen for graupel range anywhere from about -0.4 dB to ~1.3 dB (Fig. 4.13). This is well in line with observed literature values (S00; DR09). Additionally, the decrease (increase) in Z_{dr} with increasing radar elevation angle for oblate (prolate) particles is observed, as was seen with the simulations in the original T-Matrix, Mueller matrix simulations (Sec. 4.1). This is seen for all LUT Z_{dr} visualizations. Snow aggregate Z_{dr} values have a large range in possible values (Fig. 4.7), ranging anywhere from 0 dB to just over 5 dB. Of course, these values are likely associated with the small axis ratio chosen, and potentially an unrealistic size/temperature/elevation angle combination as well. The bulk of the values, however, tend to range from 0 – 3 dB, which better compares with previous literature values (S00; DR09; Thompson et al. 2014). The assumptions for which Z_{dr} values much above 1 dB occur are associated with extremely oblate hydrometeors (axis ratios of 0.2, which are too large for aggregates), and that may be the cause of some of the unphysically large Z_{dr} values. Hence, results there show what one would likely expect for too large an axis ratio assumption. Ice crystal Z_{dr} values vary the most of any of the three ice hydrometeors input to the LUT visualization framework. Values from ~-0.5 dB to 10 dB are seen (Fig. 4.10). The largest Z_{dr} values logically occur with the most oblate axis ratio assumptions (herein, for axis ratio assumptions of 0.125). These large values could also be the result of known model instabilities that occur for axis ratios $\sim < 0.1$. According to literature (e.g. S00 and DR09), ice crystals are generally associated with Z_{dr} values from 0-6, depending on the ice crystal habit. So the large Z_{dr} values from the oblate assumptions are likely not

realistic representation of ice crystals, and thereby would not be representative if input to the POLARRIS framework. Even simply a 0.2 increase in axis ratio resulted in more realistic values in comparison with literature (reaching a maximum of just under 2 dB).

An interesting note to be made about variations in the Z_{dr} values is that there is actually at times a large difference in Z_{dr} output values as a function of standard deviation of canting angle input to the simulations. For example, for ice crystals with an axis ratio assumption of 0.125, at the low radar elevation angle set, changing the amount to which a particle tumbles from 15° to 30° results in a maximum Z_{dr} value change of ~10 dB to 8 dB, respectively. Certainly, this is not a small change, and something to keep in mind when dealing with extremely oblate particles (as this is not nearly as large a difference for more spherical, or slightly prolate particles). However, when considering the low radar elevation angle set, for assumptions of an axis ratio of 0.125 and a standard deviation of canting angle of 15°, and then an axis ratio of 0.35 and a standard deviation of canting angle of 15°, the resulting change in maximum simulated Z_{dr} value is ~10 dB to ~2.8 dB. Thus, the axis ratio still has the largest impact on the resulting simulated polarimetric radar variable value. This also holds true to all LUT simulations of K_{dp}, as seen in the associated figures (Fig. 4.6, 4.9, and 4.12, for snow, ice crystals, and graupel, respectively).

Similar decreases (increases) in K_{dp} with increasing radar elevation angle occur for oblate (prolate) axis ratios as with Z_{dr}, and as was seen in the original T-Matrix, Mueller matrix framework (Sec. 4.1). These results help ensure that the LUT simulations are working as they should to simulate Z_{dr} and K_{dp} for changing radar elevation angles. Simulated specific differential phase values for graupel are, as with Z_h and Z_{dr} values, well in line with literature values (S00; DR09). Values range anywhere from ~-0.4 ° km^{-1} to ~ 1.3 ° km^{-1}. Indeed, any one of the set of assumptions shown for graupel would be appropriate (based on previous literature) to input into the POLARRIS framework.

Ideally, however, some kind of range of values would be simulated together to get closer to the full range of polarimetric radar variable values seen in observations. As for snow aggregates, K_{dp} values typically range from 0.0 ° km^{-1} to about 1 ° km^{-1} at best (Fig. 4.6; S00; DR09; Thompson et al. 2014). In this LUT visualization, the bulk of the values are skewed closer to 0 ° km^{-1} to 1 ° km^{-1}, with the larger values corresponding to more oblate (and probably unrealistic) simulated aggregates. That being said, these are outlier values, and do not correspond to the location of the bulk of simulated snow aggregate K_{dp} values. In general, depending on the habit, K_{dp} values for ice crystals (Fig 4.9) are shown in literature to range anywhere from -0.6 ° km^{-1} to about 0.6 °km^{-1} or (S00; DR09; Thompson et al. 2014). For most of the sets of assumptions, this is indeed the case. However, with an assumed axis ratio of 0.125, values are wildly large (for example, the low radar elevation angle set has the bulk of values ranging from ~2 ° km^{-1} to about 15 ° km^{-1}, with outliers reaching as high as ~46 ° km^{-1}). It is only for the high radar elevation angle set that the bulk of the values, excluding outliers, come close to fitting the range of values shown in literature. These values are incredibly unrealistic. This could partially be due to the incredibly oblate nature of the axis ratio, in addition to the size/temperature plotted, though the values are likely enlarged to this point due to a model instability. Certainly, an assumed axis ratio of 0.125 for ice crystals will not be an appropriate assumption for runs through the POLARRIS framework. That is, it would not be an appropriate axis ratio assumption to simulate values most closely related to what is seen in C-POL/C-SAPR observations. However, it would be good to run this axis ratio and canting angle assumptions through the POLARRIS framework as a check on whether or not the expected unrealistic values for this set of assumptions occurs when looking at iPOLARRIS results.

Overall, it would appear that the DR09 values capture the largest range of values observed in the LUT simulations, though the more oblate values (ice crystals axis ratio

of 0.125 and snow aggregate axis ratio of 0.2) do not generally seem to fit with what is shown in literature and has been observed. The smallest and largest axis ratios (and the two different associated canting angle assumptions) will be input to POLARRIS framework, in order to ensure that iPOLARRIS results look unreasonable (as they should for the especially extreme oblate axis ratio values). Likely, a range of values somewhere between the smallest and largest assumed axis ratios from the DR09 assumptions will be the most appropriate for reaching model results that are comparable with observations. Therefore, leveraging the results of iPOLARRIS with these sets of assumptions, more tests were run with varying axis ratios, the exact values of which were decided upon based on the iPOLARRIS results from the smallest and largest axis ratios from DR09 assumptions simulated for each hydrometeor in the LUT simulations (See Tables 4.1 and 4.2). This range (or for the majority of the results herein, the assumed axis ratio/canting angle assumptions that yields the most comparable results with observations) is important, since the goal is to arrive at a set of assumed inputs that will help guide polarimetric radar simulations for graupel, ice crystals, and snow aggregates (or simply, aggregates). Since results from SBM were not available from LUT simulations, this work assumes the same assumptions as used for 4ICE.

4.3 *MC3E CASE ANALYSIS: 23 MAY 2011*

To begin with, the smallest and largest axis ratio assumptions (as well as whatever various standard deviations of canting angle were considered) used in the LUT simulations for DR09, for each hydrometeor, were run through POLARRIS-f, and then through iPOLARRIS, where polarimetric radar variable co-variance plots (such as those of Fig. 3.2) were used to compare the model results with observations. It was quickly determined that a majority of these assumptions were not appropriate for narrowing the gap between iPOLARRIS results and observations after running the

assumptions through the POLARRIS framework and comparing iPOLARRIS results between the model and observations. Therefore, the runs listed in Table 4.1 were run to better determine the appropriate axis ratio and canting angle assumptions for each hydrometeor (aggregates, graupel, and ice crystals), and for each microphysics assumption (4ICE and SBM). The assumptions that were eventually chosen for each hydrometeor, and for each microphysical scheme, were the ones producing results most comparable with observations (highlighted in blue).

In order to determine the set of axis ratio and canting angle assumptions that produced the most comparable results from POLARRIS-f output with observations, 2D density (co-variance) plots of radar variables were used. For each microphysical scheme, for each regime, for each hydrometeor, Z-Z_{dr}, Z-K_{dp}, and K_{dp}-Z_{dr} plots were considered between model output and observations. First, we will consider the case of 4ICE MC3E.

4.3.1. 4ICE MC3E CONSIDERATION OF "BEST" ASSUMPTIONS

For each hydrometeor in the 4ICE MC3E runs, co-variance plots for the integrated 22 Z hour were compared to the integrated 22 Z hour period of MC3E observations. The use of one integrated hour of data to create and utilize a methodology in this work was done to ensure that any small-scale trends were not "washed out", or averaged out, by integrating data over an entire day or case. This could introduce the potential that if model-generated convection lagged in time from convection in observations, that not exactly the same hour in the storm cycle is shown between observations and convection. Hence, results here in are not taken as ground truth, but rather as an indicator of the POLARRIS framework's capabilities for using HID to evaluate model microphysical performance with respect to observations, as well as the effect that different microphysical schemes have on the resulting HID. In order to indicate whether differing regimes were better simulated, or not, by the POLARRIS

framework (and if one microphysical scheme truly performed “better” than the other) would likely require a longer integrated time period, and more cases.

Rain, snow aggregate, ice crystal, and graupel plots are shown in Figs. 4.14 – 4.17, respectively, for MC3E for both model (4ICE) and observations. These plots portray the output from the assumptions for each hydrometeor, in the case of 4ICE MC3E simulations, that was the most comparable with similar plots in observations (after having been run through the CSU HID; see blue values in Table 1). These same types of plots were also considered for every other input assumption displayed in Table 4.1, though are not shown in the figures.

In general, rain compares the best with observations when compared to the simulated ice hydrometeors (Fig. 4.14). This is not surprising considering the vast amount of literature that details the way falling rain behaves, the proper particle size distribution of rain, the shape of rain, and empirical rain rate relationships (derived from comparisons with polarimetric radar data and disdrometer data). Overall, the shape of the co-variance curves among simulated radar variables co-variance plots fits well the shape of the observations. However, while the full range of reflectivity is normally able to be simulated, for the most part the full Z_{dr} and K_{dp} ranges seen in observations are never reached. To fix this, a distribution of axis ratios is likely needed, or perhaps a canting angle distribution driven by turbulence, otherwise results (in 4ICE) results will always be too narrow.

The results are not quite as comparable when ice hydrometeors are under consideration. Simulated snow aggregates (Fig 4.17) perform the best of the ice hydrometeors, largely because an axis ratio – size dependent relationship from MC3E in-situ Citation II data was available as input to POLARRIS-f. In general, for aggregates and the other two simulated ice hydrometeors species, Z_h is too low. Simulated aggregate reflectivities are at least similar to reflectivities seen in observations, however the maximum reflectivities in observations are not captured in the simulated output.

Again, as was the case for rain, Z_{dr} and K_{dp} simulated values, while within the range of that seen in observations (with the most frequently simulated values of Z_{dr} and K_{dp} fairly well matched with the most frequently simulated values of those variables in observations), do not have as broad a range of values as in observations. This is extremely evident in the K_{dp}-Z_{dr} co-variance plot (Fig. 14c), when contrasted with the matching observation plot (Fig. 4.14f). These differences between what is seen for model output for aggregates and observations are more pronounced for ice crystals (Fig 4.15) and graupel (Fig 4.16). Reflectivity values simulated for both of these ice hydrometeors is significantly too low. Simulated ice crystal reflectivities never reach 0 dBZ, whereas reflectivity values from observations for ice crystals extends from -10 dBZ to almost 30 dBZ. Worse yet are simulated reflectivity values for graupel, which reach 22 dBZ at best, while in observations values from ~20 dBZ to just over 50 dBZ are simulated. Simulated graupel reflectivity values almost never reach the lowest observed reflectivity values for graupel from observations. Based on the issues with the proper simulation of the range of observed reflectivity values for the three ice hydrometeors under consideration, the choice of the set of axis ratio and canting angle assumptions for each hydrometeor was based largely on whether or not Z_{dr} and K_{dp} for each assumption did, or did not, fall within the observed range.

Of course, part of the lack of comparability between simulated ice crystal polarimetric variable values and observed ice crystal values could have to do with the complex nature of ice crystals in nature that is not fully taken into account in the 4ICE runs (nor the SBM runs, since the same axis ratio input and set of canting angle assumptions were used for dendrites, plates, and needles). This same issue is apparent in the TWP-ICE simulations as well. Ice crystals have a seemingly endless set of shapes they can take on, from how they grow (c- versus a-axis growth), density, their level of complexity (e.g, dendrites vs. simple plates), axis ratios, all due to the particular surrounding region of air's properties (e.g., temperature or relative humidity). The task

of being able to adequately simulate these characteristics is indeed an important one, but for the sake of simplicity, and due to a lack of in situ data in the ice regions at the times specified for this case (and especially the TWP-ICE case), a singular axis ratio and set of canting angle assumptions are employed. Thus, a single shape for ice crystals is allowed, no matter the size of the ice crystal (the case for graupel as well). Additionally, a singular value of density (0.9 g cm^{-3}) was employed for ice crystals, which is not generally what occurs in nature. This was the same case for graupel and aggregates, possibly explaining some of the discrepancies there as well. The ability to make comparable simulations of the polarimetric radar variables for ice crystals with respect to those of observations is limited by these facts.

PPIs were considered of reflectivity and mixing ratio for simulations where mixing ratios of everything but graupel was set to zero. This was done in the attempt to limit the consideration of hydrometeor species to only graupel. While there were reasonable values for graupel mixing ratio, the reflectivity values were more in line with that of snow aggregates (~30-35 dBZ at most). Thus, something had to be causing the decrease in reflectivity, despite the high presence of graupel. The reasoning then, for the POLARRIS framework's inability to simulate adequate reflectivity values for graupel potentially has to do with the selected graupel density in the model. It was set in the model to be 0.3 g cm^{-3}, which is on the low-end of the acceptable ranges of values for even low-density graupel (according to DR09), and is also towards the low end of overall graupel in S00. This could have resulted in simulated values for graupel being low, no matter the amount of occurring graupel in a convective region. Although the density of ice crystals was that of pure ice (0.9 g cm^{-3}), the reflectivities (as discussed above), were quite low. This may have something to do with the PSD allowing a large amount of very small ice to exist, which would never achieve a high reflectivity due to their size. Additionally, the reasoning that aggregate reflectivity was more comparable with observations may have had to do with the PSD, as the simulated reflectivity was

quite low (0.05 g cm^{-3}) (S00; DR09; Thompson et al. 2014). The inclusion of an axis ratio – size dependent relationship may have also aided in raising reflectivity values. Perhaps despite the low density, there were enough large snow aggregates to drive the reflectivity higher.

4.3.2. SBM MC3E CONSIDERATION OF "BEST" ASSUMPTIONS

SBM results were quite different compared to 4ICE for MC3E. 2D radar covariance plots for SBM MC3E assumptions are shown in Fig. 4.18 (aggregates), Fig. 4.19 (ice crystals), Fig. 4.20 (graupel), and Fig. 4.21 (rain). In general, there was more broadening of the range of values simulated for each polarimetric radar variable. However, certain patterns may have been better simulated under 4ICE microphysical assumptions. For example, while the overall ranges of K_{dp} and Z_{dr} are better represented in the SBM runs, the overall shape of the rain curves (Fig 4.21) is much less evident for SBM MC3E runs than it was for 4ICE MC3E runs. Additionally, the 4ICE rain curves for Z-Z_{dr}, Z-K_{dp}, and K_{dp}-Z_{dr} compare better with these same types of covariance plots shown in literature (e.g. Figs. 7.23, 7.24, and 7.85a from Bring and Chandrasekar 2001). There is a slight curve seen in the Z-Z_{dr} and Z-K_{dp} plots, however the general rain curve seen in the observations and in 4ICE simulations is not very evident in SBM simulations. The difference between 4ICE and SBM simulations of MC3E rain could be related to the fact that SBM allows a size distribution to develop organically, while the PSD of 4ICE is prescribed.

The ice hydrometeors plots can all be discussed in bulk terms of the general Z-Z_{dr}, Z-K_{dp}, and K_{dp}-Z_{dr} plots. In general, the broadness of Z_{dr} and K_{dp} values seen in observations is grossly simulated with SBM microphysics (or, at least the values come much closer to those seen in observations than in the case of 4ICE). Also, reflectivity values now manage to capture reflectivities seen in observations. However, reflectivity values also extend beyond the observed ranges with SBM. There does not appear to be

a distinct range of reflectivities simulated for aggregates vs. ice crystals vs. graupel. This could be problematic in terms of HID classification, since reflectivity is the most heavily-weighted variable, and has a large hand in driving the HID classification. Thus, while certain aspects of the SBM simulations are more comparable with observations than was the case with 4ICE simulations, the fact that ranges of reflectivity exist in SBM simulations that do not in observations is concerning.

Here we delve a bit deeper into the differences between MC3E SBM simulations and observations. Although the aggregate co-variances plot (4.18) shows the majority of the most-frequently identified reflectivities in the range shown for observations, Z-Z_{dr} and Z-K_{dp} plots show those values also extending from -10 – 50 dBZ. Observations extend anywhere from about 0 – 40 dBZ at most. Similar trends are seen with ice crystals, where the model shows the bulk of values concentrated in a region from 0 – 40 dBZ (with a tail extending to 50 dBZ, though with less identified points on average), while observations show values ranging mostly from 0 – 25 dBZ at most. Interestingly, graupel co-variance plots show a large range, with double peaks at ~ - 0.5 dB and 0 dB (Fig. 4.20a), with reflectivity values at the first peak concentrated from 0 to 50 dBZ, and the values at the second peak reached from -10 to about 30 dBZ. Observations kept values in the range of ~ 35 – 50 dBZ. Similar trends were seen for Z-K_{dp} in the model and in observations (Fig 4.20b,e).

It would seem that the increased degrees of freedom with SBM brought with them an increase in uncertainty of boundaries for the polarimetric radar variables ranges associated with each hydrometeor. An interesting occurrence with SBM was that although the mixing ratios were set to zero for hydrometeor variables other than the ones under consideration, in the iPOLARRIS results, nonzero mixing are observed for all variables. The reasoning behind this is not well understood, but perhaps has to do with the additional degrees of freedom in SBM simulations. Keep in mind, however, that there may be a slight disconnect in the hour of this MC3E case's storm cycle that is

seen in observations vs. what is seen in simulations. Differences may also be attributable to that fact.

4.3.3. RESULTS OF "BEST" RUNS FROM 4ICE AND SBM MC3E SIMULATIONS AS COMPARED TO OBSERVATIONS

After comparing polarimetric radar variable ranges between 4ICE and SBM MC3E and CSAPR observations, these "best" sets of axis ratio and canting angle assumptions for each hydrometeor were aggregated into an overall "best" assumptions run, this time with all hydrometeors allowed (Table 4.1, blue text). The assumptions that yield the most comparable results with observations are ideally the same between regimes, and between microphysics. However, it was found herein that this was not always the case. Generally, using the axis ratio – size dependent relationship found with the UND Citation II data resulted in the most comparable result between MC3E simulated results and observations. Likely, this was because of the fact that the axis ratio – size dependent relationship came closer to achieving a realistic representation of axis ratios in nature (since nature does not in general have one accepted oblateness). This relationship also improved model simulations in TWP – ICE (Figs. 4.23 and 4.27), even though the data that went into the axis ratio relationship for aggregates was taken in aggregate and ice crystal regions of the 23 May 2011 supercell MC3E cases. Additionally, the use of a rain axis ratio – size dependent relationship (Brandes et al. 2002) for both 4ICE and SBM, for MC3E and TWP – ICE (Figs. 4.14, 4.21, 4.26, 4.30) helped improve those simulations as well.

Whenever axis ratio – size dependent relationships were not available, however, a reliance on the closest as possible simulation to the area where the bulk of the Z_{dr} and K_{dp} values occurred in observations was the goal. For ice crystals, this ended up being different from 4ICE to SBM, though inputs to MC3E and TWP – ICE one from the other did not change (see Tables 4.1 and 4.2). For 4ICE, a larger (less oblate, more spherical) axis ratio was required. Otherwise, values were too large for Z_{dr} and K_{dp}

(while being too low overall for Z_h). In SBM, the most comparable result, however, was achieved with a smaller (more oblate, less spherical) axis ratio. σ also changed for ice crystals from 4ICE to SBM (it decreased from 30°to 15°, see Tables 4.1 and 4.2). The need for a larger amount of fluttering/tumbling of ice crystals as they fell in the case of 4ICE perhaps points to the fact that with the set PSD in 4ICE, larger variations in the particle's simulated movement were required to reach realistic values. The same was the case for graupel in both TWP – ICE and MC3E (see Tables 4.1 and 4.2), for perhaps the same reason. For graupel, a smaller axis ratio was required for 4ICE than for SBM for both TWP – ICE and MC3E. Otherwise, the values were forced towards zero for both Z_{dr} and K_{dp} too much compared to observations.

Interestingly, the same axis ratio was not used in SBM graupel for MC3E and TWP – ICE, which was not the case in 4ICE (both used axis ratios of 0.5 for 4ICE). MC3E was best simulated with respect to observations with a slightly prolate axis ratio (1.25), while TWP – ICE had a slightly oblate axis ratio (0.9). Truthfully, an axis ratio of 0.9 would also have worked for MC3E with the goal of simulating values close to the bulk of values in observations (i.e. with the attempt to simulate values colored as white in the co-variance plots in observations). However, the smaller axis ratio resulted in model output that did not also capture the negative Z_{dr} and (slightly negative) K_{dp} values found in observations. Evidently, there were graupel particles that took on a more conical shape in MC3E observations that was not seen for those of TWP – ICE. This potentially points to a difference in the types of precipitation occurring in this particular integrated hour of MC3E vs. TWP – ICE. This fact points out the need for some kind of axis ratio – or canting angle – size dependent relationship, since one implemented axis ratio fails to capture the ensure breadth of values seen for Z_{dr} and K_{dp} in this case. These differences between 4ICE and SBM also highlight the fact that the handling of the microphysics is important, and certainly has an impact on the simulated polarimetric data.

Ideally, the results of both 4ICE and SBM assumptions will match fairly well what is seen in CSAPR observations. The most logical way to validate the iPOLARRIS results, and the use of each microphysical scheme, was to look at SFADs of HID, partitioned into convective and stratiform regions. In doing this, the use of HID as a diagnostic tool for evaluating model performance is also revealed.

Fig. 4.22 shows the results for 4ICE, SBM, and observation convective-stratiform partitioned SFADs of HID. While there are significant differences between each microphysics scheme and observations in terms of the polarimetric ranges for each hydrometeor species, model results are fairly comparable with observations in terms of HID. Interestingly, although the 2D covariance plots between 4ICE and SBM were vastly different, the HID SFADs look quite similar. Indeed, it would seem that, at least, in the case of this integrated hour for MC3E, despite large differences in simulated radar observables, the HID is a robust tool that it can still produce reasonable results.

Despite the above statements, there are some differences between 4ICE and SBM, and between model output and observations that deserve some attention. In the convective MC3E HID SFAD, almost no big drops are identified in SBM (Fig. 4.22c), while there is a noticeable portion in the lowest 5 km of the 4ICE HID SFAD (Fig. 4.22a, which better matches better the appearance of big drops in the lowest 5 km of observations). Hail in both 4ICE and SBM convection is over-identified at lower- to mid-levels (from ~3-10 km altitude). However, SBM does allow hail to reach the ground, which is seen in observations, while 4ICE has no hail below 3 km altitude. In general, for both 4ICE and SBM convection, low-density graupel is under-identified at upper levels (~15-18 km in altitude) compared to observations, while high-density graupel is overidentified, at the expense of identifying less aggregates and low-density graupel. Overall, aggregates are underidentified in both 4ICE and SBM convection, and allow more ice crystals and hail instead in comparison with observations. Both 4ICE and SBM convection allow too much rain to form from 0-3 km, whereas this rain in observations is

replaced instead by hail and big drops. The largest difference, however, between 4ICE/SBM and observations is the extreme lack of wet snow from 4-5 km in comparison with observations. Wet snow in observations at that level accounts for over 20 % of identified hydrometeors at that level, while it accounts for less than 5 % for 4ICE and SBM at that level. However, the explicit scattering of melting hydrometeors was not allowed (i.e. in the T-Matrix, Mueller Matrix scattering, particles with a frozen center and an outer melting shell were not simulated). This perhaps was part of the reason that instead of more melting, high-density graupel was identified instead. Of course, all of these differences between the model and observations should be viewed knowing that the model might not be simulating the exact same moment in the storm cycle as is occurring in observations. The same fact should be kept in mind as we continue to the stratiform regions. Regardless of that fact however, and the differences seen between the model results and observations, both 4ICE and SBM did compare decently to observations for the convective areas.

Stratiform HID SFADs (Fig. 4.22 b, for 4ICE, d, for SBM, and f, for observations) highlight this stark contrast between the abundance of wet snow at 4-5 km in observations and the lack thereof in the model simulations. Almost the entirety of the 4-5 km level in the C-SAPR stratiform HID is wet snow, save for a small amount of drizzle and rain. In both 4ICE and SBM, wet snow makes up ~ 10 % or less of identified hydrometeors at that level. Instead a large amount of drizzle and some rain (more drizzle identified in SBM than 4ICE) replaces this wet snow. Though, this may again be related to the model's current incapability to explicitly simulate melting hydrometeors. At least, from 0-3 km in 4ICE and SBM, only drizzle and rain are identified (correctly identifying then hail and graupel as being convective instead). At mid-levels, model output struggles to generate the same amount of aggregates as is seen with C-SAPR observations, and in general a bit too much low-density graupel is identified in the model output (especially with 4ICE, which also slightly overidentifies high-density

graupel as well). However, ice crystals, which should comprise the majority of identified hydrometeors above 12 km in observations, is well captured by both 4ICE and SBM. Although there may be a slight lag in the storm cycle simulated in the model as compared to observations, the 4ICE and SBM simulations actually are fairly comparable to observations, save for the lack of wet snow in the stratiform region in particular. Thus, if not exactly the same hour in time is being simulated, the model is still producing a similar type of convection as is occurring in observations. It would be interesting to see if the subsequent hours were as well simulated with the POLARRIS framework.

Overall, though there were differences between 4ICE and SBM results, the two microphysics schemes produced fairly similar results. Both microphysical schemes had components that compared with observations better than the other microphysical scheme. Despite the large differences seen between these two microphysical schemes' co-variance plots, the resultant HID was quite similar. Saying that one scheme did better than the other is a bit difficult to say, considering the fact that a short integration time period was used, and considering that there is not 100 % certainty that the model hour is simulating the exact same hour of the storm cycle in observations. It is encouraging to note that 4ICE performed similarly with SBM, since there are more assumptions that go into running a 4ICE simulation than SBM (where more parameters are allowed to evolve naturally), and since the assumptions for ice crystals between 4ICE and SBM were different. Also encouraging is the fact that SBM results looked not unreasonable in comparison with observations, despite some difficulties in simulating the proper reflectivity ranges seen in each of the individual polarimetric quantities for each hydrometeor. Comparing these results with TWP-ICE simulations could provide some insight on whether or not changing meteorological regimes has a large impact on these findings.

4.4 *TWP-ICE CASE ANALYSIS: 23 JANUARY 2006*

The methodology for choosing the sets of axis ratio and canting angle assumptions was the same as was followed for MC3E. Table 4.2 shows the various input sets of assumed axis ratio and canting angle assumptions for both 4ICE and SBM TWP-ICE runs. The assumptions chosen as the “best” (i.e. those that yield results most comparable with observations) are highlighted in blue. Input assumptions are overall the same ones run for MC3E, and the only selected “best” assumptions that differed in the end from MC3E input was that of SBM graupel assumptions. For MC3E both axis ratio of 0.9 and 1.25 produced fairly similar results for graupel, but an axis ratio of 1.25 yielded slightly more comparable results with CSAPR observations. In the case of TWP-ICE SBM assumptions, an axis ratio of 0.9 yielded more comparable results with respect to CPOL observations. This was explained in more detail in Section 4.3.3, and had to do with the need to simulate the occurrence of negative Z_{dr} and K_{dp} values seen in MC3E co-variance plots, that were not also seen in TWP – ICE co-variance plots.

4.4.1. 4ICE TWP-ICE CONSIDERATION OF “BEST” ASSUMPTIONS

TWP-ICE 4ICE 2D covariance plots (plotted for the 18 Z integrated hour) were compared to the integrated 18 Z hour period of TWP-ICE (C-POL) observations. Snow aggregates, ice crystals, graupel, and rain plots are shown in Figs. 4.23 – 4.26, respectively. These plots portray the output from the assumptions for each hydrometeor, in the case of 4ICE TWP-ICE simulations, that was the most comparable with similar plots in observations (after having been run through the CSU HID).

iPOLARRIS results for 4ICE TWP-ICE simulations were quite similar to those from 4ICE MC3E simulations. Minute differences are noted between plots for each regime, for each hydrometeor. However, these two regime’s 4ICE simulations compare well enough that a discussion of each plot type for each hydrometeor, and the components that were and were not comparable with CPOL observations is not

warranted. The same shortcomings seen in MC3E 4ICE simulations are also observed in TWP-ICE 4ICE simulations. Specifically, that overall, simulated reflectivities were too low and differential reflectivity and special differential phase values were not broad enough. For a recap on the discussions therein, the reader is referred to section 4.3.1.

4.4.2. SBM TWP-ICE CONSIDERATION OF "BEST" ASSUMPTIONS

While 4ICE TWP-ICE simulation results were quite similar to those of MC3E, similarities between TWP-ICE and MC3E SBM were less apparent. Co-variance plots for snow aggregates, ice crystals, graupel, and rain are found in Figs. 4.27 – 4.30, respectively. Generally, TWP-ICE SBM simulations are "cleaner"-looking than for MC3E SBM simulations. That is, the large breadth in all of the simulated Z_{dr} and K_{dp} values seen in the co-variance plots for MC3E SBM simulations is not as evident in the TWP-ICE SBM plots, where ranges are more constricted. Additionally, negative Z_{dr} and negative K_{dp} values seen in most MC3E SBM plots, particularly in the graupel K_{dp} vs. Z_{dr} plots are not evident in TWP-ICE simulations. This, however, isn't surprising considering prolate axis ratios were not simulated in TWP – ICE graupel simulations. The need to have simulated prolate graupel in MC3E points to the differing storm microphysics between the two regimes. Other hydrometeor species simulated in MC3E SBM also showed some negative tendencies in their co-variance plots that was not also seen in TWP – ICE co-variance plots. There is also a double maximum in the Z-Z_{dr} covariance plots for TWP – ICE SBM that is not seen as much in MC3E, or at least is only hinted at with a second tail of higher densities of Z_{dr} values at higher reflectivities (see Figs. 4.27a, 4.28a, and 4.29a as compared to MC3E Figs. 4.18a, 4.19a, and 4.20a). This could potentially be a result of how SBM generates the PSDs for each of the two regimes.

Certainly, one could find many differences to pick apart in the plot shapes/radar variable values between TWP-ICE and MC3E SBM simulations. They are indeed

simulations of two completely different microphysical regimes (one being for a tropical, monsoonal, MCS environment, and the other for a mid-latitude supercell case), and so differences are not unexpected. However, there were also similarities that rendered these two regime's SBM simulations quite similar. Although the shapes of the output iPOLARRIS results for TWP-ICE and MC3E were different, the fact that neither of the regimes accurately captured Z-Z_{dr}, Z-K_{dp}, and K_{dp}-Z_{dr} ranges of values seen in C-POL and C-SAPR observations still remains. This is more surprising for MC3E, where the convection generated by the model seemed fairly comparable to the convection seen in C-SAPR. In general, for both aggregates and ice crystals, simulated reflectivities values do capture the range seen in observations, however, SBM simulations also simulate reflectivity values that are both too low and too high compared to observations. Graupel reflectivities seen in observations are also captured by SBM, although too low of reflectivity values with respect to observations are also produced by the model. Finally, again, the range of rain reflectivities in observations is reproduced in SBM simulations, though too low of reflectivity also result. There is also not nearly as evident a curve towards higher Z_{dr}/K_{dp} values with increasing Z_h values in SBM simulations as is seen in observations. Indeed, in comparison with literature values from Bringi and Chandrasekar (2001) for these particular kinds of co-variance of radar variable plots, TWP – ICE and MC3E SBM simulations both had difficulties in simulating the correct form for these curves (Figs. 4.23, 4.24, and 7.85a from Bringi and Chandrasekar 2001). In the end, all of these differences could be the result of several different factors, including: the way SBM evolves the PSD; an issue of not capturing the correct density of particles in the model; another feature inherent to SBM. It would be interesting to see the results of these simulations for a longer integrated period to see if these same differences still exist or not. These runs were not completed in this work for the sake of time, but could easily be done in future work.

4.4.3. RESULTS OF "BEST" RUNS FROM 4ICE AND SBM TWP-ICE SIMULATIONS AS COMPARED TO OBSERVATIONS

Fig. 4.31 shows SFADs of HID, partitioning data into convective and stratiform regions, for 4ICE and SBM TWP-ICE simulations of the "best" assumptions aggregated together and run with all mixing ratios allowed, as well as for CPOL observations. First, from a cursory glance, it is evident that 4ICE and SBM simulations are quite different, which not not as evident in MC3E. Additionally, C-POL convective precipitation looks interesting. In C-POL observations (Fig. 31e) there are hardly any big drops at, and just above, the surface. Furthermore, there is an interestingly large classification of aggregates identified above 6 km in the convective region, and for that matter, the stratiform region as well. Aggregates are the major identified hydrometeor at and above 7 km in both precipitation types. These results seem to point to the fact that this hour of the TWP – ICE observations may have been almost completely dominated by stratiform precipitation. This would make sense, based on the factors identified above. In order to test this hypothesis, reflectivity contoured frequency by altitude diagrams (CFADs) for the integrated hour for both convective and stratiform precipitation in CPOL observations were considered.

In Fig. 4.32, we see these diagrams for the convective (a) and the stratiform (b) portions of the integrated 18 Z storm hour. Indeed, while the occurrence of 40-50 dBZ reflectivities are observed in the convection reflectivity CFAD, the bulk of these values are below ~ 5 km, while the bulk of the values above ~ 5-6 km do not reach more than 40-45 dBZ and drop off from there. Initially, it seems strange that those reflectivity values, which are a bit small for convection with respect to other CFADs through convective regions of MCSs, are shown. However, the convective-stratiform partitioning employed in this work is based on the Powell et al. (2016) methodology, where convection is identified at an altitude of 2 km. Then, the classification is extended throughout the column. PPIs and RHIs of radar reflectivity throughout the hour (not

shown) illustrated the progression of a small convective core on the western edge of the domain, that exited as the storm propagated westward before the hour had past. Since the convection was identified at 2 km, and actual convective precipitation was limited to low levels, this explains the appearance of low reflectivities at altitude above ~ 5-6 km in the convective reflectivity CFAD. The abundance of snow aggregates at upper levels in the TWP – ICE observations convective SFAD seem logical then, due to convective reflectivities that match more so that of snow than that of graupel, hail, big drops, and other more convective-type hydrometeor species (S00; DR09; Thompson et al. 2014). This could point to a need to slightly modify the convective-stratiform partitioning reflectivity threshold set in iPOLARRIS for convection that is more tropical, MCS like in nature. This also could be a feature of just this specific 18 Z hour in TWP – ICE observations. In future work, the integrated 23 January 2006 MCS case should be tested to see if this finding holds true for the overall storm.

In the SBM convection regions, the HID SFAD (Fig 4.31c) shows a good amount of low-density graupel classified through mid- to upper-levels of the precipitation that is not seen in observations convective precipitation (Fig. 4.31e). Additionally, there is also an absence of big drops in SBM convection, where in observations, despite the small amount of convection that occurred for the 18 Z hour, there were still some big drops at lower levels. Again, this difference could be the fact that the model is not simulated at exactly the same time in the storm cycle as in observations. This could also be due to how the PSDs evolved in SBM. Hail is observed in SBM convection at midlevels while none is seen in observations, which points to the likelihood of stronger convection simulated in the SBM results than what is actually occurring in observations at that time.

In the case of TWP-ICE 4ICE simulations, the convective region (Fig. 4.31a) does see plenty of big drops from 5 km down in altitude, reaching the ground, as well as a small amount of hail at the midlevels (though less than was produced by SBM). The 4ICE convective HID SFAD does not simulate even half the amount of low-density

graupel seen throughout the storm in the SBM convective HID SFAD (Fig. 4.31c). Some low-density graupel is present in the 4ICE convection, but there is still a good amount of of aggregates at mid-levels and then ice crystals at upper levels.

Overall, the simulations look a bit more convective in nature than what is seen in the observations. RHIs (not shown) through convection in 4ICE showed stronger convection than was seen in observations (reaching up to 60-65 dBZ) that was confined to below 10 km AGL, but was present throughout the entire 22 Z hour, while SBM simulations showed slightly weaker maximum reflectivities, but allowed the 40 dBZ contour to reach up to 15 km in height for most of the simulated 22 Z hour. This resulted in the differences seen between 4ICE and SBM HID, and also explains why more convective-type species were seen in the model convective SFADs, while the observed convective SFADs showed more muted convection and a dominance of stratiform-type precipitation overall.

The same type of convection was obviously not simulated between observations and the model. Thus, the main interest in this discussion is the differences observed between 4ICE and SBM simulations, which differed much more than was the case for MC3E convective regions. The stratiform precipitation regions did not differ as greatly between 4ICE (Fig. 4.31b) and SBM (Fig. 4.31d) for TWP – ICE. The biggest difference was a larger classification of low-density graupel in SBM vs. 4ICE. This is not surprising considering SBM (as mentioned earlier) allowed higher reflectivities to be present throughout almost the entire vertical extent of simulated precipitation.

One goal of this work was to examine, at least for this specific set of simulations, whether the HID results were driven more by regime (tropical MCS vs. mid-latitude supercell), or if HID results were more sensitive to the microphysical scheme employed. The answer to this question is a complicated one, as both 4ICE and SBM simulations revealed differences in how the convective and stratiform HID SFADs were characterized for both MC3E and TWP-ICE, however differences were much more

noticeable in TWP-ICE. In the case of MC3E simulations, despite the vastly different 2D co-variance plots between SBM and 4ICE simulations, the HID SFADs for both convective and stratiform regions were fairly similar, and both were overall comparable to observations. In TWP-ICE, it would appear that the differences between 4ICE and SBM did have a large impact on HID classification. However, is that to say that differing regimes is the largest influence on HID classification? It seems unreasonable to say that that means automatically that the regime has a bigger hand in affecting HID classification, simply because the differences in TWP-ICE were starker than for MC3E, especially considering the fact that the simulated convection seems to not be the same as that occurring in observations for TWP – ICE for the 18 Z integrated hour. Additionally, to truly answer that question, longer simulated time periods need to be considered. For the moment, the answer to the question of which factor has a larger impact on HID classification is that both play a role in determining HID classification, and choosing one over the other is not possible in this case.

A concerning problem for the majority of this work was the need to appropriately simulate a range of observed axis ratios and canting angles, as in nature each hydrometeor type does not embody one shape and each type does not cant in the same fashion as they fall. However, without in situ data to drive axis ratio – size dependent relationships, or in situ data of canting angles, where the range of canting angles is driven by turbulence, this study was limited to one assumed axis ratio, one assumed θ, and one assumed σ for graupel and ice crystals. Thus the true breadth of polarimetric variables was never achieved for the case of 4ICE simulations. The use of the Citation II values improved the resulting output, especially in the case of 4ICE co-variance plots for both MC3E and TWP-ICE. Even though the data was taken in the aggregate/ice crystal region of an Oklahoma supercell during MC3E, the relationship actually greatly improved simulations for TWP – ICE as well. It would be interesting to see the resulting HID SFADs if such a size-based relationship were also found and employed for graupel

and ice crystals. Thus, this work points towards the need for more in situ data taken in these regions, in order to improve not only POLARRIS results, but the results from any polarimetric radar simulator.

While the canting angle and axis ratio assumptions certainly played a role in the resulting simulated polarimetric radar data, the differences between the handling of microphysics between the single-moment 4ICE scheme and the SBM scheme also hold a large role in determining the look of the synthetic polarimetric radar data. For example, consider Figure 11 from M17 (Figure 4.63 here) showing various PSD assumptions for the 23 May 2011 case from MC3E. As is explained in Matsui et al. (2017), the black line shows the PSD taken on 23 May 2011 measured with the Citation HVPS-3 (at a height of ~8 km). Solid and dotted blue lines show what the PSD would look like with assumptions for aggregates derived from DR09 (for 0.5 mm hr^{-1} and 10 mm hr^{-1} equivalent snowfall rate, respectively). Comparisons between the flight path, images of particles within the flight path (taken with the high-resolution cloud particle imager), and HID performed on CSAPR data led to the conclusion that the region was stratiform, and aggregates dominated the path (Matsui et al. 2017). In the simulations, ice crystal maximum diameters are set to be generally < 1000 μm (1 mm), so that simulated PSDs included, for the most part, only snow aggregates. Model output is given from 23 UTC 23 May 2011 to 0130 UTC 24 May 2011, in 10 minute intervals. The green and red lines show the PSDs from 4ICE and SBM, for simulations completed close to how the aircraft would have "seen" these PSDs. This is explained further in-depth in Iguchi et al. 2012b, however, basically the model microphysics PSD is re-sampled into bulk PSD bin sizes that are arranged as an aircraft would have measured them. These are then integrated over the domain in order to obtain a mean PSD. This is done from 7-9 km (inclusive) in height, since those were the heights in which the Citation II aircraft operated (M17).

The resultant curves show some enlightening results. The 4ICE PSD curve follows closely that of the DR09 assumptions for an equivalent snowfall rate of 0.5 mm hr^{-1}. The SBM PSD curve follows the same pattern until about 3-4 mm diameter, and then the slope lessens (compared to the 4ICE curve). The SBM PSD then displays a bi-modal distribution by showcasing a secondary mode around 8 mm. At that point, the steepness of the curve is quite similar to what was seen for 4ICE. Certainly, this shows that while similar for smaller size aggregate particles, the 4ICE and SBM PSD distributions are not similar for medium-to-larger sized snow aggregates. Indeed, the ability to have a second mode in the SBM PSD around 8 mm explains some of the ability of SBM to have overall larger Z_h values for snow aggregates than what was seen in 4ICE. Similarly, the bi-modal distribution, with a secondary mode around 8 mm in diameter, in the SBM PSD partially explains the ability of SBM to exhibit wider breath in Z_{dr} and K_{dp} values. Figure 4.63 shows only results for MC3E data, as this type of data was not available for the same case for the 23 January 2006 TWP-ICE case. It would be interesting to see if there had been similar tests performed for TWP-ICE, if the findings would be similar to those found for the 23 May 2011 case in MC3E. However, this figure helps to summarize, to an extent, the impact of the choice of PSD itself. The axis ratio and canting angle assumptions, important as they may be, are only a part of the potential explanations for any differences seen between TWP-ICE and MC3E, or between models and observations.

4.5 *SENSITIVITY TESTS ON THE IMPACT OF CHANGING AXIS RATIO AND CANTING ANGLE ASSUMPTIONS ON RADAR OBSERVABLES*

In addition to considering the impact of different regimes and different microphysics schemes on resulting HID classifications, also taken into account was the impact of changing axis ratio and canting angle input (and in the case of rain, which axis ratio – size dependent rain relation was used) on the most-frequently occurring radar observable as a function of height. That is, this section tested the uncertainty/sensitivity

in the resulting polarimetric radar data to changes in the assumptions input to the POLARRIS framework. The methodology for this is presented in Sec. 3.8. Figs. 4.33-4.35 show these results for snow aggregates, Figs. 4.36-4.38 show these results for ice crystals, Figs. 4.39-4.41 show these results for graupel, and Figs. 4.42-4.44 show these results for rain.

In general, changing axis ratio and canting angle assumptions does not have a large impact on the most-frequently identified reflectivity value, save for a couple sets of assumptions in MC3E and TWP-ICE SBM simulations and TWP-ICE 4ICE simulations for ice crystals (Fig. 4.36). The same can be said of the most-frequently occurring specific differential phase values, save for ice crystals which also saw a small bit of change depending on the axis ratio and canting angle assumptions (Fig. 4.37). This lack of change in Z_h and K_{dp} with respect to differing axis ratio and canting angle inputs (for aggregates, graupel, and rain) is robust for 4ICE and SBM for both TWP-ICE and MC3E (Figs. 4.33, 4.34, 4.39, 4.40, 4.42, and 4.43). Differential reflectivity values, however, are more sensitive to axis ratio and canting angle assumptions (Figs. 4.35, 4.38, 4.41, and 4.44 for aggregates, ice crystals, graupel, and rain, respectively). Generally, the axis ratio chosen was more important than the standard deviation of canting angle chosen (at least, for these small 10°-15° changes in value, where a slightly larger value just forced the radar observable value closer to zero). Overall (outside of graupel), 4ICE simulations were more sensitive to the change in axis ratio and canting angle assumptions. Changes in these assumptions produced a large spread of Z_{dr} values. Some variability in SBM simulations was seen for changing axis ratio and canting angle input, but not to the same extent as was seen for 4ICE. The result of SBM simulations being less sensitive than 4ICE to changes in the assumed axis ratio and canting angle assumptions was also observed in the co-variance plots. If not one, but multiple values of axis ratio, or standard deviation of canting angle, occur in nature, then this analysis highlights the importance of finding the appropriate range of these two parameters.

Narrowing simulations down to one axis ratio and one standard deviation of canting angle greatly limits the extent to which the appropriate range of Z_{dr} can be simulated.

4.6 *MODIFICATIONS TO CSU HID*

The uncertainty and sensitivity of the HID retrieval itself to changes in the shape of the MBFs were the final tests conducted. The methodology for this is described in section 3.9. The resulting HID SFADs for convective and stratiform rain for TWP-ICE 4ICE and SBM simulations, and TWP-ICE C-POL observations are shown in Fig 4.45 (the original HID SFADs were shown in Fig. 4.31) and the HID SFADs for convective and stratiform rain for MC3E 4ICE and SBM simulations, and MC3E C-SAPR observations is shown in Fig. 4.46 (the original HID SFADs for MC3E were shown in Fig. 4.22). However, in order to better quantify differences in the simulations and observations due to the modified MBFs, HID pie chart plots were created (for TWP-ICE Figs. 4.47, 4.48 and 4.51, and for MC3E Figs. 4.49, 4.50 and 4.52). These plots help to, both visually and numerically, understand the sensitivity of the HID to the change in MBFs, with an emphasis placed on the variables simulated herein. In the end, no changes were made to the correlation coefficient MBFs, as the values of this radar observable for CSU HID – identified hydrometeors for CSAPR and CPOL were too noisy to be used for these sensitivity tests. The original and modified MBFs, where frequency of occurrence of radar observables, identified for each hydrometeor via the CSU or POLARRIS HID, are overlaid to illustrate the reasoning for the modifications made, are shown in Figs 4.53-4.62.

From a cursory glance at the HID SFADs for both MC3E (Fig. 4.46) and TWP-ICE (Fig. 4.45) model simulations (comparing between these SFADs based on the newly-modified MBFs and the HID SFADs made with the original MBFs) one detail is clear: the presence of aggregates for both regimes (tropical vs mid-latitude), and for both microphysical schemes, is small in comparison to graupel, hail, and ice crystal

categories in the convective region. Indeed, with the modified MBFSs, TWP – ICE now sees the presence of hail in convective regions reaching the ground (Fig 4.45 a, c, and e). This seems a bit unrealistic based on studies done in the for other MCSs in the Darwin area during their monsoon season (Dolan et al. 2013). Additionally, big drops are now identified in convective SBM simulations for both TWP-ICE and MC3E for 4ICE, SBM, and observations whereas with the original MBFs whereas before both MC3E and TWP – ICE SBM convective precipitation saw no, or next to no, big drops.

To get a better idea of the sensitivity of the bulk ice categories which were simulated (aggregates, graupel, ice crystals, along with rain) to the modified MBFs affected, HID pie chart plots are considered (see Sec. 3.9 where this as introduced). In the TWP-ICE 4ICE convective regions (Fig. 4.47), especially from 6-8 km, the increase in identified graupel (both high- and low-density graupel) severely reduces the amount of identified aggregates. From 8-12 km the main driver in decreasing aggregate classification is more so related to an increase in ice crystal classification. In the stratiform HID, at lower levels (4-6 km) an increase in identified rain and graupel leads to a decrease in aggregates from almost 50% to only 20%. Above this, the increase mainly in identified ice crystals results in a lower number of identified aggregates. In TWP-ICE SBM stratiform regions (Fig. 4.48), however, the decrease in identified aggregates has more to do with the increase in graupel in general, in tandem with the increase in ice crystals. In convective regions, the TWP-ICE SBM simulations identify both less aggregates and ice crystals due to the increase in identified graupel from 2 km and up in altitude.

In MC3E 4ICE simulations (Fig. 4.49), the reasoning behind decreases in aggregates for convective regions is very similar to that of TWP-ICE, although graupel increasing at almost every altitude is a bigger driver than any increases in identified ice crystals. In fact, very few aggregates are identified in MC3E convective regions (for either 4ICE or SBM). This is not necessarily a negative aspect of the modified HID, as

convective regions in mid-latitude supercells do not necessarily see an abundance of aggregate classification (e.g. Jensen et al. 2016). Indeed, similar to 4ICE simulations, the increase in graupel identification (and some increases in identified ice crystals) led to very little identified aggregates in MC3E SBM simulations (Fig. 4.50).

What is perhaps the most shocking example of the sensitivity of the HID to MBF modification, however, is the almost complete disappearance of identified aggregates in stratiform rain regions for both SBM and 4ICE MC3E simulations. For both microphysical schemes, from ~4-10 km in height, aggregates dominated the HID classification with the original MBFs, and with the modified MBFs a mere 7 % (15 %) of hydrometeors from 4-6 km for 4ICE (SBM) are classified as aggregates. The biggest driver in the lower amount of identified aggregates in both scenarios for stratiform precipitation was the increase in identified ice crystals (as was the case for TWP-ICE 4ICE simulations, and, to an extent, TWP-ICE SBM simulations). This would seem to go against logic, as these types of systems usually do see aggregates in the stratiform region (e.g. Matthews 2014). However, it is important to note that the aggregates category includes random “ice junk” (i.e. ice that is not pristine ice, yet also not rimed enough to be classified as graupel) in addition to snow aggregates that grow via the aggregation process. The changes made for aggregates and other species (discussed below) that resulted in the changes seen in these HID pie charts illustrate the sensitivity of the HID retrievals to these MBF changes. These changes obviously produce a large amount of uncertainty of potential ranges for identified hydrometeors (especially for aggregates), and thus in future work on actual improvement of the HID MBFs, extreme care should be taken in considering the MBFs for these species.

As was discussed above, the classification of aggregates in model simulations was heavily influenced by the change in MBFs. In TWP-ICE observations (Fig. 4.51), however, there was still a large abundance of aggregates above 4 km identified throughout the integrated storm after MBF modification. There were some decreases for

convective regions in aggregate classification due to increases in the classification of graupel (which decreased classification of aggregates – and rain – classification up through ~ 12 km) and ice crystals (which depressed aggregate classification from ~ 8 – 16 km). In stratiform regions, some increases in ice crystals resulted in reduced amounts of classified aggregates. For MC3E observations (Fig. 4.52), in the convective regions increases in graupel throughout the simulated storm resulted in decreases in rain, aggregate, and ice crystal classification. Increases in ice crystal classification also resulted in some decreases in aggregate classification for stratiform precipitation. However, the overall abundance of aggregates was not nearly as reduced as in 4ICE or SBM simulations for TWP – ICE, and especially for MC3E. Hence, it would seem that the model HID simulations, for these specific simulation time periods at least, were more sensitive to the change in MBFs than CSAPR or CPOL observations.

Why did these modifications lead to such a decrease in identified aggregates, generally in favor of graupel for convective regions, and ice crystals (and some graupel) in stratiform regions? Likely the answer to that question is related to the various modifications made to the MBFs, particularly how the shape and breadth of reflectivity MBF contours changed (since reflectivity is the most heavily-weighted variable in the CSU HID retrieval employed by iPOLARRIS). Indeed, when looking at the modified MBFs (Figs. 4.53 - 4.62), the snow aggregate reflectivity MBF (Fig. 4.53) was shifted to include reflectivities below -5 dBZ, since C-POL aggregates reach below that value. The fact that CPOL aggregate reflectivity does extend beyond the range set by the MBFs seems odd since HID results are heavily driven by reflectivity. These reflectivities should theoretically not have occurred. Thus, perhaps there are some small ice “junk” particles that did not fit the specification for pristine ice crystals that were classified as aggregates. This would then produce low reflectivities for aggregates, which resulted in the change of the aggregate reflectivity MBF to include those lower values. Along with a shift in the aggregate reflectivity MBF, the differential reflectivity MBF was modified to

include lower values of Z_{dr} produced by C-SAPR. The actual values that CSAPR aggregate Z_{dr} data reached seemed a bit low compared to literature (e.g. DR09; Dolan et al. 2013; Thompson et al. 2014). The lower Z_{dr} values seen in the CSAPR observations may be the result of differential attenuation that was not able to be corrected for in its entirety. However, since the aim of the MBF modifications was to test the sensitivity in the HID retrievals to changes in the MBFs, the lower aggregate Z_{dr} values (as was the case for Z_h values) were allowed in order to observe what would occur if that were allowed.

Some have made the argument (i.e. Wen et al. 2015) that this differential attenuation is a characteristic of the radar signal quality, and as such it should be included in the hydrometeor classification process. Wen et al. (2015) argue that this attenuation, or noise, would likely have an impact on the polarimetric variable PDFs derived from the radar that describe individual hydrometeor types. Hence, attenuation and noise, by that logic, should actually be included in the hydrometeor identification membership beta functions. This is an interesting counterpoint to the typical efforts to eliminate, as much as possible, noise, differential attenuation, etc. seen in the radar data QC process.

Clearly, more than just the snow aggregate MBFs were modified. Changes in other hydrometeors' MBFs likely also affected the outcome of aggregate classification. In future work, changes to each of the polarimetric radar MBFs for each hydrometeor should be tested to see the extent to which HID retrievals are sensitive to each individual MBF. CSAPR and CPOL reflectivity values for ice crystals (see Fig 4.54) were larger than the original MBFs allowed, and so the higher-end threshold of the ice crystal reflectivities was changed from ~20 dBZ to ~30 dBZ. Differential reflectivity signatures from observations required a large shift in the MBFs from ranging from 0-6 dB originally, to now -2 to 3 dB). Additionally, the low-density graupel MBF (Fig 4.55) was allowed to shift to slightly lower reflectivities, allowing now reflectivities to ~20 dBZ instead of ~25

dBZ. The high-density graupel MBF (Fig 4.56) did not require any modification to the reflectivity MBF, however, as was the case with low-density graupel, the differential reflectivity contours were modified to include much lower Z_{dr} values. Although hail (Fig. 4.61) is not one of the variables shown in the pie chart plots, in the HID SFADs there was a noticeable increase in hail amounts in both TWPICE and MC3E convective regions. Perhaps in TWP – ICE this was more likely an increase in high-density graupel than hail?

Large amounts of hail in MCSs observed in the Darwin region were not generally observed, but rather high-density graupel was seen with a small amount of hail at upper levels that turned into big drops at lower levels (Dolan et al. 2013). Though the reflectivity MBF was not modified much for hail, it was shifted down to allow reflectivities down to ~40 dBZ instead of previously-defined 45 dBZ. The Z_{dr} and K_{dp} contours were more severely modified, with Z_{dr} ranges changing from -1 to 1 dB to ~ -2.5 to 3 dB, based on observations (though results past 3 dB were not included simply because of the large probability that those signatures were probably noise that was not able to be filtered out and not actual hail signatures). Wen et al. (2015), however, might have argued against that decision. This, along with other hydrometeors' reflectivity MBF modifications (as well as Z_{dr} and K_{dp} MBF modification, though these variables are less-heavily weighted than Z_h), was enough to allow more hail classifications, shunting the classification of aggregates at that time.

Note that while reflectivity certainly has a large hand in the resultant HID, Z_{dr} and K_{dp} also affect HID retrievals (even though they are not weighted as heavily as reflectivity or temperature). Indeed, some large changes to the MBF structure for Z_{dr} occurred, as is stated above for the hydrometeors pertinent to this study. K_{dp} was also affected, though for most of the HID's simulated species, the MBFs needed only slight modification to fit the observations. The species that differed included high-density graupel (Fig. 4.56), hail (Fig. 4.61), and rain (Fig. 4.57), which all required a stricter

range in K_{dp} values than what was seen for the original MBFs. Quite often, shifts in the MBF location for Z_{dr} had to do with low biases in radar observables seen in C-SAPR observations. This is likely a result of the differential attenuation that was not able to be completely removed in the QC process. Again, some might argue that that is appropriate to leave those noise signals in the data for MBF modification (Wen et al. 2015).

These modified MBFs are not meant to replace the original MBF functions, as many more datasets would be required to "train" the MBFs. Additionally, more in situ data validating the defined MBF ranges for each hydrometeors are required to give enough confidence to define a new, novel MBF set based on values seen in nature. Currently, the CSU HID results for C-SAPR and C-POL are used to modify the MBFs. To use these results to create a new set of MBFs (in this work, for C-Band radar) would be a bit circular, and thus no attempt was made to set out to make a completely new MBF set. Of course, without in situ data to validate HID results, that circularity is a bit difficult to avoid. Rather, the modification of the MBFs and the comparison of results from POLARRIS-f and CSAPR and CPOL observations was done to test the sensitivity of the HID retrievals to changes in the MBF sets as a means of characterizing the uncertainty associated with the HID algorithm. Furthermore, the differences seen in the HID retrievals resulting from modifications to the MBFs highlight the fact that the HID from observations should not be considered 'truth'. Although the HID retrievals from observations were not as susceptible to changes based on MBF modification as for model output, they were affected. Thus, the challenge of closing the gap between model simulations and observations is attacked from two sides: 1) defining inputs to a radar simulator such that HID results are comparable between model simulations and observations and understanding the uncertainties therewith, and 2) defining the uncertainty associated with the HID algorithms themselves and the extent to which that uncertainty affects HID retrievals and comparability between models and observations.

Table 4.1: Inputs to POLARRIS-f for MC3E, 4ICE and SBM, aggregates, ice crystals, graupel and rain. θ indicates the mean canting angle at which a hydrometeor falls, and σ indicates the amount to which a particle flutters as it falls (i.e. the standard deviation of the mean canting angle). Items highlighted in blue indicate the input axis ratio and canting angle assumptions chosen as the most comparable with respect to observations.

	4ICE			SBM		
	Axis ratios	***θ***	***σ***	**Axis ratios**	***θ***	***σ***
Aggregates	0.2,0.3,0.4,0.5,0.6,0.7,0.8,0.9 Citation relationship: axis ratio=0.003*d^2+0.05*d+0.70 GE15: 0.65	0° 27° 14°	15°,30° 10° 14°	0.2,0.3,0.4,0.5,0.6,0.7,0.8,0.9 Citation relationship: axis ratio=0.003*d^2+0.05*d+0.70 GE15: 0.65	0° 27° 14°	15°,30° 10° 14°
Ice Crystals	0.125,0.25,0.35,0.45,0.55,0.65,0.75	0°	15°,30°	0.09,0.125,0.35,0.45	0°	15°,30°
Graupel	0.5,0.9,1.25 GE15: 0.75	0° 14°	10°,20° 16°	0.5,0.9,1.25 GE15: 0.75	0° 14°	10°,20° 16°
Rain	Brandes et al. (2002), Chuang and Beard (1990), Jameson (1983), Green (1975), Pruppacher and Pitter (1971), Jones (1959i), Jones (1959ii), Goddard and Cherry (1984)	0°	10°	Brandes et al. (2002), Chuang and Beard (1990), Jameson (1983), Green (1975), Pruppacher and Pitter (1971), Jones (1959i), Jones (1959ii), Goddard and Cherry (1984)	0°	10°

Table 4.2: Inputs to POLARRIS-f for TWP-ICE, 4ICE and SBM, aggregates, ice crystals, graupel and rain. θ indicates the mean canting angle at which a hydrometeor falls, and σ indicates the amount to which a particle flutters as it falls (i.e. the standard deviation of the mean canting angle). Items highlighted in blue indicate the input axis ratio and canting angle assumptions chosen as the most comparable with respect to observations.

	4ICE			SBM		
	Axis ratios	***θ***	**σ**	**Axis ratios**	***θ***	**σ**
Aggregates	0.2,0.3,0.4,0.5,0.6,0.7,0.8,0.9	0°	15°,30°	0.2,0.3,0.4,0.5,0.6,0.7,0.8,0.9	0°	15°,30°
	Citation relationship: axis ratio=0.003*d^2+0.05*d+0.70	27°	10°	Citation relationship: axis ratio=0.003*d^2+0.05*d+0.70	27°	10°
	GE15: 0.65	14°	14°	GE15: 0.65	14°	14°
Ice Crystals	0.125,0.25,0.35,0.45,0.55,0.65,0.75	0°	15°,30°	0.09,0.125,0.35,0.45	0°	15°,30°
Graupel	0.5,0.9,1.25	0°	10°,20°	0.5,0.9,1.25	0°	10°,20°
	GE15: 0.75	14°	16°	GE15: 0.75	14°	16°
Rain	Brandes et al. (2002), Chuang and Beard (1990), Jameson (1983), Green (1975), Pruppacher and Pitter (1971), Jones (1959i), Jones (1959ii), Goddard and Cherry (1984)	0°	10°	Brandes et al. (2002), Chuang and Beard (1990), Jameson (1983), Green (1975), Pruppacher and Pitter (1971), Jones (1959i), Jones (1959ii), Goddard and Cherry (1984)	0°	10°

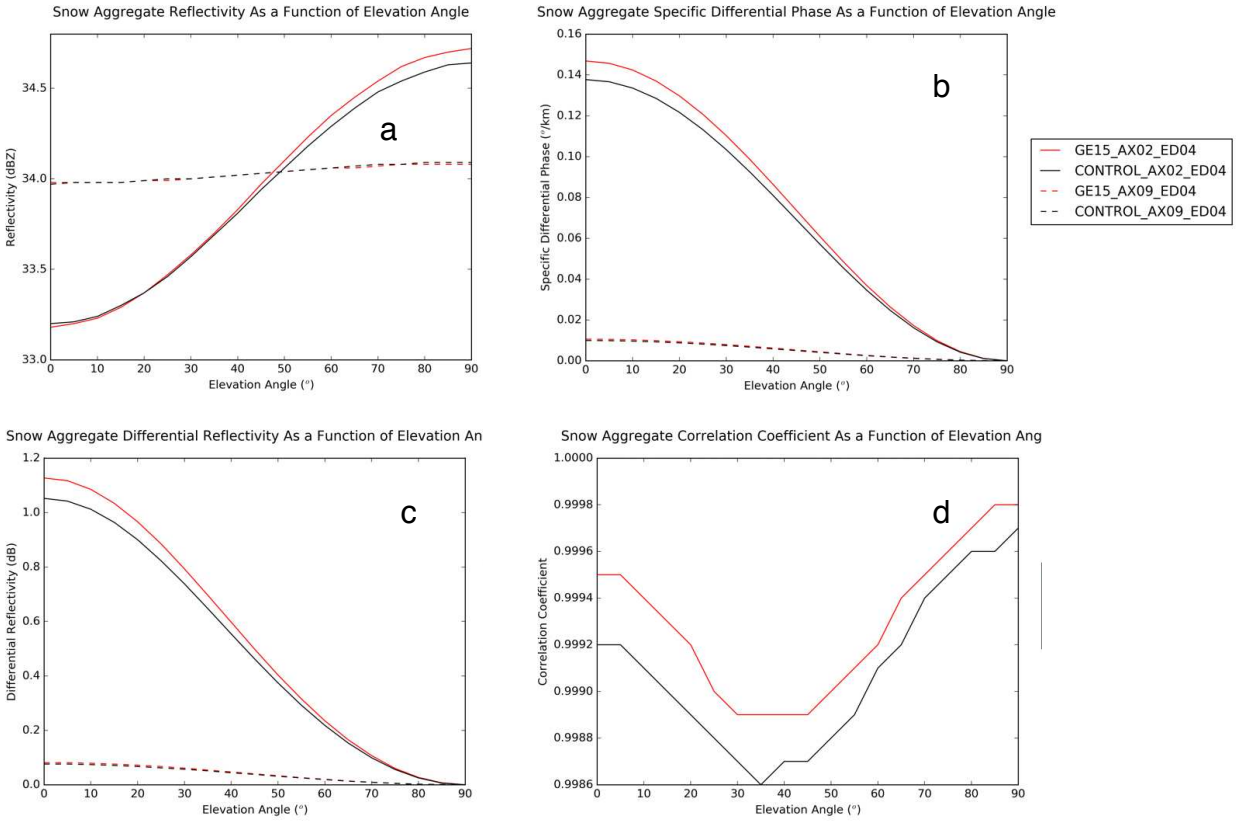

Figure 4.1: Results for aggregates using the original T-Matrix, Mueller Matrix framework, where reflectivity is shown in (a), specific differential reflectivity in (b), differential reflectivity in (c), and correlation coefficient in (d). Red lines denote canting angle and standard deviation of canting angle assumptions from GE15, while black lines denote those of DR09. Dotted lines denote axis ratios of 0.9 (nearly spherical), and solid lines denote axis ratios of 0.2 (very oblate particles).

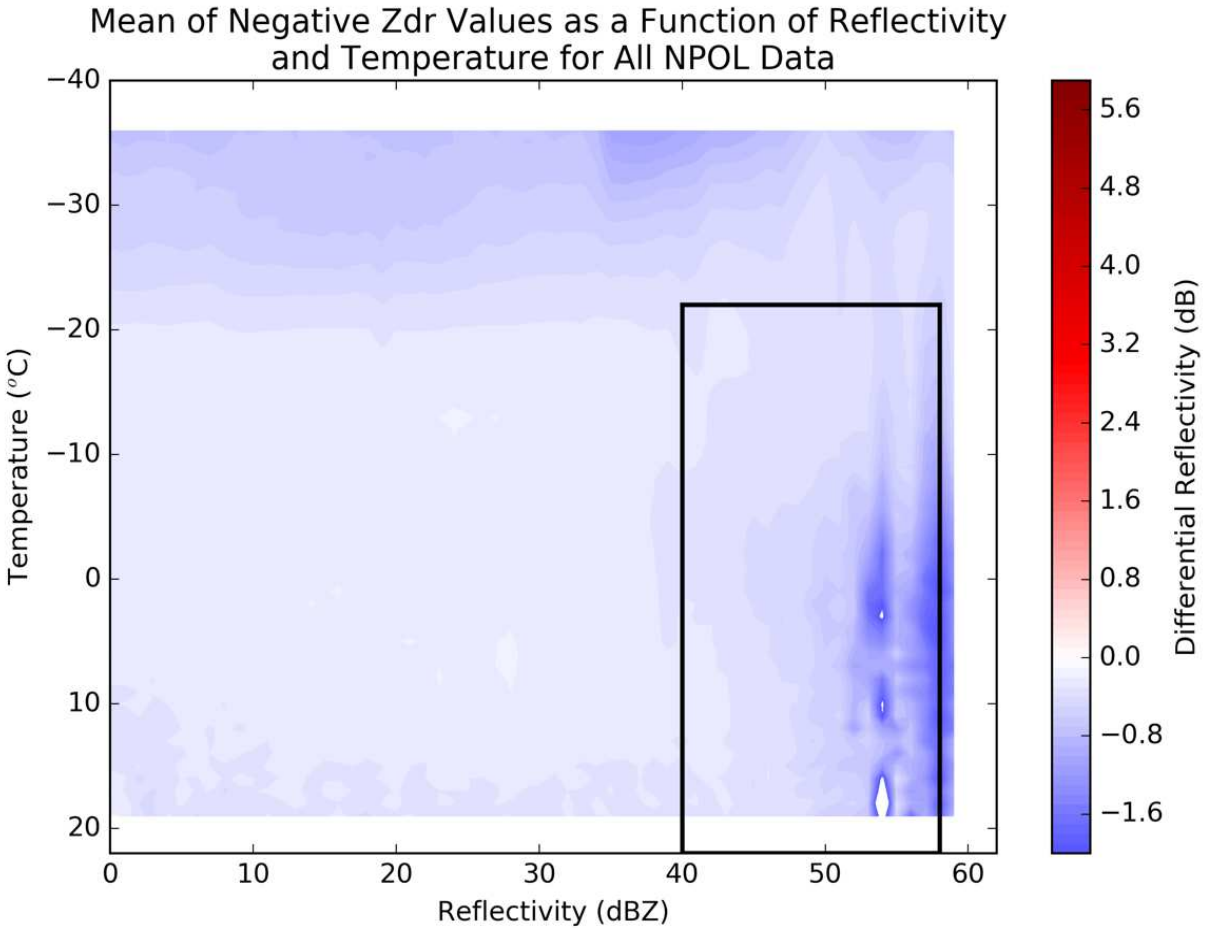

Figure 4.2: Heat map of mean negative Z_{dr} values as a function of reflectivity and temperature for NPOL data from April and May 2011. The black box indicates the temperatures and reflectivities at which the CSU HID MBF for low-density graupel resides.

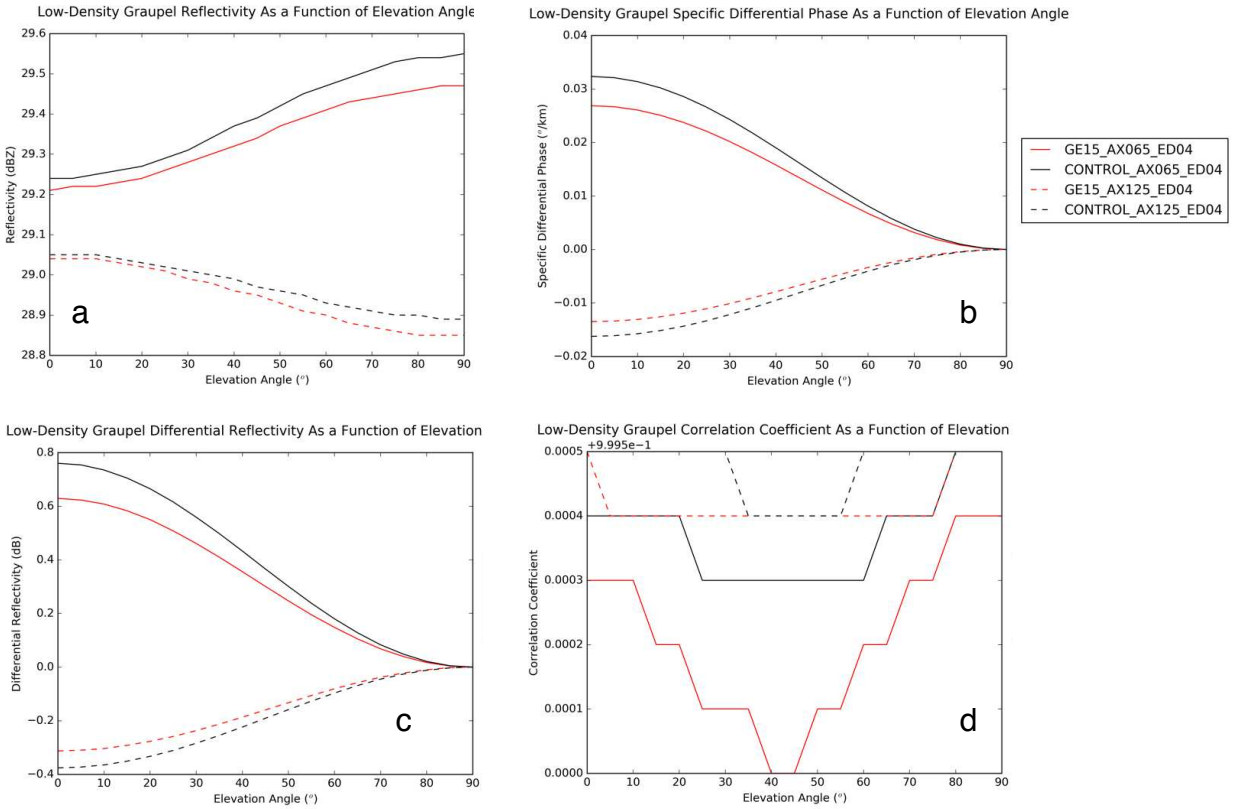

Figure 4.3: Results for low-density graupel using the original T-Matrix, Mueller Matrix framework, where reflectivity is shown in (a), specific differential reflectivity in (b), differential reflectivity in (c), and correlation coefficient in (d). Red lines denote canting angle and standard deviation of canting angle assumptions from GE15, while black lines denote those of DR09. Dotted lines denote axis ratios of 1.25 (prolate), and solid lines denote axis ratios of 0.65 (somewhat oblate particles).

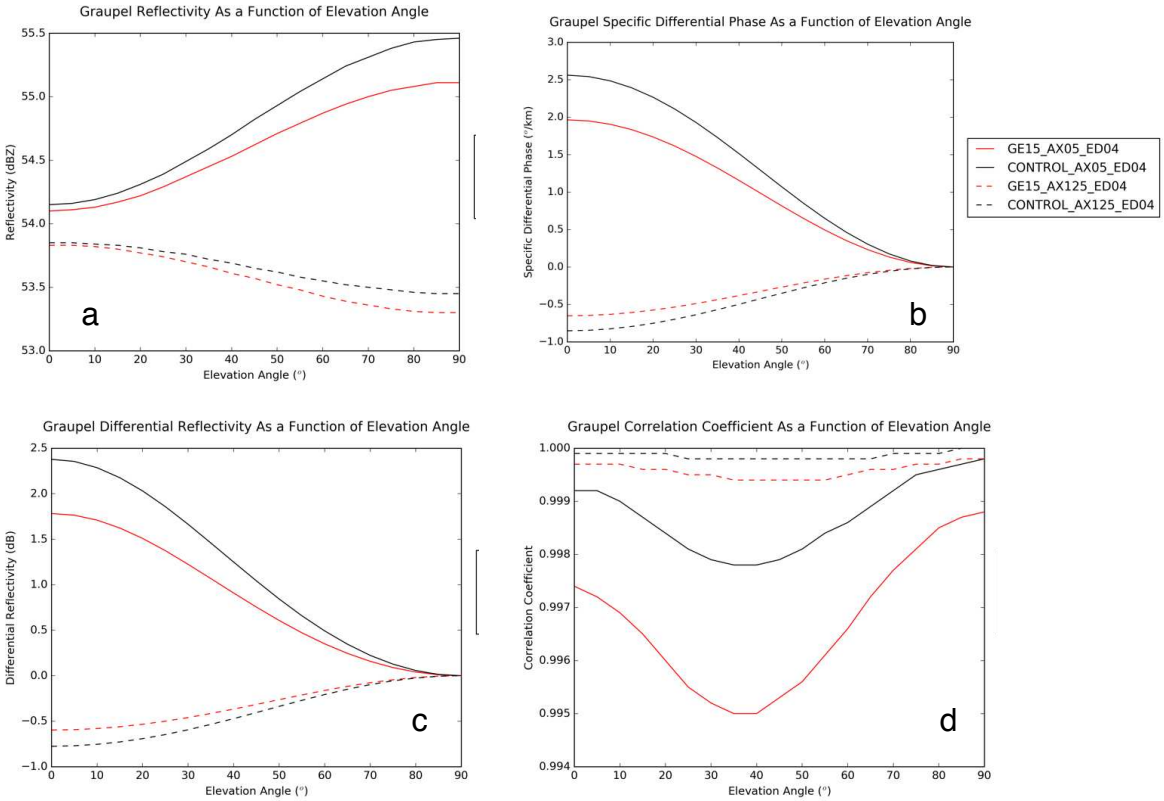

Figure 4.4: Results for high-density graupel (graupel) using the original T-Matrix, Mueller Matrix framework, where reflectivity is shown in (a), specific differential reflectivity in (b), differential reflectivity in (c), and correlation coefficient in (d). Red lines denote canting angle and standard deviation of canting angle assumptions from GE15, while black lines denote those of DR09. Dotted lines denote axis ratios of 1.25 (prolate), and solid lines denote axis ratios of 0.5 (fairly oblate particles).

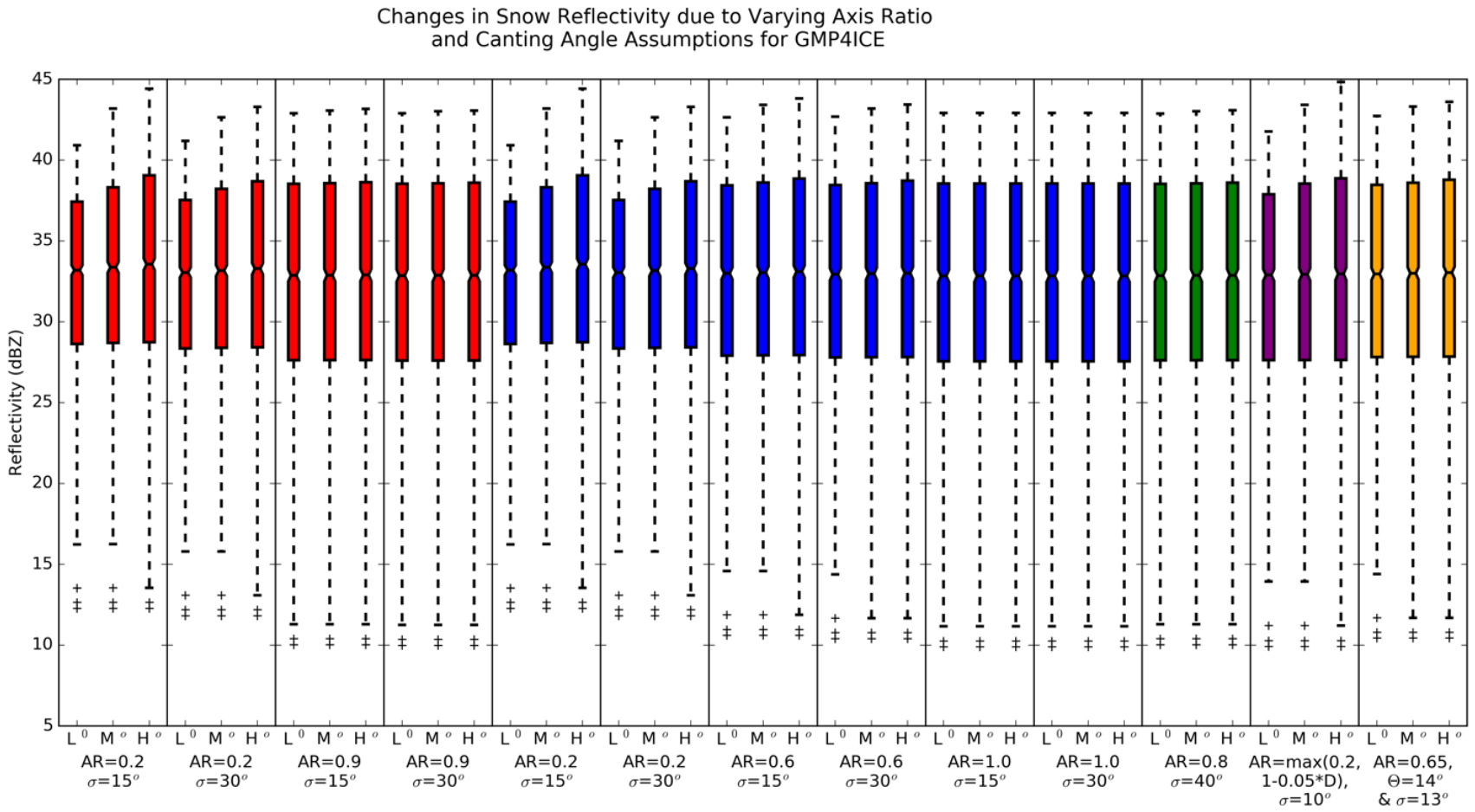

Figure 4.5: Box and whisker plot LUT visualizations for 4ICE Aggregate reflectivity. The first box and whisker plot denotes the “low” radar elevation angle (0°-30°), the middle box denotes the “medium” radar elevation angle (30°-60°), and the third box denotes the “high” radar elevation angle (60°-90°). Red colors are associated with DR09 assumptions blue colors with S00 assumptions, green with R11 assumptions, purple with “control” assumptions, and yellow with GE15 assumptions.

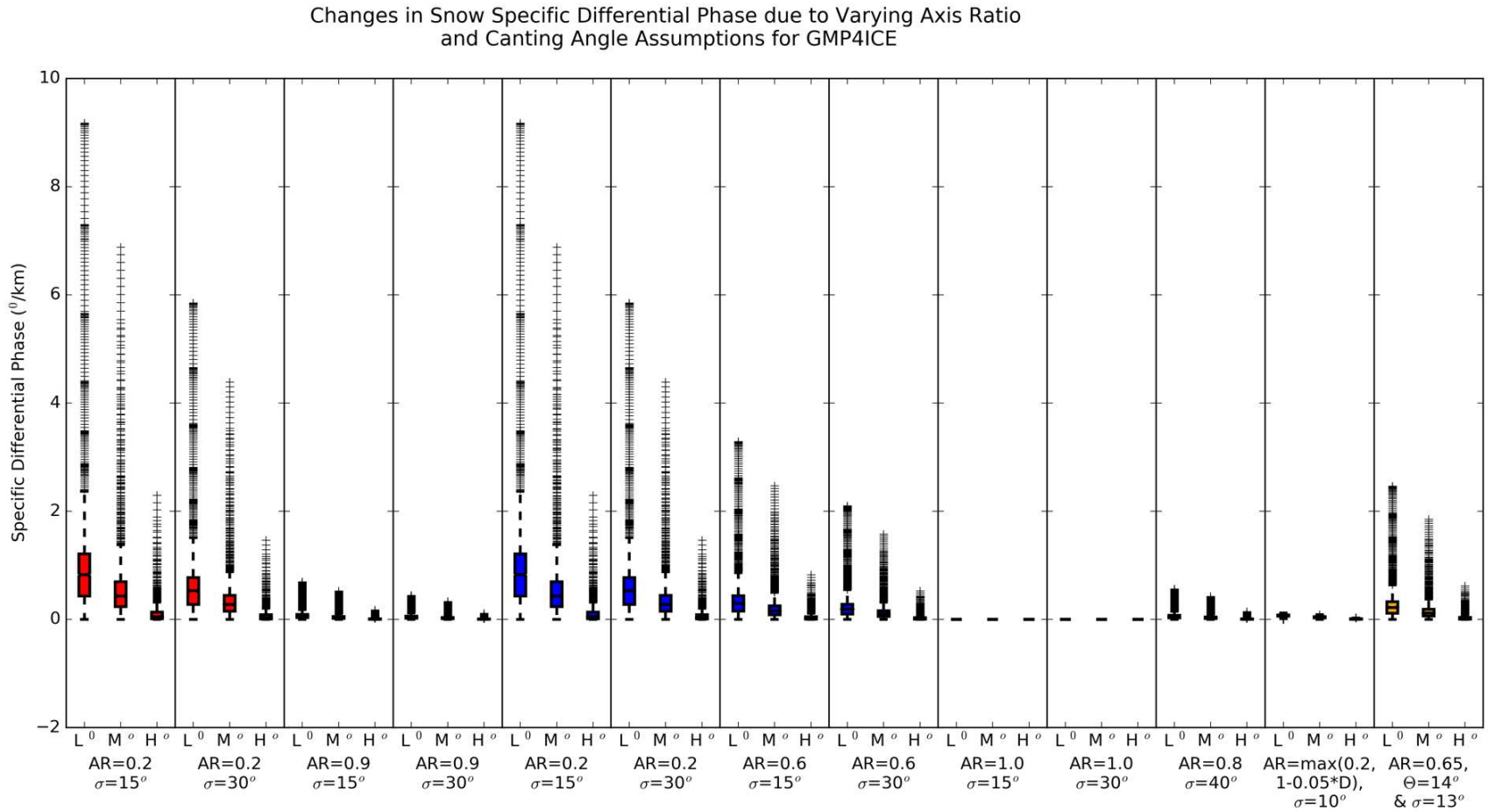

Figure 4.6: Box and whisker plot LUT visualizations for 4ICE Aggregate specific differential phase. The first box and whisker plot denotes the “low” radar elevation angle (0°-30°), the middle box denotes the “medium” radar elevation angle (30°-60°), and the third box denotes the “high” radar elevation angle (60°-90°). Red colors are associated with DR09 assumptions blue colors with S00 assumptions, green with R11 assumptions, purple with “control” assumptions, and yellow with GE15 assumptions.

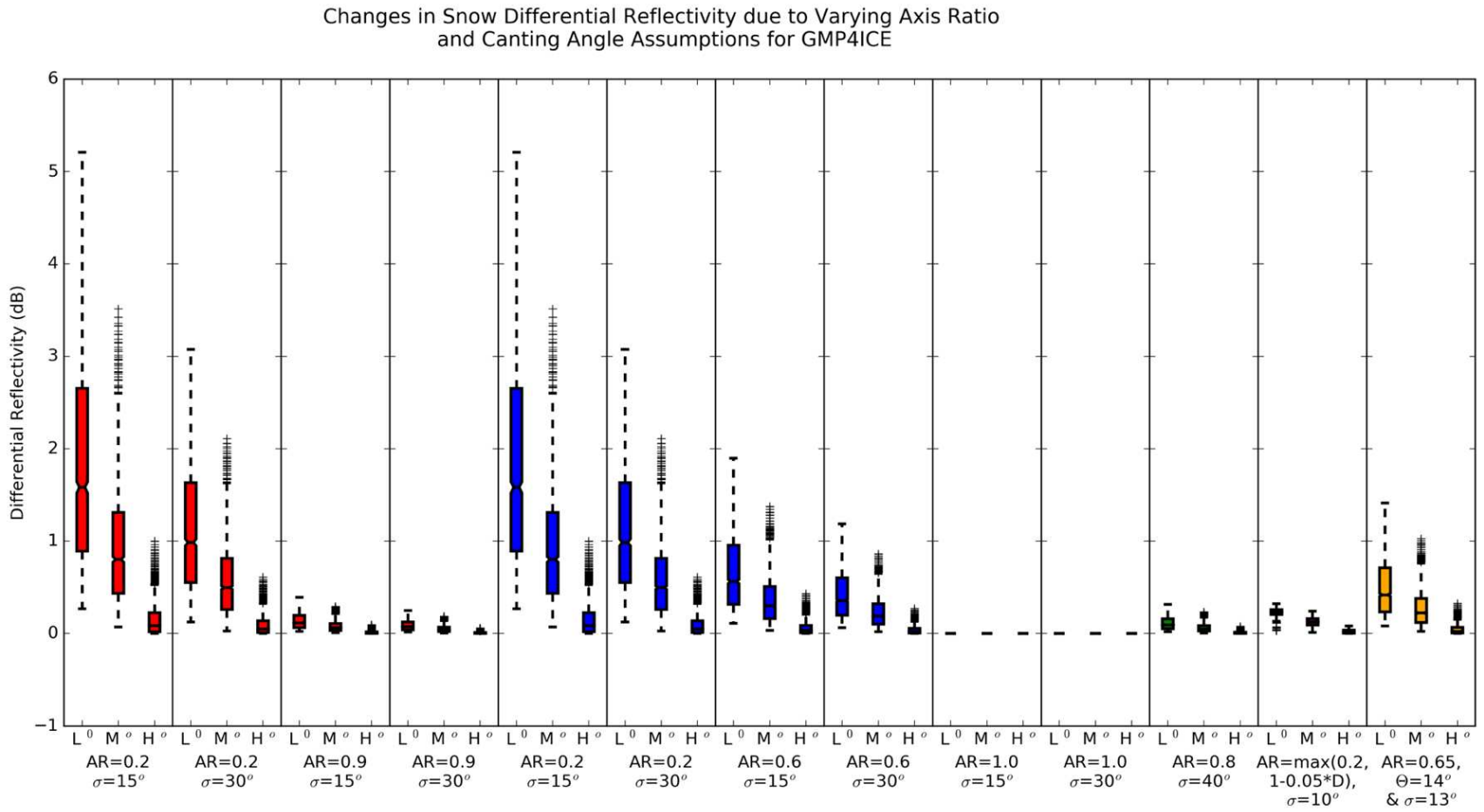

Figure 4.7: Box and whisker plot LUT visualizations for 4ICE Aggregate differential reflectivity. The first box and whisker plot denotes the “low” radar elevation angle (0°-30°), the middle box denotes the “medium” radar elevation angle (30°-60°), and the third box denotes the “high” radar elevation angle (60°-90°). Red colors are associated with DR09 assumptions blue colors with S00 assumptions, green with R11 assumptions, purple with “control” assumptions, and yellow with GE15 assumptions.

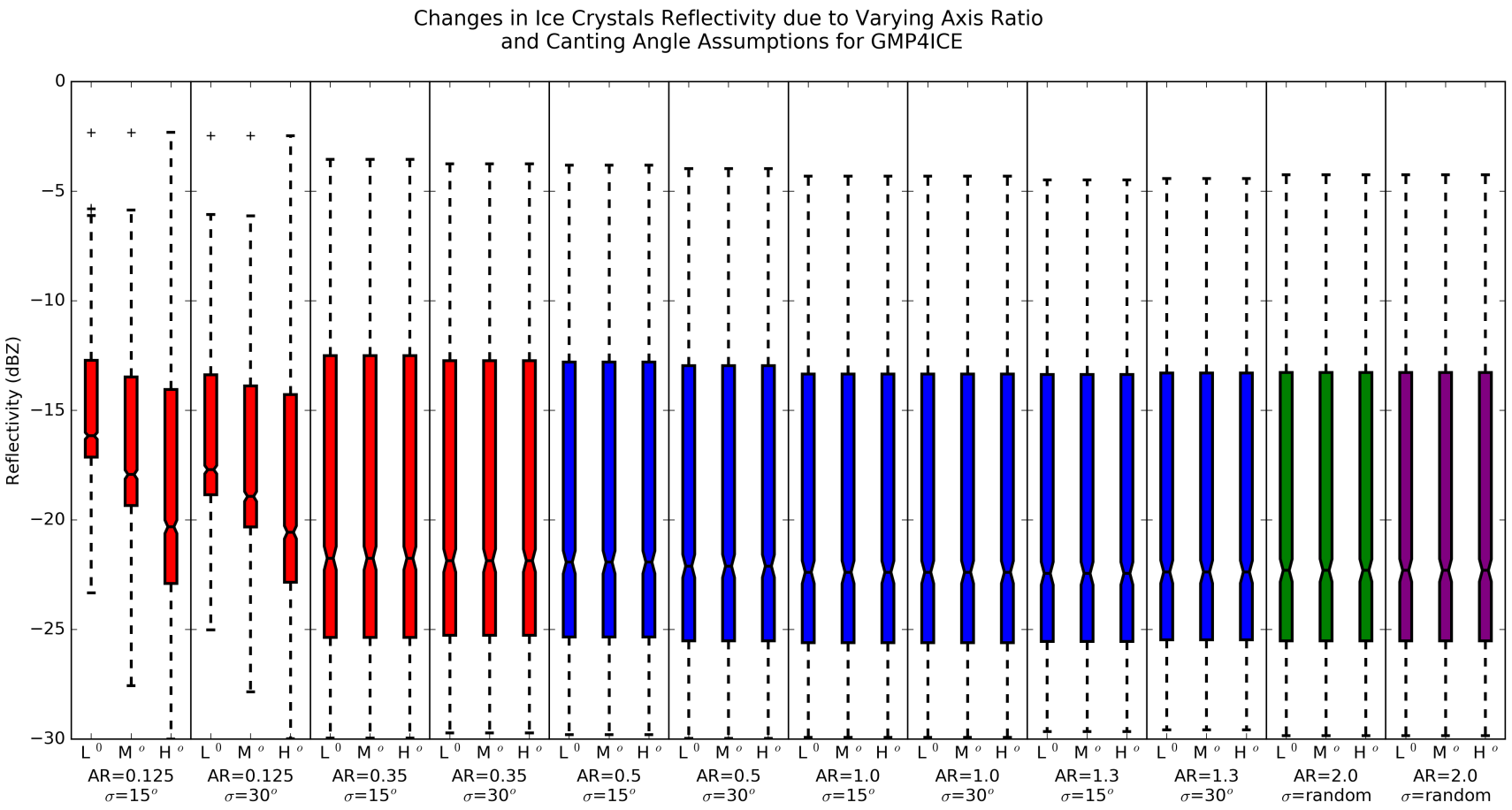

Figure 4.8: Box and whisker plot LUT visualizations for 4ICE Ice Crystal reflectivity. The first box and whisker plot denotes the “low” radar elevation angle (0°-30°), the middle box denotes the “medium” radar elevation angle (30°-60°), and the third box denotes the “high” radar elevation angle (60°-90°). Red colors are associated with DR09 assumptions blue colors with S00 assumptions, green with R11 assumptions, purple with “control” assumptions, and yellow with GE15 assumptions.

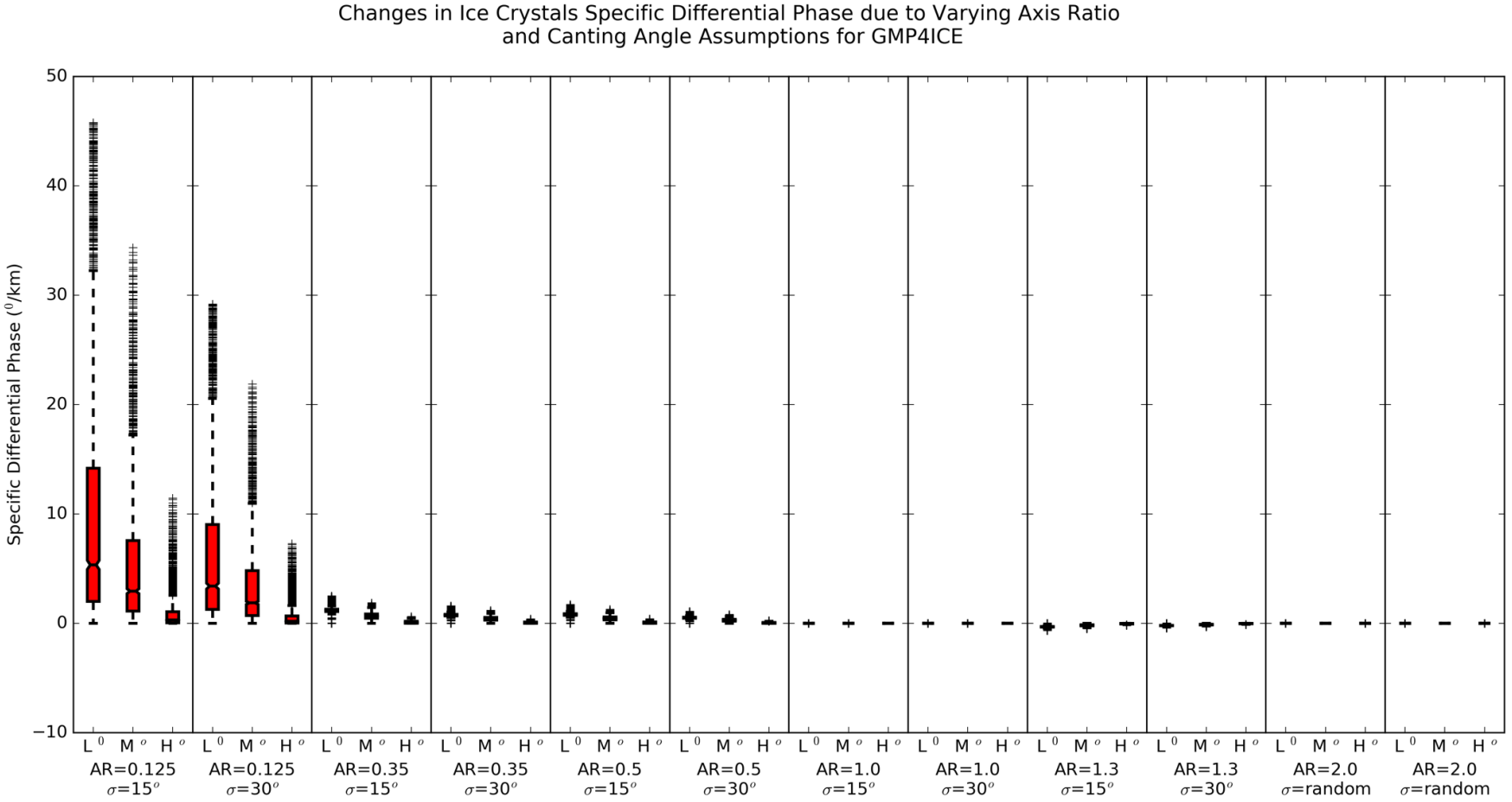

Figure 4.9: Box and whisker plot LUT visualizations for 4ICE Ice Crystal specific differential phase. The first box and whisker plot denotes the “low” radar elevation angle (0°-30°), the middle box denotes the “medium” radar elevation angle (30°-60°), and the third box denotes the “high” radar elevation angle (60°-90°). Red colors are associated with DR09 assumptions blue colors with S00 assumptions, green with R11 assumptions, purple with “control” assumptions, and yellow with GE15 assumptions.

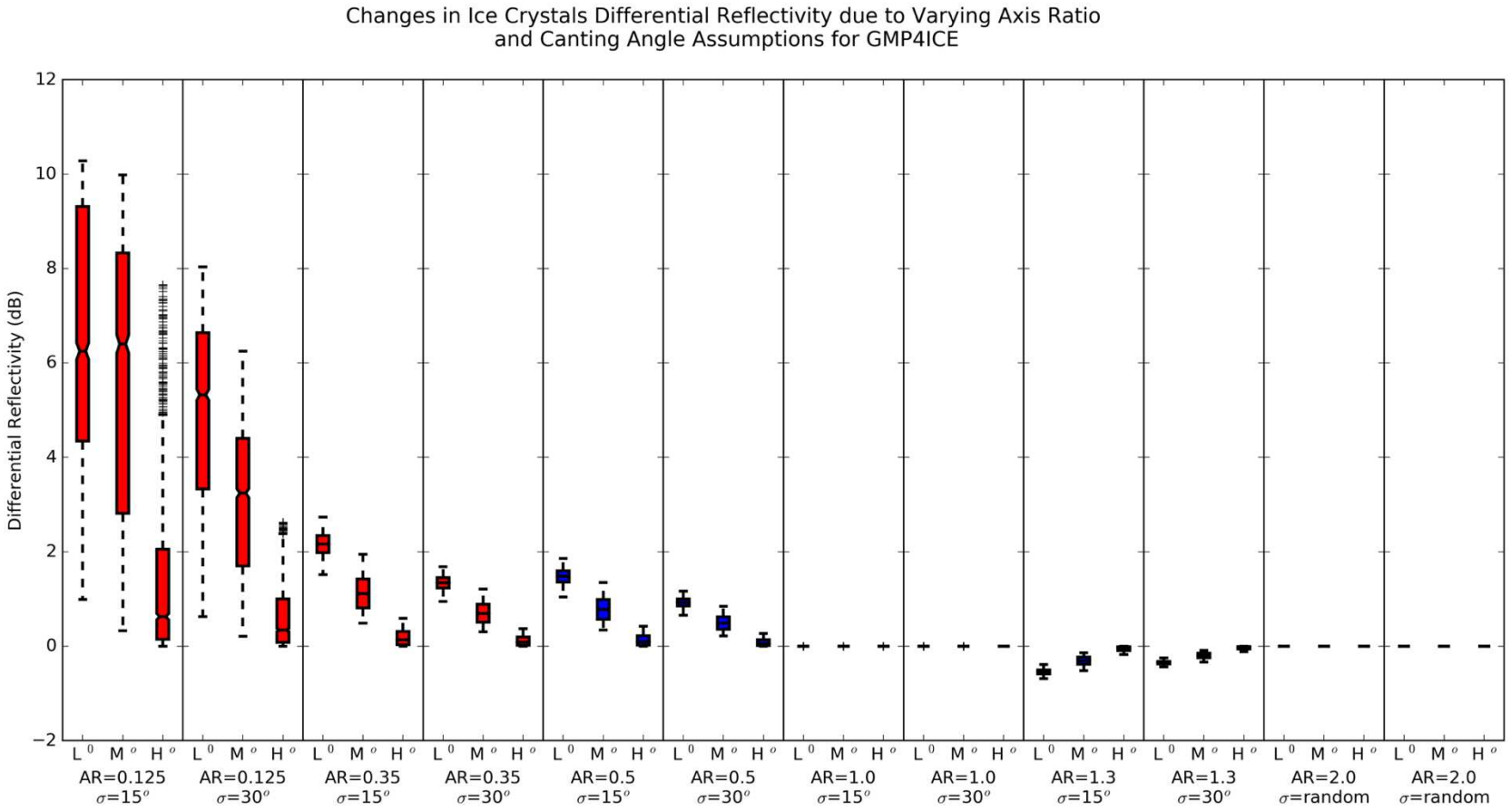

Figure 4.10: Box and whisker plot LUT visualizations for 4ICE Ice Crystal differential reflectivity. The first box and whisker plot denotes the “low” radar elevation angle (0°-30°), the middle box denotes the “medium” radar elevation angle (30°-60°), and the third box denotes the “high” radar elevation angle (60°-90°). Red colors are associated with DR09 assumptions blue colors with S00 assumptions, green with R11 assumptions, purple with “control” assumptions, and yellow with GE15 assumptions.

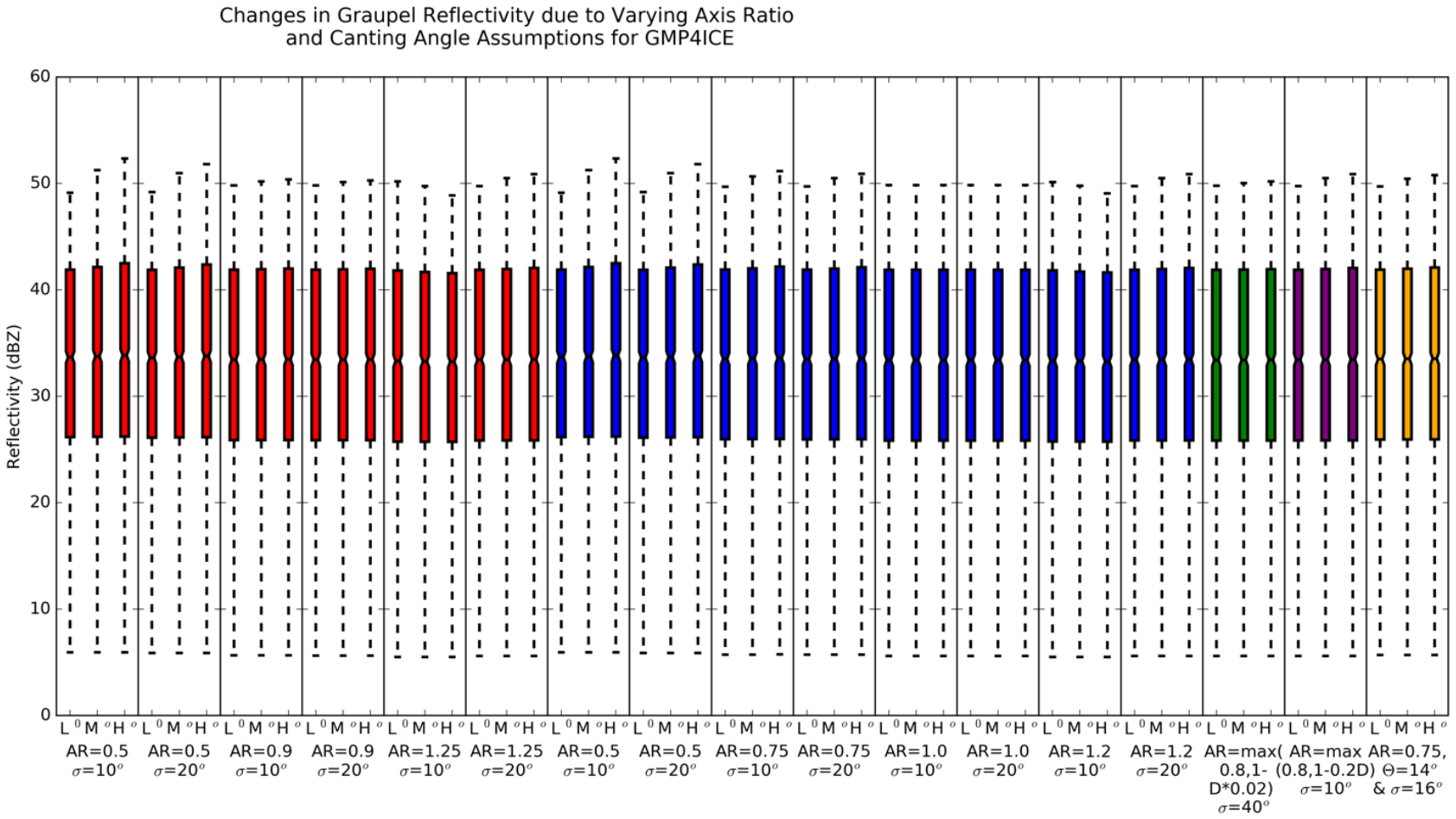

Figure 4.11: Box and whisker plot LUT visualizations for 4ICE Graupel reflectivity. The first box and whisker plot denotes the “low” radar elevation angle (0°-30°), the middle box denotes the “medium” radar elevation angle (30°-60°), and the third box denotes the “high” radar elevation angle (60°-90°). Red colors are associated with DR09 assumptions blue colors with S00 assumptions, green with R11 assumptions, purple with “control” assumptions, and yellow with GE15 assumptions.

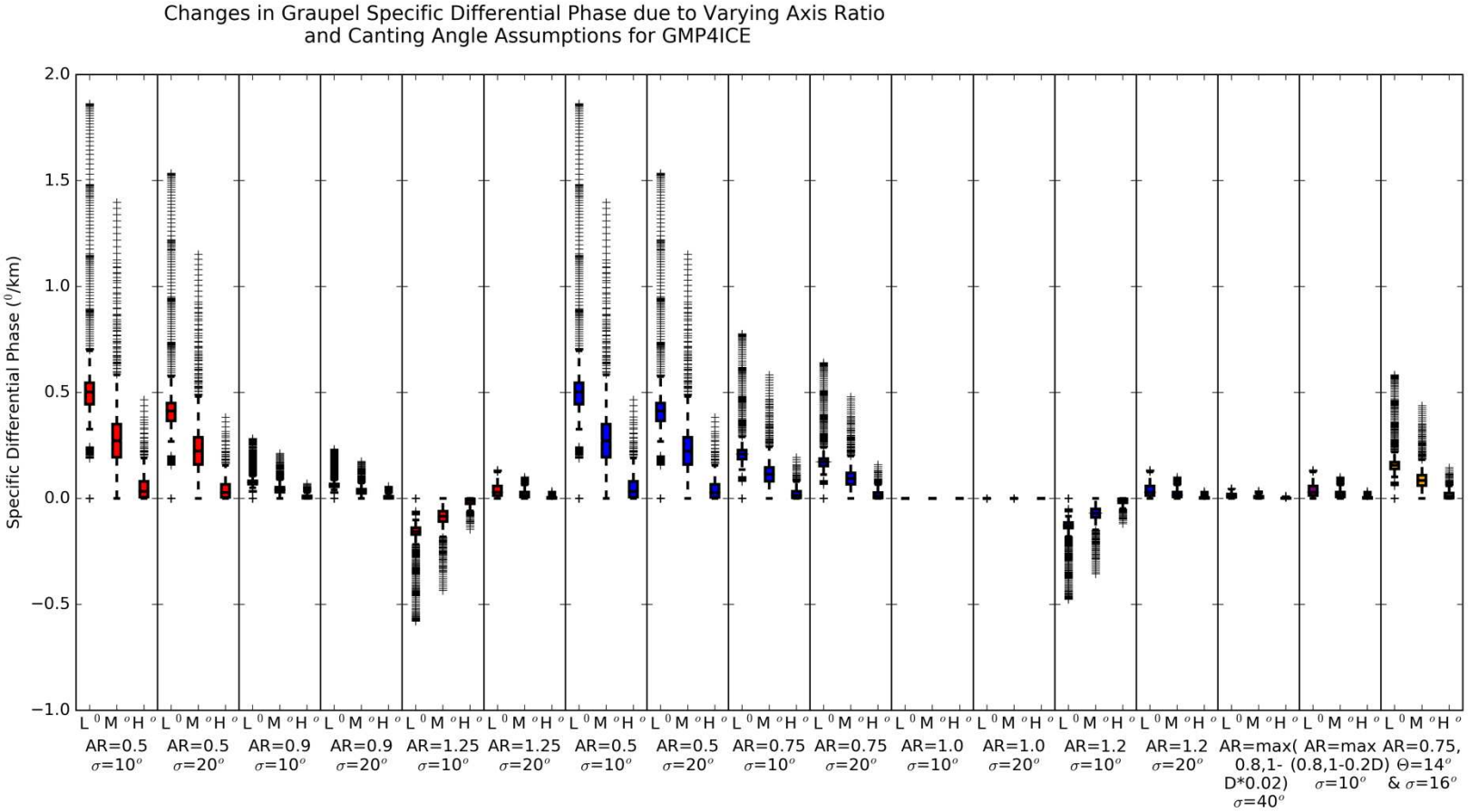

Figure 4.12: Box and whisker plot LUT visualizations for 4ICE Graupel specific differential phase. The first box and whisker plot denotes the “low” radar elevation angle (0°-30°), the middle box denotes the “medium” radar elevation angle (30°-60°), and the third box denotes the “high” radar elevation angle (60°-90°). Red colors are associated with DR09 assumptions blue colors with S00 assumptions, green with R11 assumptions, purple with “control” assumptions, and yellow with GE15 assumptions.

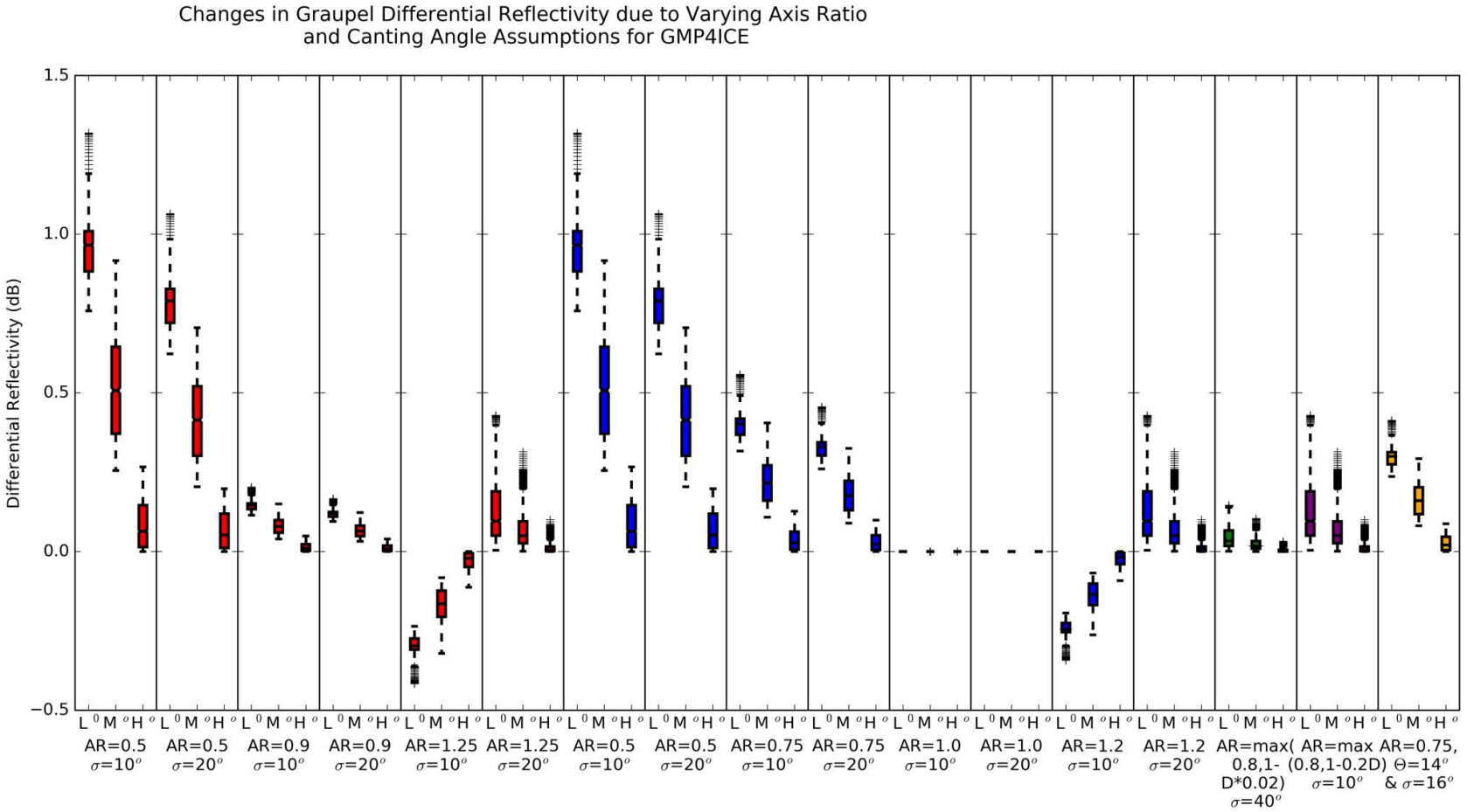

Figure 4.13: Box and whisker plot LUT visualizations for 4ICE Graupel differential reflectivity. The first box and whisker plot denotes the “low” radar elevation angle (0°-30°), the middle box denotes the “medium” radar elevation angle (30°-60°), and the third box denotes the “high” radar elevation angle (60°-90°). Red colors are associated with DR09 assumptions blue colors with S00 assumptions, green with R11 assumptions, purple with “control” assumptions, and yellow with GF15 assumptions.

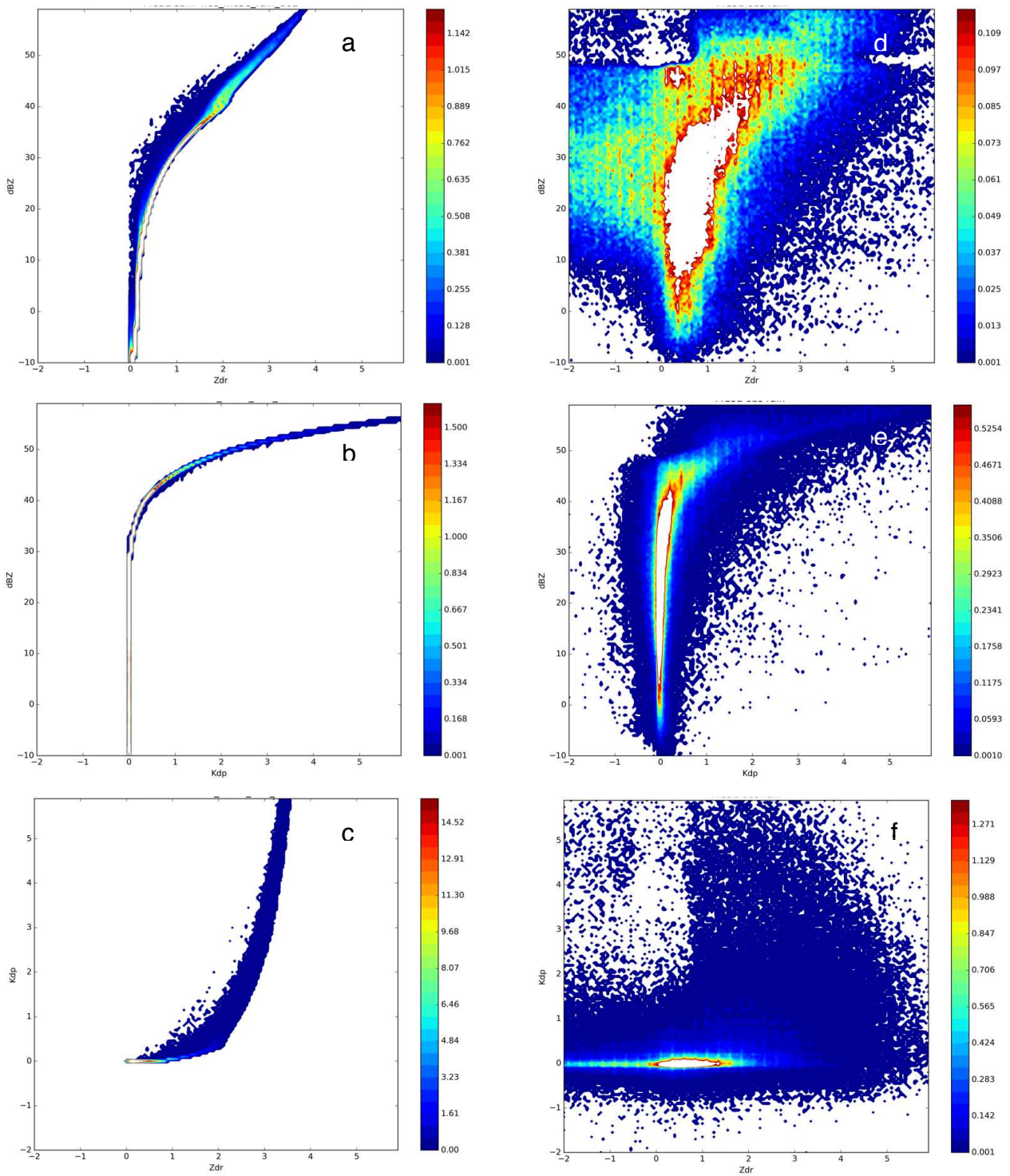

Figure 4.14: Rain co-variance plots of Z-Z_{dr}, Z-K_{dp}, and K_{dp}-Z_{dr} for (a-c) MC3E 4ICE and (d-f) MC3E observations. Model results are shown to the left and observations to the right.

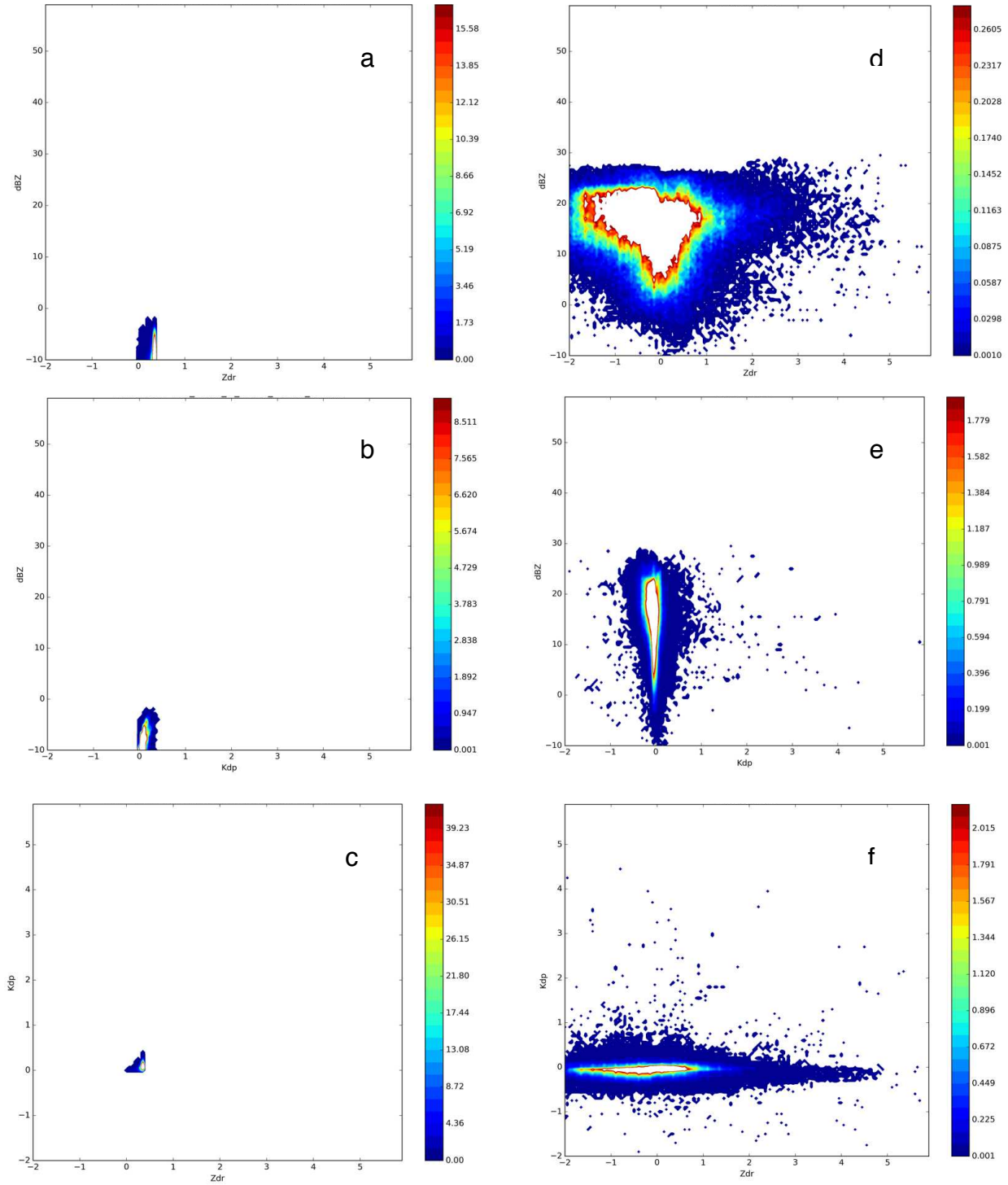

Figure 4.15: Ice Crystal co-variance plots of Z-Z_{dr}, Z-K_{dp}, and K_{dp}-Z_{dr} for (a-c) MC3E 4ICE and (d-f) MC3E observations. Model results are shown to the left and observations to the right.

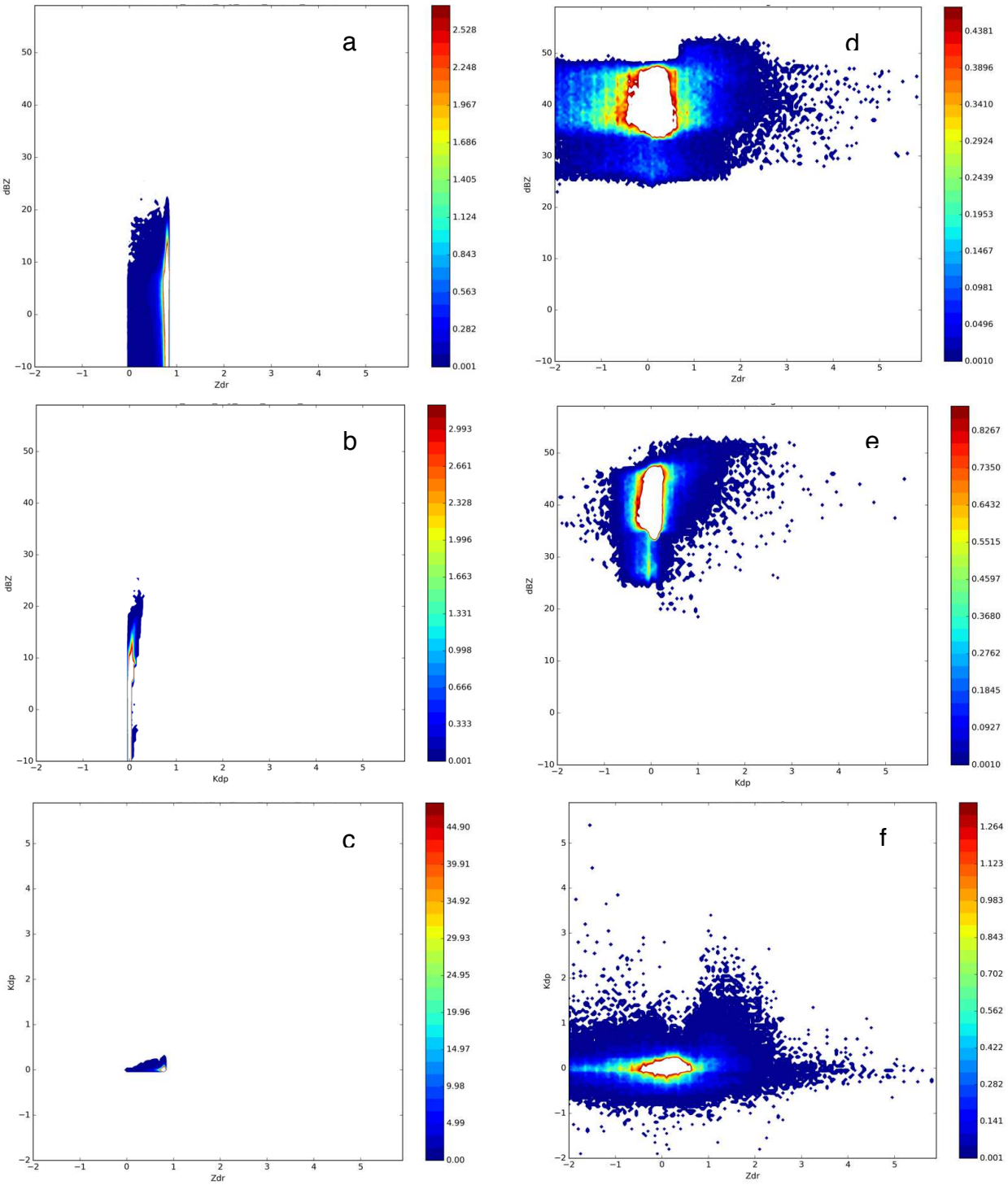

Figure 4.16: Graupel co-variance plots of Z-Z_{dr}, Z-K_{dp}, and K_{dp}-Z_{dr} for (a-c) MC3E 4ICE and (d-f) MC3E observations. Model results are shown to the left and observations to the right.

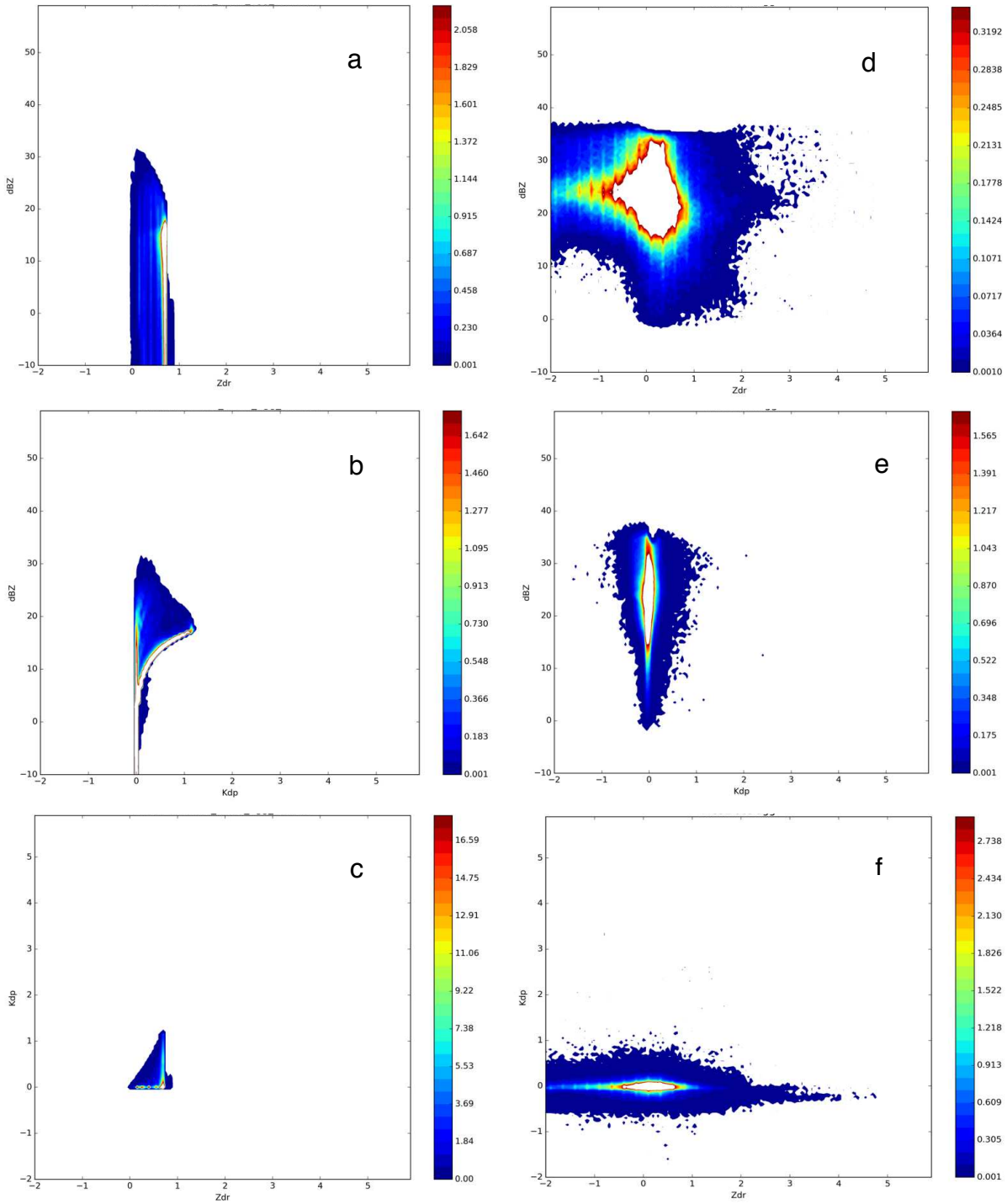

Figure 4.17: Aggregate co-variance plots of Z-Z_{dr}, Z-K_{dp}, and K_{dp}-Z_{dr} for (a-c) MC3E 4ICE and (d-f) MC3E observations. Model results are shown to the left and observations to the right.

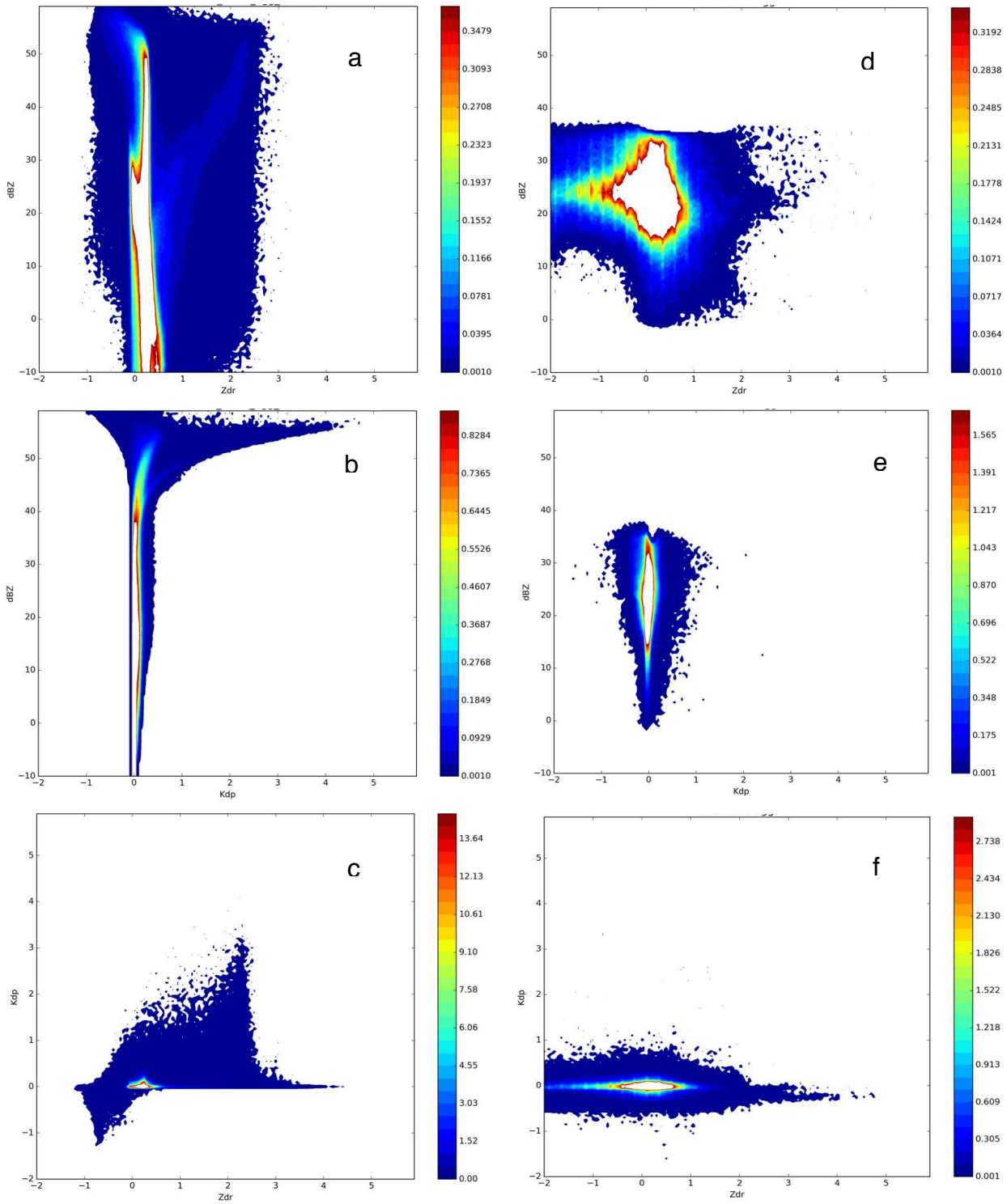

Figure 4.18: Aggregate co-variance plots of Z-Z_{dr}, Z-K_{dp}, and K_{dp}-Z_{dr} for (a-c) MC3E SBM and (d-f) MC3E observations. Model results are shown to the let and observations to the right.

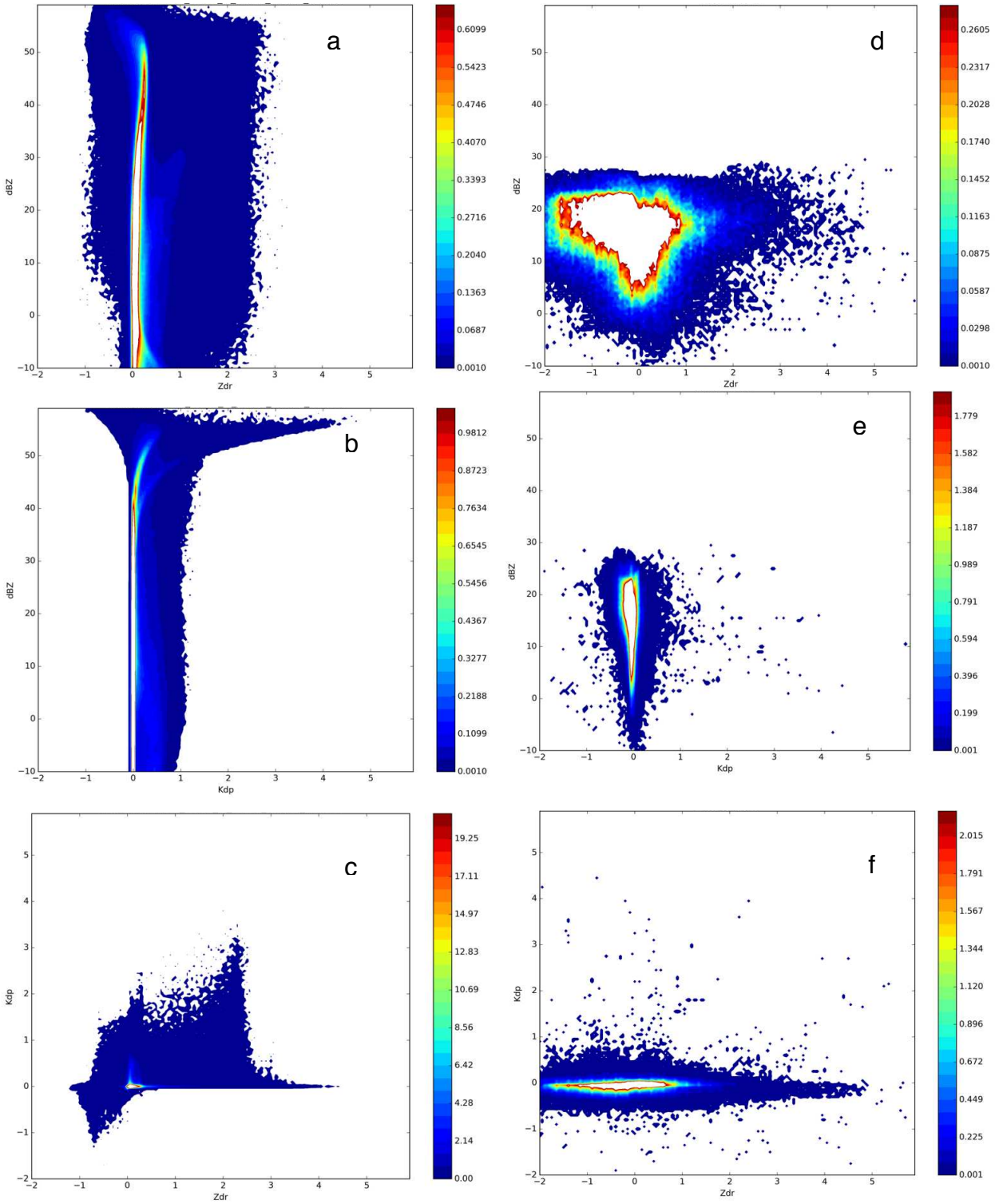

Figure 4.19: Ice Crystal co-variance plots of Z-Z_{dr}, Z-K_{dp}, and K_{dp}-Z_{dr} for (a-c) MC3E SBM and (d-f) MC3E observations. Model results are shown to the left and observations to the right.

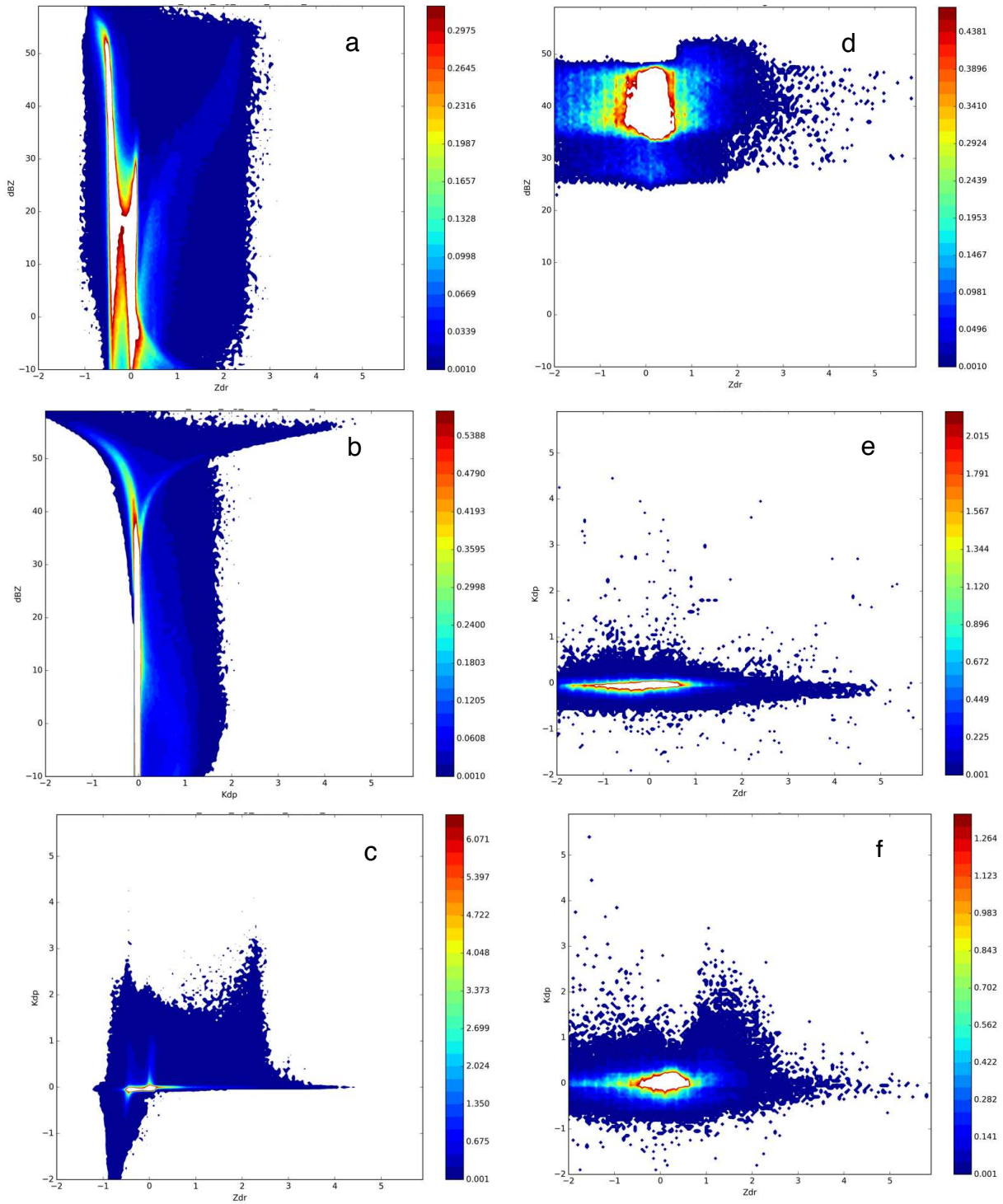

Figure 4.20: Graupel co-variance plots of Z-Z_{dr}, Z-K_{dp}, and K_{dp}-Z_{dr} for (a-c) MC3E SBM and (d-f) MC3E observations. Model results are shown to the left and observations to the right.

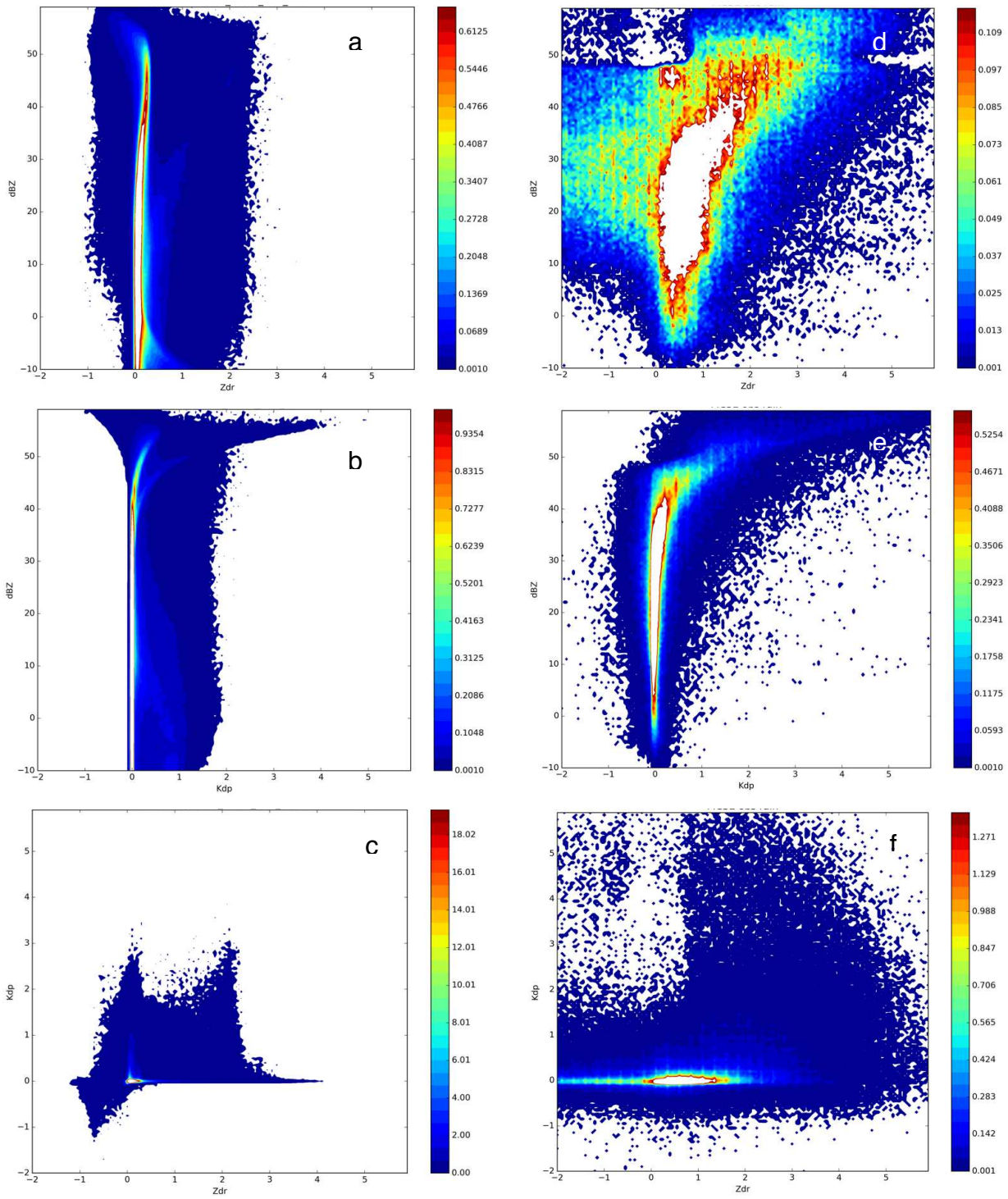

Figure 4.21: Rain co-variance plots of Z-Z_{dr}, Z-K_{dp}, and K_{dp}-Z_{dr} for (a-c) MC3E SBM and (d-f) MC3E observations. Model results are shown to the left and observations to the right.

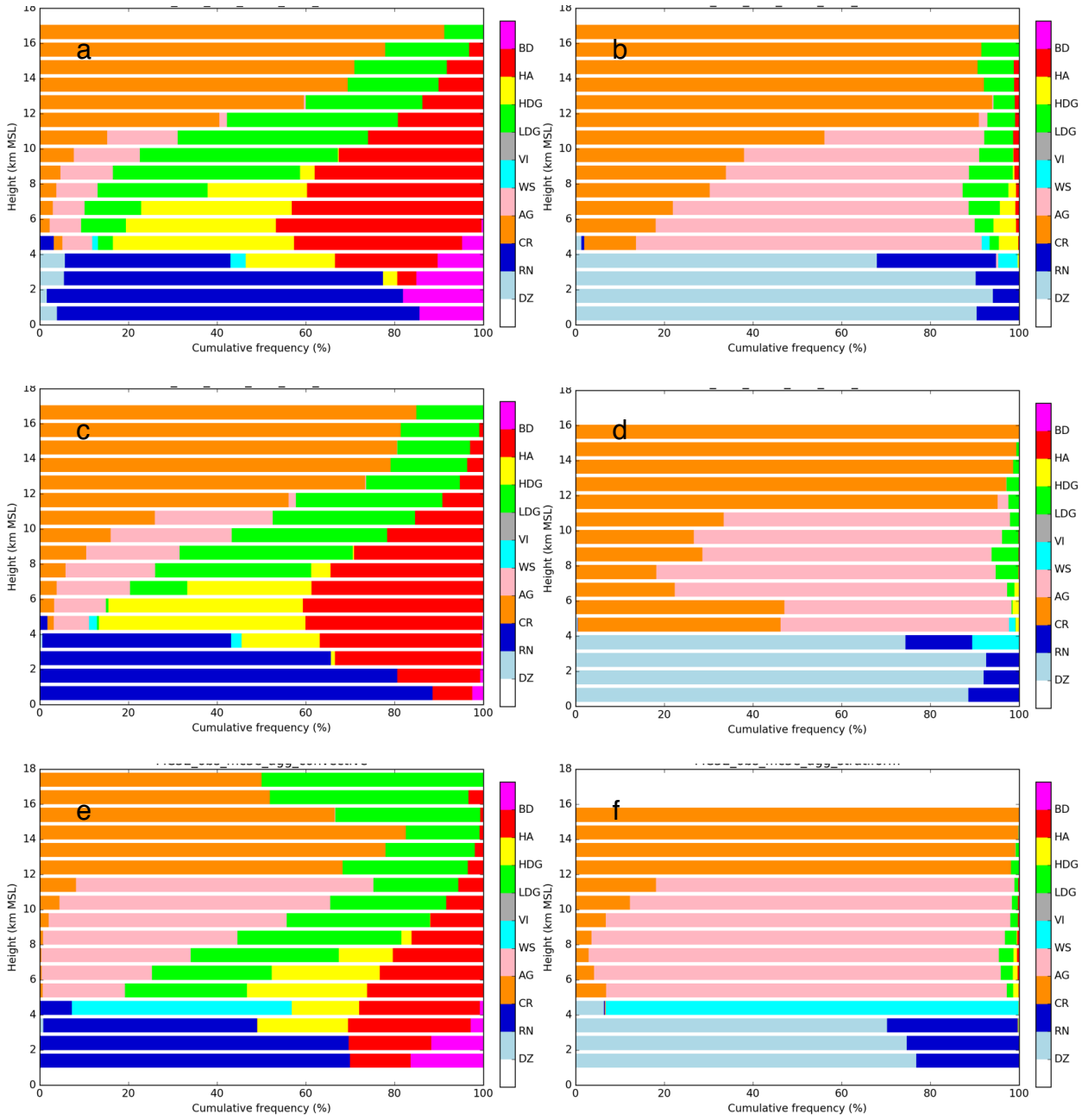

Figure 4.22: HID CFAD plots from the “best” assumptions for (a,b) convective and stratiform MC3E 4ICE, the “best” assumptions for (c,d) convective and stratiform MC3E SBM, and then for (e,f) convective and stratiform MC3E observations.

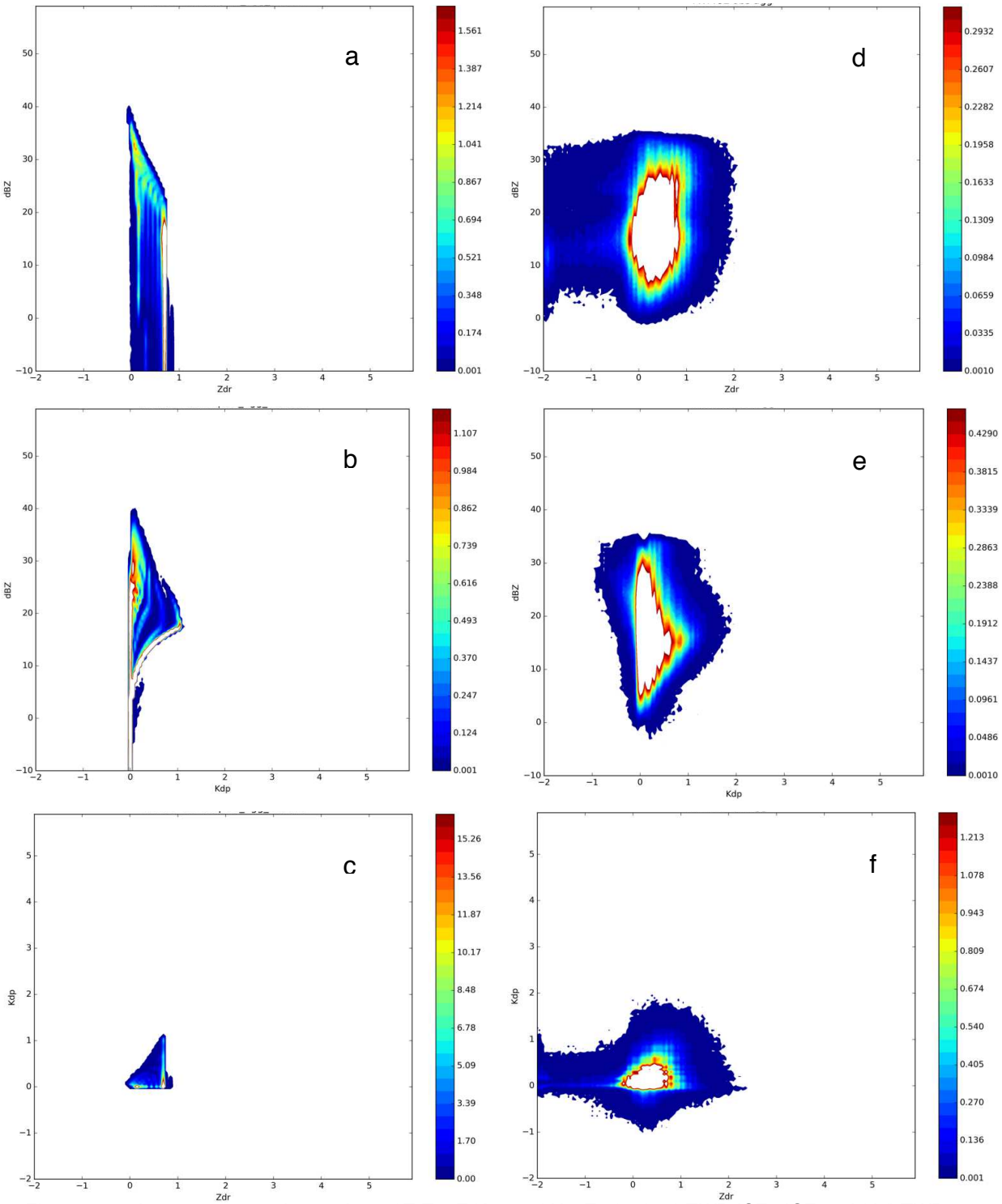

Figure 4.23: Aggregate co-variance plots of Z-Z_{dr}, Z-K_{dp}, and K_{dp}-Z_{dr} for (a-c) TWP-ICE 4ICE and (d-f) TWP-ICE observations. Model results are shown to the left and observations to the right.

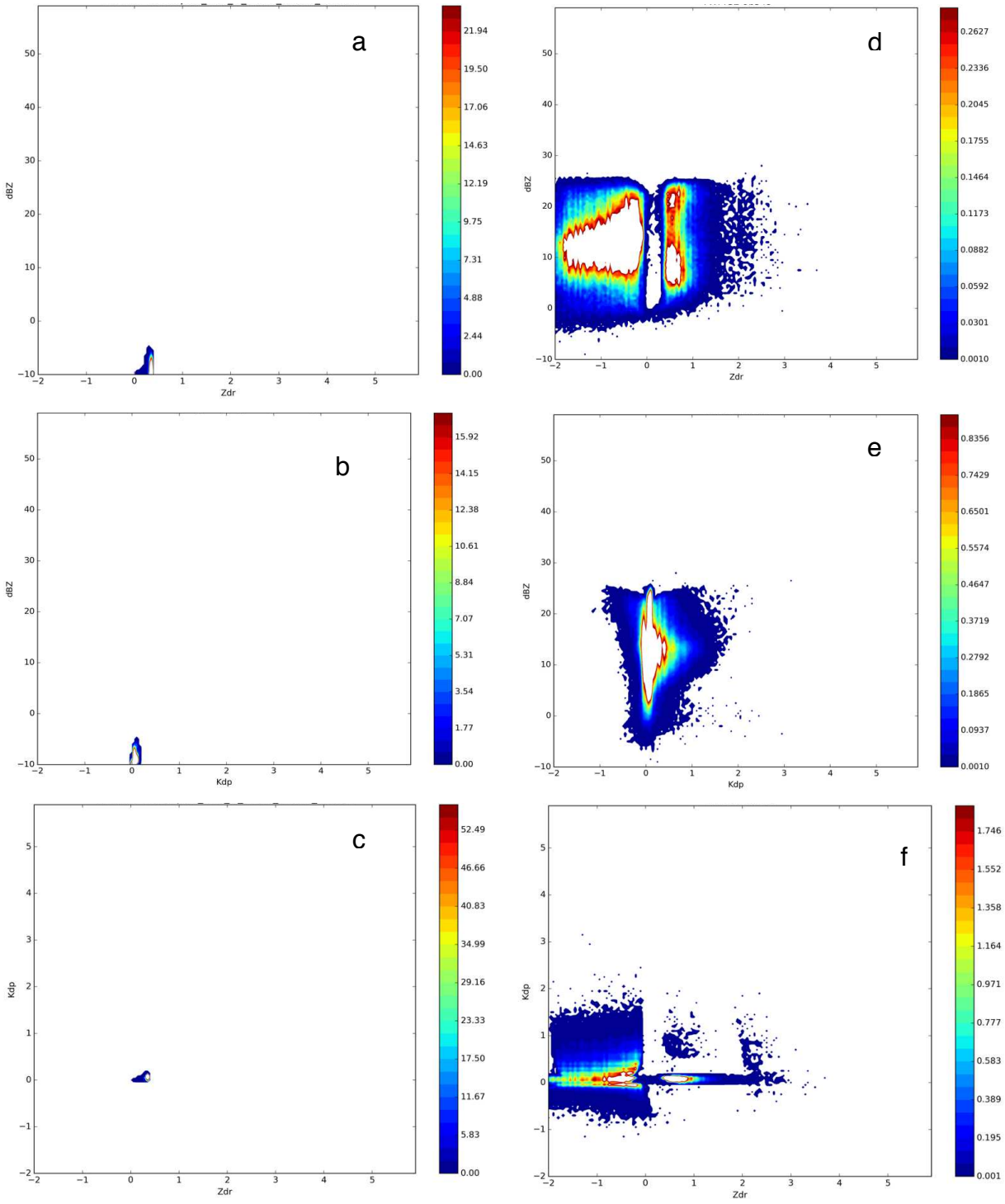

Figure 4.24: Ice Crystal co-variance plots of Z-Z_{dr}, Z-K_{dp}, and K_{dp}-Z_{dr} for (a-c) TWP-ICE 4ICE and (d-f) TWP-ICE observations. Model results are shown to the left and observations to the right.

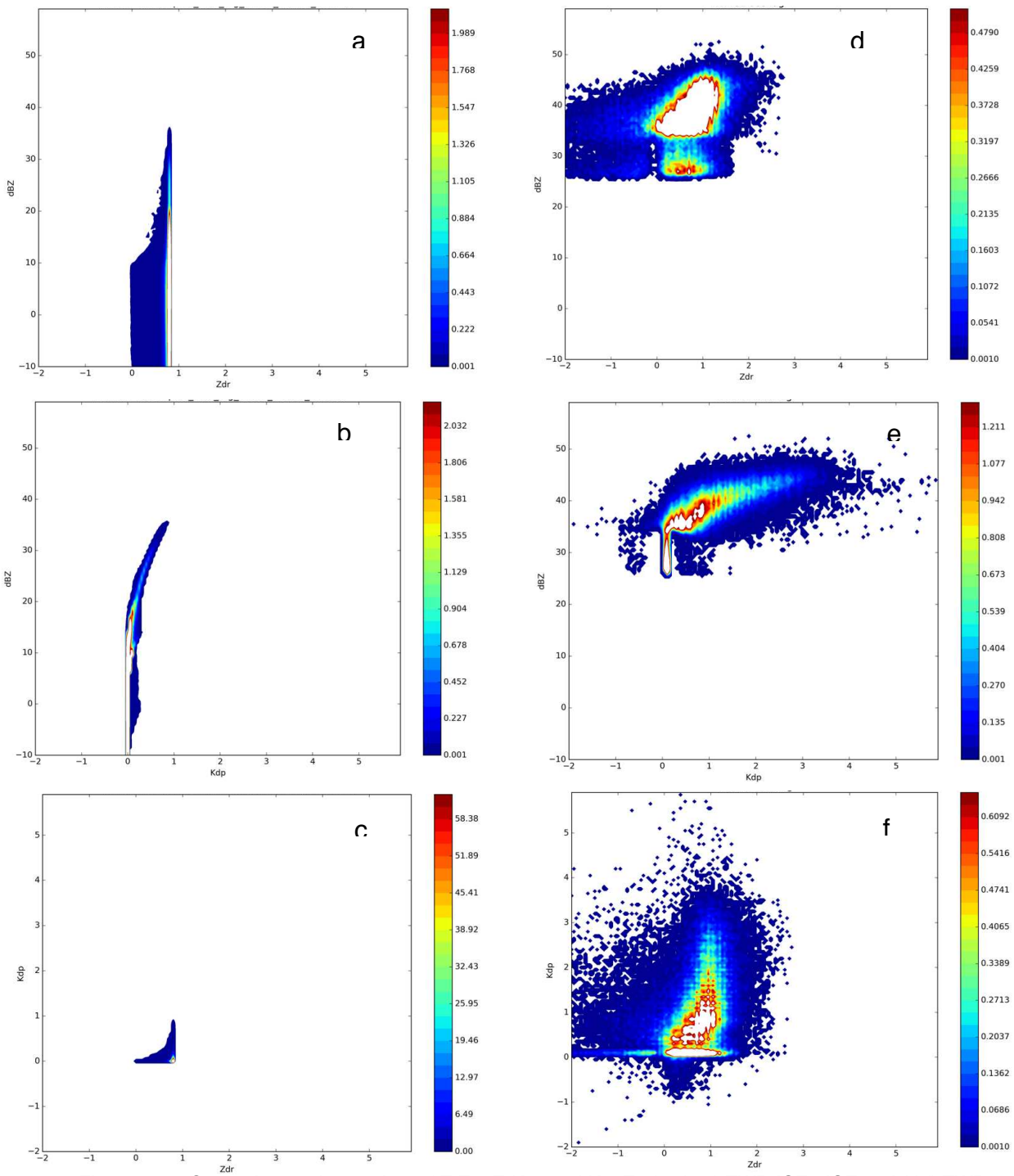

Figure 4.25: Graupel co-variance plots of Z-Z_{dr}, Z-K_{dp}, and K_{dp}-Z_{dr} for (a-c) TWP-ICE 4ICE and (d-f) TWP-ICE observations. Model results are shown to the left and observations to the right.

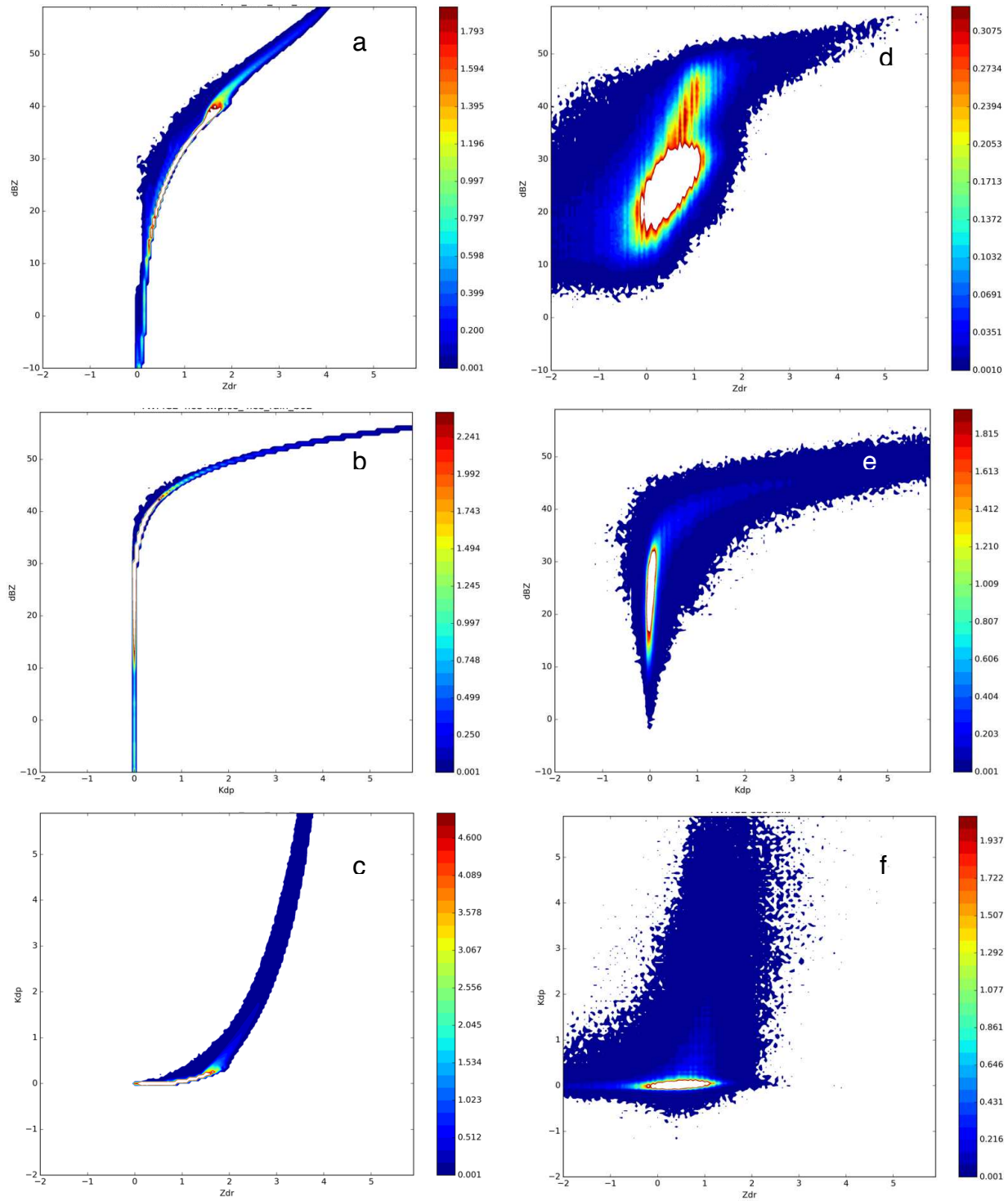

Figure 4.26: Rain co-variance plots of Z-Z_{dr}, Z-K_{dp}, and K_{dp}-Z_{dr} for (a-c) TWP-ICE 4ICE and (d-f) TWP-ice observations. Model results are shown to the left and observations to the right.

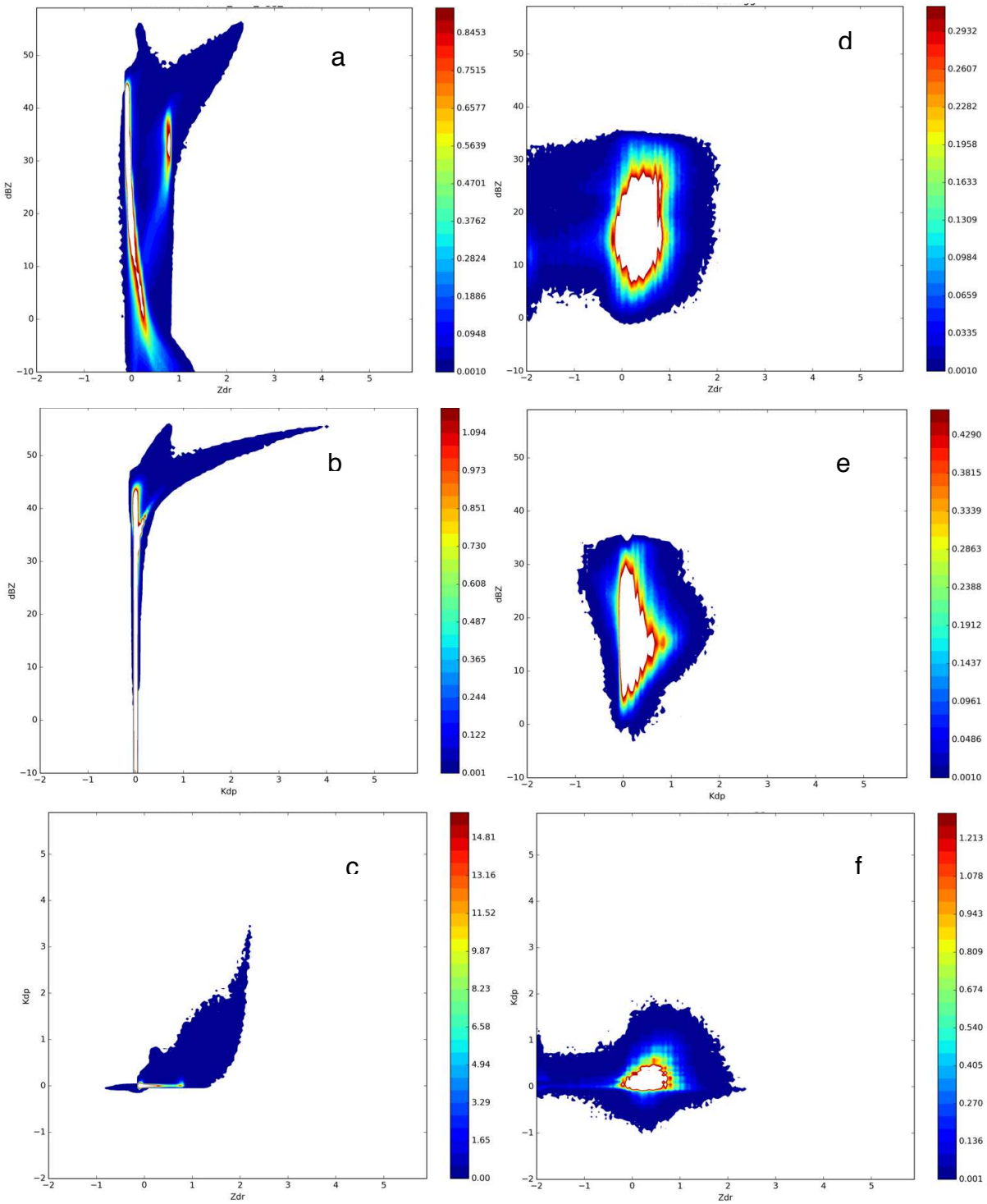

Figure 4.27: Aggregate co-variance plots of Z-Z_{dr}, Z-K_{dp}, and K_{dp}-Z_{dr} for (a-c) TWP-ICE SBM and (d-f) TWP-ICE observations. Model results are shown to the left and observations to the right.

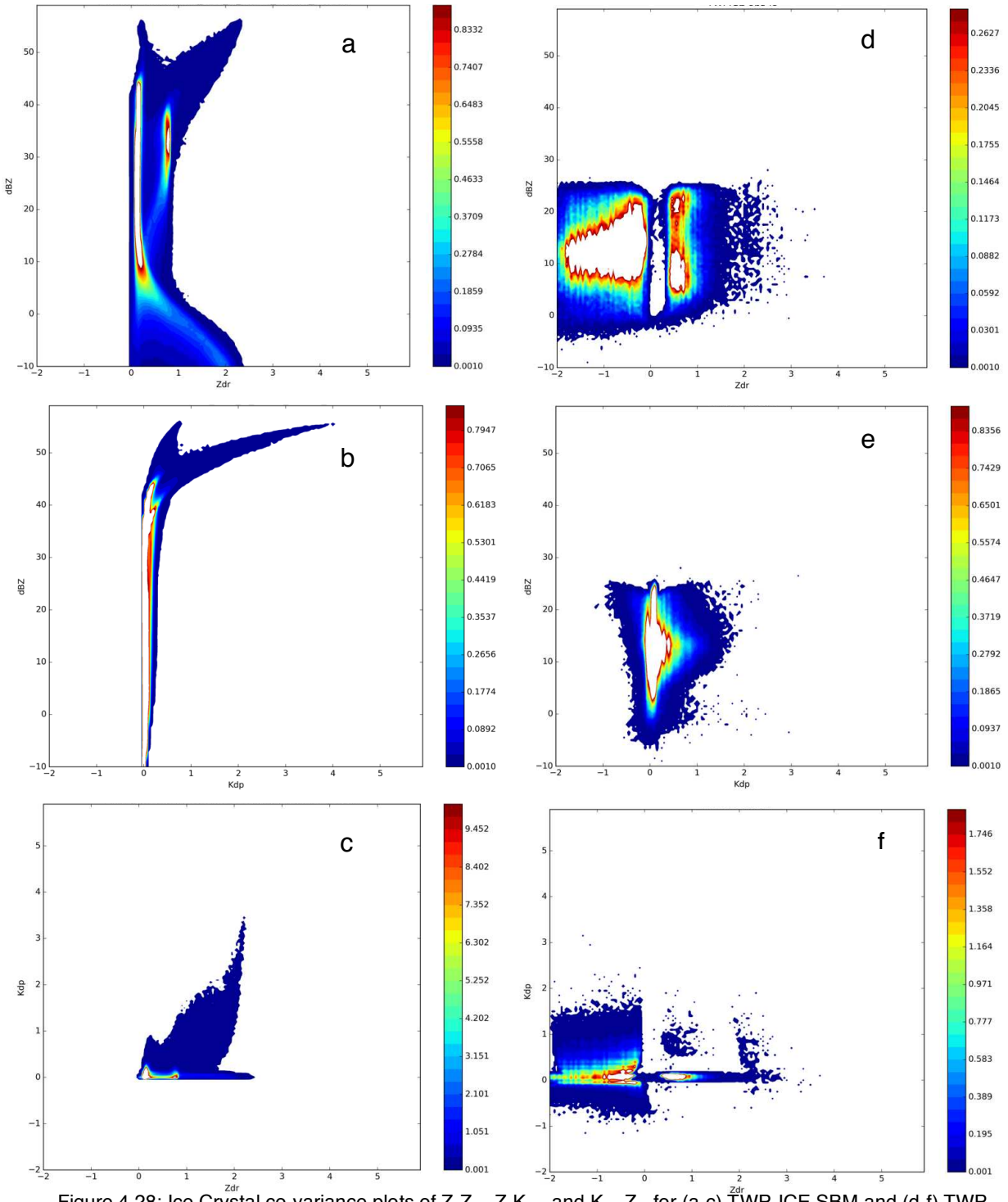

Figure 4.28: Ice Crystal co-variance plots of Z-Z_{dr}, Z-K_{dp}, and K_{dp}-Z_{dr} for (a-c) TWP-ICE SBM and (d-f) TWP-ICE observations. Model results are shown to the left and observations to the right.

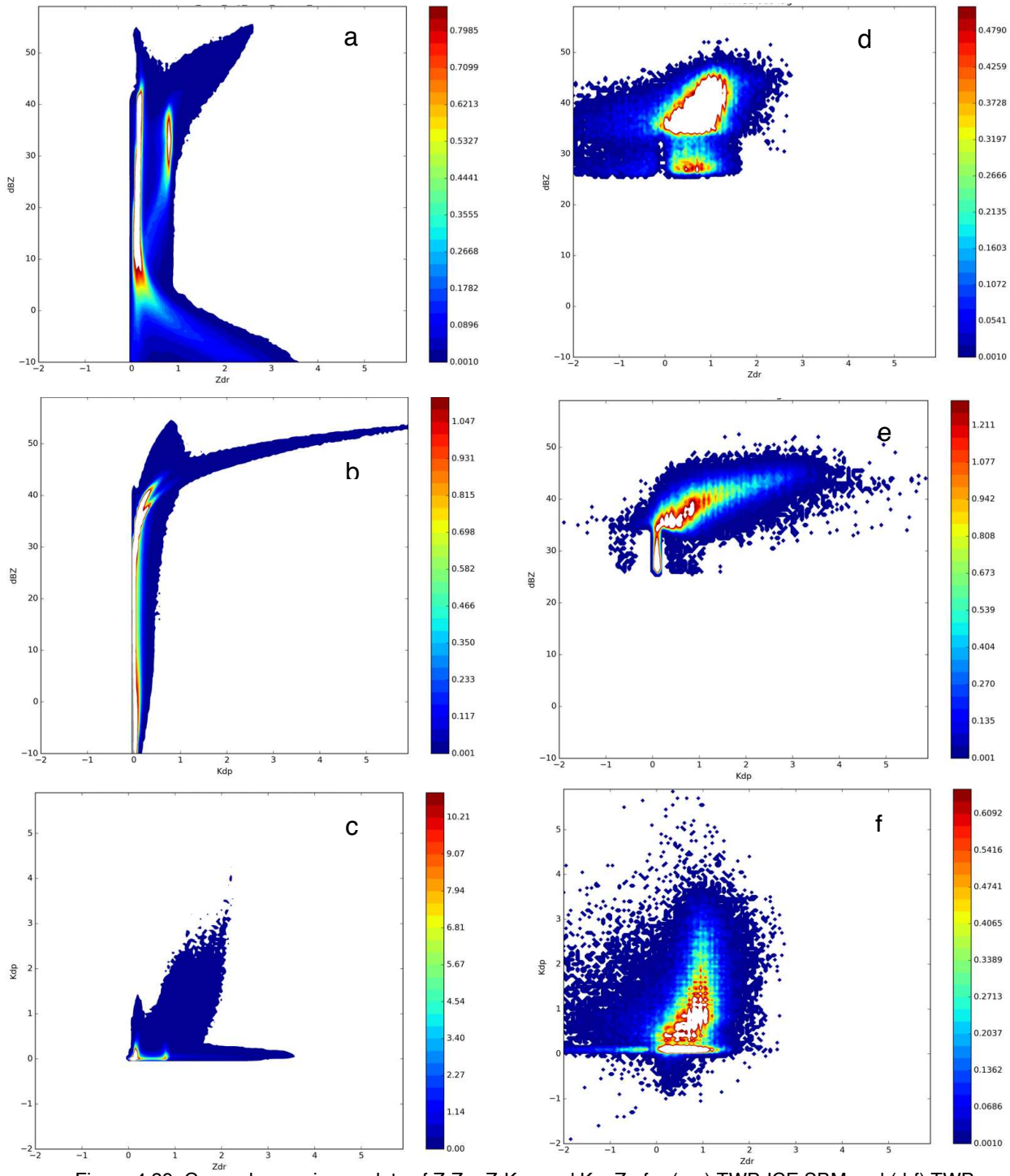

Figure 4.29: Graupel co-variance plots of Z-Z_{dr}, Z-K_{dp}, and K_{dp}-Z_{dr} for (a-c) TWP-ICE SBM and (d-f) TWP-ICE observations. Model results are shown to the left and observations to the right.

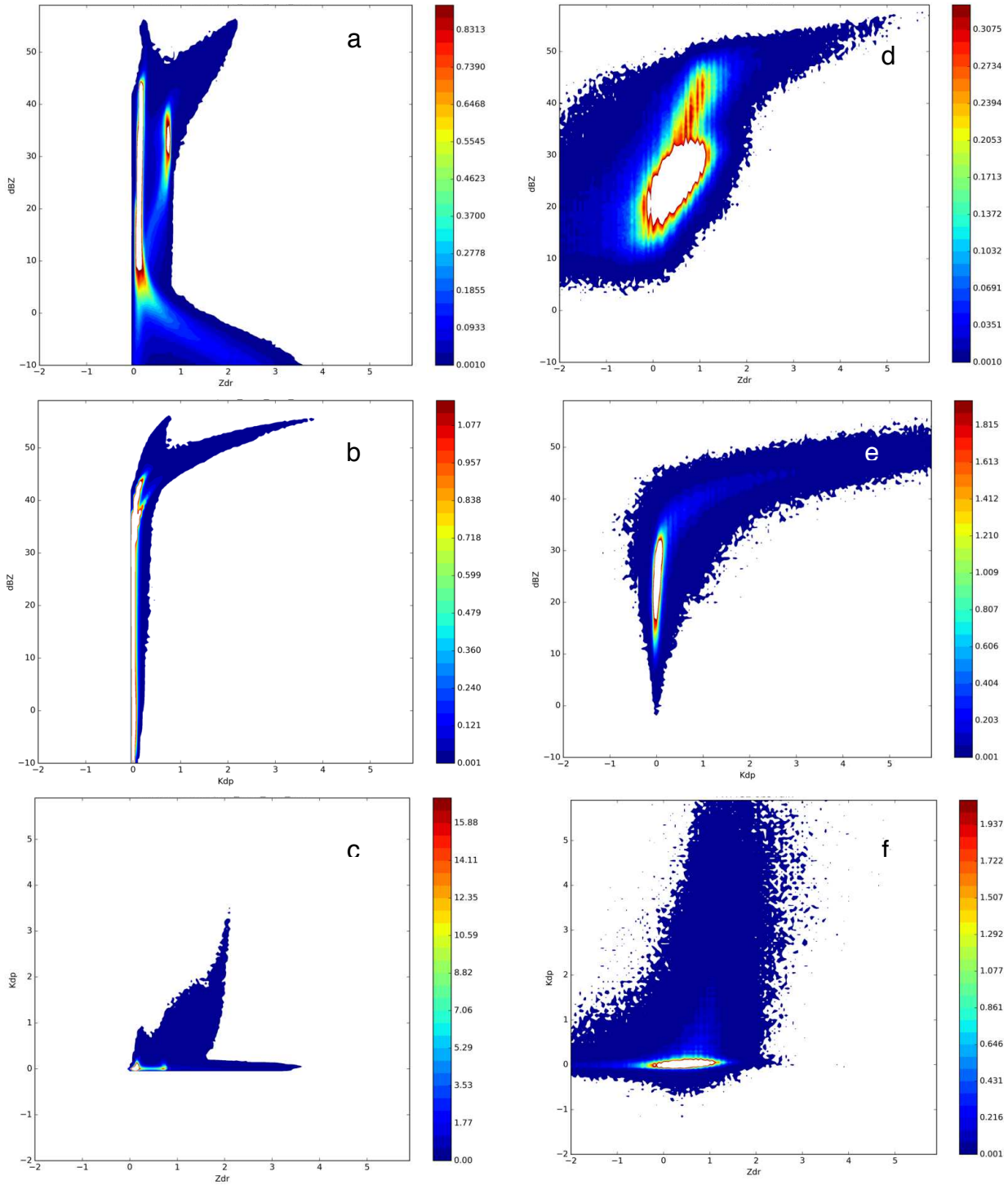

Figure 4.30: Rain co-variance plots of Z-Z_{dr}, Z-K_{dp}, and K_{dp}-Z_{dr} for (a-c) TWP-ICE SBM and (d-f) TWP-ice observations. Rain co-variance plots of Z-Z_{dr}, Z-K_{dp}, and K_{dp}-Z_{dr} for (a-c) TWP-ICE SBM and (d-f) TWP-ice observations. Model results are shown to the left and observations to the right.

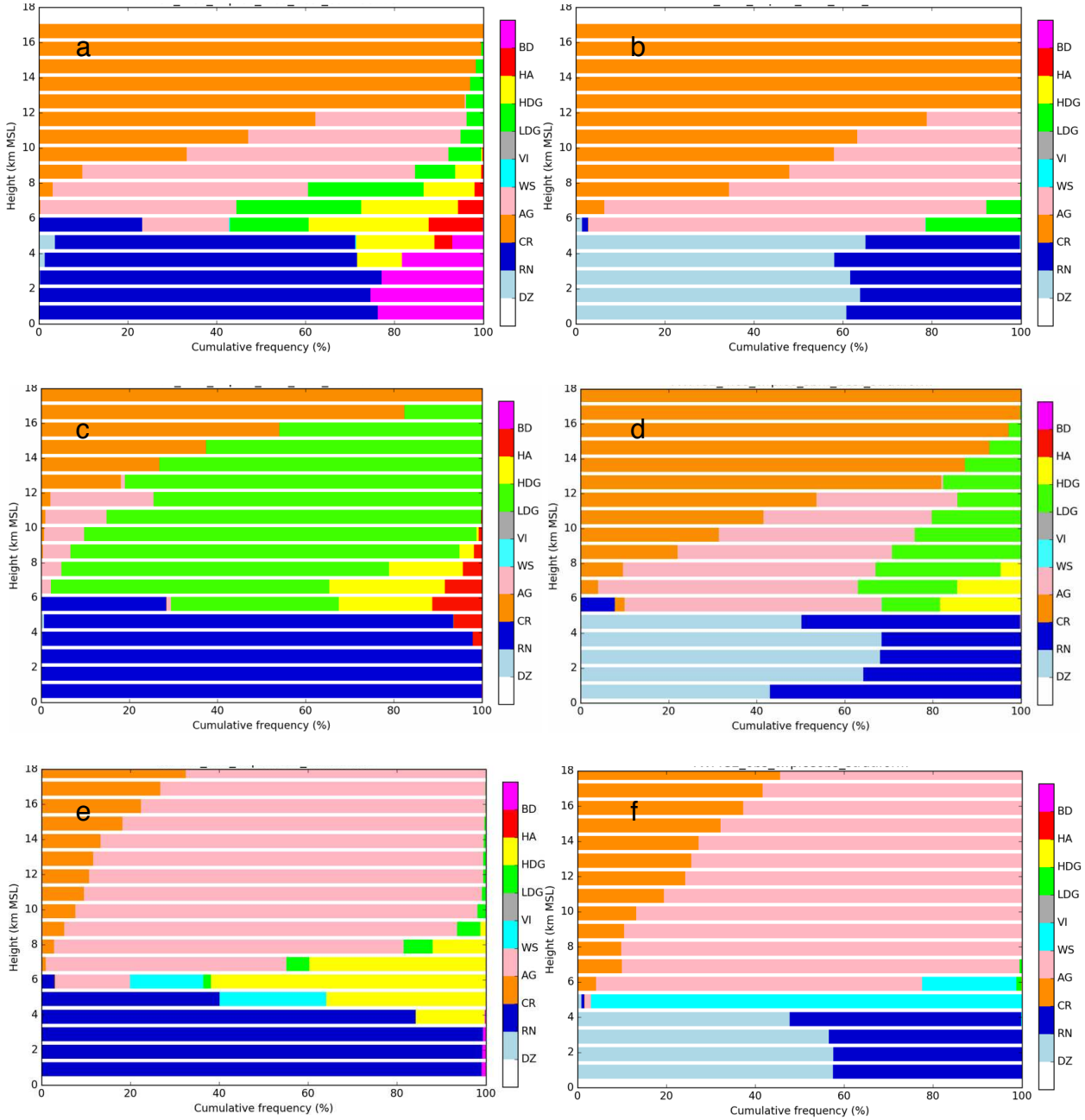

Figure 4.31: HID CFAD plots from the “best” assumptions for (a,b) convective and stratiform TWP-ICE 4ICE, the “best” assumptions for (c,d) convective and stratiform TWP-ICE SBM, and then for (e,f) convective and stratiform TWP-ICE observations.

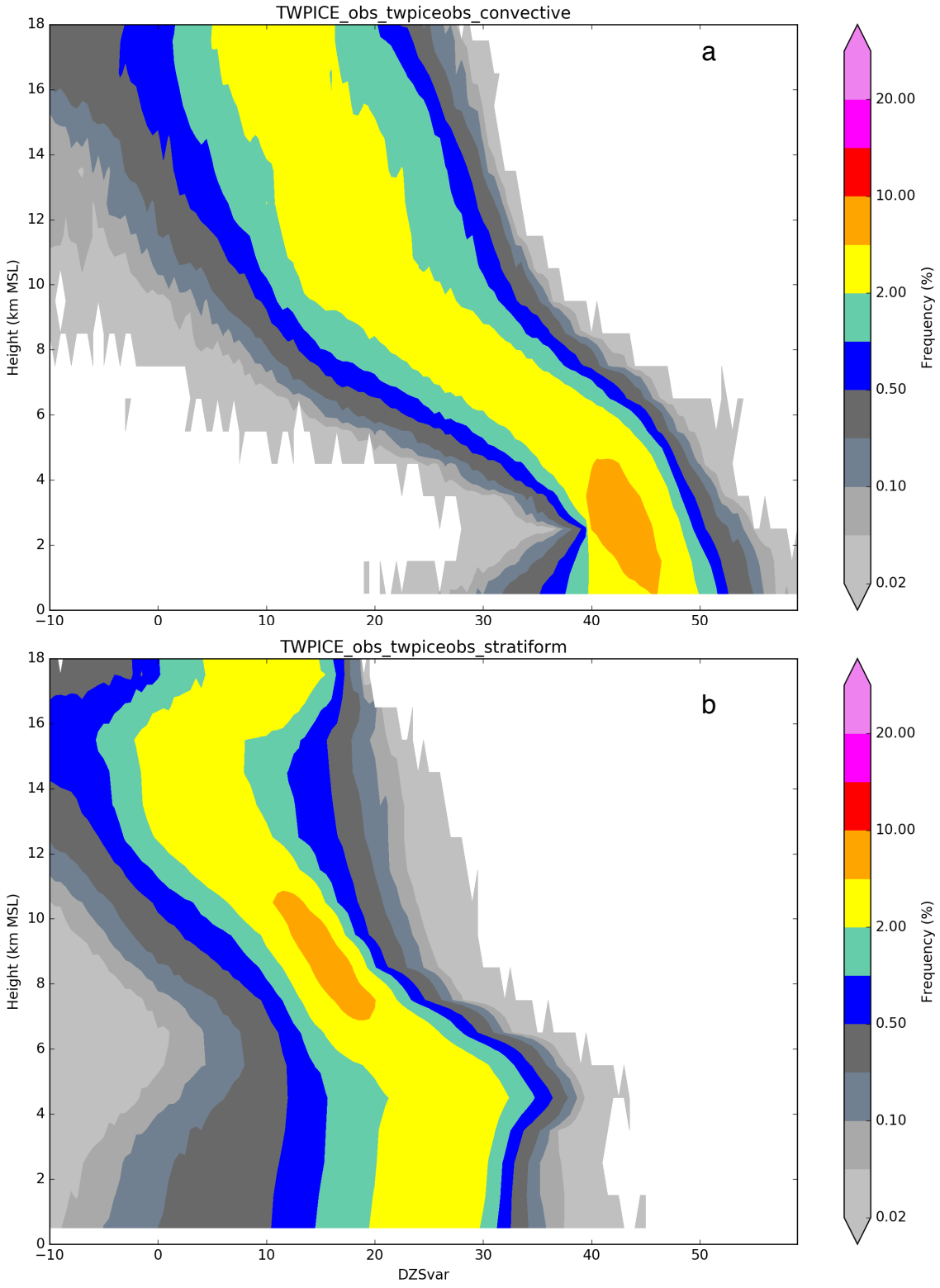

Figure 4.32: Reflectivity contours for TWP – ICE CPOL observations during the 22 Z hour for a) convective precipitation and b) stratiform precipitation.

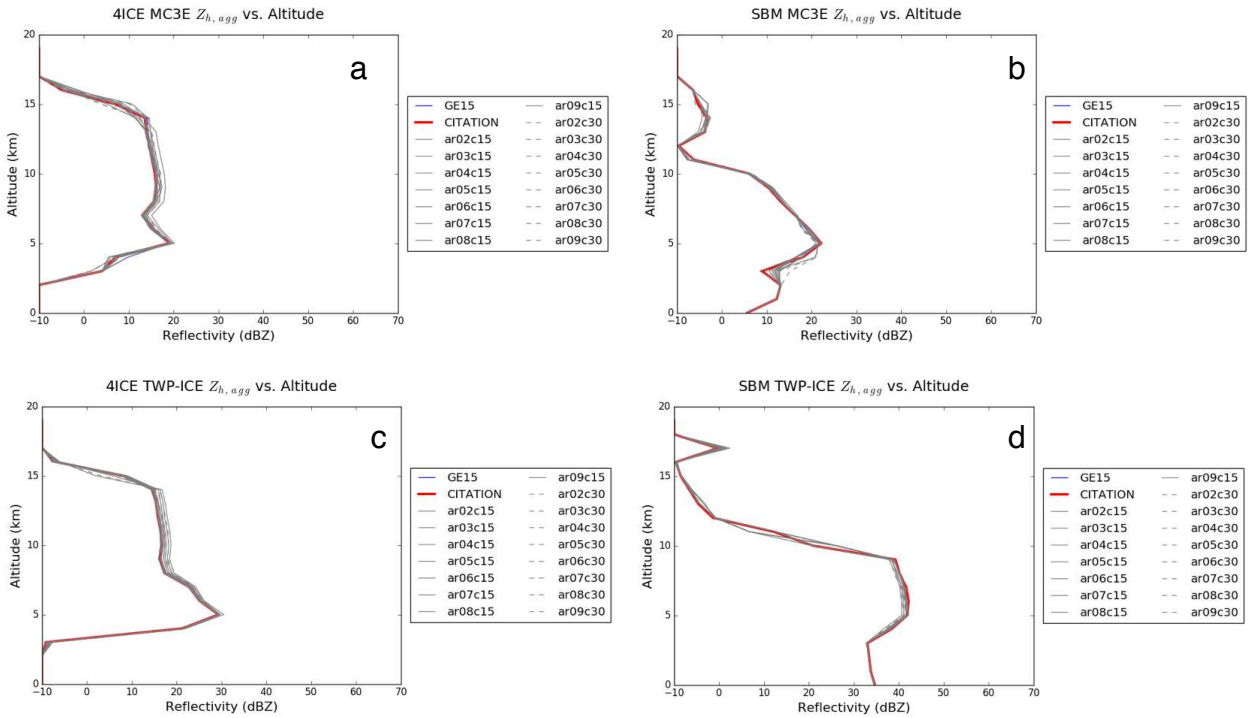

Figure 4.33: Mean of the most frequently occurring reflectivity as a function of altitude for assumed sets of aggregate axis ratio and canting angle assumptions for a) 4ICE MC3E, b) SBM MC3E, c) 4ICE TWPICE, and d) SBM TWPICE.

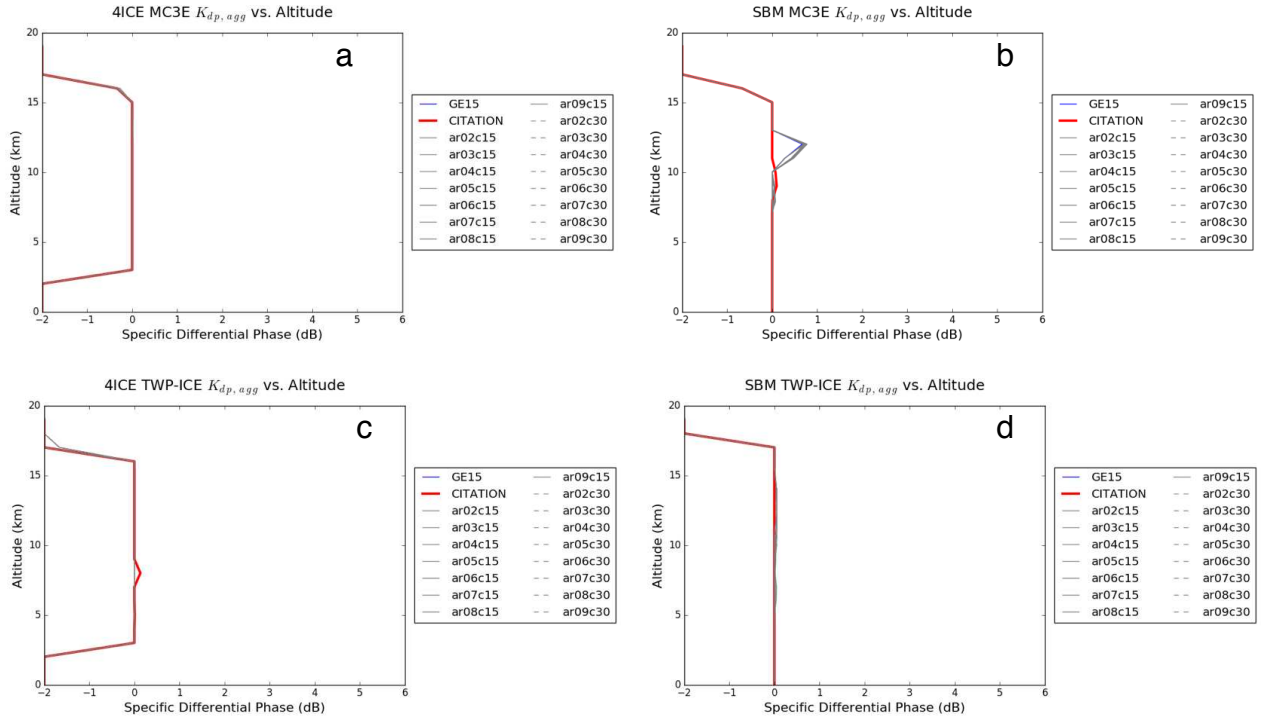

Figure 4.34: Mean of the most frequently occurring specific differential phase as a function of altitude for assumed sets of aggregate axis ratio and canting angle assumptions for a) 4ICE MC3E, b) SBM MC3E, c) 4ICE TWPICE, and d) SBM TWPICE.

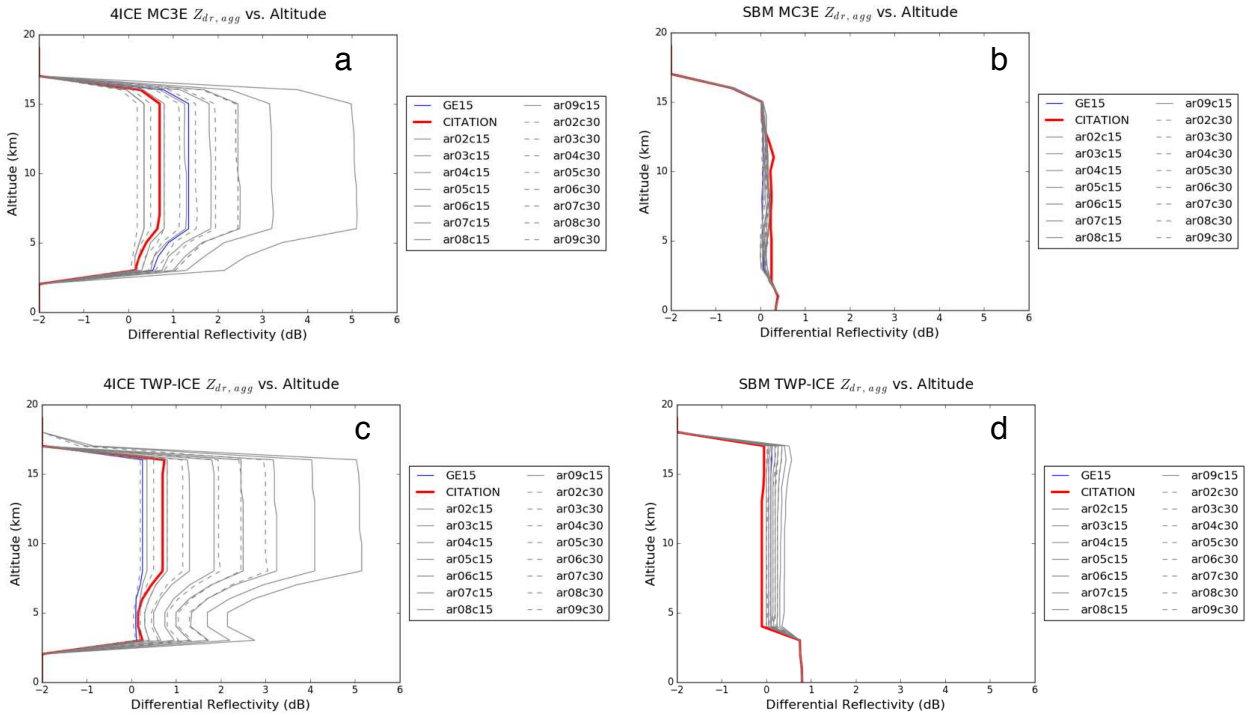

Figure 4.35: Mean of the most frequently occurring differential reflectivity as a function of altitude for assumed sets of aggregate axis ratio and canting angle assumptions for a) 4ICE MC3E, b) SBM MC3E, c) 4ICE TWPICE, and d) SBM TWPICE.

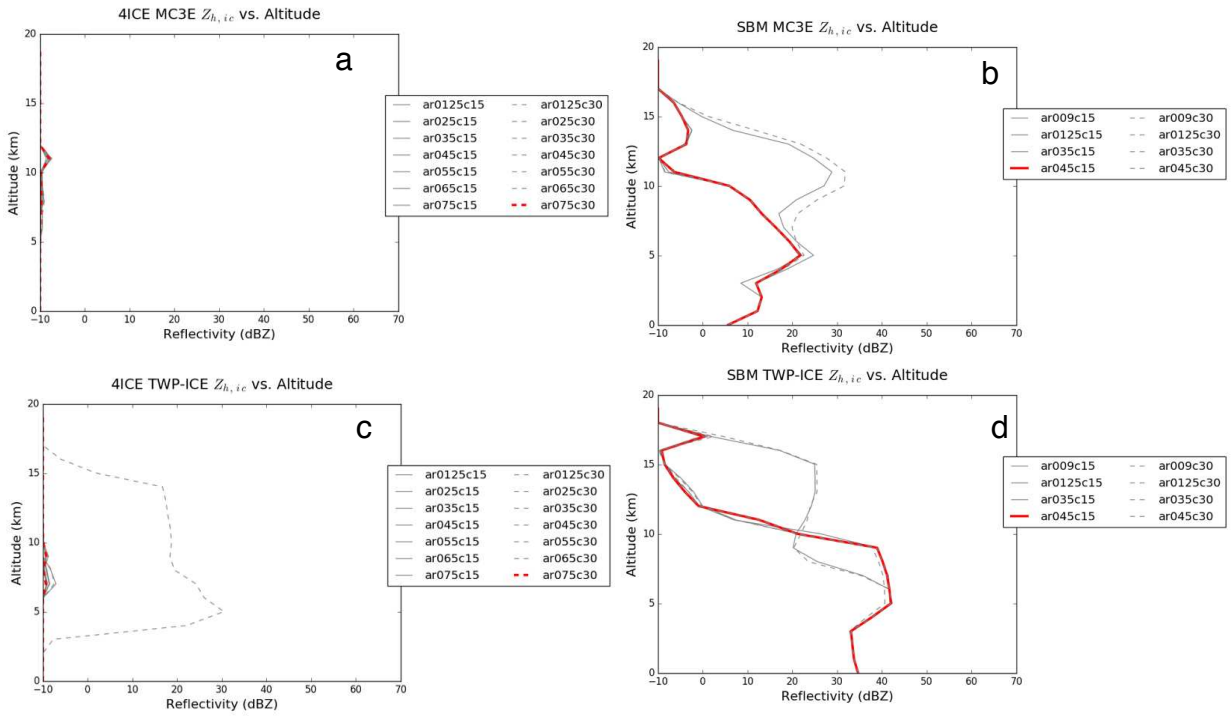

Figure 4.36: Mean of the most frequently occurring reflectivity as a function of altitude for assumed sets of ice crystal axis ratio and canting angle assumptions for a) 4ICE MC3E, b) SBM MC3E, c) 4ICE TWPICE, and d) SBM TWPICE.

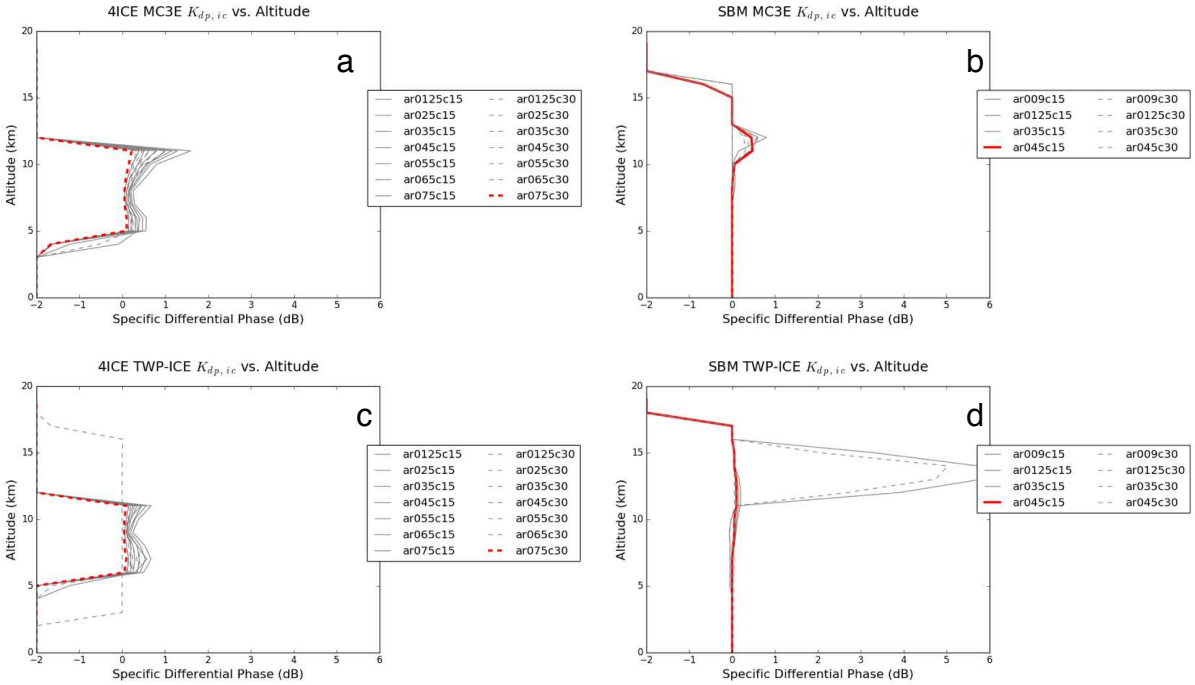

Figure 4.37: Mean of the most frequently occurring specific differential phase as a function of altitude for assumed sets of ice crystal axis ratio and canting angle assumptions for a) 4ICE MC3E, b) SBM MC3E, c) 4ICE TWPICE, and d) SBM TWPICE.

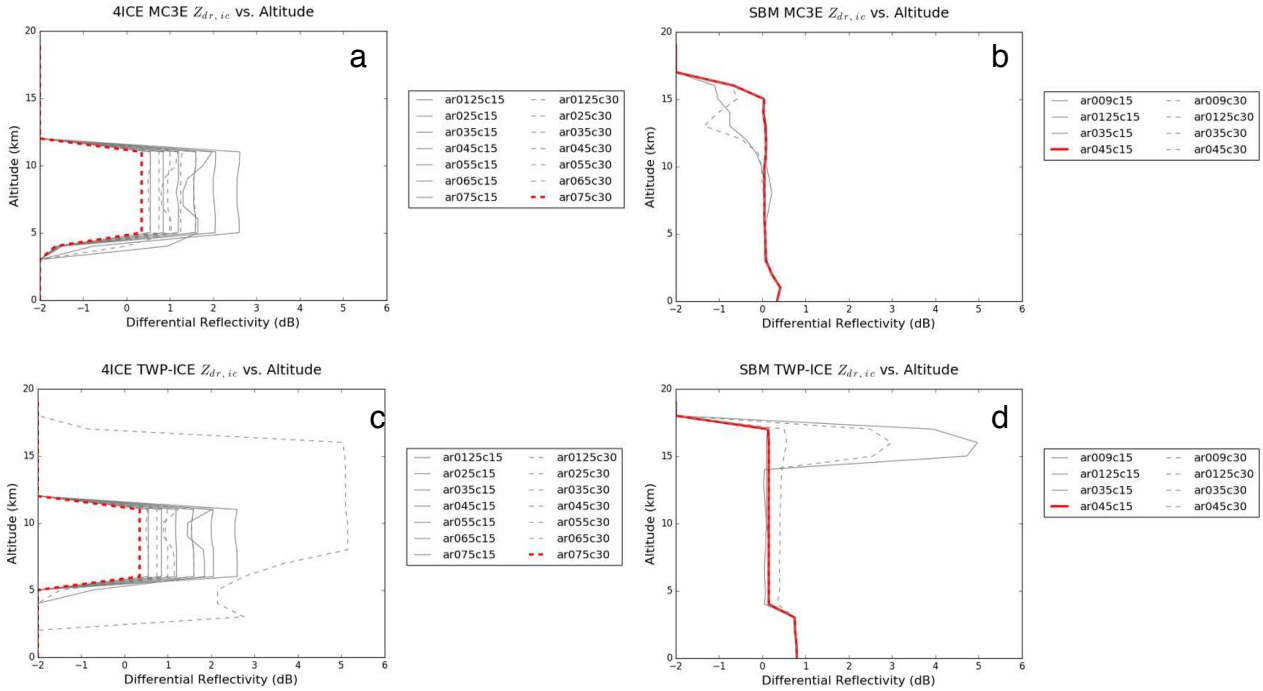

Figure 4.38: Mean of the most frequently occurring differential reflectivity as a function of altitude for assumed sets of ice crystal axis ratio and canting angle assumptions for a) 4ICE MC3E, b) SBM MC3E, c) 4ICE TWPICE, and d) SBM TWPICE.

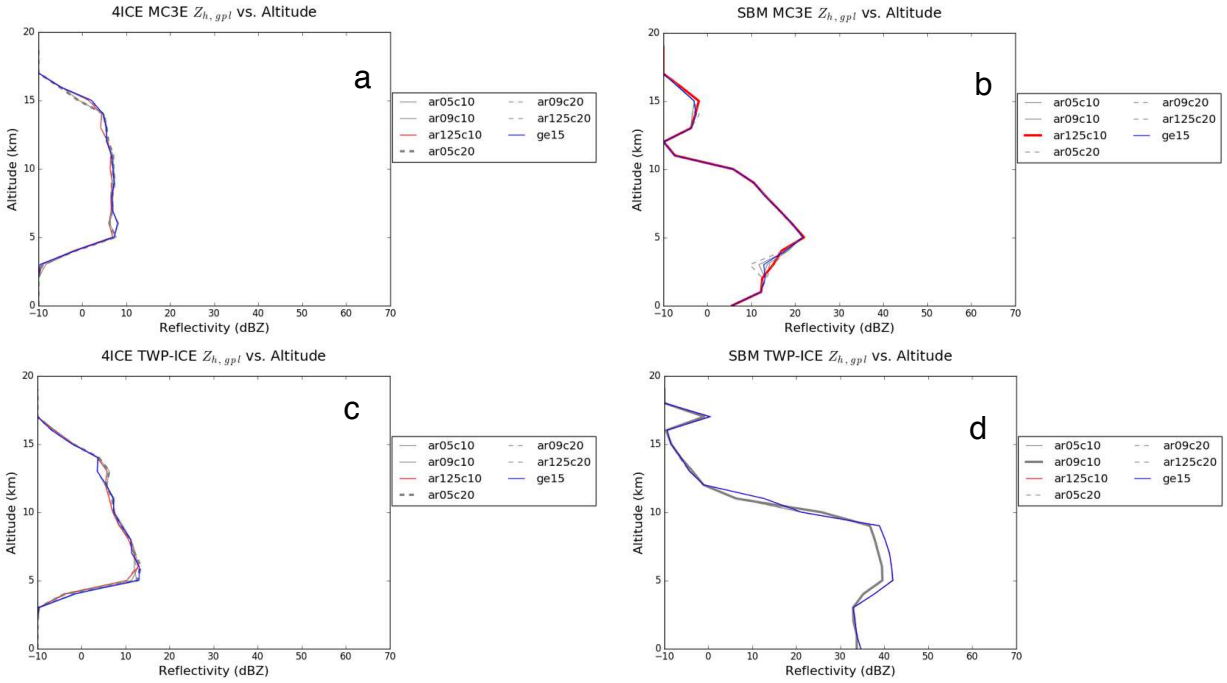

Figure 4.39: Mean of the most frequently occurring reflectivity as a function of altitude for assumed sets of graupel axis ratio and canting angle assumptions for a) 4ICE MC3E, b) SBM MC3E, c) 4ICE TWPICE, and d) SBM TWPICE.

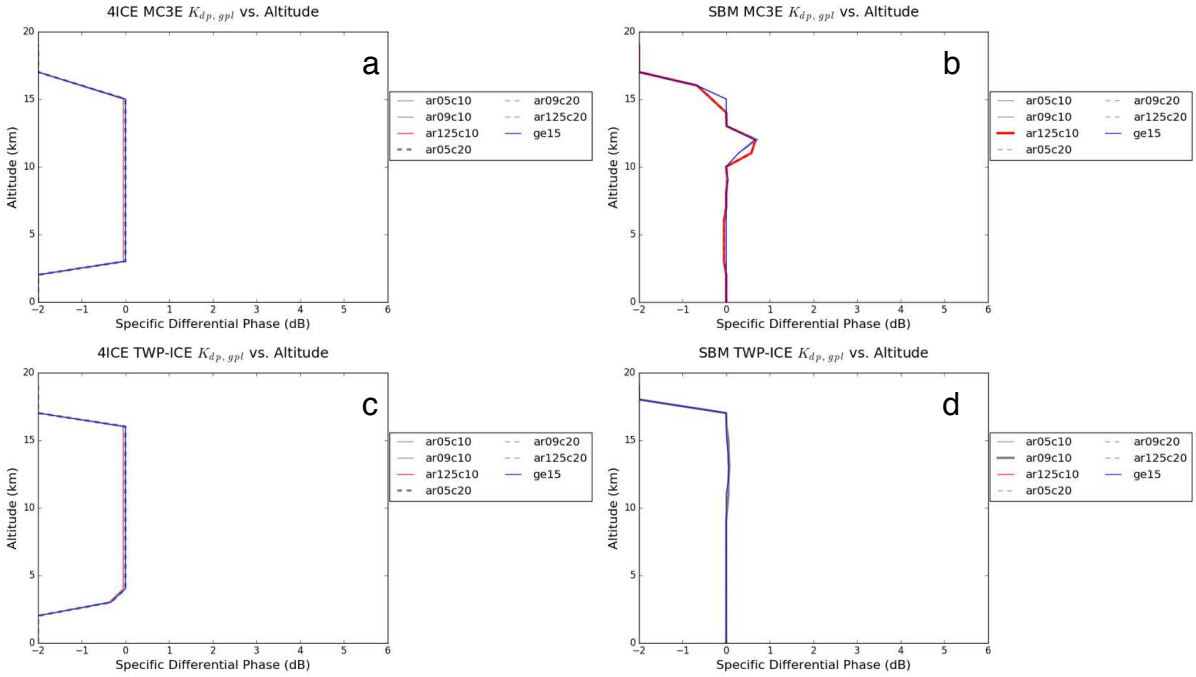

Figure 4.40: Mean of the most frequently occurring specific differential reflectivity as a function of altitude for assumed sets of graupel axis ratio and canting angle assumptions for a) 4ICE MC3E, b) SBM MC3E, c) 4ICE TWPICE, and d) SBM TWPICE.

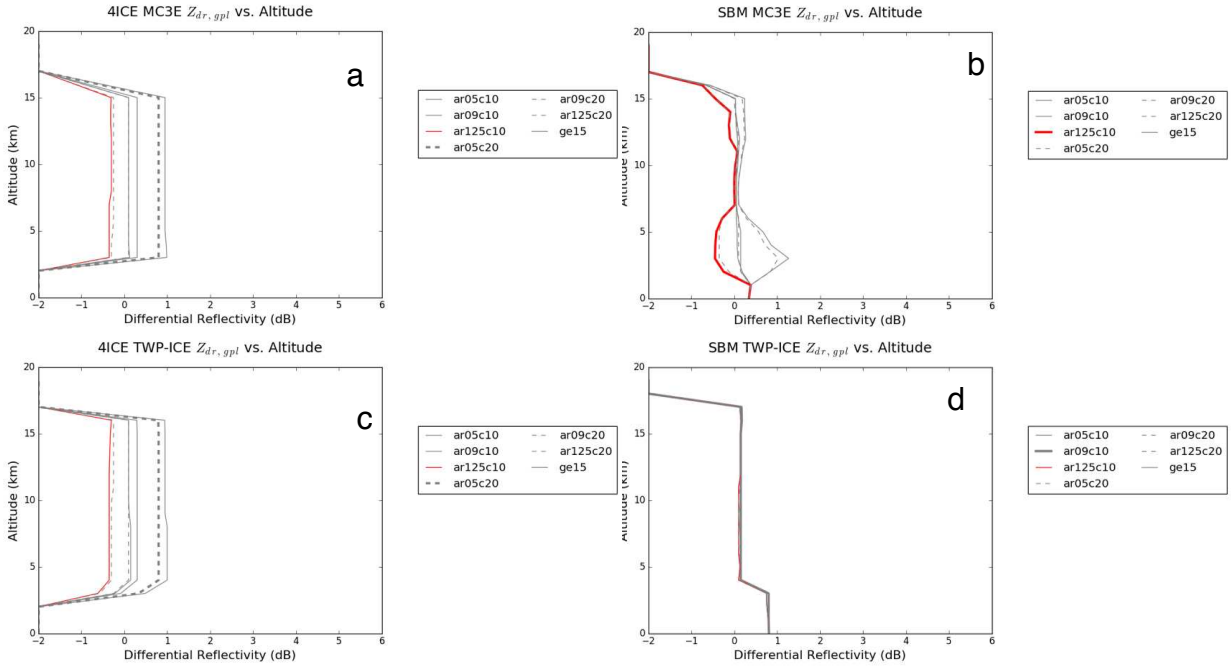

Figure 4.41: Mean of the most frequently occurring differential reflectivity as a function of altitude for assumed sets of graupel axis ratio and canting angle assumptions for a) 4ICE MC3E, b) SBM MC3E, c) 4ICE TWPICE, and d) SBM TWPICE.

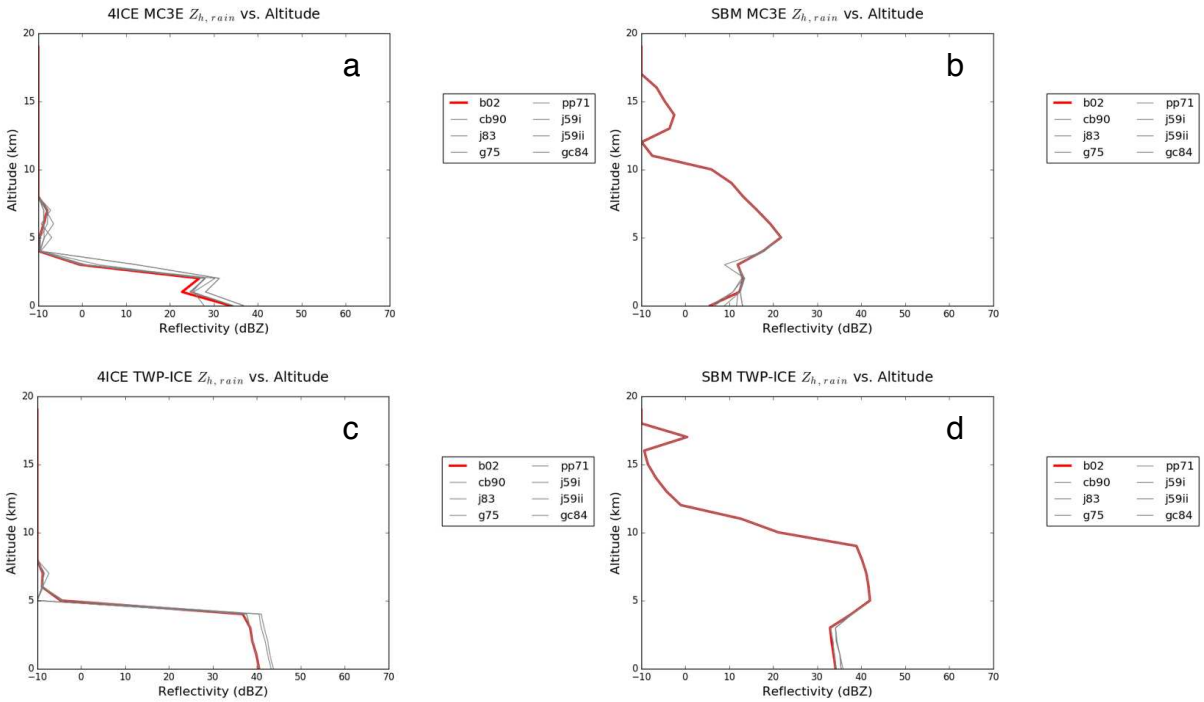

Figure 4.42: Mean of the most frequently occurring reflectivity as a function of altitude for assumed sets of rain axis ratio and canting angle assumptions for a) 4ICE MC3E, b) SBM MC3E, c) 4ICE TWPICE, and d) SBM TWPICE.

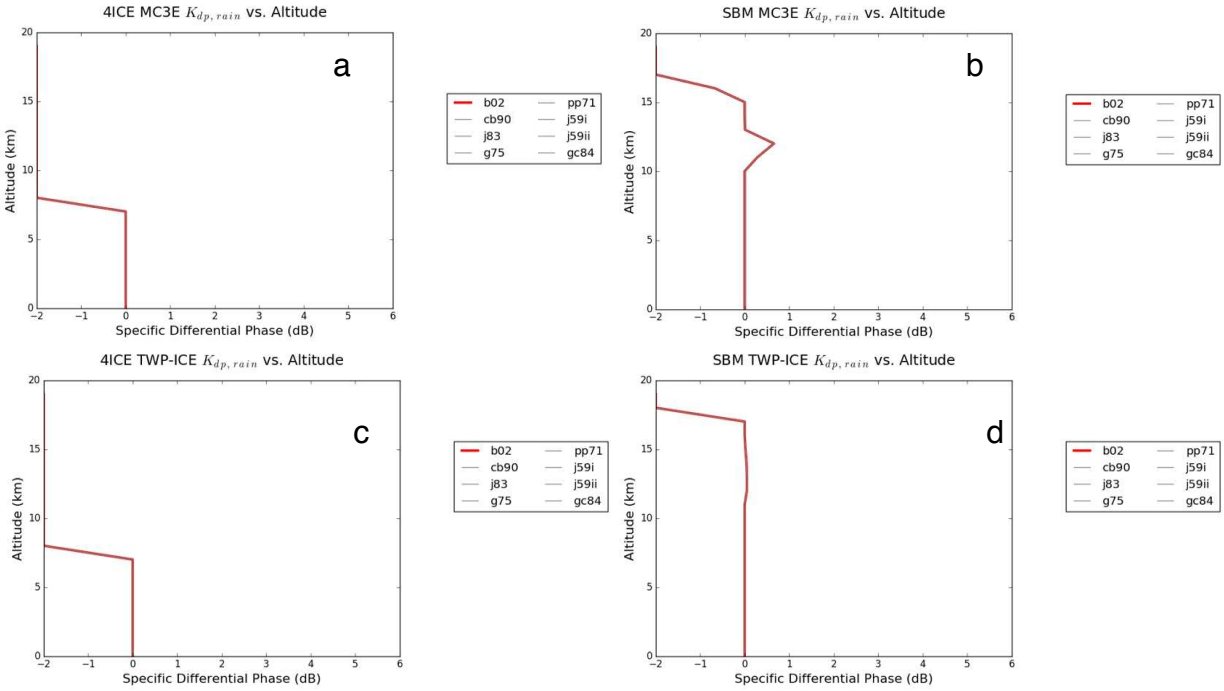

Figure 4.43: Mean of the most frequently occurring specific differential phase as a function of altitude for assumed sets of rain axis ratio and canting angle assumptions for a) 4ICE MC3E, b) SBM MC3E, c) 4ICE TWPICE, and d) SBM TWPICE.

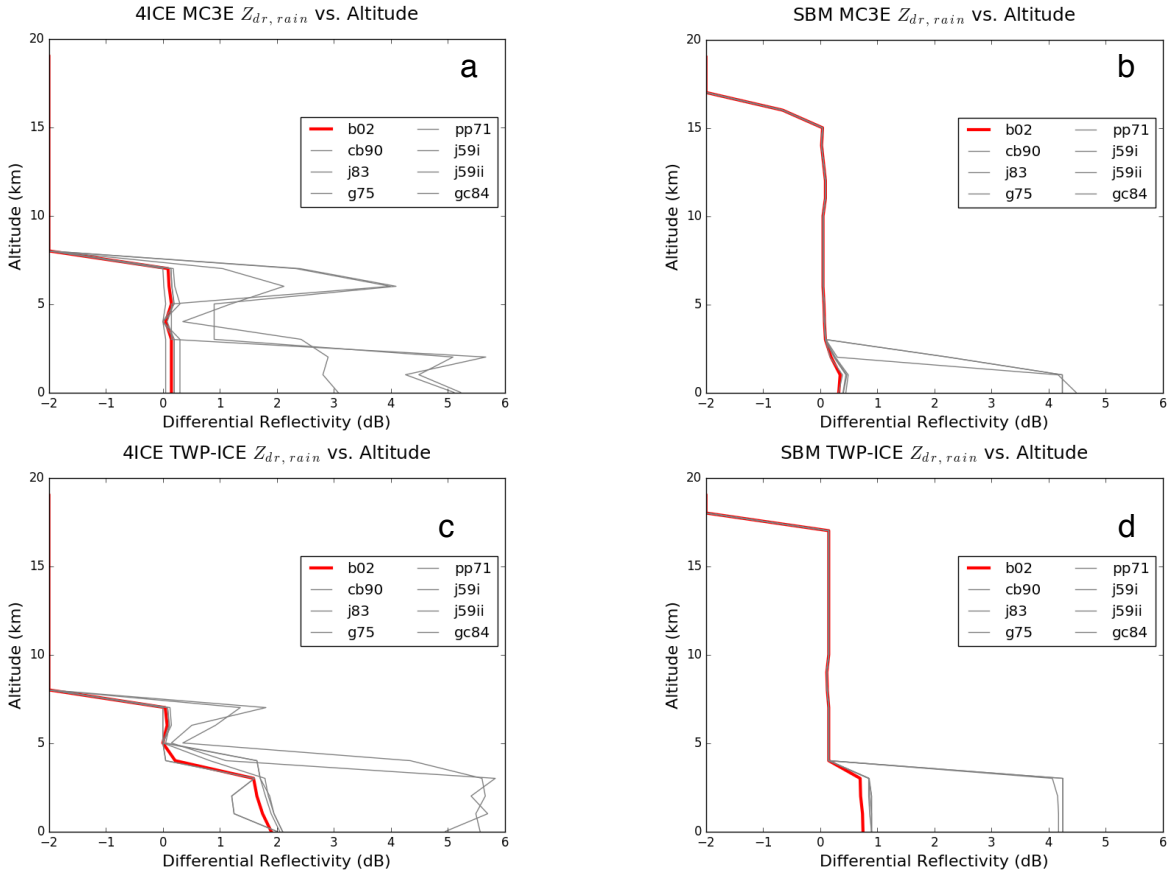

Figure 4.44: Mean of the most frequently occurring differential reflectivity as a function of altitude for assumed sets of rain axis ratio and canting angle assumptions for a) 4ICE MC3E, b) SBM MC3E, c) 4ICE TWPICE, and d) SBM TWPICE.

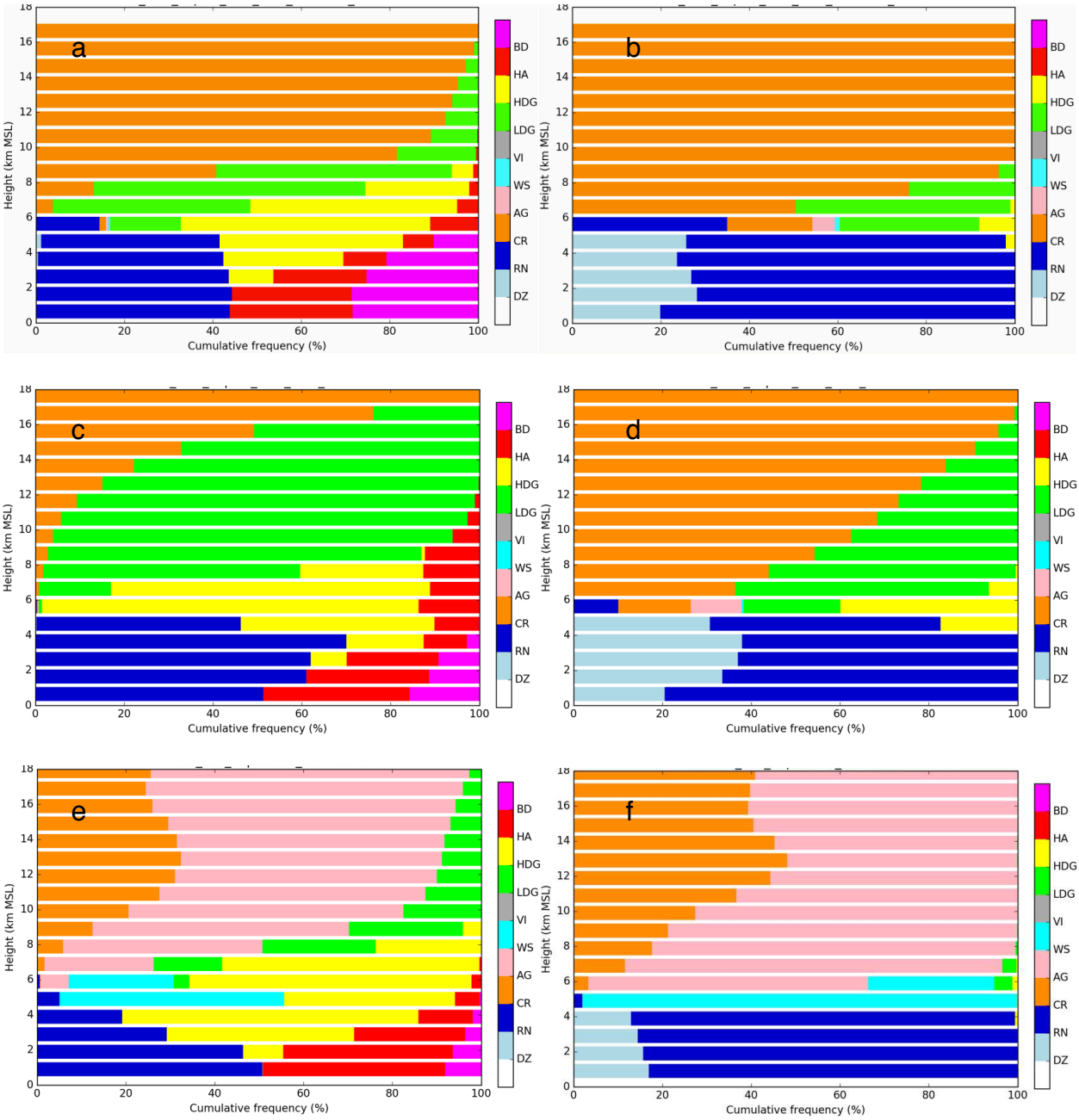

Figure 4.45: HID CFAD plots, with modified MBFs, from the “best” assumptions for (a,b) convective and stratiform TWP-ICE 4ICE, the “best” assumptions for (c,d) convective and stratiform TWP-ICE SBM, and then for (e,f) convective and stratiform TWP-ICE observations.

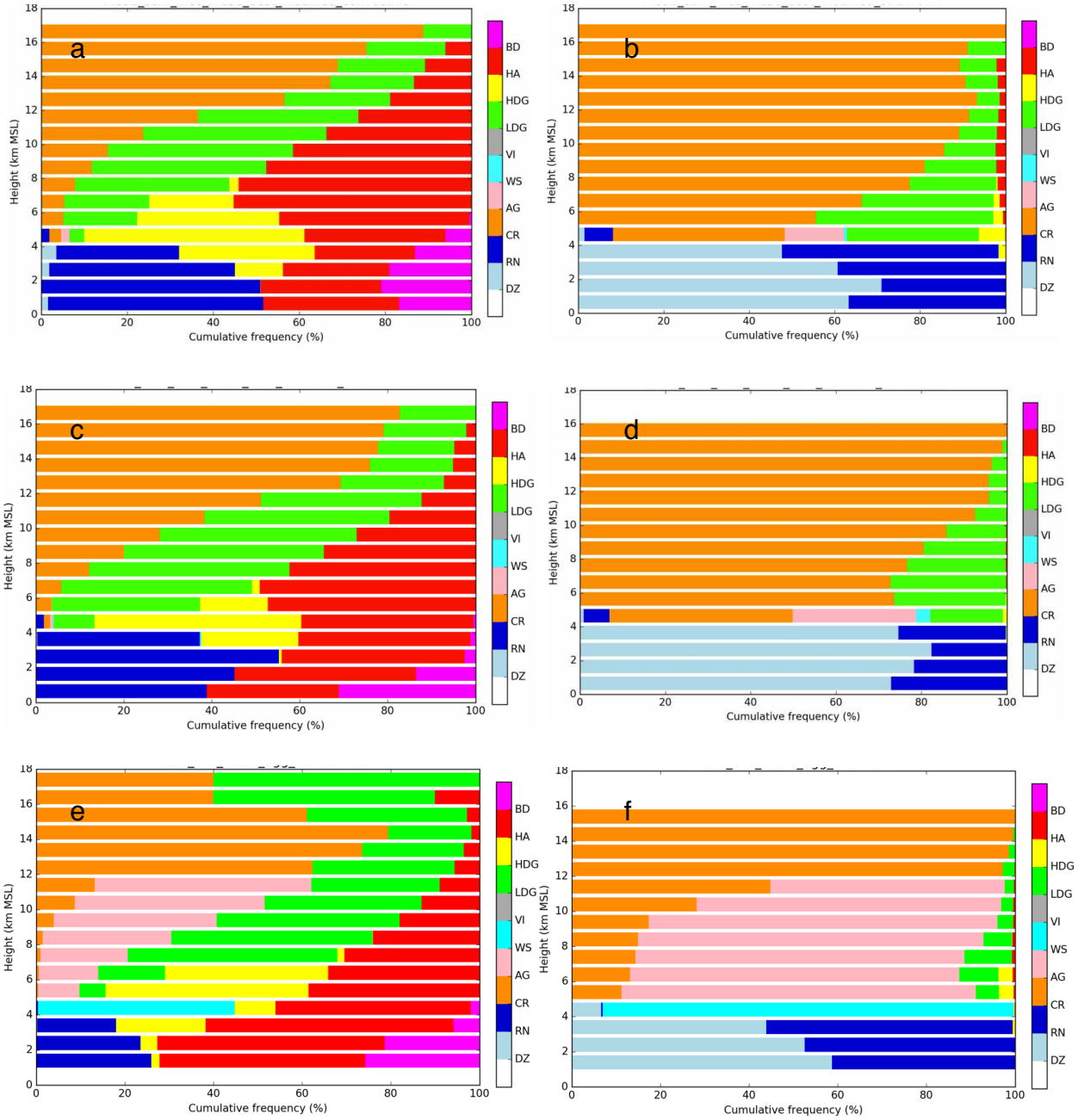

Figure 4.46: HID CFAD plots, with modified MBFs, from the “best” assumptions for (a,b) convective and stratiform MC3E 4ICE, the “best” assumptions for (c,d) convective and stratiform MC3E SBM, and then for (e,f) convective and stratiform MC3E observations.

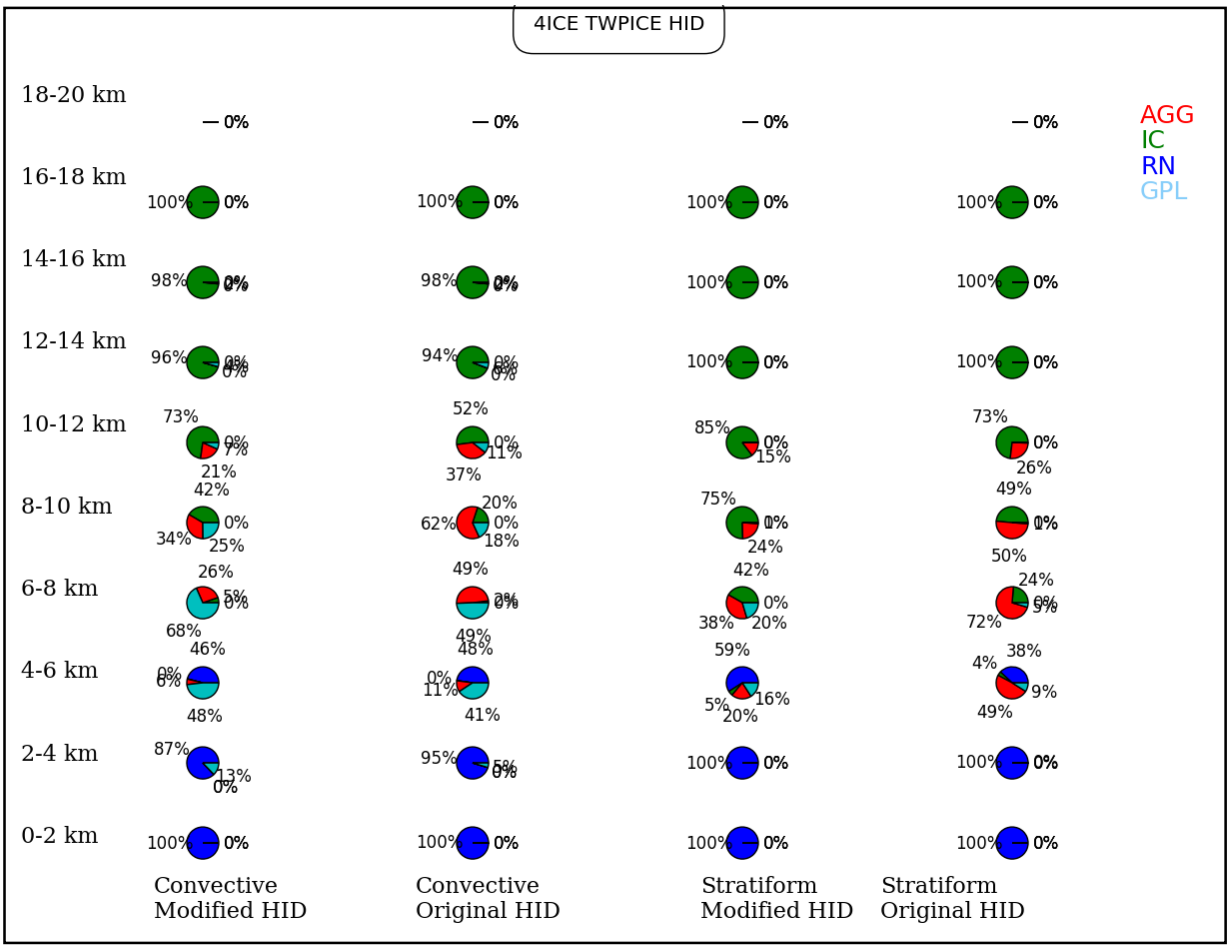

Figure 4.47: HID pie chart plots for 4ICE TWP-ICE HID, showing convective HID in the left two plots, for modified and original MBFs, and stratiform HID in the right two plots, for modified and original MBFs. As is indicated in the legend, blue represents rain, light blue represents graupel, red represents aggregates, and green represents ice crystals.

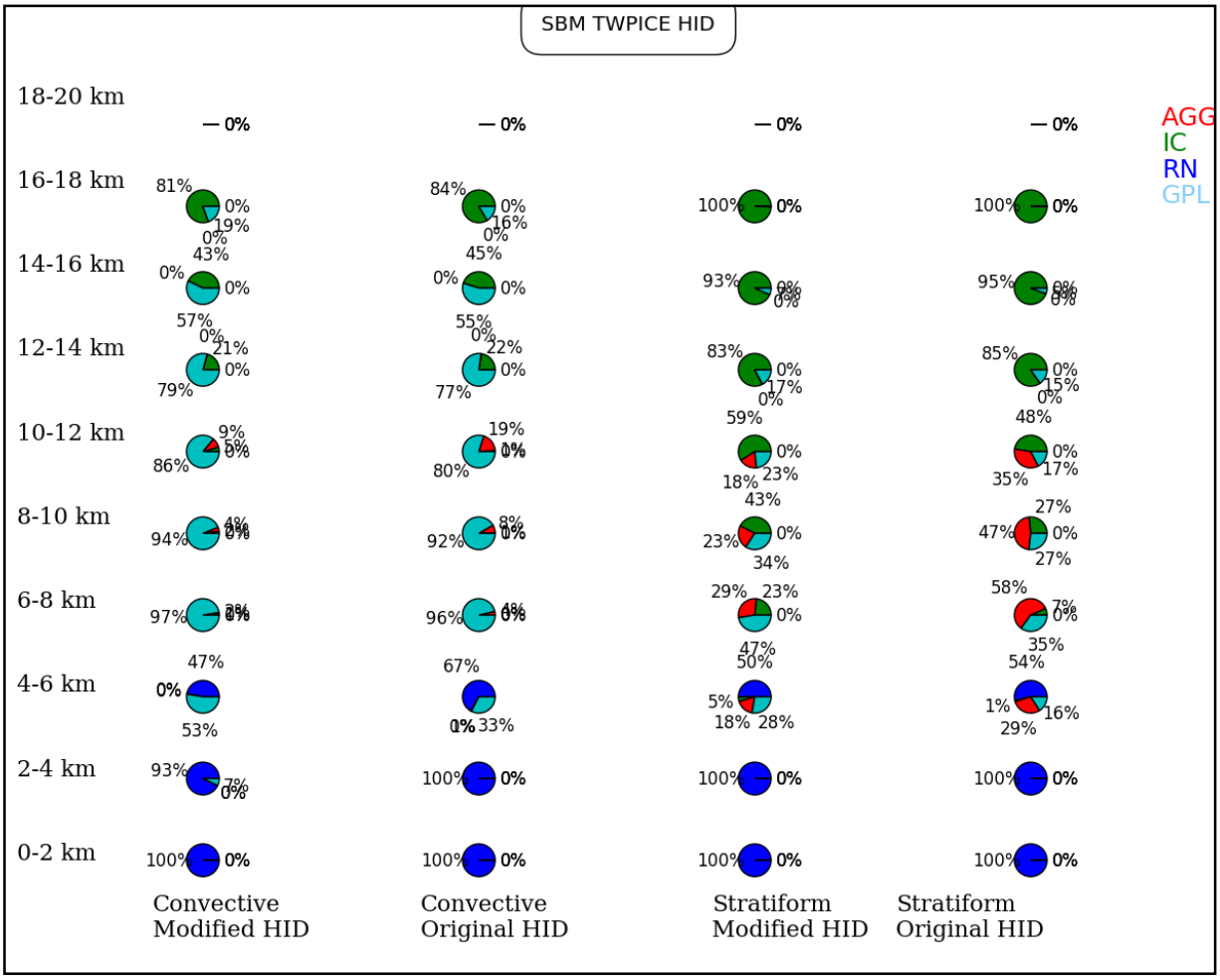

Figure 4.48: HID pie chart plots for SBM TWP-ICE HID, showing convective HID in the left two plots, for modified and original MBFs, and stratiform HID in the right two plots, for modified and original MBFs. As is indicated in the legend, blue represents rain, light blue represents graupel, red represents aggregates, and green represents ice crystals.

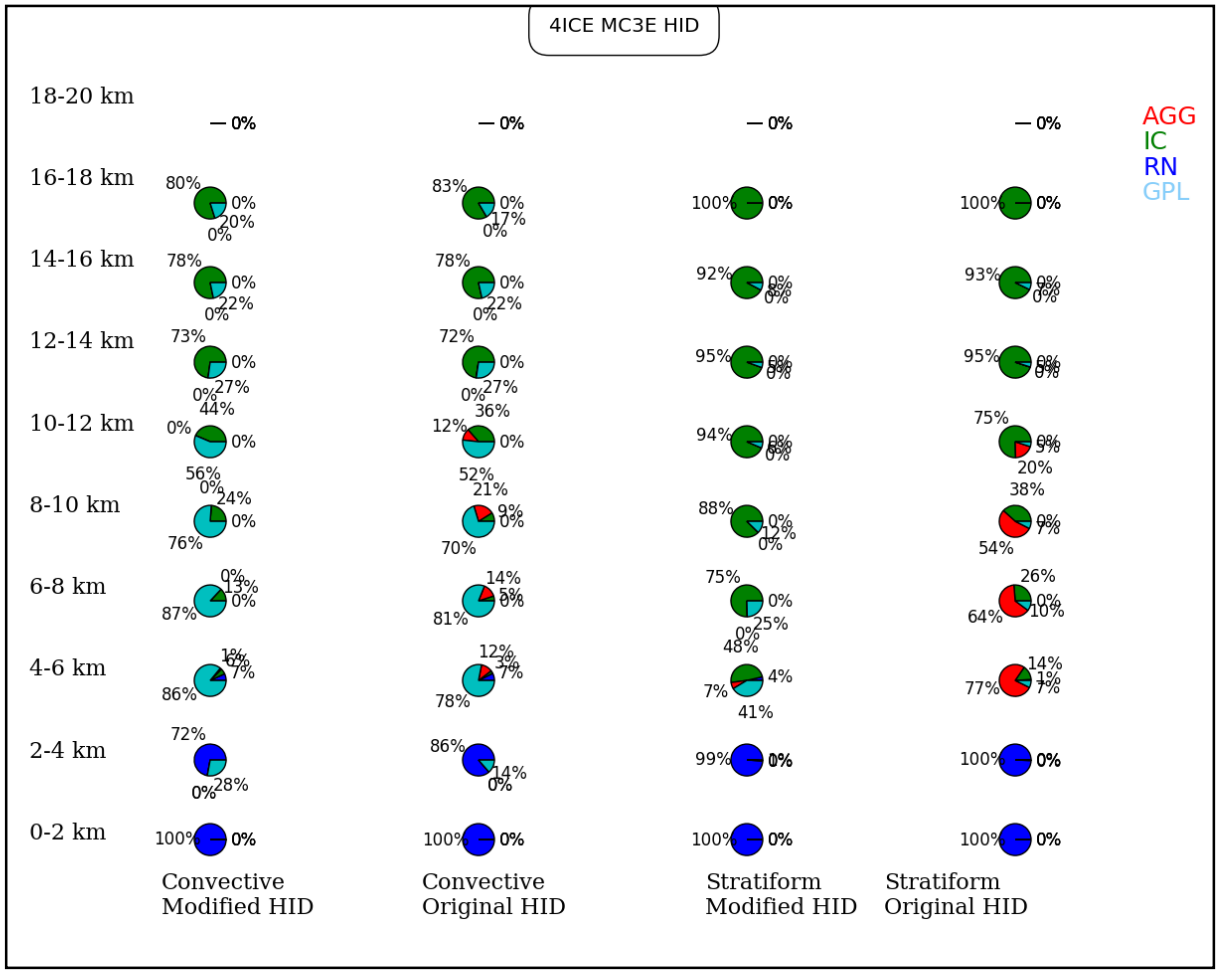

Figure 4.49: HID pie chart plots for 4ICE MC3E HID, showing convective HID in the left two plots, for modified and original MBFs, and stratiform HID in the right two plots, for modified and original MBFs. As is indicated in the legend, blue represents rain, light blue represents graupel, red represents aggregates, and green represents ice crystals.

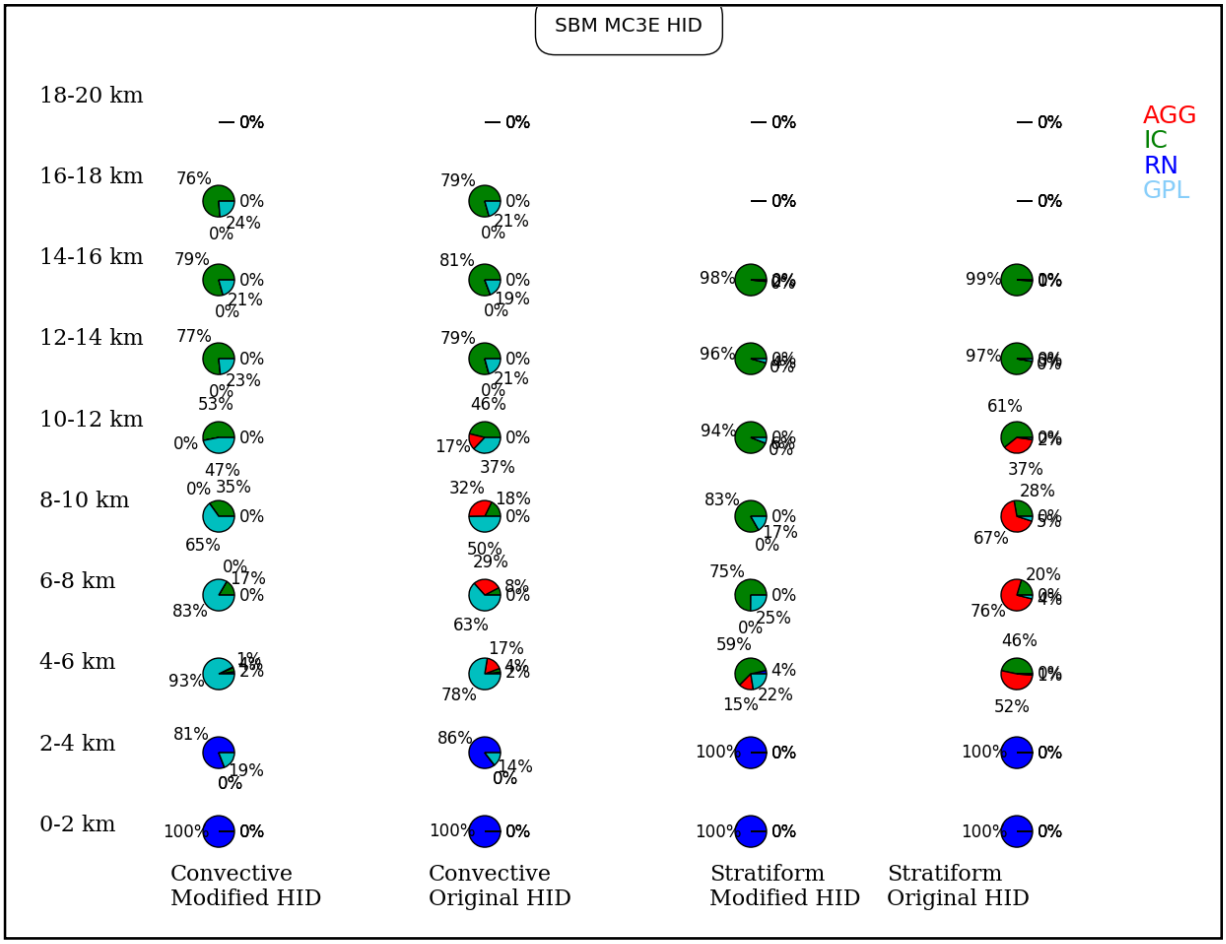

Figure 4.50: HID pie chart plots for SBM MC3E HID, showing convective HID in the left two plots, for modified and original MBFs, and stratiform HID in the right two plots, for modified and original MBFs. As is indicated in the legend, blue represents rain, light blue represents graupel, red represents aggregates, and green represents ice crystals.

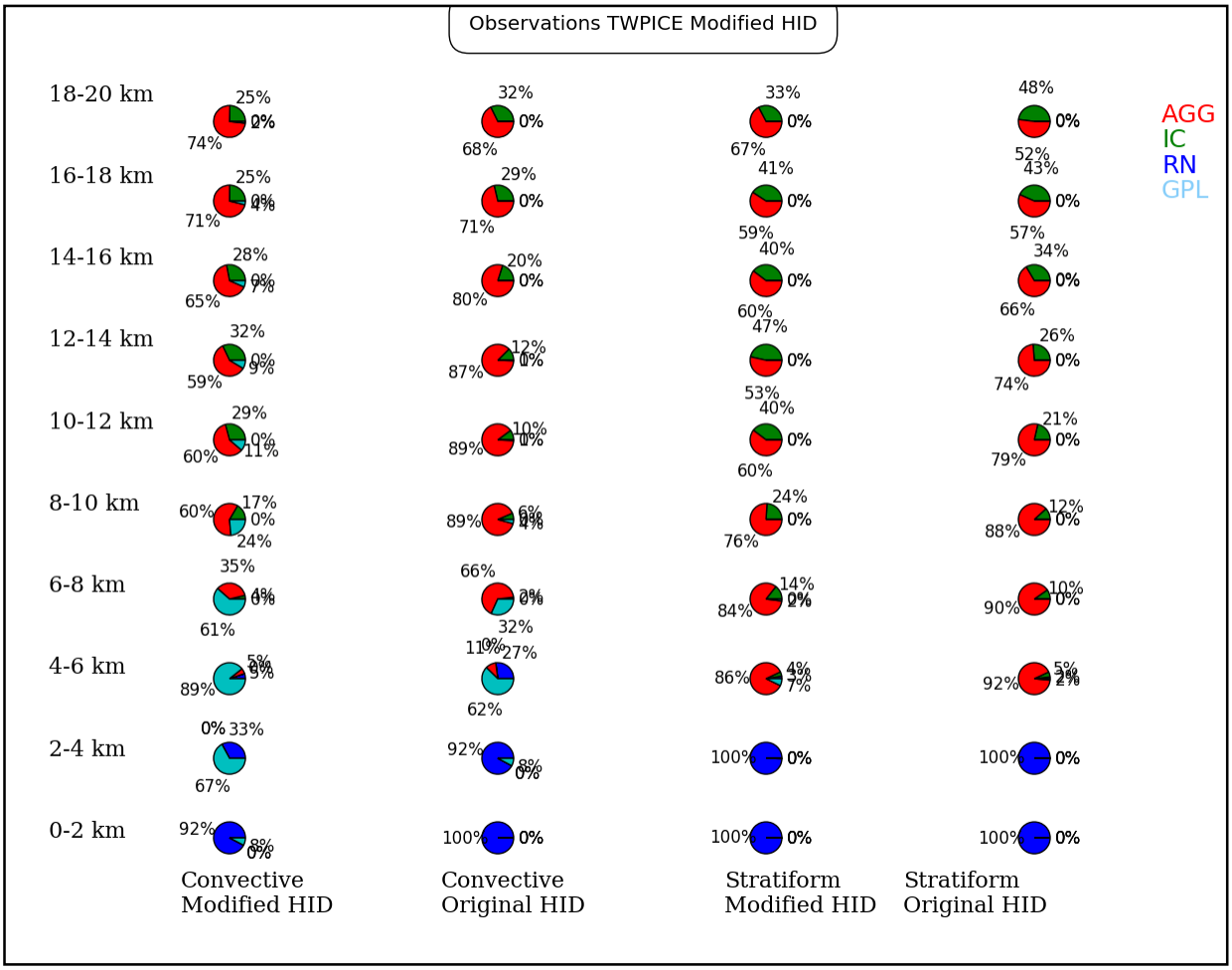

Figure 4.51: HID pie chart plots for TWP-ICE observations HID, showing convective HID in the left two plots, for modified and original MBFs, and stratiform HID in the right two plots, for modified and original MBFs. As is indicated in the legend, blue represents rain, light blue represents graupel, red represents aggregates, and green represents ice crystals.

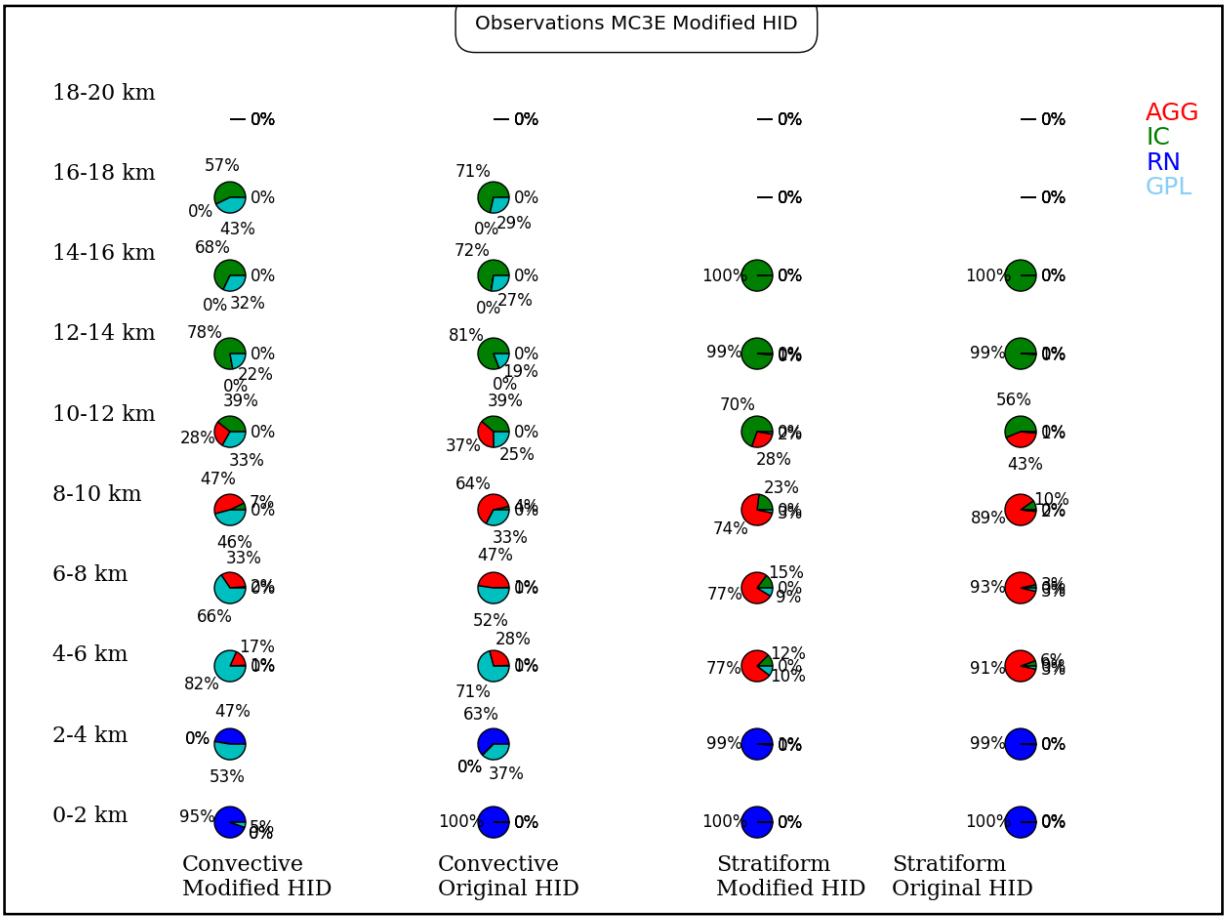

Figure 4.52: HID pie chart plots for MC3E observations HID, showing convective HID in the left two plots, for modified and original MBFs, and stratiform HID in the right two plots, for modified and original MBFs. As is indicated in the legend, blue represents rain, light blue represents graupel, red represents aggregates, and green represents ice crystals.

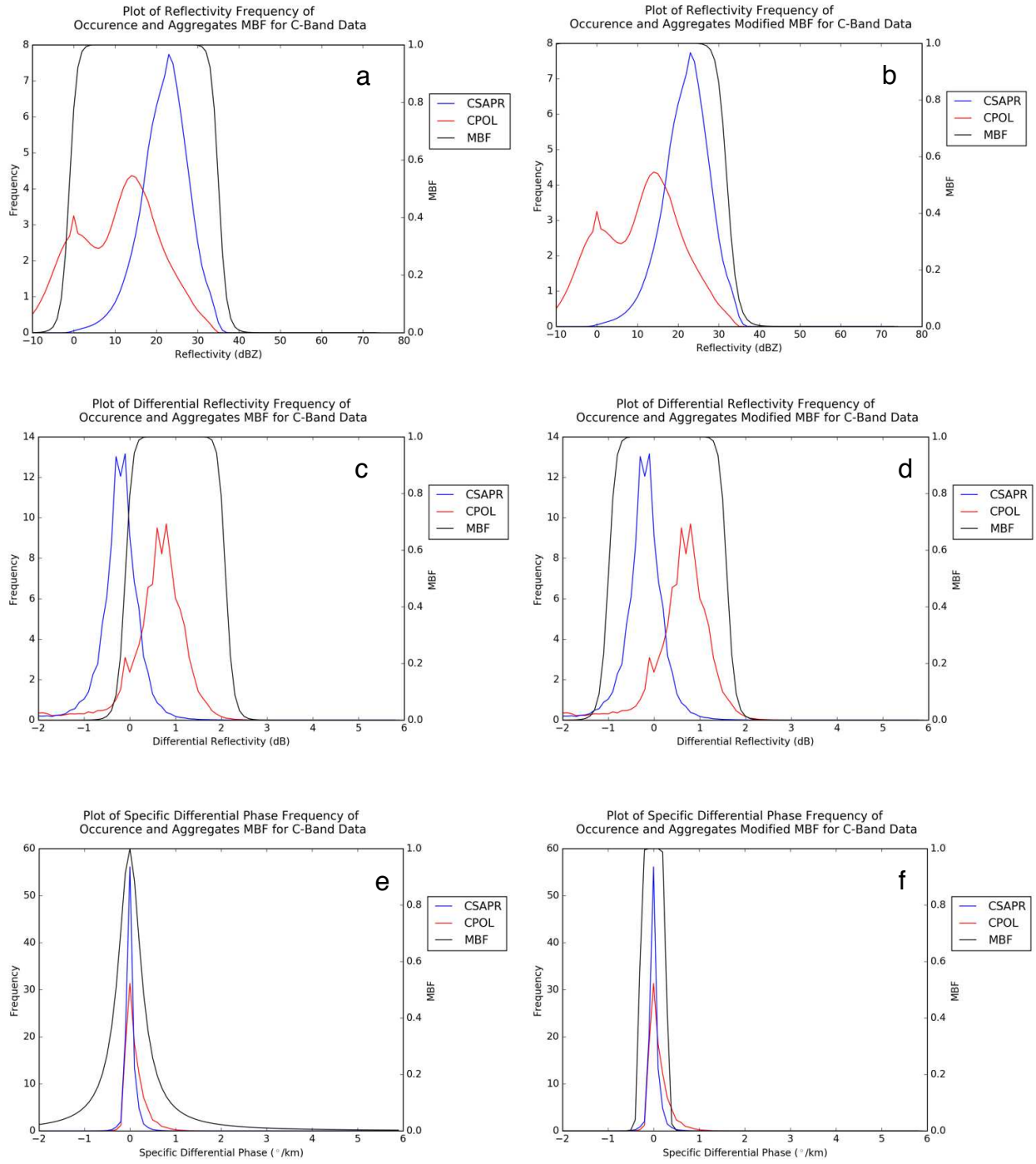

Figure 4.53: Plots of aggregate MBFs (black) for the original (left) framework and the modified (right), with frequency of occurrence for CPOL (red) and CSAPR (blue) HID-identified aggregates for (a,b) reflectivity, (c,d) differential reflectivity, and (e,f) specific differential phase.

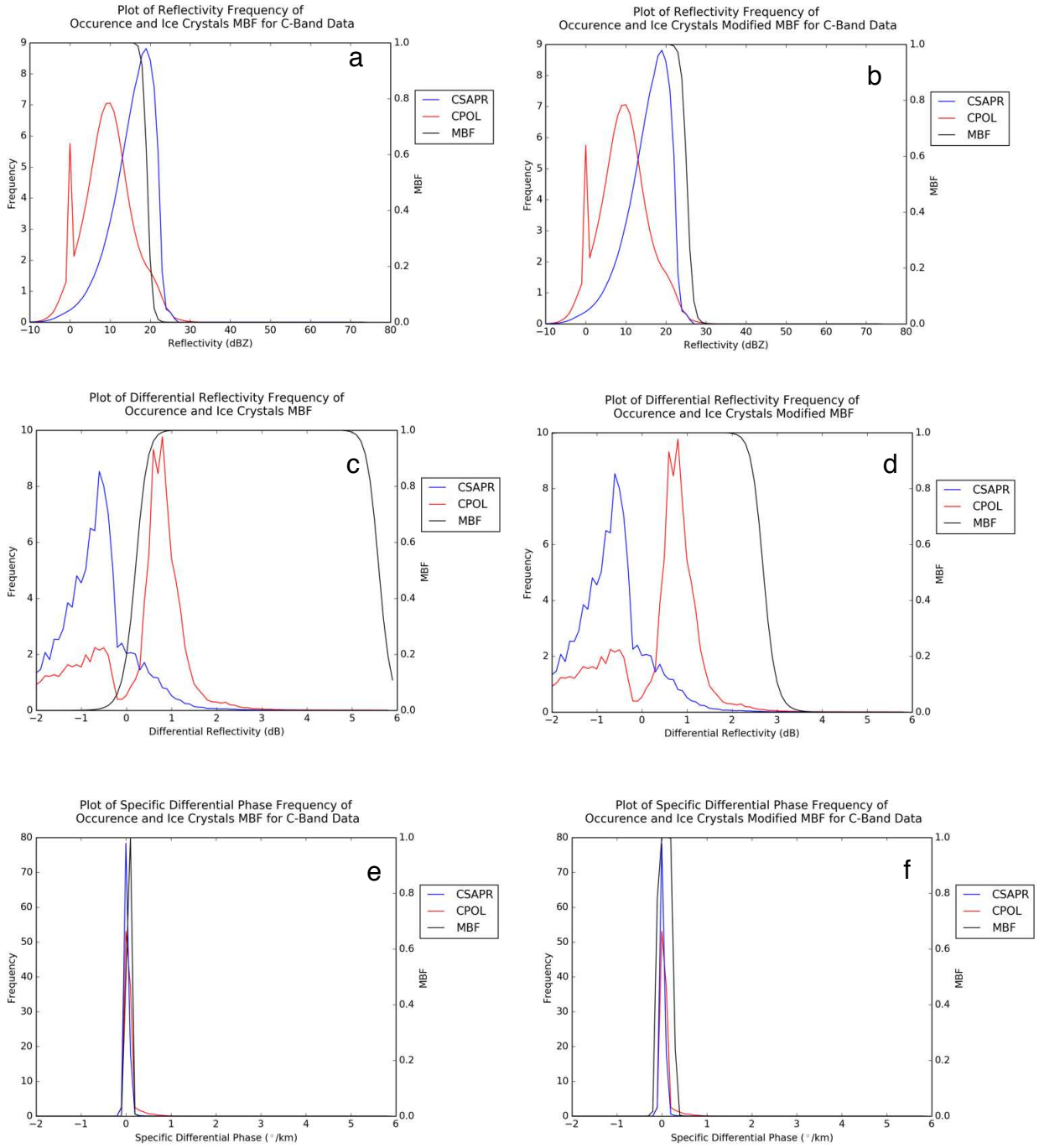

Figure 4.54: Plots of ice crystal MBFs (black) for the original (left) framework and the modified (right), with frequency of occurrence for CPOL (red) and CSAPR (blue) HID-identified ice crystals for (a,b) reflectivity, (c,d) differential reflectivity, and (e,f) specific differential phase.

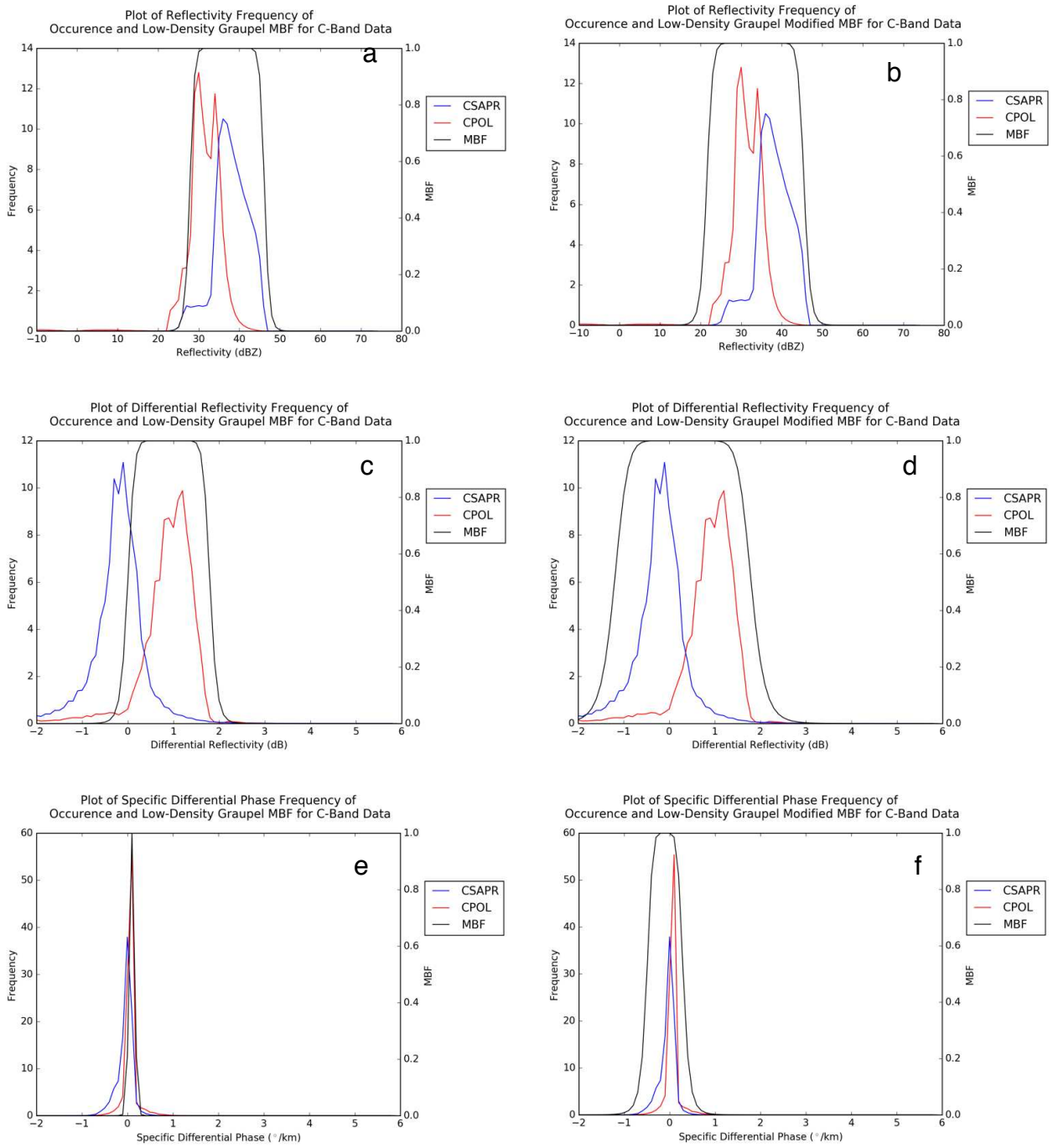

Figure 4.55: Plots of low-density graupel MBFs (black) for the original (left) framework and the modified (right), with frequency of occurrence for CPOL (red) and CSAPR (blue) HID-identified low-dentisty graupel for (a,b) reflectivity, (c,d) differential reflectivity, and (e,f) specific differential phase.

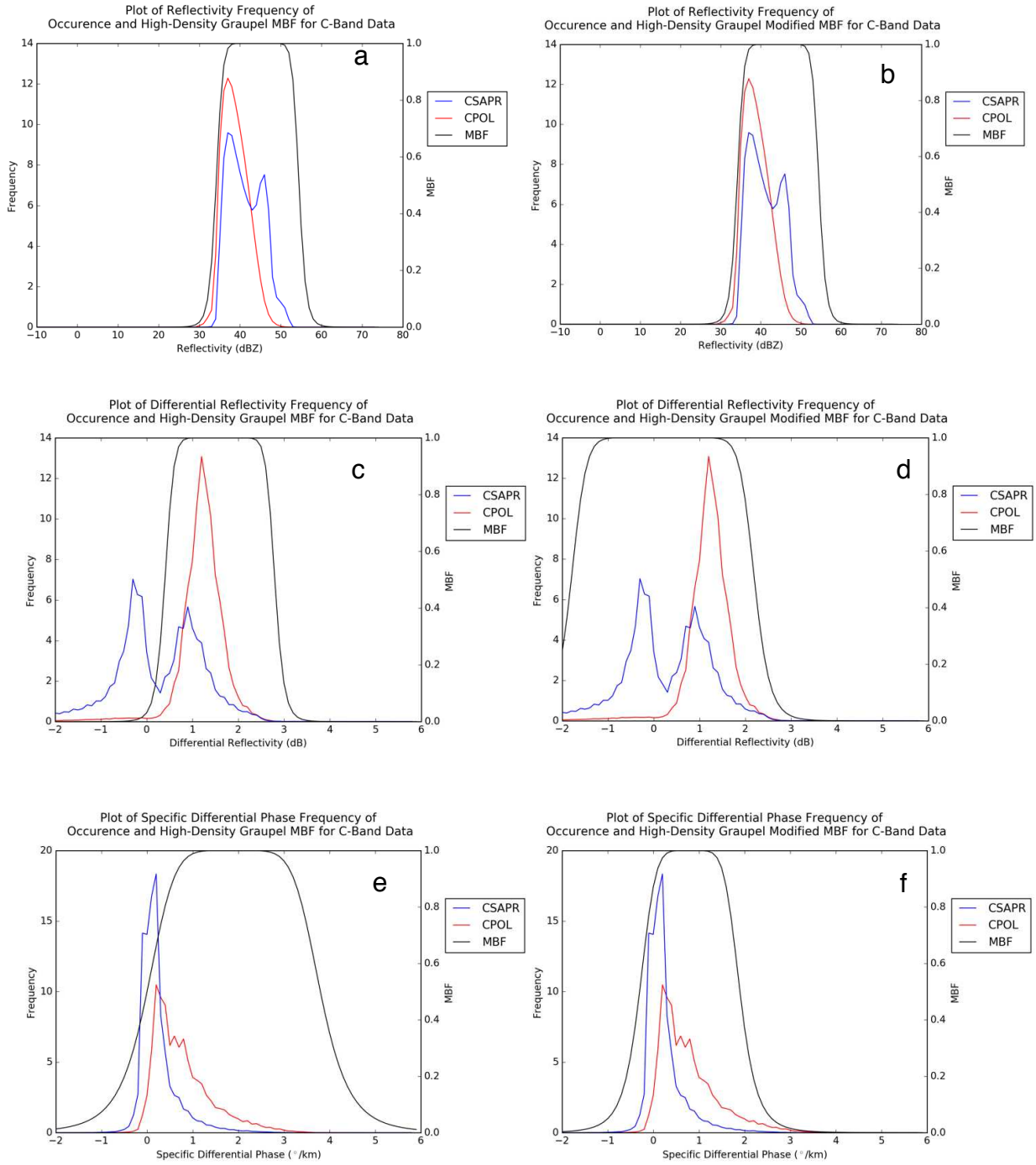

Figure 4.56: Plots of high-density graupel MBFs (black) for the original (left) framework and the modified (right), with frequency of occurrence for CPOL (red) and CSAPR (blue) HID-identified high-density graupel for (a,b) reflectivity, (c,d) differential reflectivity, and (e,f) specific differential phase.

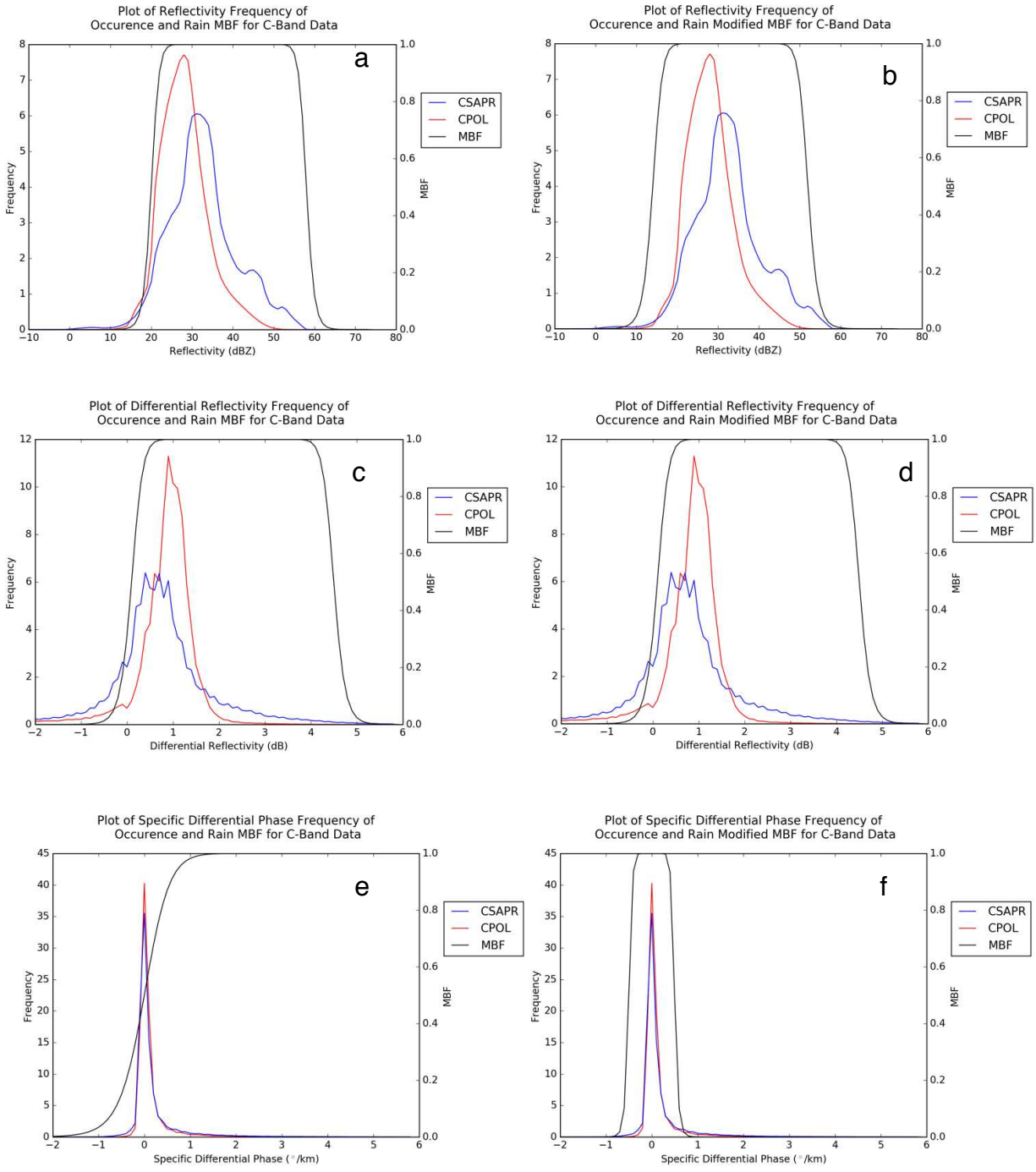

Figure 4.57: Plots of rain MBFs (black) for the original (left) framework and the modified (right), with frequency of occurrence for CPOL (red) and CSAPR (blue) HID-identified rain for (a,b) reflectivity, (c,d) differential reflectivity, and (e,f) specific differential phase.

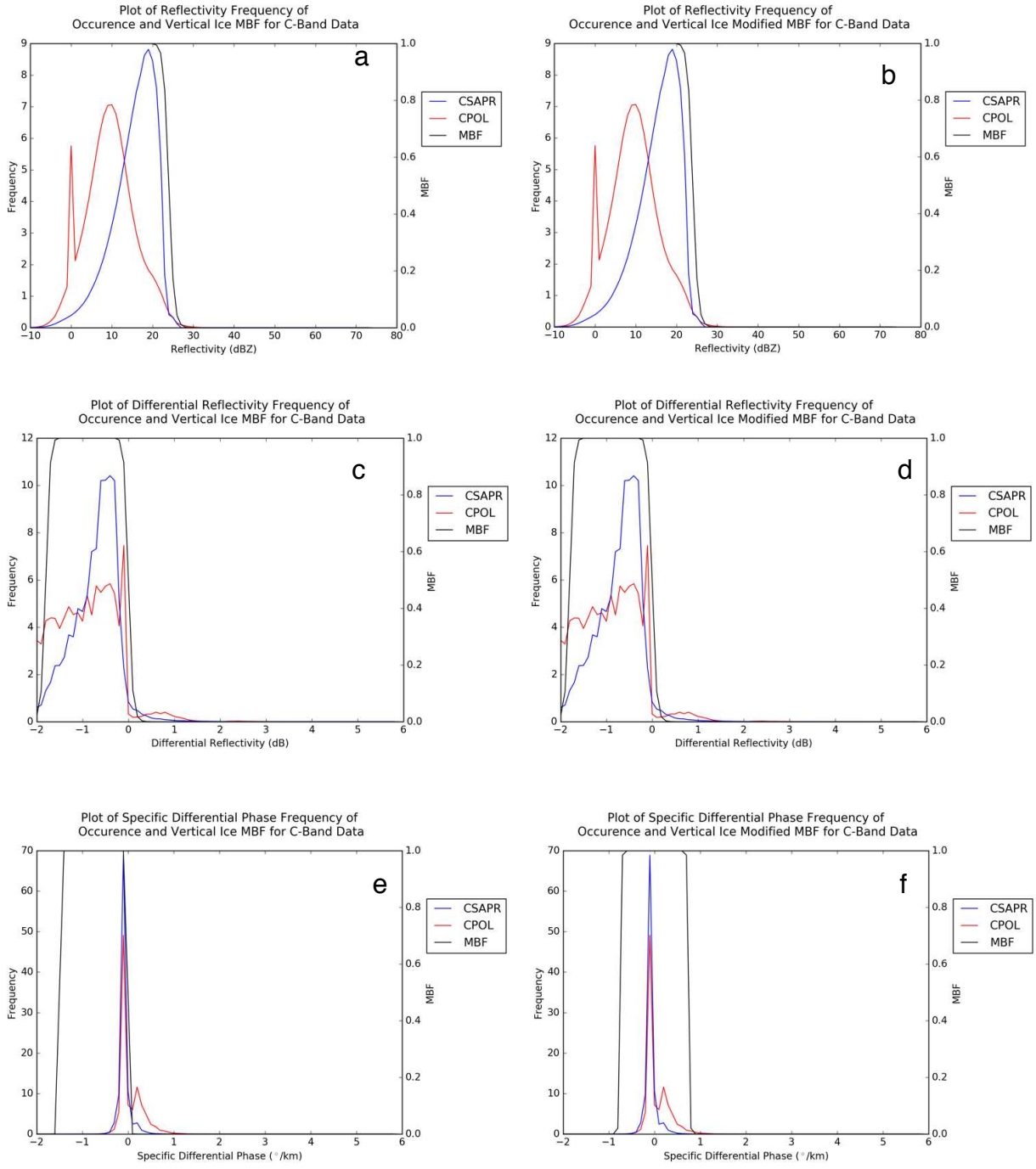

Figure 4.58: Plots of vertical ice MBFs (black) for the original (left) framework and the modified (right), with frequency of occurrence for CPOL (red) and CSAPR (blue) HID-identified vertical ice for (a,b) reflectivity, (c,d) differential reflectivity, and (e,f) specific differential phase.

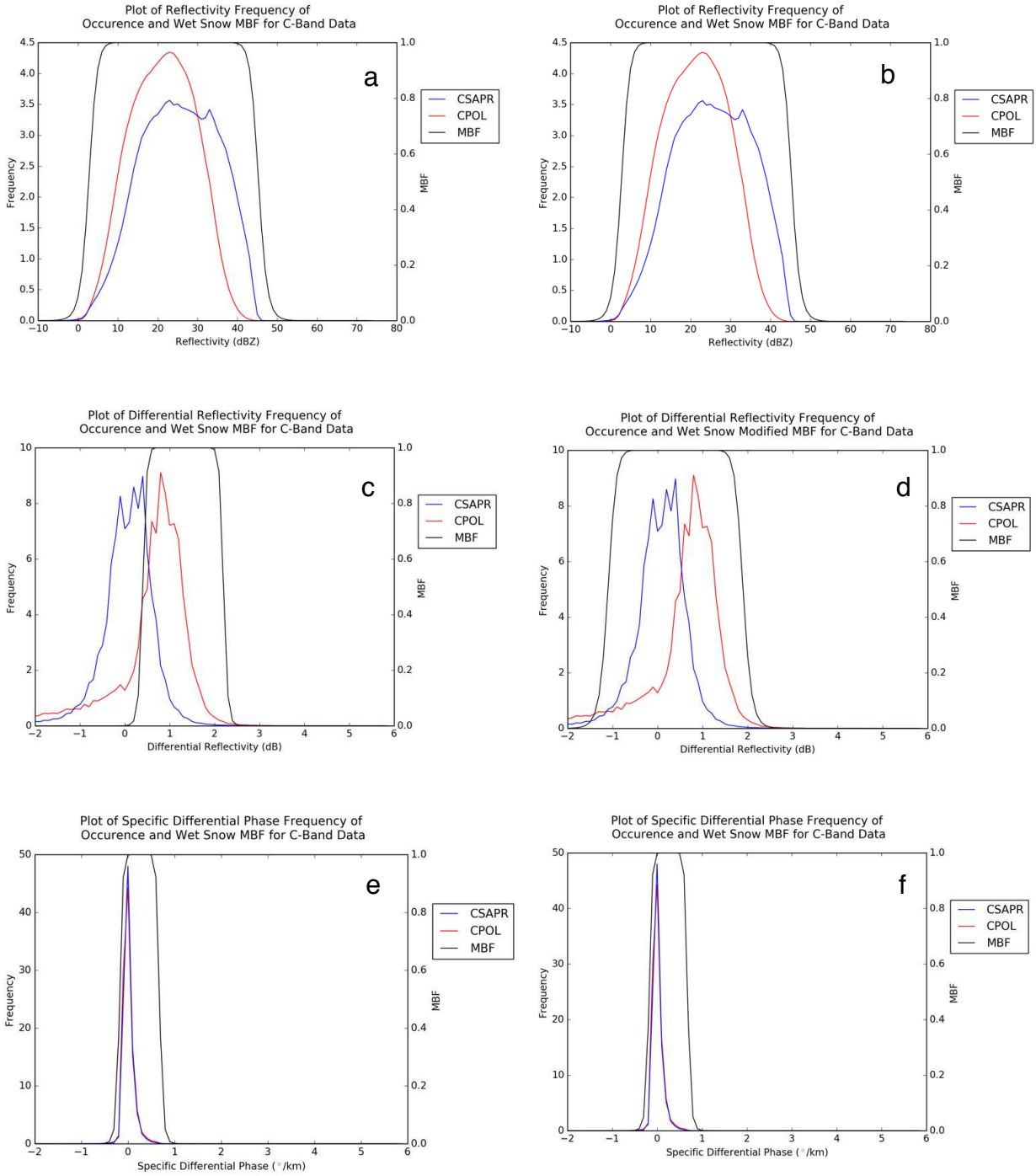

Figure 4.59: Plots of wet snow MBFs (black) for the original (left) framework and the modified (right), with frequency of occurrence for CPOL (red) and CSAPR (blue) HID-identified wet snow for (a,b) reflectivity, (c,d) differential reflectivity, and (e,f) specific differential phase.

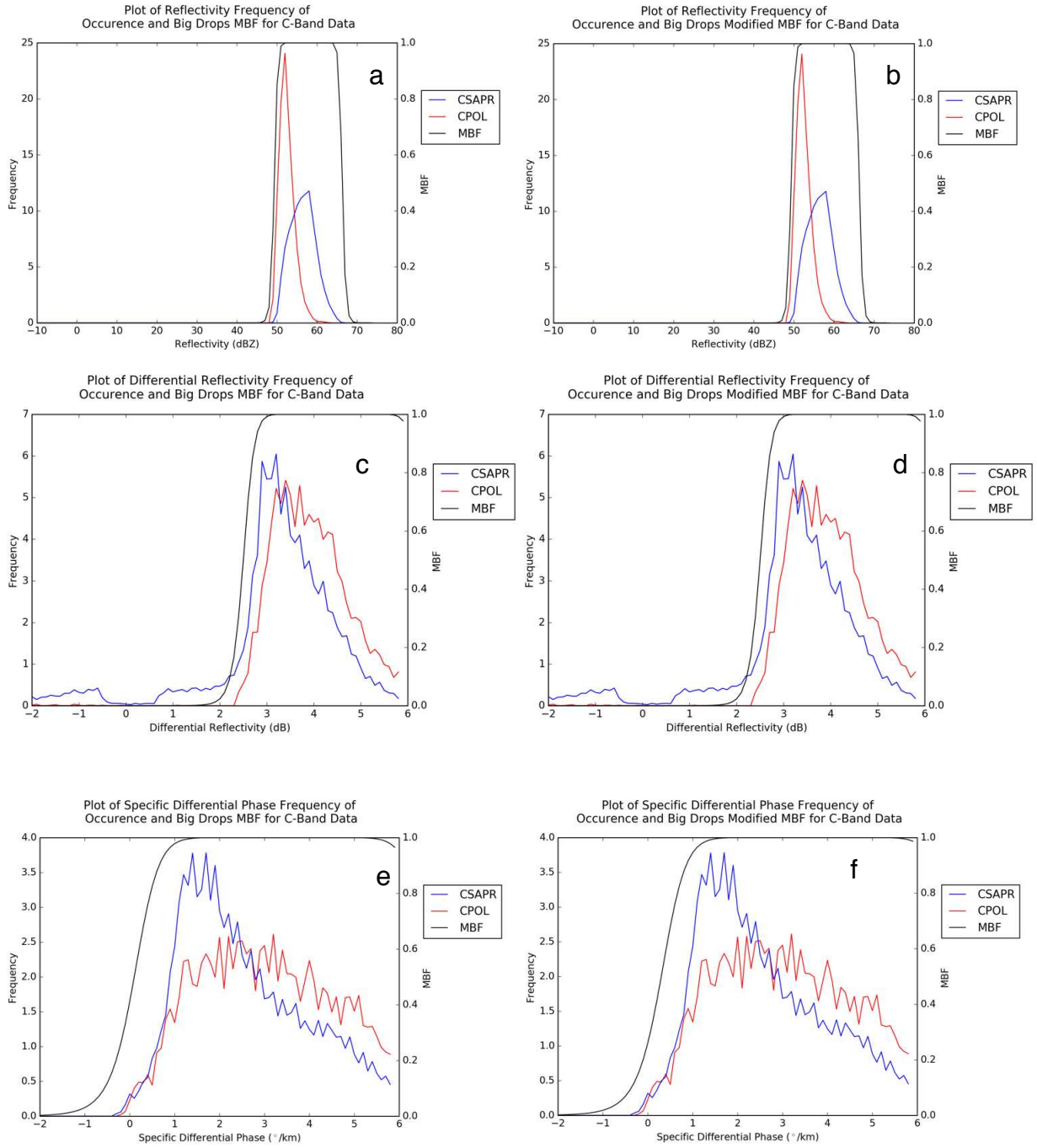

Figure 4.60: Plots of big drops MBFs (black) for the original (left) framework and the modified (right), with frequency of occurrence for CPOL (red) and CSAPR (blue) HID-identified big drops for (a,b) reflectivity, (c,d) differential reflectivity, and (e,f) specific differential phase.

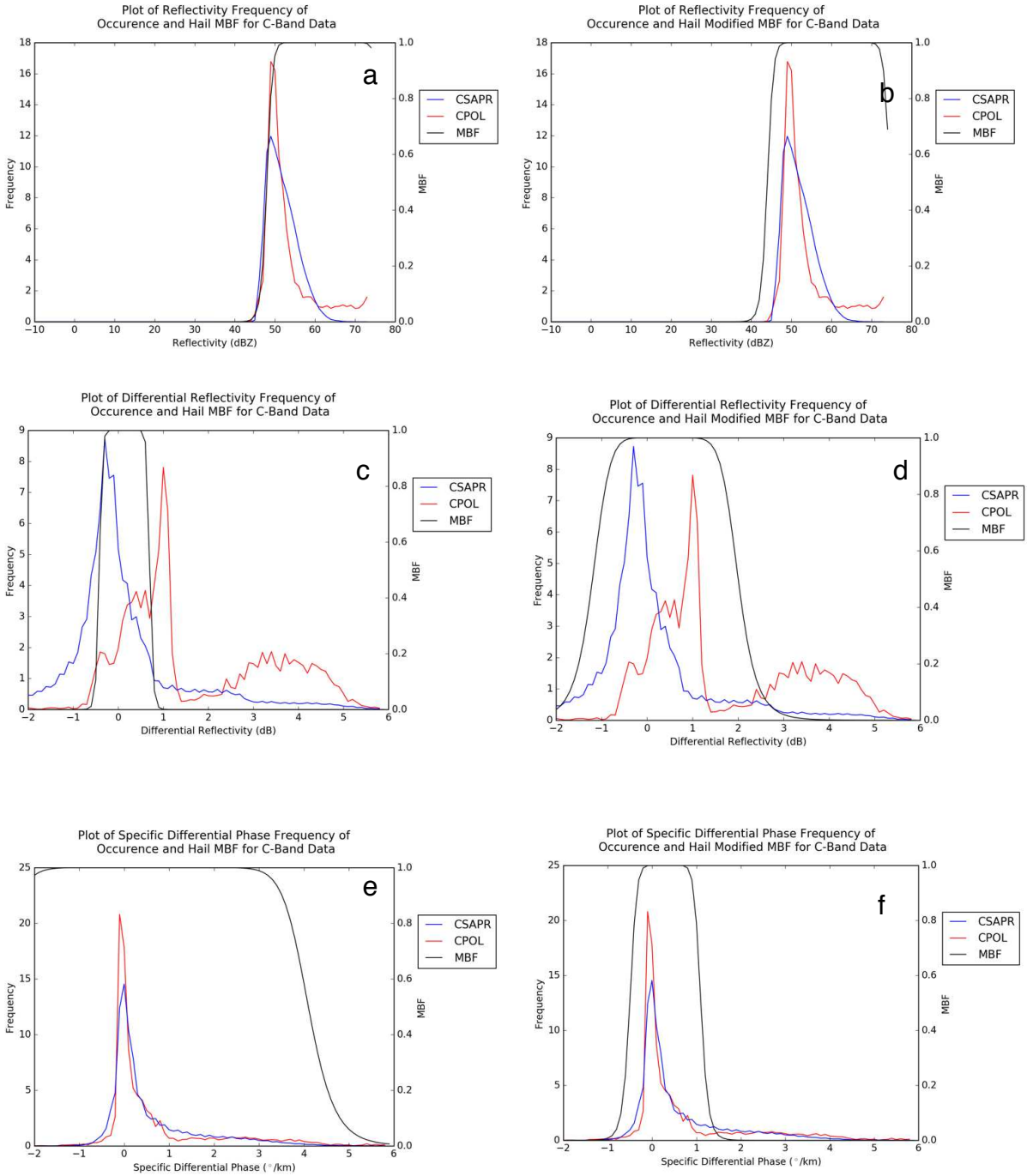

Figure 4.61: Plots of hail MBFs (black) for the original (left) framework and the modified (right), with frequency of occurrence for CPOL (red) and CSAPR (blue) HID-identified hail for (a,b) reflectivity, (c,d) differential reflectivity, and (e,f) specific differential phase.

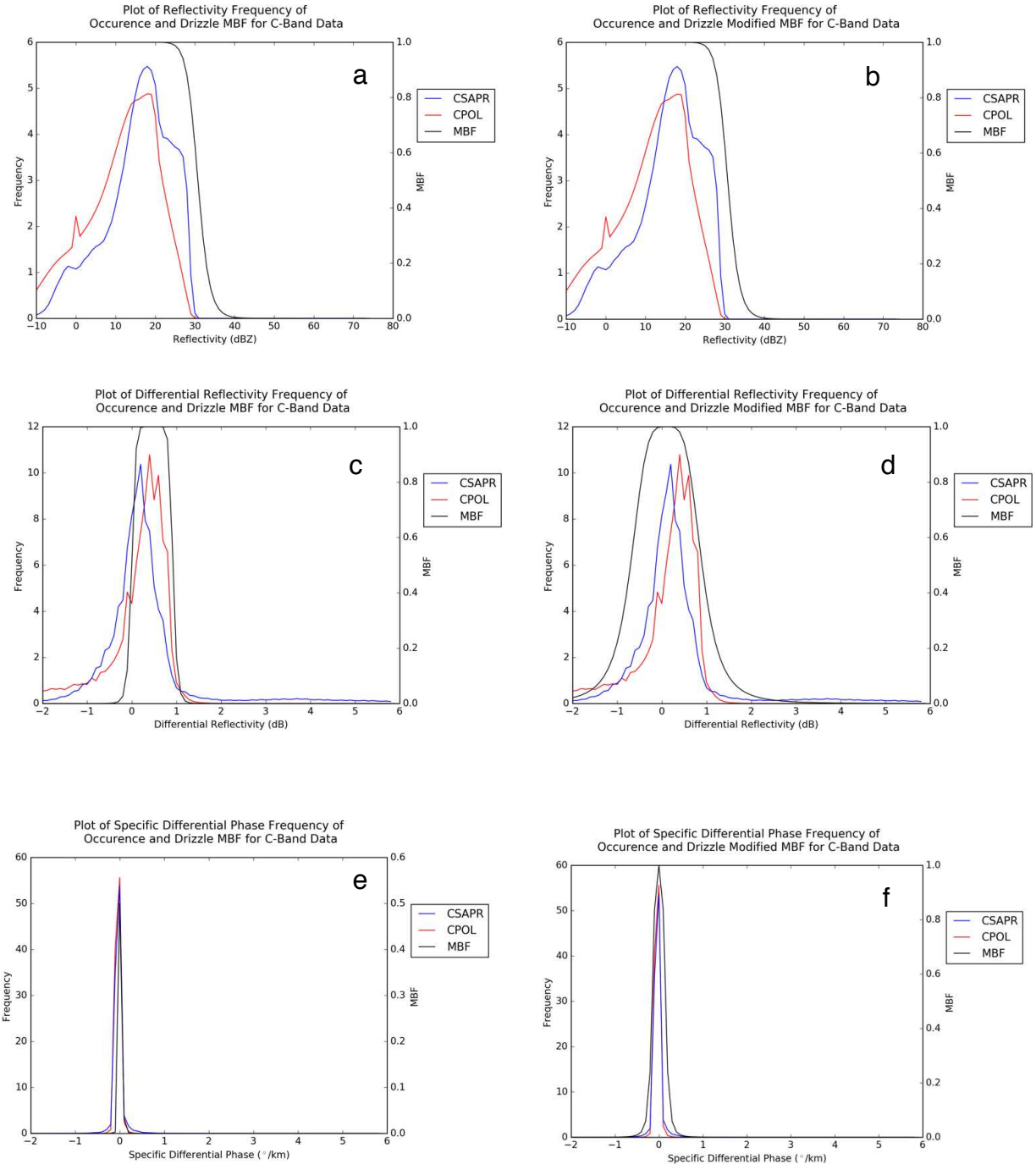

Figure 4.62: Plots of drizzle MBFs (black) for the original (left) framework and the modified (right), with frequency of occurrence for CPOL (red) and CSAPR (blue) HID-identified drizzle for (a,b) reflectivity, (c,d) differential reflectivity, and (e,f) specific differential phase.

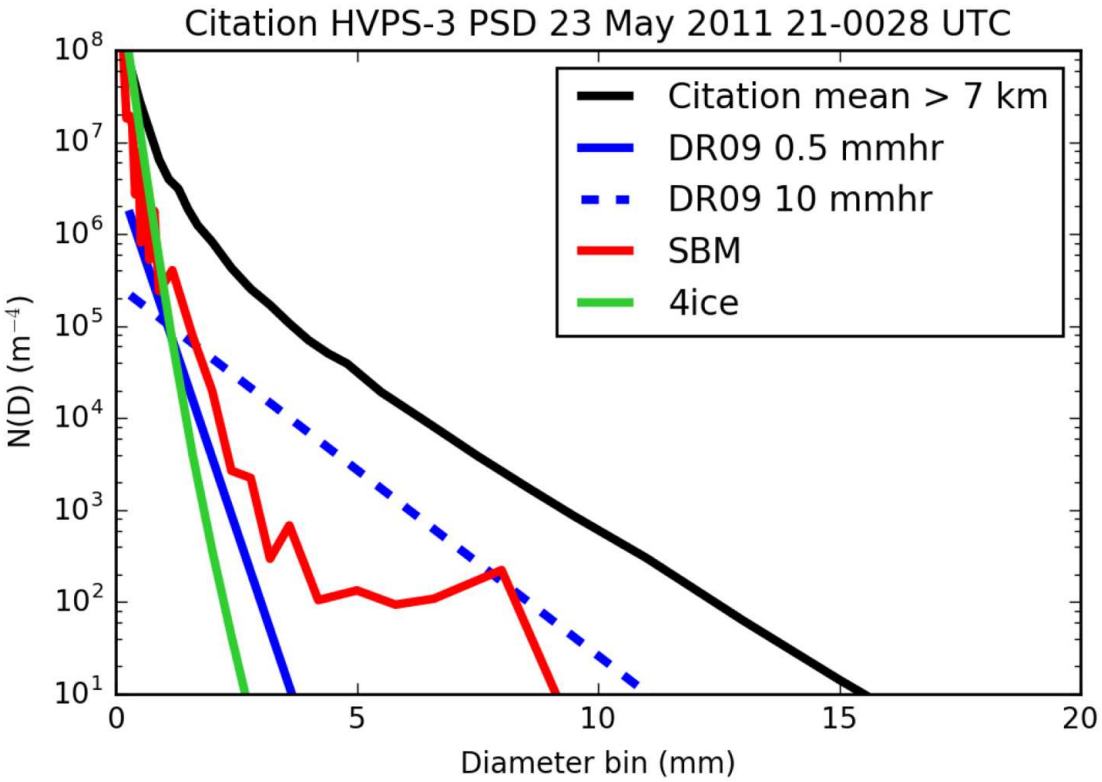

Figure 4.63: Figure 11 from M17. PSD curve for the Citation HVPS-3 snow aggregate data taken from 0021-0028 UTC on 23 May 2011 MC3E case (black line), and then equivalently-modelled curves for assumptions from DR09, with an assumed equivalent snowfall rate of 0.5 mm hr^{-1} and 10 mm hr^{-1} (for the solid and dotted blue lines, respectively), as well as the 4ICE modelled data (green line), and the SBM modelled data (red line). Modelled data was output at 10 minute intervals from 23 UTC 23 May 2011 to 0130 UTC 24 May 2011.

CHAPTER 5: CONCLUSIONS

A methodology for evaluating cloud resolving model performance by simulating radar observables and comparing to radar-based observations has been investigated. Evaluations were performed via HID. Thus, the sensitivity of the HID to the two regimes types employed (tropical MCS vs. mid-latitude supercell), and the two microphysical schemes utilized (Goddard 4ICE and HUCM SBM) were tested. Tests on the HID retrieval's uncertainty were performed via changing the input MBFs. Finally, characterizations of the uncertainty associated with the mean of the most frequently identified polarimetric radar variables changed with respect to height were made by changing axis ratio and canting angle assumptions input to the POLARRIS framework. These extensive tests, performed to evaluate both the HID retrieval and simulations of polarimetric data, were completed via the newly developed POLARRIS framework. This framework includes a forward model component, POLARRIS-f, where radar observables are simulated from CRM output combined with certain user assumptions (e.g. axis ratio, θ, and σ) which are used in a T-Matrix, Mueller matrix framework. An inverse component, iPOLARRIS, was also developed where the same retrievals can be applied to both observations and synthetic data generated by POLARRIS-f output. Though this work focuses on utilizing POLARRIS framework, the results could certainly apply to other attempts to simulate polarimetric radar variables based on models, including the addition of other radar wavelengths, and well as to investigate assumptions inherent in HID retrievals.

In summary, this work has resulted in the following important findings:

1. Axis ratio has a larger impact than canting angle assumptions on simulating radar polarimetric signatures. That is, when run through the range of potential

axis ratios, or θ and σ assumptions, changes in axis ratio result in larger changes to the resultant radar polarimetric signatures.

In both the sensitivity tests performed in the original T-Matrix, Mueller matrix framework, as well as the LUT sensitivity tests (where similar questions as to how radar observable values changed with respect to the values of the inputs, as well as a general check on the realism of the generated values were tested), it was found that axis ratio had a larger impact on the resulting polarimetric radar variables than did changes to the canting angle. Knowing this, several different axis ratios were run through POLARRIS-f and iPOLARRIS in the attempt to determine the value that would yield the closest comparison with observations, while generally only 1-2 different σ values were tested for each hydrometeor type. When examining the sensitivity tests of the most-frequently identified polarimetric radar variable value with respect to height, for each hydrometeor type, and for each regime, it seemed that Z_{dr} was the most impacted by the changes in θ, and σ. This was particularly the case for 4ICE, in both MC3E and TWP-ICE. The fact that SBM was not as affected likely points to the differences in the handling of PSDs in the model. If multiple axis ratio and canting angle assumptions are valid for each hydrometeor type (which seems likely as nature does not tend to follow a certain set of "rules") then especially if one wants to catch the range of potential Z_{dr} values for a given hydrometeor type, an axis ratio – size dependent relationship (and perhaps one for canting angle assumptions) need to be established (See Tables 4.1 and 4.2 for values input to the model here in for 4ICE and SBM, i.e. the values highlighted in blue).

2. Although 4ICE MC3E results were the most comparable with observations, results could have been improved. Defined axis ratio – size dependent relationships for aggregates and rain helped improve the comparability between

the model and observations. However, graupel and ice crystals utilized one set of axis ratio and canting angle assumptions simulated too small of reflectivity values, and often converged to a single Z_{dr} and K_{dp} value. It is clear that a single axis ratio applied to all data within a grid point will not reproduce the breadth of polarimetric data observed in nature, and axis ratio – size dependent relationships and/or canting angle assumptions driven by turbulence are needed to more appropriately simulate polarimetric variables.

Co-variance of radar observables with respect to one other revealed, especially for 4ICE (for both TWP-ICE and MC3E), illustrate the need to implement an axis ratio – size dependent relationship in order to better simulate the range of values seen in radar observations. Tests where relationships such as these were implemented (i.e. the Citation II axis ratio – size dependent relationships for snow aggregates and the Brandes et al. 2002 rain axis ratio – size dependent relationship), resulted in values that seemed to better match what was shown in observations. However, tests where only one axis ratio and one set of canting angle assumptions were used yielded much smaller ranges in general of all radar observables. That is, mostly in the case of 4ICE, tests with one axis ratio, one θ value, and one σ value, resulted in results converging in on one value of Z_{dr} and K_{dp}. Additionally, for 4ICE, reflectivity values were much too small. To an extent, the lack of turbulence applied to the simulated hydrometeors in the scattering simulations, and the chosen PSD probably influenced the lack of variability in the simulated polarimetric radar variable values. That is, the lack of ranges in Z_{dr} and K_{dp} values and too small of values in Z_h were potentially a result of the parameterized PSD (while the broader ranges in Z_h, Z_{dr}, and K_{dp} in SBM were a result of how the PSD developed), the lack of turbulence applied in the scattering simulations, or even the assumed density. The exact answer to these issues needs to be explored further, with

more tests done in the model and in the POLARRIS framework to help improve the simulations.

3. There are important differences in the results from SBM and 4ICE. Likely, these are due to the physical assumptions inherent in 4ICE (particle densities, prescribed PSDs) and the extra degrees of freedom in SBM (an evolving rime fraction and PSDs which are allowed to evolve organically).

SBM results were less clear in general than 4ICE (for both TWP-ICE and MC3E), where the stricter ranges of radar variables for each hydrometeor seen in observations was not as evident in SBM. The general reasoning for this may have to do with the inherent nature of more degrees of freedom present in the way SBM's PSD and rime fraction evolves. SBM results for TWP-ICE and MC3E were not nearly as comparable as was the case for 4ICE and observations, but both shared the issue of ill-defined polarimetric radar variable ranges for the four different hydrometeors simulated (aggregates, ice crystals, graupel, and rain).

4. Despite the inability to truly capture the range of values for polarimetric data seen in observations, the HID was fairly robust and revealed important model shortcomings such as the general overproduction of graupel and hail with respect to observations.

In the case of MC3E, 4ICE and SBM results were not night and day in terms of differences in one from the other for HID SFADs. Both compared relatively well with C-band radar observations, though some differences, such as the large production of hail and graupel compared to observations were noted. The largest difference between observations and MC3E model simulations was the almost complete void of any wet

snow in the transition region across the melting level that is clearly seen in the observations (in stratiform precipitation, though the convective precipitation also identified wet snow as well). This result is due to the fact that melting was not allowed in POLARRIS-f. Regardless of this fact, there is also the knowledge that the hour simulated by the model was not necessarily the same hour seen in the storm cycle in observations. Thus, the more important result from this thesis is rather the sensitivity of the resultant HID to a different handling of microphysics. 4ICE and SBM results were not identical, although they were more similar in for MC3E than for TWP – ICE. Thus the differences between the microphysics schemes also had a hand in overall hydrometeor identifications.

TWP-ICE HID SFADs were not nearly as comparable with observations (including the lack of wet snow, which makes sense given the above discussion), although after considerations of reflectivity RHIs for convective and stratiform regions for CPOL observations and for 4ICE and SBM, it was revealed that the 18 Z hour in the model contained more convection than the simulated hour in CPOL. This mismatch between model and observations HID SFADs would potentially diminish with a longer integration time that fully captured the storm lifecycle in both observations and model simulations.

5. The resulting HID can be quite sensitive to changes in the MBFs, where modifications can cause certain hydrometeor species to be identified much more frequently than others, such as favoring graupel and ice crystals over aggregate classifications. This was especially true for the simulated data, while observations were less sensitive to these changes.

Modifications to the MBFs produced interesting results in both the model and observationally-based HIDs. In general, for both regimes, for both microphysical schemes (bulk and bin), model simulations where the HID MBFs were modified resulted

in less identification of aggregates, in favor of the inclusion of more of the other ice hydrometeor types. A discussion of these differences can be found in Sec. 4.5, where the accompanying figures are Figs. 4.31 and 4.45 for the original- and modified-MBF cases for TWP – ICE, and 4.22 and 4.46 for the original- and modified-MBF cases for MC3E. However, it generally appeared as though increases in hail, low- and high-density graupel, and ice crystals (at mid- to upper-levels) were the reason behind decreases in aggregate production overall. The MC3E 4ICE simulation in particular was sharply impacted by the change in MBFs. Observations were less so affected by this change. Thus, the decision for values related to MBFs can have a large effect on the resulting HID classifications. Special care should be given to the values input to MBFs, and more simulations for other regions should be performed as well, to further test the sensitivity of the HID to MBF modification. It would be interesting to train the MBFs with not only more cases from each field campaign, but for more field campaigns in different locations (here, only a tropical MCS and a mid-latitude supercell are tested). This would also be a good methodology to apply to multiple radar wavelengths (i.e. include this study for S- and X-band as well).

In general, MC3E seemed to compare better between model output and observations than did TWP-ICE. One could impulsively then state that the regime chosen has a larger impact on the resultant HID simulated than the chosen microphysics scheme. However, it is difficult to say this with certainty since a short period of time (22 Z integrated hour for MC3E on 23 May 2011 and the 18 Z integrated hour for TWP-ICE on 23 January 2006) was chosen to simulate for each region. Additionally, especially for TWP – ICE, it would appear that the simulated convection in the model does not necessarily correspond to the same hour of convection in the storm cycle in observations (based on Figs. 4.31 and 4.32, as well as several simulated convective and stratiform RHI reflectivity scan for 4ICE and SBM – not shown). MC3E's simulated convection in both 4ICE and SBM were not far off from the convection

simulated in CSAPR observations, however, that does not mean that the exact same hour in time in the observations corresponded to the hour simulated (Fig. 4.22, as well as several simulated convective and stratiform RHI reflectivity scan for 4ICE and SBM – not shown). Although comparisons between model results and observation results were not always entirely comparable, details about the resulting simulations between 4ICE and SBM are still useful. Since changes were observed between 4ICE and SBM HID simulations (as well as simulations of the mean of the most frequently identified radar observable with respect to height), the type of microphysics scheme chosen does seem to have at least a measurable impact on the resulting HID (see Figs. 4.22, 4.31, 4.33-4.46).

5.1 FUTURE WORK

Much work has already been done to simulate radar observables. However, the "best" inputs for axis ratio, θ (mean canting angle), and σ (the amount to which a particle tumbles) are still uncertain. For graupel and ice crystals, only one set of axis ratio and canting angle assumptions are implemented, which resulted in unrealistically small Z_h, Z_{dr}, and K_{dp} values in the co-variance plots for 4ICE (and to an extent, SBM). This work has shown that these assumed inputs do indeed cause changes in the simulated polarimetric radar variable values, particularly in the case of 4ICE Z_{dr} values. Axis ratios overall seem to have a larger impact on the resultant simulated radar observables than does canting angle assumption changes. However, canting angle changes greater than 15° from one assumption to the next were not tested and should be investigated to find the extent to which axis ratio inputs have more influence than canting angle assumptions). More in situ data which identify axis ratio and canting angle relationships as related to particle size for ice hydrometeors would be helpful in making model results more comparable with observations. The methodology herein outlines how to utilize the POLARRIS framework for evaluating various axis ratio and canting angle assumptions,

thus the inclusion of more of the kinds of requested relationships would be easy to implement and test with observations.

HID has been shown to be a robust method for evaluating model output with respect to observations. Differences between HID SFADs for 4ICE and SBM for the two different regimes chosen show that the handling of the microphysics scheme can make a significant difference in HID classification. The regime itself also impacts resulting HID retrievals (that is, the specific microphysical processes characterizing those regimes influence HID retrievals). However, in order to further investigate which has a larger role in determining HID classification, longer time periods for multiple days for TWP-ICE and MC3E would need to be run. Additionally, it would be helpful to include more locations as well. No matter the location or microphysics simulated, however, model output in struggles to capture the occurrence of wet snow. This is due to the fact that melting hydrometeors were not simulated in the POLARRIS framework. Thus, tests that include melting hydrometeors should be pursued to help improve the simulation of the melting layer.

The MBFs also play a role in the HID classification. The HID classifications are fairly sensitive to modifications in the MBFs, particularly in the extent to which snow aggregates are or are not classified with respect to other ice hydrometeors. Thus, it was shown that there is a decent amount of uncertainty associated with the HID retrievals themselves to changing MBF inputs. The handling of these MBFs should be exercised with extreme caution, as changes can yield wildly different results. Herein, efforts were directed solely at testing the variability of the HID to changes in the MBFs. At the moment, with the simulated time periods and locations, the sample size is too small to call these modified MBFs a “new” set of MBFs to use as ground truth. In order to attack that challenge, longer time periods need to be considered from TWP-ICE and MC3E, as well as other locations.

REFERENCES

American Meteorological Society, cited 2017: “Velocity Aliasing”. Glossary of Meteorology. [Available online at http://glossary.ametsoc.org/wiki/Velocity_aliasing].

Barber, P., and C. Yeh, 1975: Scattering of electromagnetic waves by arbitrarily shaped dielectric bodies. *Appl. Opt.*, **14**, 2864-2872.

Beard, K. V., and C. Chuang, 1987: A new model for the equilibrium shape of raindrops. *J. Atmos. Sci.*, **44**, 1509–1524, doi: 10.1175/1520-0469(1987)044<1509:ANMFTE>2.0.CO;2.

Besic, N., J. Figueras i Ventura, J. Grazioli, M. Gabella, U. Germann, and A. Berne, 2016: Hydrometeor classification through statistical clustering of polarimetric radar measurements: A semi-supervised approach. *Atmos. Meas. Tech.*, **9**, 4425–4445, doi: 10.5194/amt-2016-105.

Brandes, E. A., G. Zhang, and J. Vivekanandan, 2002: Experiments in rainfall estimation with a polarimetric radar in a subtropical environment. *J. Appl. Meteor.*, **41**, 674–685, doi:10.1175/1520-0450(2002)041,0674:EIREWA.2.0.CO;2.

Bringi, V. N., and V. Chandrasekar, 2001, Polarimetric Doppler Weather Radar, Cambridge University Press, 636 p.

Bruggeman, D. A. G., 1935: Berechnung verschiedener physikalischer Konstanten von heterogenen Substanzen: I. Dielectrizitatskonstanten und Leitfahigkeiten der Mischkorper aus isotropen Substanzen (Calculation of difference physical constants of heterogeneous substances: I. Dielectric constants and conductances of mixtures of isotropic substances). *Ann. Phys.*, **24**, 636-679.

Carey, L. D., and S. A. Rutledge, 1996: A multiparameter radar case study of the microphysical and kinematic evolution of a lightning producing storm. *Meteor. Atmos. Phys.,* **59**, 33-66.

Caylor, J. and V. Chandrasekar, 1996: Time-varying ice crystal orientation in thunderstorms observed with multiparameter radar. *IEEE Trans. Geosci. Remote Sens.*, **34**, 847-858.

Debye, P., 1929: Polar Molecules. The Chemical Catalog, New York.

Dolan, B., and S. A. Rutledge, 2009: A theory-based hydrometeor identification algorithm for X-band polarimetric radars. *J. Oceanic Atmos. Technol.,* **46**, 1196-1213, doi 10.1175/2009JTECHA1208.1.

Dolan, B., and S. A. Rutledge, 2010: Using CASA IP1 to diagnose kinematic and microphysical interactions in a convective storm. *Mon. Wea. Rev.*, **138**, 1613-1634, doi:10.1175/2009MWR3016.1.

Dolan, B., S. A. Rutledge, S. Lim, V. Chandrasekar, and M. Thurai, 2013c: A robust C-

band hydrometeor identification algorithm and application to a long-term polarimetric radar dataset. *J. Appl. Meteor. Climatol.*, **52**, 2162-2186.

Collis, S., S. Giangrande, A. Theisen, M. Dunn, B. Dolan, A. Rowe, K. North, and P. Kollias, 2012: ARM radar status and products for MC3E: Remote sensing products to enable MC3E science. 2012 *ASR Science Team Meeting, MC3E Breakout*, Argonne National Laboratory, Lemont, IL, ASR. [Available online at https://asr.science.energy.gov/meetings/stm/2012/presentations/collismc3e.pdf]

Evaristo, R., Bals-Elsholz, T., Williams, E., Fenn, A. J., Donovan, M., and Smalley, D., 2013: Relationship of graupel shape to differential reflectivity: theory and observations, in: 2013 *AMS 29th Conference on Environmental Information Processing Technologies*, Austin, USA. [Available online at https://www.researchgate.net/profile/Raquel_Evaristo/publication/268147218_Relationship_of_Graupel_Shape_to_Differential_Reflectivity_Theory_and_Observations/links/54621aa70cf2c1a63c029462.pdf]

Garrett, T. J., S. E. Yuter, C. Fallgatter, K. Shkurko, S. R. Rhodes, and J. L. Endries, 2015: Orientations and aspect ratios of falling snow. *Geophys. Res. Lett.*, **42**, 4617–4622, doi: 10.1002/2015GL064040.

Giangrande, S.E., S. Collis, J. Straka, A. Protat, C. Williams, and S. Krueger, 2013: A summary of convective-core vertical velocity properties using ARM UHF wind profilers in OKLAHOMA. *J. Appl. Meteor. Cliimatol.*, **52**, 2278-2295, doi: 10.1175/JAMC-D-12-0185.1.

Goddard, J. W. F., S. M. Cherry, and V. N. Bringi, 1982: Comparison of dual-polarized radar measurements of rain with ground-based disdrometer measurements. *J. Appl. Meteor.*, **21**, 252–256, doi: 10.1175/1520-0450(1982)021<0252:CODPRM>2.0.CO;2.

Goddard, J. W. F., and S. M. Cherry, 1984: The ability of dualpolarization radar (copolar linear) to predict rainfall rate and microwave attenuation. *Radio Sci.*, **19**, 201–208, doi: 10.1029/RS019i001p00201.

Green, A. W., 1975: An approximation for shapes of large drops. *J. Appl. Meteor.*, **14**, 1578–1583, doi: 10.1175/1520-0450(1975)014<1578:AAFTSO>2.0.CO;2.

Guy, N., A. Gama, T. Lang, and P. Hein, 2015: artview: ARTview release 1.0. doi: http://dx.doi.org/10.5281/ zenodo.27358

Heistermann, M., and Coauthors, 2015: The emergence of open source software for the weather radar community. *Bull. Amer. Meteor. Soc.*, **96**, 117–128, doi:10.1175/BAMS-D-13-00240.1.

Helmus, J., T. Lang, K. North, P. Kollias, and S. Collis, 2015: Two novel, general purpose algorithms for unfolding Doppler velocities. *37th Conf. on Radar Meteorology*, Norman, OK, Amer. Meteor. Soc., https://www.ametsoc.org/ams/index.cfm/meetings-events/ams-meetings/37th-conference-on-radar-meteorology/.

Helmus, J.J. & Collis, S.M., 2016: The Python ARM Radar Toolkit (Py-ART), a Library for Working with Weather Radar Data in the Python Programming Language.

Journal of Open Research Software, **4(1)**, p.e25, doi: http://doi.org/10.5334/jors.119

Huang, G.-J., V. Bringi, S. van den Heever, and W. Cotton, 2005: Polarimetric radar signatures from RAMS microphysics. Preprints, 32nd Int. Conf. on Radar Meteorology, Albuquerque, NM, Amer. Meteor. Soc., P11R.6. [Available online at http:// ams.confex.com/ams/pdfpapers/96261.pdf.]

Iguchi, T., and Coauthors, 2012a: Numerical analysis using WRF-SBM for the cloud microphysical structures in the C3VP field campaign: Impacts of supercooled droplets and resultant riming on snow microphysics. *J. Geophys. Res.*, **117**, D23206, doi: 10.1029/2012JD018101.

Iguchi, T., T. Matsui, A. Tokay, P. Kollias, and W.-K. Tao, 2012b: Two distinct modes in one-day rainfall event during mc3e field campaign: Analyses of disdrometer observations and wrf-sbm simulation. *Geophys. Res. Lett.*, **39**(24), L24805, doi: 10.1029/2012GL053329.

James, C. N., and R. A. J. Houze Jr., 2001: A real-time four dimensional Doppler dealiasing scheme. *J. Atmos. Oceanic Technol.*, **18**, 1674–1683, doi:10.1175/1520-0426(2001)018,1674: ARTFDD.2.0.CO;2.

Jensen, M. P., and Coauthors, 2015: The Midlatitude Continental Convective Clouds Experiment (MC3E), *Bull. Amer. Meteor. Soc.*, 1667-1686, doi: 10.1175/BAMS-D-14-00228.1.

Jung, Y., G. Zhang, and M. Xue, 2008: Assimilation of simulated polarimetric radar data for a convective storm using the ensemble Kalman filter. Part I: Observation operators for reflectivity and polarimetric variables. *Mon. Wea. Rev.,* 136, 2228–2245, doi: *10.1175/2007MWR2083.1*.

Jung, Y., M. Xue, and G. Zhang, 2010: Simulations of polarimetric radar signatures of a supercell storm using a two-moment bulk microphysical scheme. *J. Appl. Meteor. Climatol.,* 49, 146–163, doi: 10.1175/2009JAMC2178.1.

Keenan, T., and R. E. Carbone, 1992: A preliminary morphology of precipitation systems in tropical northern Australia. *Quart. J. Roy. Meteor. Soc.*, **118**, 283-326, doi: 10.1002/qj.49711850406.

Keenan, T. D., L. D. Carey, D. S. Zrnic´, and P. T. May, 2001: Sensitivity of 5-cm wavelength polarimetric radar variables to raindrop axial ratio and drop size distribution. *J. Appl. Meteor.*, **40**, 526–545, doi: 10.1175/1520-0450(2001)040<0526:SOCWPR>2.0.CO;2.

Kennedy, P.C., Kleinkort, C., Huang, G.-J., Thurai, M., Newman, A., Hubbert, J., Rutledge, S., Bringi, V.N., Notaros, B.M., 2015: Preliminary results from the multi-angle snowflake camera and radar (MASCRAD) project. *AMS 37th Conference on Radar Meteorology*, Norman, OK, USA, 14–18 September 2015.

Khain, A. P. and Sednev IL., 1995: Simulation of hydrometeor size spectra evolution by water-water, ice-water, and ice-ice interactions. *Atmos. Res.*, **36**, 107-138, doi: 10.1016/0169-8095(94)00030-H.

Khain, A., P. Rosenfeld, U. Blahak, A. Ryzhkov, 2011: The role of CCN in precipitation and hail in a mid-latitude storm as seen in simulations using a spectral (bin) microphysics model in a 2D dynamic frame. *Atmos. Res.*, **99**, 129-146, doi: 10.1016/j.atmosres.2010.09.015.

Khain, A. P., and Coauthors, 2015: Representation of microphysical processes in cloud-resolving models: Spectral (bin) microphysics versus bulk parameterizations, *Rev. Geophys.*, **53**, 247-322, doi: 10.1002/2014RG000468.

Knight, C.A., and N.C. Knight, 1973: Conical Graupel. *J. Atmos. Sci.*, **30**, 118-124.

Kollias, P., and Tatarevic, A., 2017: User's Guide CR-SIM SOFTWARE v 2.2 (http://www.meteo.mcgill.ca/~aleksandra/CR-SIM/crsim-UserGuide-v2.0.pdf).

Kumjian, M.R., S. Mishra, S. E. Giangrande, T. Toto, A. V. Ryzhkov, and A. Bansemer, 2016: Polarimetric radar and aircraft observations of saggy bright bands during MC3E. *J. Geophys. Res. Atmos.*, **121**, 3584-3607, doi: 10.1002/2015JD024446.

Lang, S. E., W.-K. Tao, R. Cifelli, W. Olson, J. Halverson, S.R. Rutledge, and J. Simpson, 2007: Improving simulations of convective systems from TRMM LBA: Easterly and westerly regimes. *J. Atmos. Sci.*, **64**, 1141-1164, doi 10.1175/JAS3879.1.

Lang, S. E., X. Zeng, and Y. Li, 2011: Reducing the biases in simulated radar reflectivities from a bulk microphysics scheme: Tropical convective systems. *J. Atmos. Sci.*, **68**, 2306-2320, doi: 10.1175/JAS-D-10-05000.1.

Lang, S.E., W.-K. Tao, J.-D. Chern, D. Wu, and X. Li, 2014: Benefits of a fourth ice class in the simulated radar reflectivities of convective systems using a bulk microphysics scheme. *J. Atmos. Sci.*, **71**, 3583-3612, doi: 10.1175/JAS-D-13-0330.1.

Lerach, D. G., S. A. Rutledge, C. R. Williams, and R. Cifelli, 2010: Vertical structure of convective systems during NAME 2004. *Mon. Wea. Rev.*, **138**, 1695–1714.

Liao, L., and Meneghini, R., 2016: A Dual-wavelength radar technique to detect hydrometeor phases. *IEEE Trans. Geosci. Remote Sens.,* **54**, 7292-7298.

Lim S., V. Chandrasekar, and V. N. Bringi, 2005: Hydrometeor classification system using dual-polarization radar measurements; model improvements and *in situ* verification. *IEEE Trans. Geosci. Remote Sens.*, **43**, 792-801.

Lin, Y-L., R. D. Farley, and H. D. Orville, 1983: Bulk parameterization of the snow field in a cloud model. *J. Appl. Meteor.*, **22**, 1065-1092, doi: 10.1175/1520-0450(1983)022<1065:BPOTSF>2.0.CO;2.

Liu, H., and V. Chandrasekar, 1998: Classification of hydrometeor type based on multiparameter radar measurements. Preprints, Int. Conf. on Cloud Physics, Everett, WA, Amer. Meteor. Soc., 253–256.

Liu, H., and V. Chandrasekar, 2000: Classification of hydrometeor based on polarimetric radar measurements: Development of fuzzy logic and neuro-fuzzy systems, and in situ verification. *J. Atmos. Oceanic Technol.*, **17**, 140–164.

Matsui, T., and Coauthors, 2013: GPM satellite simulator over ground validation sites. *Bull. Amer. Meteor. Soc.*, **94**, 1653–1660, doi:10.1175/BAMS-D-12-00160.1.

Matsui, T., B. Dolan, S. Rutledge, W.-K. Tao, T. Iguchi, J. Barnum, and S. Lang, in preparation: POLARRIS: POLArimetric Radar Retrieval and Instrument Simulator. *J. Geophys. Res.*

Matthews, A., 2014: Storm microphysics and kinematics at the ARM – SGP site using Dual Polarized Radar Observations at Multiple Frequencies. *Master's Thesis, Department of Atmospheric Science, Colorado State University*, 107 pp.

Maxwell Garnett, J. C., 1904: Colours in metal glasses and in metallic films. *Philos. Trans. Roy. Soc. London*, **A203**, 285-420.

May, P.T., and A. Ballinger, 2007: The statistical characteristics of convective cells in a monsoon regime (Darwin, Northern Australia). *Mon. Wea. Rev.*, **135**, 82-92, doi: 10.1175/MWR3273.1.

May, P.T., J. H. Mather, G. Vaughan, K. N. Bower, C. Jakob, G. M. McFarquhar, and G. G. Mace, 2008: The Tropical Warm Pool International Cloud Experiment. *Bull. Amer. Meteor. Soc.*, **89**(5), 629-645, doi: 10.1175/BAMS-89-5-629.

Mohr, C. G., and L. J. Miller, 1983, CEDRIC—A software package for Cartesian space editing, synthesis and display of radar fields under interactive control. *Preprint 21st Conf. on Radar Meteorology*. Edmonton, Amer. Meteor. Soc., 569-574.

O'Brien, J. J., 1970: Alternative solutions to the classical vertical velocity problem. *J. Appl. Meteor.*, **9**, 197-203, doi: 10.1175/1520-0450(1970)009<0197:ASTTCV>2.0.CO;2.

Otto, T., 2007: On the Differenital Propagation Phase in Polarimetric Weather Radar Measurements. *Z conference of ITG commission 7.5 "Wave Propagation"*, Chemnitz, Germany, Information Technology Society Within VDE, 110-117, http://www.qucosa.de/fileadmin/data/qucosa/documents/5521/data/WFMN07_II_D4.pdf.

C. D. Peters-Lidard, and Coauthors, 2015: Integrated modeling of aerosol, cloud, precipitation and land processes at satellite-resolved scales. *Environ. Modell. Software*, **67**, 149-159, doi: 10.1016/j.envsoft.2015.01.007.

Pfeifer, M., G. C. Craig, M. Hagen, and C. Keil, 2008: A polarimetric radar forward operator for model evaluation. J. Appl. Meteor. Climatol., 47, 3202–3220, doi: 10.1175/2008JAMC1793.1.

Phillips, V., A. Khain, A. Pokrovsky, 2007: The Influence of Time-Dependent Melting on the Dynamics and Precipitation Production in Maritime and Continental Storm Clouds. *J. Atmos. Sci.,* **64(2)**, 338-359, doi: 10.117JAS3832.1.

Powell, S. W., R. A. Houze Jr., and S. R. Brodzik, 2016: Rainfalltype categorization of radar echoes using polar coordinate reflectivity data. *J. Atmos. Oceanic Technol.*, **33**, 523–538, doi:10.1175/JTECH-D-15-0135.1.

Pruppacher, H. R., and K. V. Beard, 1970: A wind tunnel investigation of the internal circulation and shape of water droplets falling at terminal velocity in air. *Quart. J. Roy. Meteor. Soc.*, **96**, 247– 256, doi: 10.1002/qj.49709640807.

Pruppacher, H.R., and R. L. Pitter, 1971: A semi-empirical determination of the shape of cloud and rain drops. *J. Atmos. Sci.*, **28**, 86–94, doi: 10.1175/1520-0469(1971)028<0086:ASEDOT>2.0.CO;2.

Putnam, B.J., M. Xue, Y. Jung, N. Snook, and G. Zhang, 2014: The Analysis and Prediction of Microphysical States and Polarimetric Radar Variables in a Mesoscale Convective System Using Double-Moment Microphysics, Multinetwork Radar Data, and the Ensemble Kalman Filter. *Mon. Wea. Rev.*, **142**, 141-162, doi: 10.1175/MWR-D-13-00042.1

Putnam, B.J., M. Xue, Y. Jung, G. Zhang, and F. Kong, 2017: Simulation of Polarimetric Radar Variables from 2013 CAPS Spring Experiment Storm-Scale Ensemble Forecasts and Evaluation of Microphysics Scheme. *Mon. Wea. Rev.*, **145**, 49-73, doi: 10.1175/MWR-D-15-0415.1.

Rinehart, R.E., 2010, *Radar for Meteorologists*, Rinehart Publications, 482 p.

Rutledge, S. A., and P. V. Hobbs, 1983: The mesoscale and microscale structure of organization of clouds and precipitation in Midlatitude cyclones. VIII: A model for the “seeder-feeder” process sin warm-frontal rainbands. *J. Atmos. Sci.*, **40**, 1185-1206. doi: 10.1175/1520-0469(1983)040<1185:TMAMSA>2.0.CO;2.

Rutledge, S.A., and P. V. Hobbs, 1984: The mesoscale and microscale structure and organization of clouds and precipitation in Midlatitude cyclones. Part XII: Adiagnostic modeling study of precipitation development in narrow cold-frontal rainbands. *J. Atmos. Sci.*, **41**, 2949-2972, doi: 10.1175/1520-0469(1984)041<2949:TMAMSA>2.0CO;2.

Rutledge, S.A., Williams, E. R., and T.D. Keenan, 1992: The Down Upper Doppler and Electricity Experiment (DUNDEE): Overview and Preliminary Results. *Bull. Amer. Meteor. Soc.*, **73**, 3-16, doi: 10.1175/1520-0477(1992)073<0003:TDUDAE>2.0.C0;2.

Ryzhkov, A., S. E. Giangrande, V. M. Melnikov, and T. J. Schuur, 2005a: Calibration issues of dual-polarization radar measurements. *J. Atmos. Oceanic Technol.*, **22**, 1138–1155, doi:10.1175/ JTECH1772.1.

Ryzhkov, A. V., T. J. Schuur, D. W. Burgess, P. L. Heinselman, and S. E. Giangrande, 2005b: The Joint Polarization Experiment: Polarimetric rainfall measurements and hydrometeor classification. *Bull. Amer. Meteor. Soc.*, **86**, 809–824, doi:10.1175/ BAMS-86-6-809.

Ryzhkov, A. V. and D. S. Zrnic, 2005: Radar polarimetry at S, C, and X bands: Comparative analysis and operational implications. Preprints, *32nd Conf. on Radar Meteorology*, Albequerque, NM, Amer. Meteor. Soc., 9R.3. [Available online at http://ams. confex.com/ams/pdfpapers/95684.pdf.]

Ryzhkov, A. V., M. Pinsky, A. Pokrovsky, and A. Khain, 2011: Polarimetric Radar Observation Operator for a Cloud Model with Spectral Microphysics. *J. Appl. Meteor. Climatol.*, **50**, 873-894, doi: 10.1175/2010JAMC2363.1.

Straka, J.M., D. S. Zrnic, and A. V. Ryzhkov, 2000: Bulk hydrometeor classification and quantification using polarimetric radar data: Synthesis of relations. *J. Appl. Meteor.*, **39**, 1341-1372.

Tao, W.-K., Wu, D., Matsui, T., Peters-Lidard, C., Lang, S., Hou, A., Rienecker, M., Petersen, W., and Jensen, M., 2013: Precipitation intensity and variation during MC3E: A numerical modeling study. *J. Geophys. Res. Atmos.*, **121**, 1278-1305, doi: 10.1002/2015JD023986.

Thompson, E. J., S. A. Rutledge, B. Dolan, V. Chandrasekar, and B. L. Cheong, 2014: A dual-polarization radar hydrometeor classification algorithm for winter precipitation. *J. Oceanic Atmos.*, **31**, 1457-1481.

Vivekanandan, J., W. M. Adams, and V. N. Bringi, 1991: Rigorous approach to polarimetric radar modeling of hydrometeor distributions. *J. Appl. Meteor.*, **30**, 1053-1063.

Vivekanandan, J., R. Raghavan, and V. Bringi, 1993: Polarimetric radar modeling of mixtures of precipitation particles. IEEE Trans. Geosci. Remote Sens., 31, 1017–1030, doi: 10.1109/36.263772.

Wang, Y., and V. Chandrasekar, 2009: Algorithm for estimation of the specific differential phase. *J. Atmos. Oceanic Technol.*, **26**, 2565–2578, doi:10.1175/2009JTECHA1358.1.

Wen, G., A. Protat, P. T. May, X. Wang, and W. Moran, 2015: A cluster-based method for hydrometeor classification using polarimetric variables. Part I: Interpretation and analysis. *J. Atmos. Oceanic Technol.*, **32**, 1320–1340, doi:10.1175/ JTECH-D-13-00178.1.

Zrnic, D. S., R. Raghavan, and V. Chandrasekar, 1994: Observations of copolar correlation coefficient through a bright band at vertical incidence. *J. Appl. Meteor.*, **33**, 45–52, doi:10.1175/ 1520-0450(1994)033,0045:OOCCCT.2.0.CO;2.

Zrnic, D. S., A. Ryzhkov, J. Straka, Y. Liu, and J. Vivekanandan, 2001: Testing a procedure for automatic classification of hydrometeor types. *J. Atmos. Oceanic Technol.*, **18**, 892-913, doi: 10.1175/1520-0426(2001)018<0892:TAPFAC>2.0.CO;2.